



Faculty of Health Sciences
Department of Pharmacy

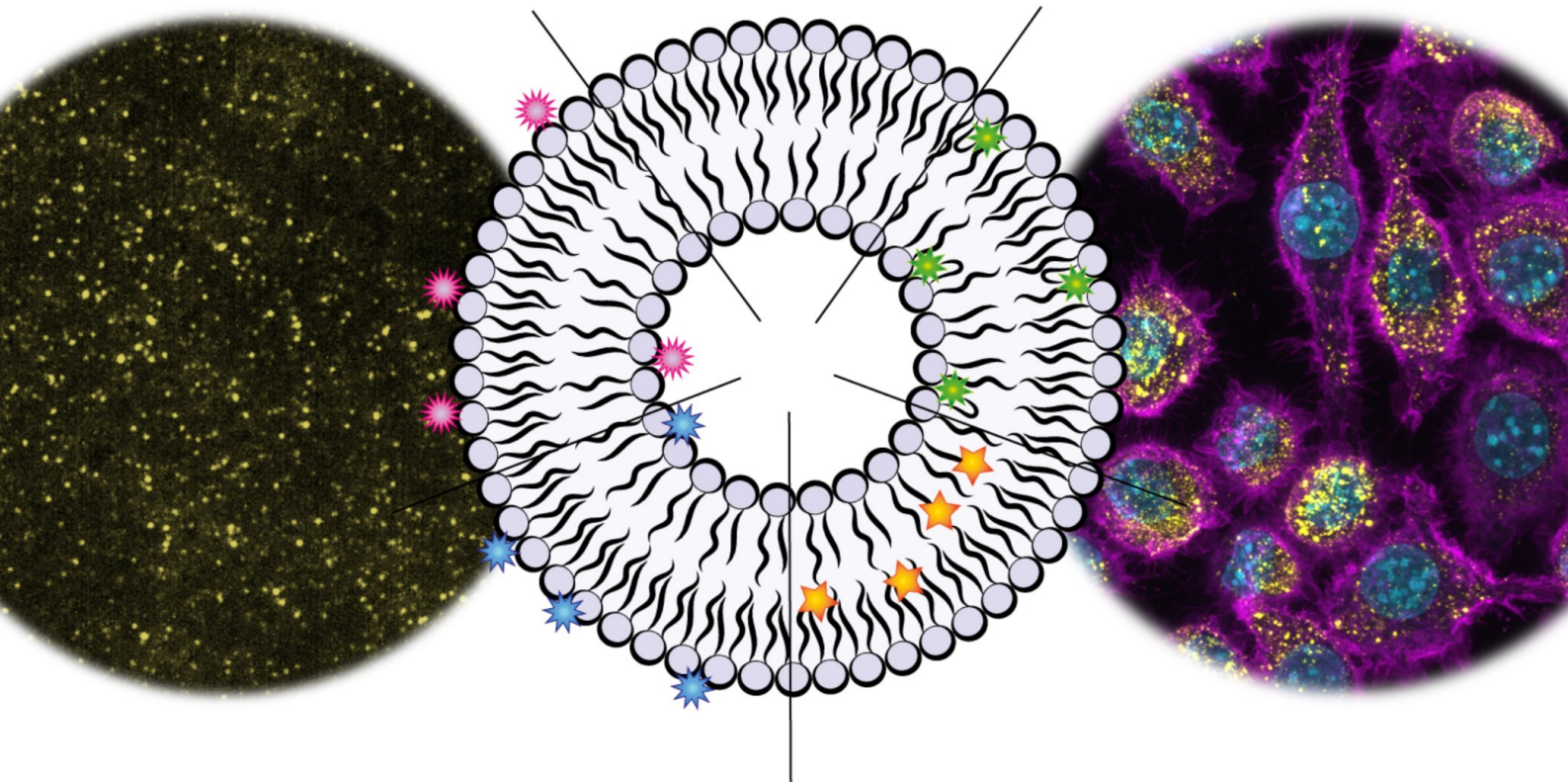
Microscopy Meets Nanomedicine: The Challenge of Liposomes

Selecting, Understanding, and Adapting Imaging Techniques
to Localize and Characterize Nanocarriers

—
Jennifer Cauzzo

A dissertation for the degree of Philosophiae Doctor

March 2022



A dissertation for the degree of Philosophiae Doctor

Microscopy Meets Nanomedicine: The Challenge of Liposomes

Selecting, Understanding, and Adapting Imaging Techniques
to Localize and Characterize Nanocarriers

Jennifer Cauzzo



Drug Transport and Delivery Research Group
Department of Pharmacy
Faculty of Health Sciences

UiT- The Arctic University of Norway

Tromsø – March 2022

SUPERVISORY TEAM

MAIN SUPERVISOR

Prof. Nataša Škalko-Basnet
Department of Pharmacy
Faculty of Health Sciences
UiT – The Arctic University of Norway
Tromsø, Norway

CO-SUPERVISOR

Assoc. Prof. Ann Mari Holsæter
Department of Pharmacy
Faculty of Health Sciences
UiT – The Arctic University of Norway
Tromsø, Norway

CO-SUPERVISOR

Dr. Aurélie Vigne
Elvesys – Microfluidics Innovation Center
Paris, France

EXAMINATION COMMITTEE

FIRST OPPONENT

Prof. Jessica Rosenholm
Department of Pharmacy
Faculty of Science and engineering
Åbo Akademi University
Åbo, Finland

SECOND OPPONENT

Prof. Ulrich Massing
Andreas Hettich GmbH &Co
Germany

LEADER OF THE COMMITTEE

Assoc. Prof. Elisabeth G Aarag Fredheim
Department of Pharmacy
Faculty of Health Sciences
UiT – The Arctic University of Norway
Tromsø, Norway

Acknowledgements

To my *research group* goes the first and foremost acknowledgement.

Thank you, Prof. **Nataša** Škalko-Basnet, for your support through the good, the bad and the ugly. For always allowing me to jump while knowing I had a strong safety net below my feet. You have challenged me, and you have given me space to grow through my own mistakes. You have taught me that the devil is in the details, but never to forget the bigger picture. You have been a true mentor.

Thank you, Assoc. Prof. **Ann Mari** Holsæter, for the research support in co-supervision and the representation in international meetings. Thank you, Prof. **Gøril** Eide Flaten and Assoc. Prof. **May Wenche** Jøraholmen, for the group discussions and especially for the input on my midway evaluation. Thank you, Prof. **Purusotam** Basnet and **Mona**, for welcoming me in your cell lab, and teaching me how to work confidently in it. Thank you **Skjalg**, **Cristiane**, **Martin** and **Kirill** for the help with bureaucracy and lab hiccups. Thank you, **Sybil**, for all the ideas and encouragement you always found the time to give me. Thank you, **Silje**, for choosing to work with me and supporting me in this project, **Eirik**, for the knowledge, pep talks, and samples exchange, and **Maxim**, for our lively greetings in the corridor. Thank you, **Lisa**, for being a true role model in science, for your strong spirit, and for being there no matter what, including revising my entire thesis beautifully. Thank you, **Alexandra**, for bringing your Latin spirit into my life, for your memes, and your ability to paint rainbows even in the grayest of Tromsø skies. Thank you, **Elena**, for being so effortlessly cool, for your delicious food, and our most exciting, relaxing, and unforgettable coffees. Thank you, **Laura**, for being the sister I never had, my emotional pillar, my knitting mentor, my cell culture keeper – for being my true friend.

Thank you Prof. **Guro** Forsdahl for leading such a great department and ensuring smoothness for my PhD. A special thanks goes to **Monica** and **Heidi** for the tremendous bureaucratic support, from start to finish. Thanks **Roy**, **Kenneth**, **Randi**, and **Tom**, from the Advanced Microscopy Core Facility, for teaching me all the microscopy techniques at your disposal and guiding me through the choices.

To my *DeLIVER-ITN* goes a warm acknowledgement.

Thank you, European Union and UiT – The Arctic University of Norway, for allowing such a team to come together. ITN stands for International Training Network: we have experienced

being citizens of the world, we have received training in multi-disciplinary science, and we have built a true resilient network. Thank you **Aurélie**, for helping me make the most out of my microfluidics secondment in Elvysys (Paris, France), and for supervising me from afar. Thank you, **David**, for going the extra mile to secure my research stay in Bayer AG (Leverkusen, Germany), and **Nedal**, for being a perfect lab buddy, an inspiration, and a friend. Thank you, Prof. **Patricia Lalor** and **Pantelitsa**, for the long-distance collaboration that we maintained in such challenging times. Thank you, **Sara**, for being an inspiration, such a pure soul, for believing in me, for our soul-reaching chats and the most delicious sandwiches ever; **Jakub**, for transmitting your calm aura and being the gym pal that I would choose if I ever did put my feet in the gym; and **Zofia**, for being my complain buddy: you just get me and validate my views of the world. Thank you, **Eva, Rita, Sherry, Alessandra, Lianne,** and **Matteo**, for the great time, experiences, support, and memes we shared. Thank you to the Nanoscopy Research Group at UiT for the several collaborations we established, with a warm mention to Assoc. Prof. **Balpreet** Singh Ahluwalia, Assoc. Prof. **Krishna** Agarwal, **Nikhil, Azeem, Sebastian, Luís** and **Ida**. Last but not least, thank you to the *McTeam* for our long-lasting collaboration, our brainstorming sessions, the long experiment days, and the occasional fancy dinners. Hence, thank you, Prof. **Peter** McCourt, **Larissa, Karolina, Christopher, Tetyana**, and the honorary members **Eike** and **Philippe Alexander**.

To the people that inspired me to pursue a PhD, I save a place in my heart. Thank you Assoc. Prof. **Massimiliano** Pio Di Cagno and Prof. **Nicola** Realdon, for the first sneak peek into research. Thanks to you I was drawn to pharmaceutical technology, as it is the duty of a pharmacist to deliver drugs, and I found out about the existence of a certain place called Tromsø. Thank you, **Elisa**, for guiding my first steps in the lab and inspiring me to proceed on my own, and **Selenia**, for your honest insights on the PhD. Thank you, **Barbara**, for being such a lab rockstar and the most supportive and genuine friend. Thank you to all the teachers and professors that really taught me well, with a special mention to Cristina Marcon, Matteo Sbrissa, Daniela Taffara, Patrizia Morabito, and Flavia Fommei. Finally, thank you, **Simone**, my dear cousin, for our ever-lasting silent competition that brought us from kindergarten to PhD (literally submitted on the same day). You are the brightest of minds and the kindest of hearts.

To my closest and oldest friends in the world goes the first personal mention.

A warm thank you to *The White Whales* and the *Bananas*, always with me from afar. Grazie **Alice** per avere sempre la parola giusta al momento giusto, con un pizzico di umorismo che ci stà, **Beatrice** per le migliori chiacchiere notturne nella Eva che ci manca tanto, e **Valentina** per essere l'altra metà del mio cervello. Grazie balene albine per non farmi sentire come una terrina di insalata senza insalata. Grazie **Eleonora** per essere il mio *Panda 1 2 3* della situazione, dall'asilo all'esame di stato e oltre. Grazie **Giulia**, perchè il tuo coraggio in tutte le tue scelte di vita mi è sempre stato di ispirazione. Grazie **Isabella**, per avere sempre trovato tempo per me (e per aver attirato già al mio primo anno la miglior aurora che io abbia visto). Grazie **Elena** ed **Ilaria** per la vostra spettacolare organizzazione di eventi e per essere sempre riuscite ad incastrarmi nei vostri piani. Grazie ragazze per avermi fatto sentire che l'Italia è ancora casa mia.

A big shout out goes to *The Seventh Semester @unipd*.

Le storie che abbiamo vissuto all'università sono tra i più bei ricordi che ho e in occasione di questa tesi vi lascio una lista di *Se Ne Sbattono*: il Taxi, il Momà, le reazioni da bilanciare, La Capannina, la tossica, il cortile interno a farmacia, il treno delle 6.05, cucchiaino e cucchiaino, i navigli. Grazie **Serena, Michele, Francesco, Martina, Isabella, Francesco, Licia, Elena, Enrico, Carlo, Sara** ed **Eleonora**.

For all the friends I made here in Tromsø I save a special mention.

Thank you, **Hilde** for welcoming me in your house as a daughter, I could not have never expected my landlady to become such a dear friend, and for taking care of my family as your own. To all my Tromsø friends that I have not mentioned already a warm thank you: Fabrizio, for always making me feel at home; **Nina, Merete, João, Chris, Alex, Margherita** and **Antal**, for taking me out of the lab, straight into the party. Skål to all the good food and wine we shared! May the *doors* of Valhalla open for us warriors! Thank you, **Joseph, Mette, Matteo, Iren**, and **Elisabeth** for such a great welcome of a lost ERASMUS student; **Philippe**, for shattering all my prejudice and being the second half to my second half; **Helene, Julia**, and the *TODOS* crew for the many nice gatherings. You all have made the long day look brighter and the long night look lighter.

To my family goes the biggest possible acknowledgement.

Alla mia famiglia devo il più grande dei ringraziamenti. Grazie di avermi lasciato scegliere la mia strada. Anche se mi ha portato lontano da voi, vi ho sempre sentiti vicini e se sono qui oggi è per il sostegno e la fiducia che mi avete dato. Mamma, sei la mia eroina. So che non ti è mai servito che venissi in Norvegia per sentire il vento freddo sulla pelle, hai sempre sentito quello che sento io. Tutta la forza che hai dimostrato in questi anni è inestimabile, spero di averne preso anche solo un briciolo da te. Papà, sei la mia roccia. Mi hai trasmesso la passione per gli esperimenti e per risolvere i problemi. Vorrei avere la tua calma e sangue freddo per affrontarli da me, ma so anche che per qualsiasi cosa tu ci sei sempre. Grazie ai miei cari zii, a mia cugina, alla mia figlioccia, alla *Compagnia dell'Orso* e alla *Compagnia della Lucia* per tutto il supporto che avete dato ai miei genitori. E ora vi nomino tutti perchè meritate il Vostro nome in grassetto: **Zaula e Roberto, Daniela e Flavio, Katia, Marta, Mariangela e Girolamo, Antonella e Renato, Emanuela e Bruno, Cristina e Massimiliano, Sofia e Cristiano, Mariangela, Luigina, Giuliana e Claudio, Alessandra e Renato, Giulia e Luca, Lucia e Umberto, Jessica, Simone, Nicola, Lisa, Emanuela e Bruno, Silvia.**

To the new half of my family goes the warmest obligations.

O meu mais sincero obrigada por me terem acolhido como se vossa filha eu fosse e como se a minha família do vosso sangue partilhasse. Por nos terem encantado com a vossa linda terra, gastronomia e cultura. Que sejam estas as raízes de uma robusta árvore. Obrigada, **Luísa, Jorge, Joana, São, Lince e Mimi.**

The PhD journey can be a very lonely place, even among amazing people. Still, one special person made sure I never felt truly alone. Thank you, **Pedro**, for walking me through the snowstorm, even when I was absolutely sure I was not going to make it, you stayed by my side and made me believe. And you were right, we did make it through the preface of our book.

My final thought goes to my grandparents.

Grazie **Assunta ed Elvio, Adele e Silvio.** My heart felt you guarding my journey as if you were physically walking it with me. You are my strongest inspiration. I dedicate this work to you.

Tromsø, March 2022



«Misura ciò che è misurabile,
e rendi misurabile ciò che non lo è»

«Measure that which is measurable
and make measurable that which is not»

– Galileo Galilei –

Table of Contents

Abstract	I
List of Abbreviations.....	III
List of papers	V
Authors' Contributions.....	VI
1 Introduction.....	1
1.1 Nanomedicine and Drug Delivery.....	1
1.1.1 Nanomedicine History and Hype	1
1.1.2 Properties and Preparation of Nanomaterials	4
1.1.3 Liposomes as Lipid-based Nanocarriers.....	7
1.2 Systemic Administration of Drugs and Body Defenses	10
1.2.1 Administration Route challenge for (Lipid-based) Nanomedicine.....	10
1.2.2 Cellular Internalization and Dispatch	14
1.3 Localizing and Following Nanocarriers	16
1.3.1 Characterization of Nanocarriers in Suspension	17
1.3.1.1 Properties of Nanocarriers in Suspension	17
1.3.1.2 Gold Standard Methods and Associated Challenges	20
1.3.2 Characterization and Imaging of Immobilized Nanocarriers	23
1.3.2.1 Background Theory of Microscopy for Nanomedicine.....	23
1.3.2.2 Gold Standard Imaging Methods and Associated Challenges	28
1.3.3 Fluorescence-based Imaging of Nanocarriers.....	30
1.3.3.1 Fluorescence as a Property of Matter	30
1.3.3.2 Use of Fluorescence in Biological Sciences.....	32
1.3.3.3 Super Resolution Fluorescence Microscopy	35
1.3.4 Label-free Light Microscopy on Nanomedicine	41
1.3.4.1 Phase Property of Light and Light Sources	41
1.3.4.2 Quantitative Phase Microscopy (QPM) in Biological Sciences	43
1.3.5 Fate of Nanocarriers in Biological Environments.....	44
1.3.5.1 In Vitro Models and Cell Selection.....	44
1.3.5.2 Tracking Nanomedicine Fate In Vitro	45
2 Aims.....	49

3	Summary of Papers	51
3.1	Paper I.....	51
3.2	Paper II (Manuscript).....	53
3.3	Paper III.....	55
3.4	Paper IV (Manuscript).....	57
4	Results and Discussion	59
4.1	Choice and Preparation of Nanocarriers.....	59
4.2	Formulation of Trackable Liposomes	61
4.3	Characterization of Liposomes	66
4.3.1	Conventional Characterization.....	66
4.3.2	Nanoparticle Immobilization for Imaging	67
4.3.3	Fluorescence-Based Characterization	68
4.3.4	Label-Free Characterization	73
4.3.5	Combination of Fluorescence and Label-Free Imaging.....	76
4.4	Internalization of Liposomes	78
4.4.1	Indirect Approaches	78
4.4.2	Fluorescence-Based Batch-Mode Approach	79
4.4.3	Fluorescence-Based Single-Cell Approach	85
4.4.4	Combination of Fluorescence and Label-Free Imaging.....	88
5	Conclusions.....	91
6	Future Perspectives.....	93
7	References.....	95

Abstract

Nanocarriers have been the success story of this century, bringing many medical advances through better diagnostics and improved drug therapy. Yet, many of the promising preclinical findings were never translated into clinical success, consequently slowing drug development as well increasing its financial burden. By predicting the nanoparticle fate, already at in vitro stage and in a reliable manner, the disappointment of suboptimal in vivo outcome could be avoided. To tackle the challenges of in vitro settings, this project aimed at gaining deeper insight on the interaction between nanocarriers and biological environment. Specifically, advance microscopy tools were used in this work to visualize, characterize, and follow the biological fate of nanocarriers. In what can be seen as a back-to-basics approach, liposomes were chosen as model nanocarriers for their versatility, biocompatibility, and clinical relevance.

From the pharmaceutical perspective, attention was given to validate and assure optimal characteristics of liposomes, always first resorting to conventional characterization methods e.g., based on dynamic light scattering. When including a fluorescent molecule in the liposomal formulation, the interplay between the different components of the nanosystem were assessed to validate the specificity of tracking. Fluorescence dye and nanocarrier were found to affect each other's properties in a manner dependent on the environmental conditions (e.g., temperature, time, medium, and dye-specific chemistry). The fluctuations of fluorescence in the sample were further analyzed through image processing algorithms to obtain super resolution information from a diffraction-limited multi-frame acquisition. Five of these computational algorithms were applied and compared in terms of background suppression, artifact reconstruction, and resolution enhancement. In parallel, to overcome some of the disadvantages often linked to the use of fluorescence (e.g., physicochemical instability and photobleaching of the fluorophore), quantitative phase microscopy was optimized as a complementary label-free technique for the localization and characterization of liposomes. Immobilized nanocarriers (in their hydrate state) could be followed over time in terms of sphericity, integrity, and size, independently from any fluorescent signal. Finally, fluorescence and label-free imaging were combined to determine the integrity of liposomes in nanofibers for topical administration. Images obtained with confocal microscopy and

scanning electron microscopy were directly correlated without the need to apply any distortions.

To understand the behavior of liposomes in cell culture, their internalization was followed using high throughput screenings, based on flow cytometry. Between 4 and 6 hours of treatment, all cells were found to emit the specific fluorescence of the liposome labeling, and the growing intensities did not show saturation of the internalization within the 24 hours of the experiment. These batch-mode results were validated in flow imaging and the timepoints of 4 and 24 hours were considered further for imaging experiments. PEGylated and naked liposomes were compared in terms of intracellular localization (through confocal imaging) and overall cellular response and stress (through ultrastructural morphological analysis on transmission electron microscopy), on high-phagocytic and low-phagocytic cells. Finally, direct volumetric correlation was attempted, discussing the power of imaging tools in detecting differences in nanomedicine behavior, as well as benefits and limitations of the methods involved.

List of Abbreviations

API	Active Pharmaceutical Ingredient
B&C	Brightness and Contrast
CCD	Charge-Coupled Device
CLSM	Confocal Laser Scanning Microscopy
CMOS	Complementary Metal Oxide Semiconductor
DDS	Drug Delivery System
DLS	Dynamic Light Scattering
dSTORM	Direct Stochastic Optical Reconstruction Microscopy
ESI	Entropy-based Super-resolution Imaging
FCM	Flow Cytometry
FF-SRM	Fluorescence Fluctuation Super Resolution Microscopy
fPALM	Fluorescence Photoactivation Localization Microscopy
HAWK	Haar Wavelet Kernel
LSCM	Light Scanning Confocal Microscopy
Lip	Liposomes
LUT	Lookup Table
MUSICAL	MULTiple Signal Classification ALgorithm
MW	Molecular Weight
NF	Nanofibers
NTA	Nanoparticle Tracking Analysis
NO	Nitric Oxide
PdI	Polydispersity Index
PEG	Polyethylene Glycol
PI	Propidium Iodide
PLL	Poly-L-lysine
PSF	Point Spread Function
PTLS	Pseudothermal Light Source
QPM	Quantitative Phase Microscopy

RES	Reticuloendothelial System
ROI	Region of Interest
RT	Room Temperature, 25°C
SACD	Super-resolution imaging based on Auto-Correlation two-step Deconvolution
SEM	Scanning Electron Microscopy
SIM	Structured Illumination Microscopy
SMLM	Single Molecule Localization Microscopy
SNR	Signal-to-Noise Ratio
SOFI	Super-resolution Optical Fluctuation Imaging
SPC	Soy Phosphatidylcholine (Lipoid S100)
SRM	Super Resolution Microscopy
SRRF	Super-Resolution Radial Fluctuations imaging
STED	Stimulated Emission Depletion
TEM	Transmission Electron Microscopy
TIR	Total Internal Reflection

The four fluorescently labeled phospholipids used are mentioned using the first letter of the name of their fluorescent moieties:

C (18:0 Cy5-PE)

1,2-distearoyl-sn-glycero-3-phosphoethanolamine-N-(Cyanine 5)

N (14:0-06:0 NBD-PC)

1-myristoyl-2-{6-[(7-nitro-2-1,3-benzoxadiazol-4-yl)amino]hexanoyl}-sn-glycero-3-phosphocholine

R (16:0 Liss Rhod PE)

1,2-dipalmitoyl-sn-glycero-3-phosphoethanolamine-N-(lissamine rhodamine B sulfonyl) (ammonium salt)

T (TopFluor®-PC)

1-palmitoyl-2-(dipyrrometheneborondifluoride)undecanoyl-sn-glycero-3-phosphocholine

List of papers

PAPER I

J. Cauzzo, M. Nystad, A. M. Holsæter, P. Basnet, N. Škalko-Basnet. Following the Fate of Dye-Containing Liposomes In Vitro. *Int J Mol Sci* **2020**, *21*, 4847. doi: 10.3390/ijms21144847

PAPER II (Manuscript)

I. S. Opstad*, S. Acuña*, L. E. Villegas Hernandez*, **J. Cauzzo**, N. Škalko-Basnet, B.S. Ahluwalia, K. Agarwal. Fluorescence fluctuations-based super-resolution microscopy techniques: an experimental comparative study. *arXiv preprint arXiv:2008.09195* **2020**.

*These authors contributed equally to the project

PAPER III

J. Cauzzo*, N. Jayakumar*, B.S. Ahluwalia, A. Ahmad, N. Škalko-Basnet. Characterization of Liposomes Using Quantitative Phase Microscopy (QPM). *Pharmaceutics* **2021**, *13*, 590. doi:10.3390/pharmaceutics13050590

*These authors contributed equally to the project

PAPER IV (Manuscript)

J. Cauzzo*, N. Darif*, L. V. Schulte-Werning, E. A. Lindeløff Rustad, A. M. Holsæter, Y. Schwab, N. Škalko-Basnet. Correlative microscopy provides insights on localization, internalization, and subcellular trafficking of liposomes. Manuscript.

*These authors contributed equally to the project

Authors' Contributions

As shown in §List of publications, this work bears the contribution of several collaborators which have shared with me the workload and guided me through my PhD journey. Although not wishing to take away their credit, I am taking responsibility for the work that this thesis brings together. I will be telling the story from my perspective, resorting to the first person singular wherever appropriate.

	Experimental design	Execution of experiments	Data analysis	Visualization	Original draft preparation
Paper I	JC, PB, NSB, AMH	JC, MN	JC	JC	JC
Paper II	KA, ISO, SA	ISO, SA, LV, JC	ISO, SA, LV, KA	ISO, SA, LV, JC	ISO, KA
Paper III	JC, NJ, AA, NSB, BSA	JC, NJ, AA	JC, NJ, AA	JC, NJ, AA	JC
Paper IV	JC, ND, NSB, AMH	JC, ND, LVSW, EALR	JC, ND, LVSW	JC, ND	JC, ND

Authors: Jennifer Cauzzo (JC), Nataša Škalko-Basnet (NSB), Mona Nystad (MN), Ann Mari Holsæter (AMH), Purusotam Basnet (PB), Ida S. Opstad (ISO), Sebastian Acuña (SA), Luís Villegas (LV), Balpreet Singh Ahluwalia (BSA), Krishna Agarwal (KA), Nikhil Jayakumar (NJ), Azeem Ahmad (AA), Nedal Darif (ND), Laura Victoria Schulte-Werning (LVSW), Eirik André Lindeløff Rustad (EALR).

NSB is responsible for funding acquisition, supervision, and early input on all manuscript preparation lead by JC. All manuscripts have been reviewed and edited by all the respective authors.

Additional supervision, training, and help in pilot experiments was found in collaboration with: Aurélie Vigne, Sybil Akua Okyerewa Obuobi, Silje Mork, Elena Markova, Lisa Myrseth Hemmingsen, Peter McCourt, Karolina Szafranska, Larissa Dorothea Kruse, Christopher Holte, and the permanent staff at the Advanced Microscopy Core Facility.

1 Introduction

Bring it in!

Drug delivery systems (DDSs) have been widely studied in the past decades for their great potential of protecting and driving the distribution of active pharmaceutical ingredients (APIs) within the body. In fact, the necessary element for any pharmacological treatment to succeed is that an API reaches its specific target to execute its activity, while interfering as little as possible with the normal functions of the rest of the body. For this reason, more often than not, the formulation of a final DDS is as important as the API itself. Various technologies were developed and evaluated to optimize DDS to best serve this purpose. Recent decades brought main attention to the formulations in nanoscale, with focus on nanocarriers. After rather encouraging success in clinics, the field of nanomedicine is now experiencing translational and regulatory delays due to the suboptimal in vitro predictions. Within this need for improved in vitro methods lies the motivation for this thesis. The availability of cutting-edge technologies, specifically in microscopy, presented itself as an opportunity to develop and challenge new methods for nanomedicine applications. A back-to-basics approach was chosen, with the simplest and most charming of nanocarriers, liposomes, to see how a small vesicle of fat can be located, seen, characterized, and followed in vitro. The delivery system will be the sole and absolute protagonist of this story, as a wish to extend the applicability of this basic science to different carriers, active ingredients, targets, and pathologies. This introduction on our nanomedicine field will tell our truths, our challenges, and some limitations within our truths.

1.1 Nanomedicine and Drug Delivery

1.1.1 Nanomedicine History and Hype

In 1959, at Caltech, a landmark lecture was held: “There is plenty of room at the bottom”. Nobel Laureate Richard P. Feynman was envisioning the unavoidable development of science towards all that is smaller, to the nanoscale and eventually to atomic maneuvering of matter. Since then, the field that is now known as nanotechnology has developed as a branched tree that permeates every aspect of the human life, as more and more nanomaterials are being developed (Saleh T.A., 2020). Nanoengineering and nanoelectronics have been harnessed in telecommunications (Hamza E.K. & Jaafar S.N., 2022), food science (Ameta S.K. et al., 2020), cosmetics (Fytianos G. et al., 2020), and medicine, with this last field currently referred to as

nanomedicine (Freitas R.A., 2005, Martins J.P., 2020). The nanomaterials have been used for prevention, diagnosis, and treatment of diseases, ranging from the detection of molecules in point-of-care devices, to the stabilization and delivery of APIs within the body (Kargozar S. & Mozafari M., 2018).

As R.P. Feynman was giving his famous speech, A.D. Bangham (1964) was already developing what would become the first nanosystem for drug delivery: liposomes (Gregoriadis G., 1973). Although liposomes are still highly relevant in both pharmaceutical research and clinics, the development of newer and smarter carriers has grown exponentially, to the point that a simple search in Google Scholar for the word “nanomedicine” results in about 54100 entries in the temporal window Jan 2018 – Jan 2022, with about 1440 of these in January 2022 alone. The enormous amount of research and funding within the field is not surprising, considering the vast potential that nanoformulations have in both handling difficult APIs (e.g., insoluble and/or impermeable, highly toxic), and driving their distribution towards a target (Tewabe A. et al., 2021) (Figure 1). In this context, nanomedicine started being considered the ultimate tool for implementing in clinics what Paul Ehrlich had envisioned in 1907 as the “magic bullet”: a site-specific therapy that would hit exclusively the cause of the disease and leave the host unharmed (Strebhardt K. & Ullrich A., 2008).

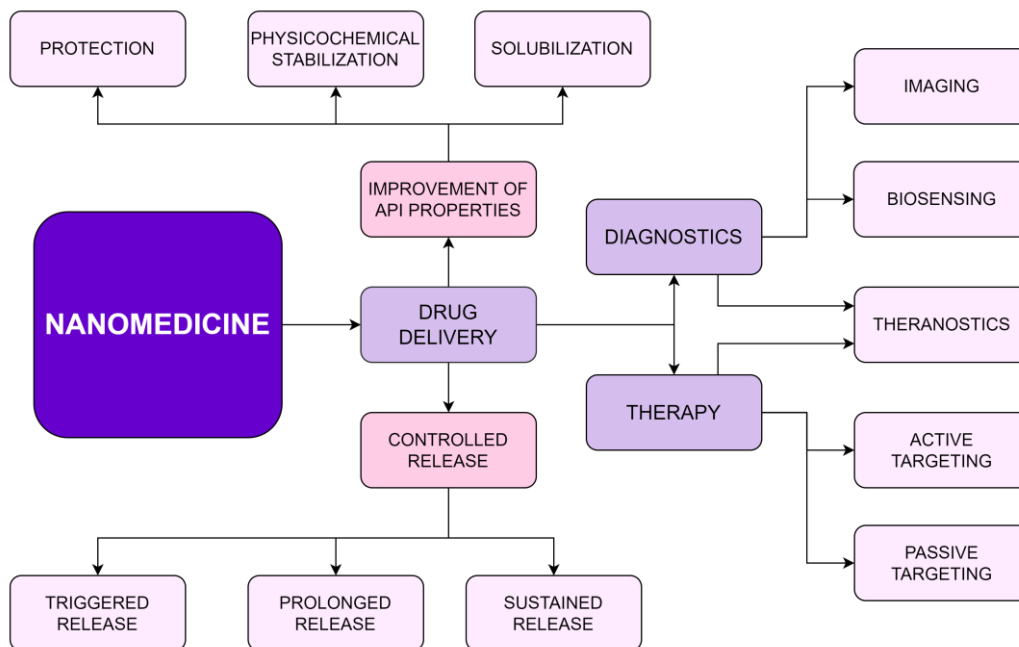


Figure 1. Potential of nanomedicine simplified in a flow chart. Abbreviation: API – active pharmaceutical ingredient. The figure was prepared using the online tool Draw.io.

Over half a century later, Prof. Kinam Park (2019), at the time editor-in-chief of the Journal of Controlled Release, proclaimed the death of nanomedicine in his editorial titled: “The beginning of the end of the nanomedicine hype”. He vividly criticized the system, too-often focused on publishing papers more than achieving actual clinical advancements, while hyping the potential of the technologies over the tangible results. More than the end of nanomedicine, his bitter opinion was the beginning of a discussion on the matter, with experts mostly disagreeing (Martins J.P. et al., 2020, Germain M. et al., 2020 and Lammers T. & Ferrari M., 2020 among others).

Since the discovery of liposomes, dozens of nanoformulations have been approved for use in clinical practice, and the pipelines of clinical trials show great promise for the field (Germain M. et al., 2020). Figure 2 presents a recent market analysis of approved nanoformulations (Park H. et al., 2022) and pipelines in clinical trial (Gadekar V. et al., 2021). All success stories culminated in 2021 with the fast-tracked approval of two COVID-19 vaccines, where mRNA was stabilized into lipid nanoparticles (Vu M.N. et al., 2021).

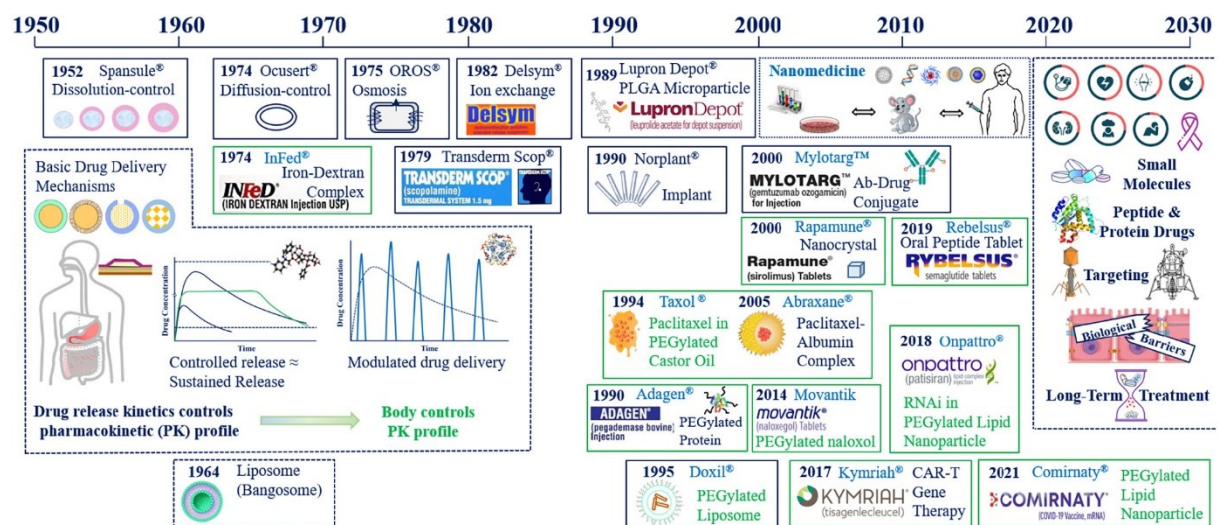


Figure 2. Visual representation of the main marketed nanoformulation (Park H. et al., 2022). Reproduced with permission from Elsevier.

Contrary to the fatalist vision in Park K. (2019), these success stories validate the great potential that nanomedicine has claimed for years. However, this should not overshadow the big challenges that the field is still experiencing. While some are working on ever smarter and fancier carriers (Huda S. et al., 2020, Sato Y. et al., 2021), others must work to address the translational and regulatory issues for the advancement of clinical practice, preparing the road for the smarter technologies to come (Foulkes R. et al., 2020).

In 2016, the Global Summit on Regulatory Science workshop addressed the need for methods to characterize nanoparticles' load and surface, to identify and quantify nanoparticles in complex media, and to describe the interaction of nanoparticles with the immunity system, recognizing these challenges as most needed documentary standards in nanomedicine characterization. Furthermore, the European Commission's Joint Research Centre workshop in 2017 defined the necessary quality and safety assessments for nanomedicines. Regarding the physicochemical characterization to ensure the quality of the product, the main Critical Quality Attributes (CQAs)¹ were the size, size distribution, surface potential, structure/morphology, physicochemical stability, purity, and sterility, with the possibility of demanding further formulation-specific information. On the toxicity assessment, recommendations were issued to focus on the effects of nanoparticles on blood and immune system, specifically on phagocytosis, complement activation, oxidative burst, and cell-dependent antibody response (Halamoda-Kenzaoui B. et al., 2019). Different nanomaterials behave differently; moreover, and the same material behaves differently whether in bulk or nanoparticle state. For this reason, understanding the properties of nanomaterials is the key not only to improve DDSs but also to accelerate the standardization of procedures and the translation of research into clinics (Foulkes R. et al., 2020).

1.1.2 Properties and Preparation of Nanomaterials²

The gold standard to describe the importance of nanomaterials' properties is elemental gold itself: the bright and shiny ingot of the well-known metal becomes a dark red liquid when gold is prepared as a suspension of nanoparticles (Merza K.S. et al., 2012). The main reason that the properties of nanoparticles differ from their bulk material is that the same amount of specific weight of material corresponds to a much higher specific surface area, when prepared as nanoparticles. In turn, the increased surface area translates into an increased surface

¹ Properties to be kept within a predefined interval to match the requirements in quality of the final product. As defined during the *International conference on harmonization of technical requirements for registration of pharmaceuticals for human use* (2009).

² According to the recommendations of the European Commission, the requirements for the identification of a nanomaterial are i) at least 50% of the particles has at least one dimension within the range 1-100 nm, and/or ii) the ratio surface area over volume is greater than 60 m²/cm³. However, these arbitrary values do not represent an abrupt change in the particle properties (Soares et al., 2018). In this thesis, I will consider a wider definition of nano, referring to the dimensional range of 10⁻⁷-10⁻¹⁰ m.

energy, which causes nanomaterials to be more reactive to the environment (Florence T.A., 2012a, Soares S. et al., 2018).

The electron confinement found in nanoparticles, especially in the case of metals, can cause shifts in optical, electrical, magnetic, and mechanical properties, which can then be tuned through different chemical compositions, sizes, shapes, surface charges and coatings (Wu Q. et al., 2021). It is in fact the tunability of nanosystems' properties that explains their wide range of applications in nanomedicine and beyond. Noting that a complex system can hardly be simplified to the sum of its individual components or properties (Florence A.T., 2012b), it is then the interplay of these that determines the fate of the nanocarriers in biological environments (Kamali S.M. et al., 2021).

The particle **size** of 10-200 nm represents one of the foremost benefits of nano-DDSs, as they can be injected without disrupting the blood flow (Foulkes R. et al., 2020). As many studies have shown, carriers of different sizes tend to be internalized, accumulated, and cleared differently (Li X. et al., 2015, Dai Q. et al., 2018). Higher miniaturization corresponds to a higher number of particles per unit of mass, which can be beneficial in therapeutic approaches such as the above-dose-threshold tumor delivery for immunity system overload (Ouyang B. et al., 2020). Additionally, smaller particles have higher diffusion rate, therefore having better stability in suspension (Florence A.T., 2012a).

For nanoparticles in water-based suspensions – a requirement for most administration routes, size is generally expressed as hydrodynamic diameter, which includes the electric dipole layers that are adsorbed onto the molecule. This measurement assumes the sphericity of the particles; however, their **shape** and morphology can influence their diffusion profile and interactions with the target site, hence affecting the overall behavior of the nanoparticles (Florence T.A., 2012a, Kamali S.M. et al., 2021). Furthermore, when nanoparticles in suspension create agglomerates/aggregates, this shape change could be affecting the fate of the primary particles (Soares S. et al., 2018). E.g., rod-shaped particles have shown higher or comparable internalization rates to the spherical ones, followed by cylindrical and cubic, but with high variability of behavior (Albanese A. et al., 2012). This variability is possibly due to the orientation of the cell-nanoparticle interaction (especially for non-spheric particles, Kamali S.M., et al., 2021), but it was also shown to be related to the cell model used and other physicochemical properties of the nanoparticles (Dai Q. et al., 2018).

Ultimately, the surface chemistry is responsible of the first interactions with the environment after administration. Electrostatic **surface charges** can increase or decrease the affinity of the nanoparticle for the cell membranes and/or for a specific target on it. Positively charged nanoparticles often show higher internalization rates, possibly because cells tend to have a slightly negative charge that could favor the interaction (Kamali S.M. et al., 2021). However, this observation cannot be transferred to all cells as highly phagocytic ones, such as macrophages, show higher recognition for negatively charged nanoparticles. This preferential internalization can result in specific cytotoxicity, for both positive and negative nanoparticles, such that neutral and neutralized particles are always included in the early developmental stages due to their overall lower toxicity (Fröhlich E., 2012, Qi P. et al., 2016). Hence, **surface modifications**, such as stealth coating of polyethylene glycol (PEG), can become useful to tailor surface charge and hydrophobicity, stabilize the nanoparticles, and reduce the adsorption of macromolecule that can increase recognition for clearance (Dai Q. et al., 2018), before adding active targeting strategies such as binding ligands on the nanoparticle surface (Tewabe A. et al., 2021).

According to the properties of the bulk material – and the desired type of nanomaterial, three production processes are available. The top-down methods involve the progressive breaking down of bulk materials into nanosystems (Fu X. et al., 2018). The bottom-up methods consist in starting from the raw material, and obtaining nanoparticles through processes of self-assembly (e.g., for lipid-based nanosystems, Large D.E. et al., 2021), agglomeration, or polymeric reactions. The third class of preparation methods consist in the combination of top-down and bottom-up approaches, which are often combining strengths of the individual processes to achieve more complex nanosystems (Fontana F. et al., 2018). Because of the great variety of available preparation methods and the tunability of the nanosystems' properties, a wide range of nanomaterials for drug delivery purpose have been developed, using different raw materials while aiming for different shapes and complexity (Figure 3). To the first generation of “naked” nanoparticles, stealth coatings and targeting ligands were added for prolonged circulation and active targeting (second generation), while more recently the third generation of DDSs has moved the focus to smarter formulations, activated by internal or external triggers (Wang Y. & Kohane D.S., 2017).

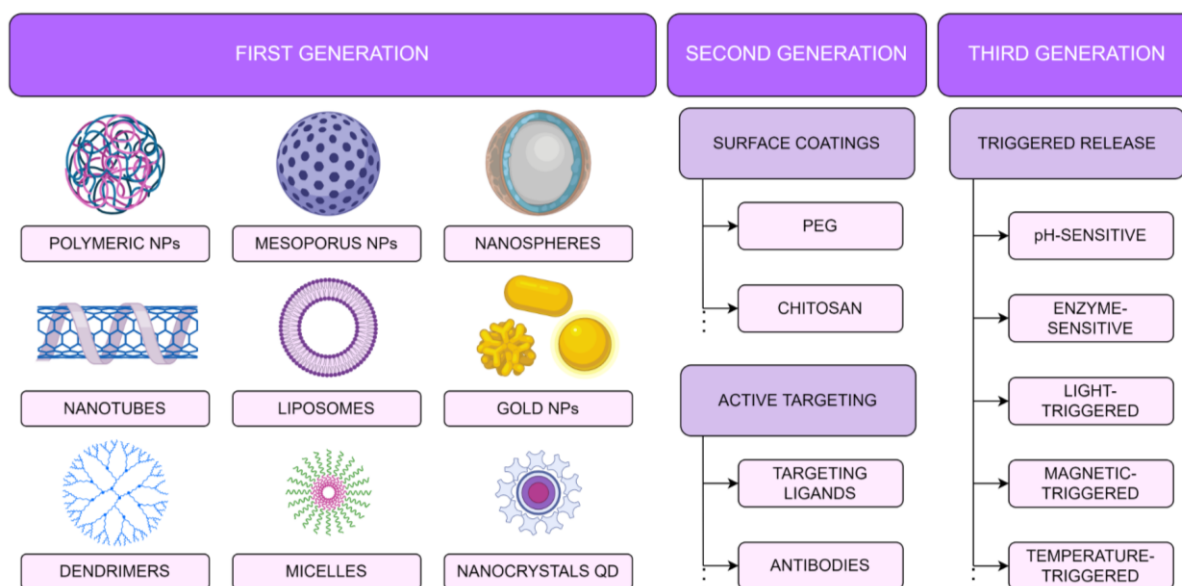


Figure 3. Examples of nanocarriers and generations of smart and smarter formulations. Abbreviations: NPs – nanoparticles, QD – quantum dots, PEG – polyethylene glycol. The figure was prepared using Biorender.com and Draw.io.

While the development and translation of complex DDSs is still requiring more efforts, more conventional formulations such as lipid-based nanocarriers are still holding their ground on the market, with many being eligible for the KISS concept (“Keep It Simple, Stupid”) that is still favorable for the industries (Crommelin D.J.A. et al., 2020).

1.1.3 Liposomes as Lipid-based Nanocarriers

As the words say, lipid-based nanocarriers are DDSs comprising a natural or synthetic lipid. The main class used for the scaffolds of these nanocarriers is found in phospholipids since these molecules present a hydrophilic head (generally zwitterionic or charged) and two organic carbon chains that are known as hydrophobic tails (Figure 4a). For these peculiar chemical structures, once exposed to a water-based environment, phospholipids tend to self-assemble into spheres with the carbon chains forming a hydrophobic compartment and the hydrophilic heads disposing themselves on the surface for positive interaction with the water molecules (Bunker A. et al., 2016).

According to the processing these lipids are subjected to, it is possible to obtain the compartments in vesicular form (known as liposomes) or in solid particle form (known as solid lipid nanoparticles), as shown in Figure 4, respectively. To drive the preparation of lipid-based nanocarriers towards one or the other form a great deal of methods has been developed over the past decades (Amoabediny G. et al., 2017). For instance, the film hydration method (firstly

developed in the original study by Bangham A.D. & Horne R., 1964) tends to give vesicular suspensions of liposomes as it consists of a gradual “peeling” of a thin film of lipids into a water-based solution, while spray drying a lipid-drug molten tends to give particulate formulations (Freitas C. & Müller R.H., 1998). However, it is the lipid formulation itself, together with the specific interaction with the active ingredient of interest, that drives the formation of either one particle (Ulrich A.S, 2002). Weakly charged phospholipids, individually pre-solubilized in organic solvents, will tend to assemble into vesicles, while strong electric interactions between highly charged components can shift the self-assembly towards solid nanoparticles, even utilizing methods known to produce liposomes (Obuobi S. et al., 2021). Hence, to ensure the preparation of particles over vesicles and avoid hybrid suspensions of the two, adjuvants, lipids in different states (e.g., solid, or liquid mass) and experimental temperature need to be considered (Duong V-A. et al., 2020).

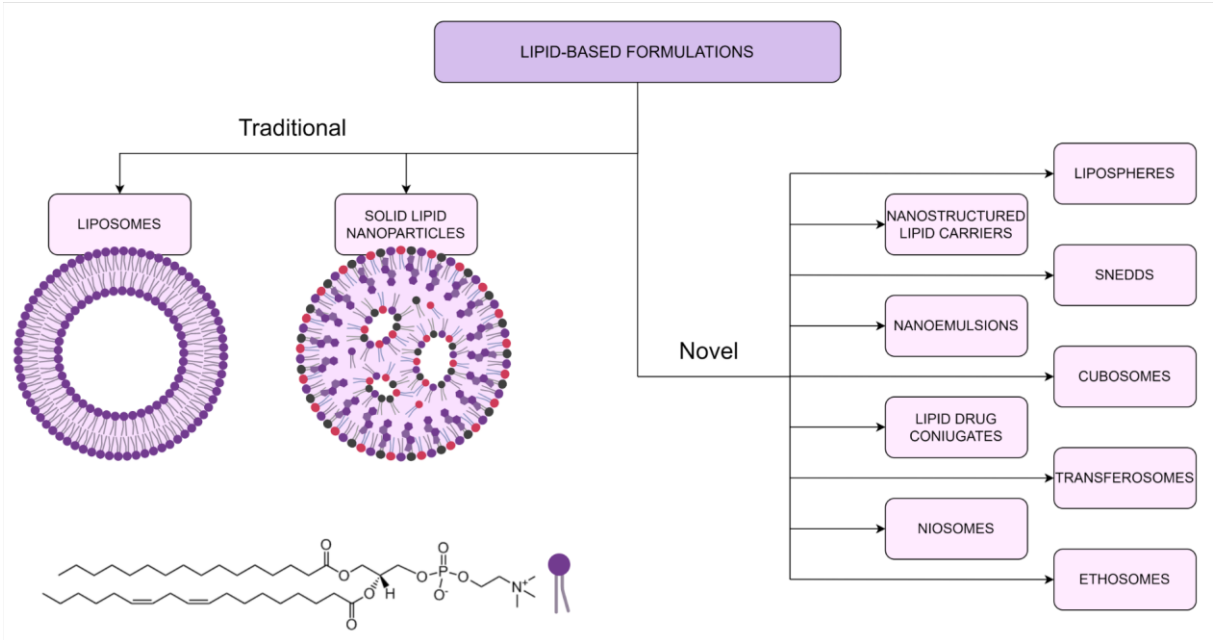


Figure 4. Basic schematics of lipid-based drug delivery systems, with highlight on the traditional formulations of liposomes and solid lipid nanoparticles. Bottom-left: chemical structure of a sample phospholipid (phosphatidylcholine) often main excipient in this type of formulations. The figure was prepared using Biorender.com and Draw.io.

Starting from a simple phospholipid bilayer, lipid-based nanocarriers have been developed into all types and generations of nanocarriers, comprising lipid nanocapsules, nanostructured lipid carriers, nanoemulsions, long-circulating formulations (after steric stabilization with PEG), ligand-exposing nanocarriers and stimuli-responding formulations for triggered release (Mishra D.K. et al., 2018).

“Liposomes were chosen for their therapeutic relevance, biosafety, and versatility”.

This is the uttermost poetic and representative sentence in liposome research, and we all have used in one of its many forms. First, the **therapeutic relevance** of lipid-based nanocarriers is well remarked by the significant success of marketed formulations (Gadekar V. et al., 2021), and the most recent approval for clinical practice of the lipid nanoparticles in two of the covid vaccines (Vu M.N. et al., 2021). Second, the **biosafety** of these nanocarriers derives from the FDA affirmation as GRAS substance (Generally recognized as safe) for most used lipids (e.g., lecithin from soybean or egg). Furthermore, being natural constituents of the human body and part of many metabolic processes, these lipids are also **biodegradable**, which adds a layer of safety to the nanocarrier, generally able to avoid accumulation issues (Antimisiaris S. et al., 2021). However, more complex formulations can contain lipid derivatives with some degree of cytotoxicity (Mydin R.B.S.M.N. & Moshawih S., 2018); highly charged particles can exhibit cell-specific cytotoxicity (Fröhlich E., 2012) while coatings can trigger immediate or delayed immune responses, such as complement activation and accelerated blood clearance (ABC) response to repeated treatment with PEGylated nanosystems (Mohamed M. et al., 2020). In fact, lipid-based nanocarriers are so **versatile** that they can cover the entire spectrum of applicability in clinics. By combining hydrophilic and hydrophobic compartments, lipid-based nanocarriers, and especially liposomes, can be loaded with either water-soluble and/or insoluble APIs to maintain them in water-based suspension (Mishra D.K. et al., 2018). Remarkably, insoluble APIs are the most represented, both on the market and in the pipelines, and nanomedicine is often the only option for delivering these APIs at all (Khan K.U. et al., 2022). Besides, lipid formulations can be tailored in composition, size, surface charge, deformability, and coating (Guimarães D. et al., 2021).

The different properties are optimal for different administration routes and targets, concept that further endorses both relevance and versatility of these nanocarriers as we find, among others, studies on cancer (Ansari M.T. et al., 2020), arthritis (Chuang, S.-Y., et al., 2018), infectious diseases (Jøraholmen M.W. et al., 2020, Ferreira M. et al., 2021), pain relief (Hua S. & Wu S.Y., 2013, Abildgaard J.T. et al., 2019), and central nervous systems diseases (Jagaran K. & Singh M., 2021, Faouzi A. & Roullin V.G., 2021), investigating all administration routes.

1.2 Systemic Administration of Drugs and Body Defenses

The human body is built to protect itself; therefore, any pharmacological treatment is seen as an attack to the intrinsic balance that the organism is maintaining, even when this balance is pathological. To understand the fate of any nanoparticle treatment, it is therefore fundamental to study their behavior towards the body defenses, such as the physiological barriers and the immune system, from administration site to body distribution and finally cellular internalization.

1.2.1 Administration Route challenge for (Lipid-based) Nanomedicine

The biological barriers at the administration site represent the first obstacle for the nanocarrier to perform its action. According to the administration route chosen, different barriers will be encountered, and the knowledge on their functioning is needed to design better nanocarriers that can overcome these barriers (Antimisiaris S. et al., 2021). In fact, according to the route of administration and the wanted target, different properties of nanocarriers are more favorable in different occasions.

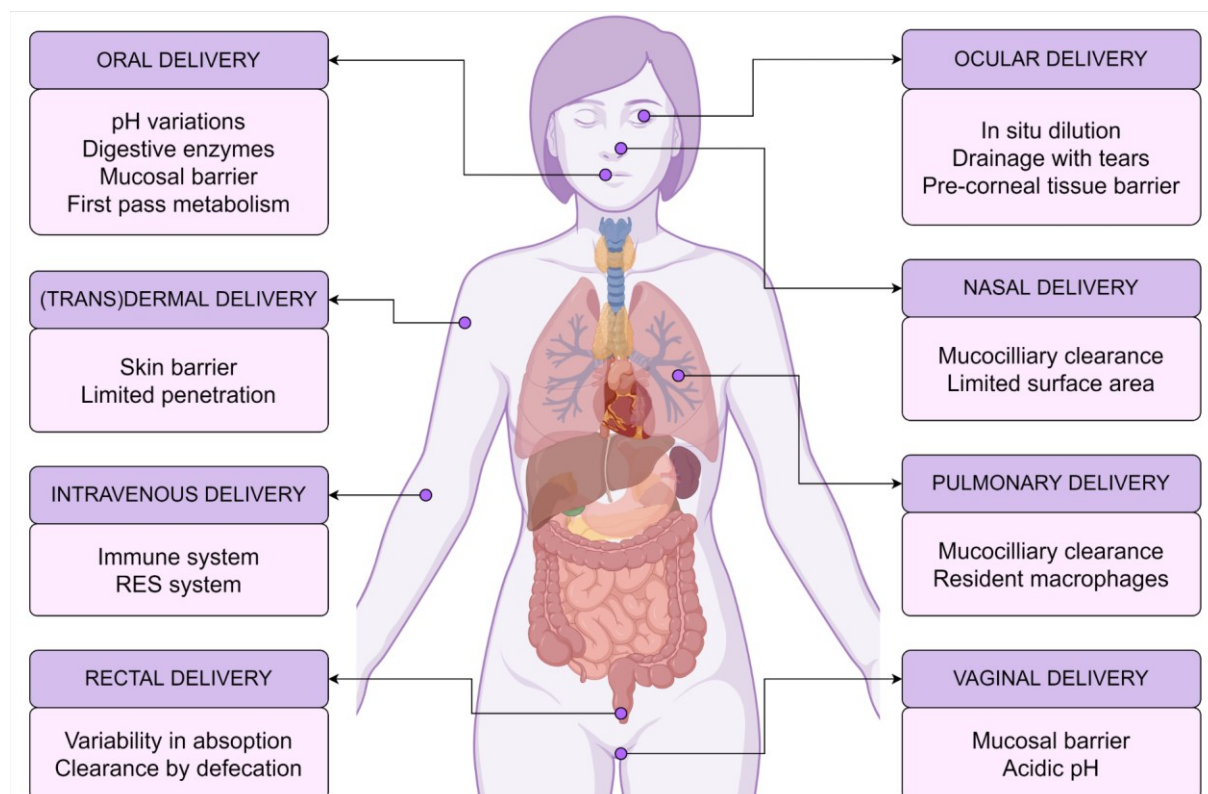


Figure 5. Schematic representation of the body barriers according to administration route.

The figure was prepared using Biorender.com and Draw.io.

The oral route, which is the least invasive and therefore always the preferred one, shows three main obstacles: the strongly acidic pH of the stomach, the high concentration of digestive enzymes and the mucosal barrier of the intestine (Poovi G. & Damodharan N., 2018). Most biodegradable nanocarriers would indeed be degraded very easily, such that lipid-based formulations would encounter the same fate of a cheesy-cheeseburger. However, while being emulsified and degraded, these nanocarriers can still increase the bioavailability of insoluble APIs or protect a sensitive load. Hence, gastric-resistant formulations can deliver the APIs to the intestine where stabilized nanocarriers can avoid the mass precipitation of the drug, slow down its degradation and even facilitate its permeation through the mucus layer (Jash A. et al., 2021). To ensure these effects, favorable tricks and properties of the nanocarriers are: chemical stability to harsh environments, hybrid lipid-polymer DDSs and mucoadhesive coatings. Although considered a niche route for lipid-based DDSs, liposomes, solid lipid nanoparticles and (nano)emulsions were all evaluated for oral delivery, down to a full deconstruction of the nanocarrier into self-nanoemulsifying drug delivery systems (SNEDDS), which self-assemble directly into the intestinal lumen (Dhaval M. et al., 2021, Haddadzadegan S. et al., 2022).

The topical administration onto skin is the second non-invasive and favorable route considering patient compliance. Here, the administration of nanocarriers is challenged with the biggest physical barrier of the body: the skin itself (Yazdi S.J.M. & Baqersad J., 2022). With a layered organization that is tens of microns thick, the intact epidermis (outermost section of the skin) creates a strongly lipophilic environment that prevents the transport of most molecules. In this environment, lipid-based nanocarriers have great potential to blend in and deliver APIs to and/or across the dermal layer (inner and thicker portion of the skin) (Carter P. et al., 2019). For this administration route, bigger sizes of nanocarriers tend to be preferred as they are generally linked to higher drug load, slower release profile and better rheological properties, which facilitate their incorporation into secondary vehicles (e.g., hydrogels) for a more comfortable application in situ (Zylberberg C. & Matosevic S., 2016, Hemmingsen L.M. et al., 2021). Furthermore, according to their deformability and lipid composition, the formulations can be destined to dermal (local) or transdermal (systemic) delivery of their API(s), with virtually no toxicity at the site of administration (Antimisiaris S. et al., 2021).

In addition to oral and dermal non-invasive routes, all available sites have been studied for the administrations of nanomedicines, designing the carrier according to the physiopathology of the barriers to encounter. To avoid at least in part the first pass metabolism typical of the oral route, nanoformulations for rectal delivery are design for both local treatment/diagnosis and for systemic administration (Melo M. et al., 2018). Mucoadhesive formulations in secondary vehicles are developed for the treatment and prevention of vaginal infections (Vanić Ž. & Škalko-Basnet N., 2017). To reach the pulmonary alveoli and treat infections, antimicrobials-in-liposomes are formulated for inhalation therapy, with careful consideration for the surfactant content (not to alter the gas exchange of the respiration) and their stability after nebulization (Bassetti M. et al., 2020).

The proximity of the nose cavities to the brain is exploited for nose-to-brain delivery, adjusting the mucoadhesive properties and osmolarity of the formulation to the rapid mucus clearance (Wu I.Y. et al., 2017, Emad N.A. et al., 2021). Anterior ocular diseases are tackled with topical DDSs that address the difficult permeation through the cornea and the quick drainage that happens in situ with the tears (Souto E.B. et al., 2019). Although all routes are being studied and harnessed for their advantages, the injection-based administration is still topping the others as it is suitable for vaccines (Chatzikleanthous D. et al., 2021), intravitreal and periocular, intra-articular, and intra-tumoral delivery (Antimisiaris S. et al., 2021), as well as intravenous systemic treatment of many cancer types, which are still one of the main evil that nanomedicine is fighting against (Mishra D.K. et al., 2018).

With any form of injection, physical barriers such as the epithelial, endothelial, and mucosal are intrinsically avoided. However, a silent barrier comes into action with even higher efficacy than the previous ones: the immune system, and specifically the reticuloendothelial system (RES) (Zahednezhad F. et al., 2019). Figure 6 summarizes the possible outcomes of nanocarriers interacting with the immune system, as the positive or negative interplay between them is crucial for both efficacy of the treatment as well as toxicity (Halamoda-Kenzaoui B. et al., 2019).

The RES comprises highly specialized cells with scavenger activity that can recognize, internalize, and dispatch the nanomedicine treatments, with the purpose of cleansing the system from foreign material.

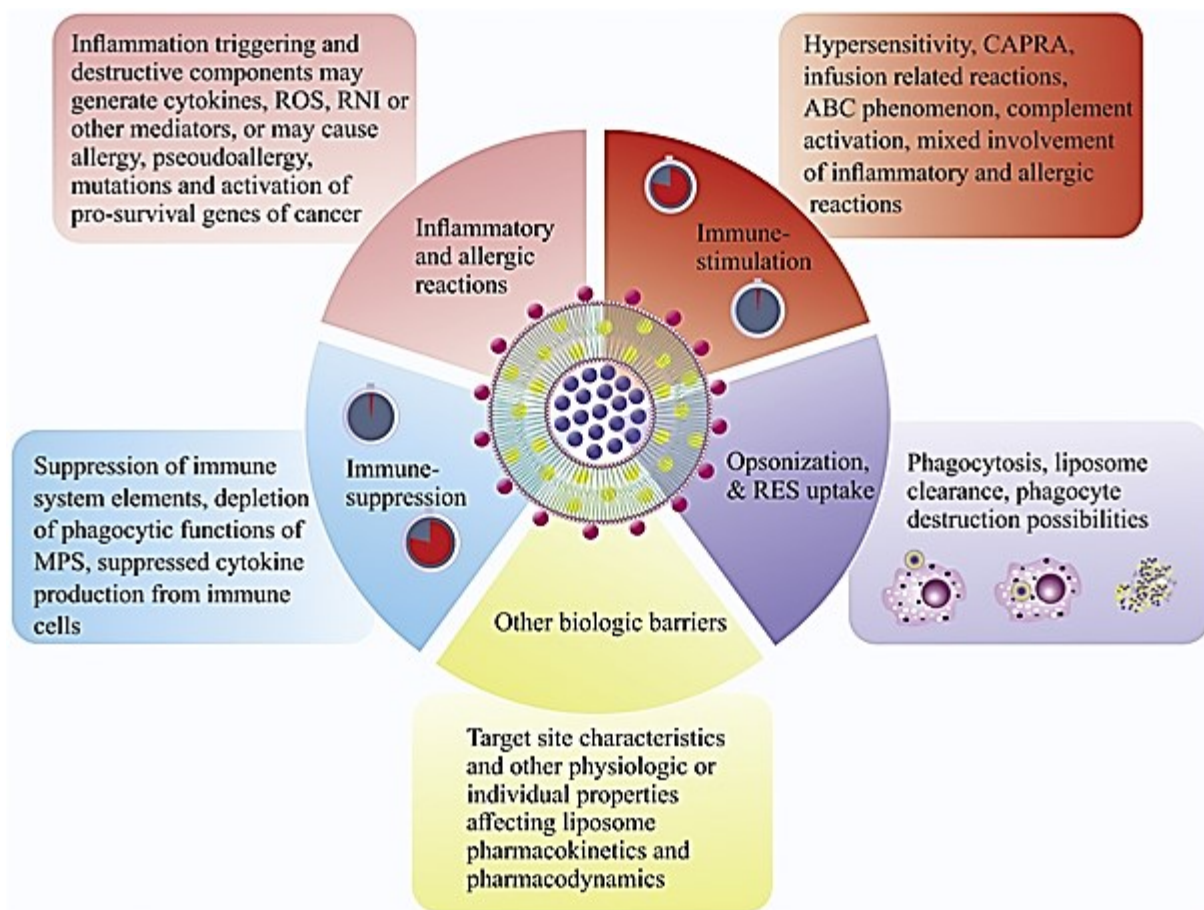


Figure 6. Interplay between nanocarriers (here, liposomes), immunity system, and biological barriers once in the systemic circulation. Abbreviations: ABC – accelerated blood clearance, CARPA – complement activation related pseudo-anaphylaxis, MPS – mononuclear phagocytic system, RNI – reactive nitrogen intermediates, ROS – reactive oxygen species. Figure reproduced from (Zahednezhad F. et al., 2019) with permission from Elsevier.

Macrophages are the main protagonists of the RES action as they both circulate in the blood stream and reside at the most relevant outposts of the immunity system (e.g., spleen and liver) (Bertrand N. & Leroux J.-C., 2012). Next to these highly phagocytic cells, specialized endothelial cells (e.g., the liver sinusoidal endothelial cells, LSECs) were found to complement the scavenging activity of macrophages through receptor-mediated endocytosis (Sørensen K.K. et al., 2012, Baboci L. et al., 2020). With this system to evade, nanocarriers need to be specifically tailored in size and surface properties. First, larger particles tend to be recognized faster by the RES, more specifically by the circulating proteins known as opsonins, which adhere to the surface of foreign objects and are in turn recognized by the RES for dispatch (Ishida T. et al., 2002, Fan Z. et al., 2020). Second, surface modifications such as uniform PEGylation can prevent nanoparticles from adsorbing opsonins, therefore shielding them from

RES recognition, up to a cut-off size of approx. 275 nm (Zylberberg C. & Matosevic S., 2016). At present, it is reasonably accepted that phagocytic cells clear microparticles above 1 μm , non-phagocytic scavengers take up rapidly nanoparticles between 20 and 50 nm, while nanoparticles below 5 nm are excreted through renal ultrafiltration (Fröhlich E., 2012, Kamali S.M. et al., 2021). However, within the size range most suitable for nanomedicine treatments, research showed quite the variability of internalization and clearance outcomes, depending on composition, size, polymeric coating, coating density, and cell model used (Ishida T. et al., 2002, Fröhlich E., 2012, Wei Y. et al., 2018, Zahednezhad F. et al., 2019, Jensen G.M. & Hodgson D.F., 2020, and Kamali S.M. et al., 2021, among others).

1.2.2 Cellular Internalization and Dispatch

Once a nanocarrier interacts with a cell, one of several mechanisms of internalization can be triggered, according to the cell type and the properties of the nanocarrier, possibly leading to different internalization rates, accumulations, and dispatch (Fröhlich E., 2012). However, the identification and even the classification of these processes is challenging and constantly evolving as they all represent dynamic complex rearrangements, and they are strongly intertwined with each other (Rennick J.J. et al., 2021). Figure 7 presents a comprehensive (yet still simplified) scheme of the internalization processes, with their related intracellular fate.

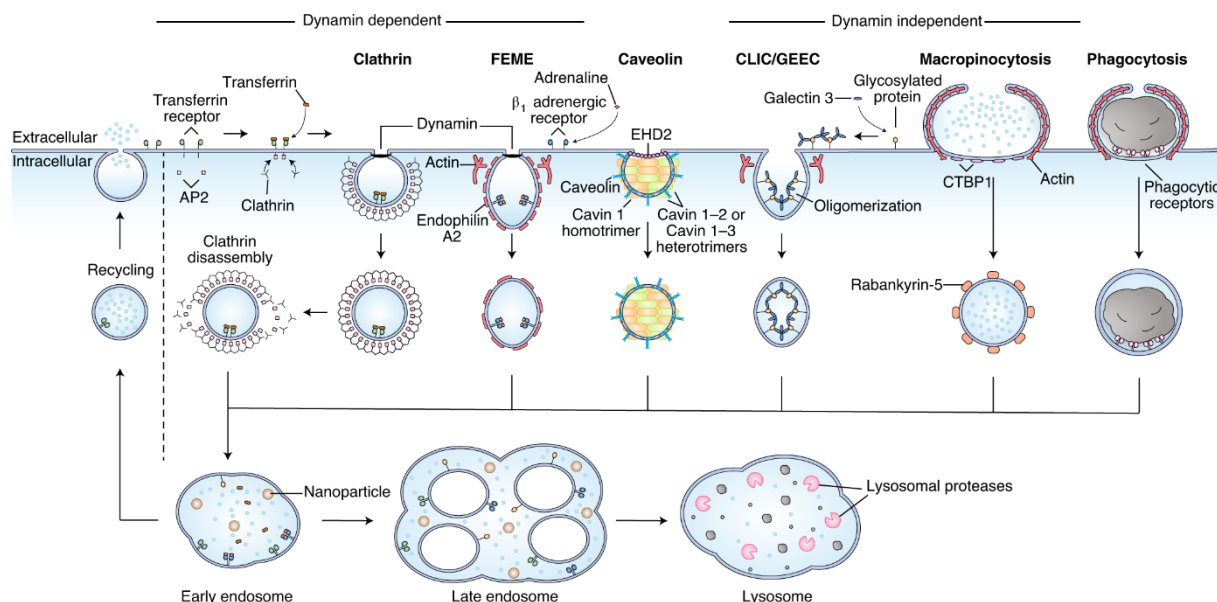


Figure 7. Schematic representation of internalization and intracellular fate, according to the most recent understanding in cell biology. Figure reproduced from (Rennick J.J. et al., 2021) with permission from Springer Nature.

We can herewith recognize 5+1 main internalization mechanisms:

- Clathrin-mediated endocytosis (CME)
- Fast endophilin-mediated endocytosis (FEME)
- Clathrin-independent carrier (CLIC) / glycosylphosphatidylinositol-anchored protein enriched early endocytic compartment (GEEC) endocytosis
- Macropinocytosis
- Phagocytosis
- Caveolin-mediated endocytosis

CME is a form of receptor-mediated endocytosis. A specific ligand-receptor interaction activates the intracellular cascade that causes the aggregation of clathrin pits, invagination of the cell membrane, and formation of clathrin-coated vesicles (approx. 100 nm), which are then carved out of the plasma membrane by the dynamin GTPase (Thottacherry J.J. et al., 2018). **FEME** is a second type of receptor-mediated endocytosis, which is dynamin-dependent but clathrin-independent. This vesicle formation (approx. 60-80 nm) is very fast as it does not require local enrichment of its mediator (endophilin) (Boucrot E. et al., 2015). **CLIC/GEEC** is a clathrin- and dynamin-independent internalization, which is also not relying on specific receptor recognition. The proposed extracellular mechanism describes galectines as the external trigger for glycosylated proteins-to-glycosphingolipid clustering, which in turn activates the invagination of the membrane into uncoated vesicles and tubular structures (Lakshminarayan, R. et al., 2014). **Macropinocytosis** and **phagocytosis** both involve actine-driven extension of the cell membrane, the first for unspecific internalization of extracellular medium (“liquid internalization”, Lim J.P. & Gleeson P.A., 2011), and the second for dispatch of large particulate material (Niedergang F. & Grinstein S., 2018). Because of the size of the macrovesicles they form (>>200 nm), these pathways are of particular interest for the delivery of medium-sized DDSs, yet much is still unknown about the interplay of the two in terms of the specificity of nanomedicine internalization (Rennick J.J. et al., 2021). **Caveolin-mediated endocytosis**, the +1 in this list, is an endocytic mechanism that has been associated to the caveolae invaginations of the plasma membrane. These bulb-shaped pits of approx. 60 nm (and an even smaller rim) have been identified and characterized in different cell types; however, their involvement in endocytic processes is still questioned – especially in terms of nanomedicine internalization (Skotland T. et al., 2021).

Once the internalization is started, independently from the specific pathway, the vesicular bodies tend to be converted to early endosomes, which can then be directed for recycling back to the plasma membrane or fused with other early endosomes into late endosomes and lysosomes (Rennick J.J. et al., 2021). The knowledge of which trigger causes which path can help design the active targeting strategies for nanocarriers (Tewabe A. et al., 2021) and eventually the organelle targeting that was already shown in vitro for lysosomes and mitochondria (Zylberberg C. & Matosevic S., 2016, Sato Y. et al., 2021) through endosomal escape (Selby L.I. et al., 2017).

A note worth remembering is that the interaction forces between target and ligand are effective only within a distance of few nanometers. Hence, strategies of active targeting can only come into place when the particle encounters the target by chance (Florence A.T, 2012a). This very stochastic principle that describes the distribution and therefore the potential efficacy of nanomedicine treatments explains the importance of including a thorough study on RES cell models in early stages of formulation development (Halamoda-Kenzaoui B. et al., 2019). Once in the blood stream, nanoparticles are progressively cleared from the system because they are running right alongside the very cells that are responsible for their disposal, increasing the probability of recognition and dispatch. At the same time, this probabilistic approach is also the explanation for the success of long-circulating (stealth) formulations, as the increased time in the blood circulation directly increases the nanocarriers chances to interact with the actual target cell (Tewabe A. et al., 2021).

1.3 Localizing and Following Nanocarriers

To understand the fate of nanoparticles, we must first understand the nanoparticles themselves. Because of their nanoscale dimensions, localizing and following the behavior of nanoparticles over time and space is challenging. Hence, first, a deep physicochemical characterization is necessary to determine the properties of the particles we aim to follow (Mahmoudi M., 2021). Only then, we can gradually increase the complexity of the experimental conditions, from simple to complex media, to in vitro cell testing. The validation of the trackability of these particles will improve the prediction of their behavior in vivo and reduce failures at later stages of development (Gadekar V. et al., 2021). For this chain of events to happen, we first need to understand the characterization methods at our disposal and therefore their applicability. When dealing with objects in the nanoscale, the driving

explanations for their behavior are laws of physics and chemistry that we all studied in school and might have forgotten soon after. Although not wanting to be too extensive, I believe it is useful to introduce some of the physics behind the methods used and discussed in this thesis, linking together concepts that usually belong to different disciplines and fields.

1.3.1 Characterization of Nanocarriers in Suspension

1.3.1.1 Properties of Nanocarriers in Suspension

An important challenge when dealing with suspensions of nanoparticles is that each particle is undergoing the so-called **Brownian motion**, with a constant and chaotic diffusion through the medium. When the particles are homogeneously distributed in their suspending medium, no prevalent direction of diffusion can be identified, and each particle will follow a stochastic segmented path (Michaelides E.E., 2015). The beauty of this natural phenomenon can be described by the Brownian motion model (Equation 1, application in 2D) and the Stokes-Einstein diffusion equation (2):

$$\overline{(x, y)^2} = 4D_0t \quad (1)$$

$$D_0 = \frac{k_B T}{3\pi\eta d} \quad (2)$$

where $\overline{(x, y)^2}$ is defined square mean step size (descriptor of the particle displacement in Brownian motion), t is the time variable, D_0 is the diffusion coefficient, k_B is the Boltzmann's constant ($1.380649 \times 10^{-23} \text{ kg} \cdot \text{m}^2 \cdot \text{K}^{-1} \cdot \text{s}^{-2}$, a defining constant in the redefinition of SI base units, 2019), T is the temperature in the system, η is the viscosity of the medium and d is the hydrodynamic diameter of the particle of interest (Jarzębski M. et al., 2017). The latter variable of Equation 2 is the most descriptive property of a spherical particle in a fluid suspension as it includes the **solvation effect**. In fact, when the surface molecules of the suspended particles interact with the molecules of the medium, Coulomb forces stabilize a double layer of electric charges or dipoles, which tend to move as one with the particle (Maguire C.M. et al., 2018). The bigger the particle, the smaller the diffusion coefficient, the slower the movement; hence, the hydrodynamic diameter can be determined by studying the Brownian motion of nanoparticles in suspension (Equation 1 & 2). This can be done by utilizing the interaction of light with matter, hence a small degression on the physics of light itself will help us understand how to harness this powerful tool.

As figure 8A shows, light is both an electromagnetic wave and a beam of photons – particles with infinitesimal mass and maximum speed in void of $c = 299792458$ m/s. Luckily, most of the phenomena addressed in this work can be explained through the wave nature of light. Here, the physics for a superficial explanation is more approachable. Amplitude a , wavelength λ , and phase φ are the properties that can describe electromagnetic waves (Figure 8B), with λ being inversely proportional to the energy E . The spectrum of visible light (Figure 8C) associates colors to the light wavelengths as the human eye can see them.

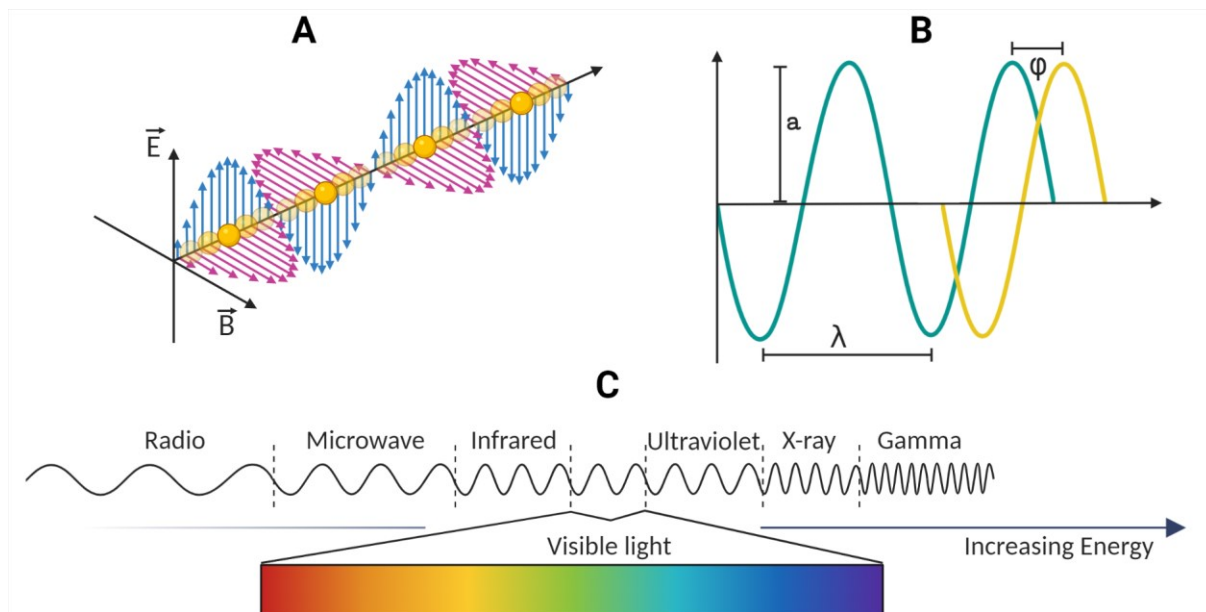


Figure 8. Light. A) Dual nature of light as a beam of photons (oscillating yellow spheres) and an electromagnetic wave, expressed as the combination of perpendicular electrical and magnetic field. B) Wave properties of amplitude a , wavelength λ , and phase shift φ . C) Spectrum of visible light with increasing wavelength and decreasing energy. The figure was prepared with Biorender.com.

When a light beam is passing through a medium, the intensity of the emerging beam is attenuated in comparison with the incident one. This phenomenon, historically referred to as extinction, is a combination of two types of interaction between light and matter: scattering and absorption (van de Hulst H., 2012). According to the physicochemical properties of the medium itself, the incident light can undergo **scattering** (describing an elastic or inelastic deviation of the light path of photons), **absorption** (associated to internal conversion of energy) or **transmission** through the medium. Hence, we define transmittance T as the ratio between transmitted radiant intensity I_t and incident radiant intensity I_i (Equation 3), deriving the absorbance A as shown in Equation 4. Specifically, when referring to a solute, the Lambert-Beer Law (Equation 5) describes the relationship between the absorbance at a given

wavelength A_λ and the molar concentration M of the solute, accounting for light pathlength l and molar extinction coefficient ε (Swinehart D.F., 1962).

$$T = \frac{I_t}{I_i} \quad (3)$$

$$A = -\log T \quad (4)$$

$$A_\lambda = \varepsilon l M \quad (5)$$

As the transmittance is a measurable quantity and the absorbance is a property of matter directly proportional to the concentration of the molecules of interest, these concepts can be applied for the determination of concentrations of solutes (Mäntele W. & Deniz E., 2017), nanoparticles in suspension (Wang X. & Cao Y., 2020), and entrapment of their cargos (Amoabediny G. et al., 2017).

As for the scattering, the math behind this phenomenon reaches complexities beyond this work's scope and applications. However, it is noteworthy to highlight that light is scattered in all directions, and the intensity of such scattered light I_s is inversely proportional to the wavelength of light λ to the power of four (Equation 6); hence, shorter wavelengths (e.g., violet and blue light) undergo significantly higher scattering emissions than longer wavelengths (e.g., yellow and red light) (Van Leeuwen S.R. & Baranoski G.V., 2018). Additionally, the size of the scattering object is also inversely proportional to the intensity of the scattered light by roughly the power of six (Equation 7), and the bigger the particles the more relevant the forward scatter will be, compared to the side and backscatter (Pecora R., 2000).

$$I_s \propto \frac{1}{\lambda^4} \quad (6)$$

$$I_s \propto \frac{1}{d^6} \quad (7)$$

These very properties of Brownian motion and predictable interaction with light can be experimentally exploited for the characterization of nanoparticles in suspension, with methods that have been extensively optimized to the point of being considered gold standards.

1.3.1.2 Gold Standard Methods and Associated Challenges

The use of light scattering to analyze the Brownian motion of nanoparticles in suspension has been validated in two well-known methods: dynamic light scattering (DLS, mostly associated to photon correlation spectroscopy, PCS) (Hassan P.A. et al., 2015) and nanoparticle tracking analysis (NTA) (Kim A. et al., 2019). Although based on the same physicochemical principles, these techniques differ in detection, software analysis and data output (Figure 9).

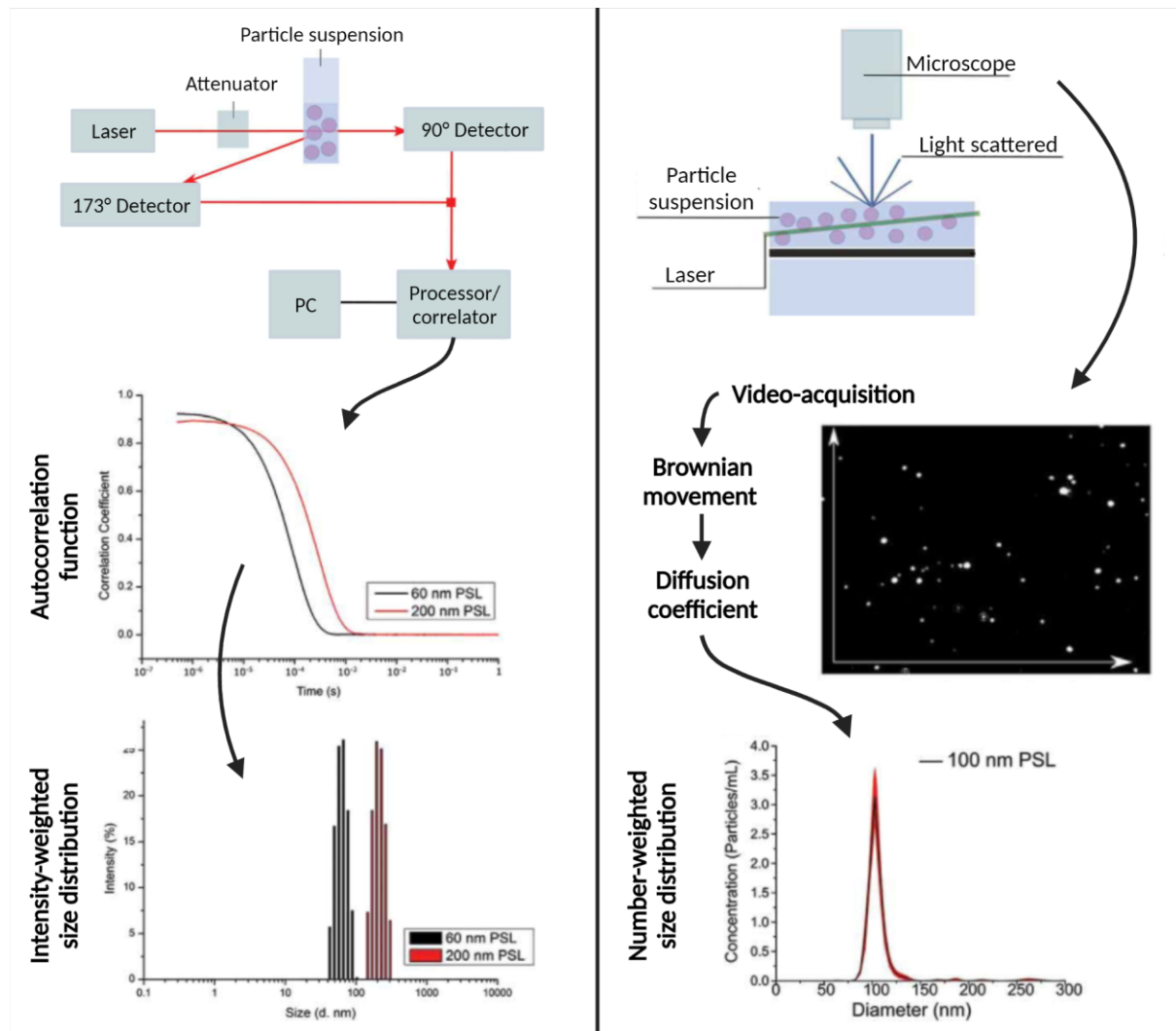


Figure 9. Visual comparison between DLS and NTA approaches. From top to bottom: set-up schematics, software analyses and data output are shown for both DLS (left) and NTA (right). The figure was adapted from Maguire C.M. et al., 2017 (reproduced according to the Creative Commons CC BY license for open access articles).

In DLS, an avalanche photodiode detects the total scattered intensity over time. At each moment, this scattered intensity depends on how the particles are positioned in respect to the detector. Hence, the fluctuations of the scattered intensity over time are a description of the Brownian motion of the scattering particles. Here, a digital correlator interprets the

fluctuations of intensities into a correlation function, which exponentially decreases to zero. The slope of this function is correlated to the size of the particles, as a steeper slope indicates faster position changes, hence faster movement, and smaller sizes (Hassan P.A. et al., 2015). Sequential iterations of these analyses in the scale of nanoseconds allow the software to render an intensity-weighted size distribution, generally fitted into a Gaussian distribution or a more challenging non-monomodal distribution (Stetefeld J. et al., 2016).

In NTA, the detector of light scattering is a microscope objective, which is connected to a digital camera for videorecording of the Brownian motion of the nanoparticles in suspension. Once optimized the frame rate, exposure time and sensitivity of the camera, the software records 30-60 s videos and analyzes them in four steps. First, a trained algorithm is used to identify the center of each particle. Second, the center of each particle is tracked throughout the video, frame by frame, to follow the Brownian motion of the individual particles in the field of view. Third, the software determines the average displacement of each particle over time (known as mean step size), used to derive the diffusion coefficient. Finally, the size of each particle is calculated through the Stokes-Einstein equation (2) and computed into a number-weighted size distribution (Maguire C.M. et al., 2017).

The advantage of both DLS and NTA methods is the description of the nanoparticle behavior in suspension, which is often the mean of administration for drug delivery purposes. However, as any experimental method, some limitations come with the validation, transferability, and comparison of results (Gioria S. et al., 2018). Two main challenges to address when relying on these techniques are the possible polydispersity of the sample and particle shape.

With particles of significantly different sizes in the same suspension, DLS-based methods encounter two main drawbacks. First, the point-by-point detection is always read as the total scattered intensity, which does not allow backtracking of the individual particles. Second, the software often first attempts to fit the size distribution into a Gaussian, which may not be adequate in the case of a multi-modal distribution (Maguire C.M. et al., 2018). The combination of these intrinsic characteristics of DLS-based methods leads to two possible sources of error. First, the resolution of different size peaks in a same sample is known to require a factor of three in mean size difference (Bhattacharjee S., 2016). Second, in polydispersed samples and according to the detection angle, the bigger particles can contribute in a greater manner to the intensity-weighted distribution, causing the mean

estimation to exhibit a systematic upward bias (Hassan P.A., et al., 2015). In the case of NTA, a single-particle tracking method, the number-weighted distribution that is obtained is often considered a more accurate description of the polydispersed sample. However, here the challenge lies in the detection of the particles themselves. As the scattering intensities depend on the wavelength of the light source and the size of the scattering object (Equations 6 & 7), shorter wavelengths would be optimal to induce scattering from the smaller particles. However, if bigger particles are also present in the suspension, their high scattering intensities may blind the camera, in turn preventing the smaller particles from being detected (Maguire C.M. et al., 2018).

To ensure the validity of these scattering-based measurements, a specific property of size distribution needs to be considered: the polydispersity index (PDI). This value is a dimensionless estimate of the width of the size distribution, and it is calculated from the hypothetical Gaussian distribution which best fits the data. When this value approaches values of 0.3 or higher, the Gaussian fitting should start being considered inadequate and insufficiently descriptive of the sample (Danaei M. et al., 2018). Moreover, in case of DLS data, alternative fittings should be considered, such as the non-negative least squares (NNLS) method, the exponential sampling method, or the constrained regularization method for inverting data (CONTIN) (Stetefeld J. et al., 2016). On the other hand, for NTA data, a careful analysis of the dynamic range of the camera and the laser used should be carefully revised (Maguire C.M. et al., 2018).

As for the second challenge of these methods, the identification of particle shape, it is important to remember that both methods determine the hydrodynamic diameter of the scattering objects, which is in itself a simplification of spheric particles. In fact, even if the NTA can be considered a microscopy technique, the first step in the software analysis is the determination of the center of the particle, which will then be considered a spheric object (Jarzębski M. et al., 2017). As we have seen earlier (§ 1.1.2), the shape of nanoparticles can influence their diffusion and behavior in general (Florence A.T., 2012a), hence for non-spheric nanoparticles both these techniques could show errors in the detection of the scattered intensities, hindering the predictability of their real behavior. For this reason, additional alternative imaging techniques are required to strengthen the characterization of nanoparticles (Foulkes R. et al., 2020).

1.3.2 Characterization and Imaging of Immobilized Nanocarriers

1.3.2.1 Background Theory of Microscopy for Nanomedicine

“Seeing is believing”.

Our eyes use the light as a probe to sense the world. However, the world of all that is smaller than 0.1 mm have been a mystery until the development of microscopes. Since the early discovery of compound microscope and over the past four centuries, we have witnessed the development of microscopy, finally leading to microscopes being essential tools in every cell lab. Whereas earlier scientists were looking up at the universe to find new and exciting big things, technological development enabled them to start looking down, at a whole other world that they could finally see and actually believe in. In an imaging experiment, there are very few requirements to observe a phenomenon. First, we need small objects to appear big enough for us to see them (magnification). Then, we want to identify the individual objects in space (spatial resolution) and eventually follow their dynamic features over time (temporal resolution). Finally, we want our objects to be clearly distinguishable from anything else in the background (contrast) (Thorn K., 2016). Although few, these aspects are strictly intertwined, generating trade-offs and challenges along the way.

Historically, to achieve the **magnification** of an object, a system of lenses was put in place to collect light shined through a sample. From the simplified version in Figure 10A, scientists developed increasingly smarter microscopes, which can self-correct for intrinsic distortion of the light path and allow for magnifications in the order of 10^3 times. Equation 8 describes the meaning of magnification,

$$\text{Magnification} = \frac{\text{object dimension in the image}}{\text{ground truth}} \quad (8)$$

where *ground truth* refers to the real dimension of an object, that depends on several optical and digital components of the microscope, such as the tube lenses, zoom factors, photographic projection lenses, eyepiece or sensor-to-monitor image size ratio, and objective lens (DeRose J.A. & Doppler M., 2018). Although all these components add to the final magnification, the contribution from the objective lens is generally the only factor reported in practice (e.g., 20x, 40x or 60x). This optical component is the closest to the sample, it is easy to adjust (generally microscopes mount at least 3 to 5 different objective lenses that can be rotated in place), and it directly contributes to both the magnification and the resolution of

an image (Figure 10B). In fact, without considering the stored resolution, increasing the magnification alone will not improve indefinitely the quality of the image (Piston D.W., 1998). The **resolution** stored in an image determines our ability to distinguish fine details when the image itself is magnified. However, as for the magnification, the resolution of an instrument cannot be increased indefinitely. In light microscopy, the lower resolving power achievable is determined by a fundamental property of light itself, diffraction. The plane light, when hitting a point object, will bend outwards and be converted into spherical wavefronts, gradually interfering with each other (Figure 10C). Because of this phenomenon, each point source in the sample plane will be represented as an airy disk in the image plane (Figure 10D), which is the intensity projection of the tridimensional point spread function (PSF, Figure 10E) (Murphy D.B. & Davidson M.W., 2012).

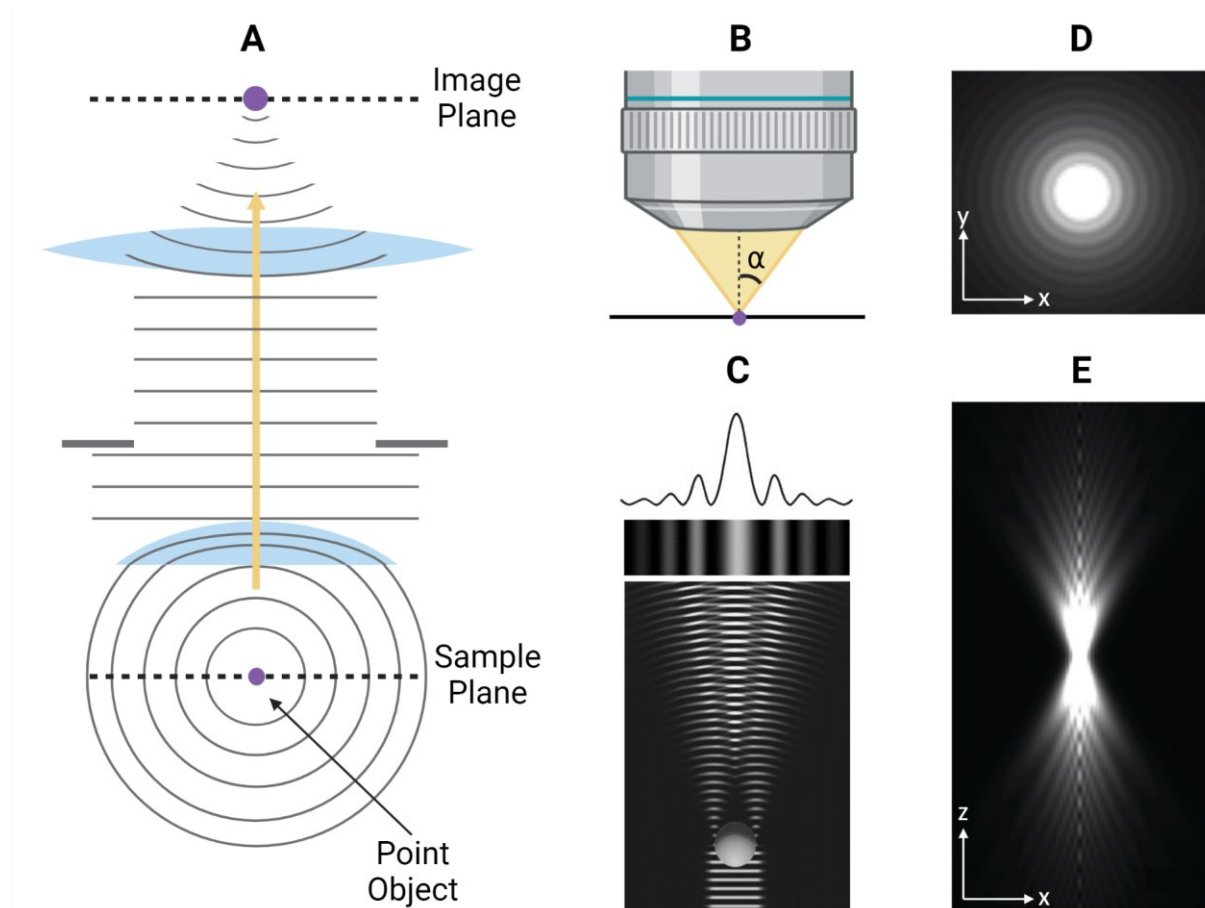
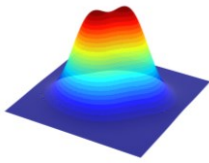


Figure 10. Image formation through the lens system of light microscopes. A) Schematic representation of a simplified lens system. B) Cone of light collection from the objective lens of a microscope. C) Diffraction of light caused by point objects. D,E) Airy disks of the point object as xy and xz intensity projection of the 3D PSF (images generated on PSF generator, plugin for ImageJ). Biorender.com was used to assemble the panels, inspired by the video course “Short Microscopy Series” on iBiology.org.

Considering two individual point objects, the minimum distance that will allow them to be distinguished as separate objects is defined as resolution of the microscope d (Figure 11). Ernst Karl Abbe, in the late XIX century, demonstrated that resolution is dependent on the wavelength of light λ , the refractive index of medium n and the half angle of light collection α , where he defined $n \cdot \sin \alpha$ as the numerical aperture NA (Figure 10B). Through his coherent imaging equation, he approximated the resolution limit of light for the image plane, as shown in Equation 9. This concept was then extended into Equation 10 for the z-resolution of out-of-focus planes (Maznev A. & Wright O., 2017).



$$d_{x,y} = \frac{\lambda}{2n \cdot \sin \alpha} = \frac{\lambda}{2NA} \quad (9)$$

$$d_z = \frac{2\lambda}{n \cdot \sin^2 \alpha} = \frac{2n\lambda}{NA^2} \quad (10)$$

Figure 11. Visual overlapping of the point spread functions (PSF) at Abbe's resolution limit.

In optimized conditions, the lateral resolution limit of light (Equation 9, also referred to as diffraction limit or Abbe's limit) approaches 220-250 nm. This is the ideal case scenario; however, the practice can involve limitations due to both instrumental and sample dependent challenges. Physicists and engineers have worked to optimize instrumental weaknesses such as unwanted deviations of the light path (aberrations) and efficiency of detection (e.g., complementary metal oxide semiconductor – CMOS, or cameras charged-coupled devices – CCD cameras) (Radhakrishna M. et al., 2021), to the point that it is not for the user to worry about these aspects anymore. However, even with the best cameras, the detection itself can limit the resolution when the sampling of intensities is not performed correctly. According to the Nyquist sampling theorem (Equation 11), to capture a function of frequency ν , it should be sampled at a frequency at least twice as high:

$$\nu_{sampling} \geq 2\nu_{event} \cdot \quad (11)$$

When referring to digital acquisition of images, the Nyquist sampling defines that the number of pixels recording individual information should be at least twice as high as the events to be recorded, hence the pixel dimensions should be below half the wanted resolution (DeRose J.A. & Doppler M., 2018). This optimization of detection, together with the correct choice of magnification according to the resolution needed, can significantly contribute to the quality of the imaging. However, the **contrast** of the structures of interest over their background can

be even more important than the maximum resolution of an instrument, as this will determine the real resolution in a specific image of a specific sample (Vijayalakshmi D. et al., 2020). As Figure 12 shows, resolving the objects of interest becomes more challenging in two instances. On one hand, the intensities deriving from these objects are comparable to the background noise, which in most cases cannot be entirely eliminated due to the thermal and electrical noise across the detector (Radhakrishna M. et al., 2021). On the other hand, when the contribution from out-of-focus planes is recorded as a single signal, as if coming from the focal plane, objects that are clearly separated in z may not be resolvable in xy (Swift S. & Trinkle-Mulcahy L., 2012).

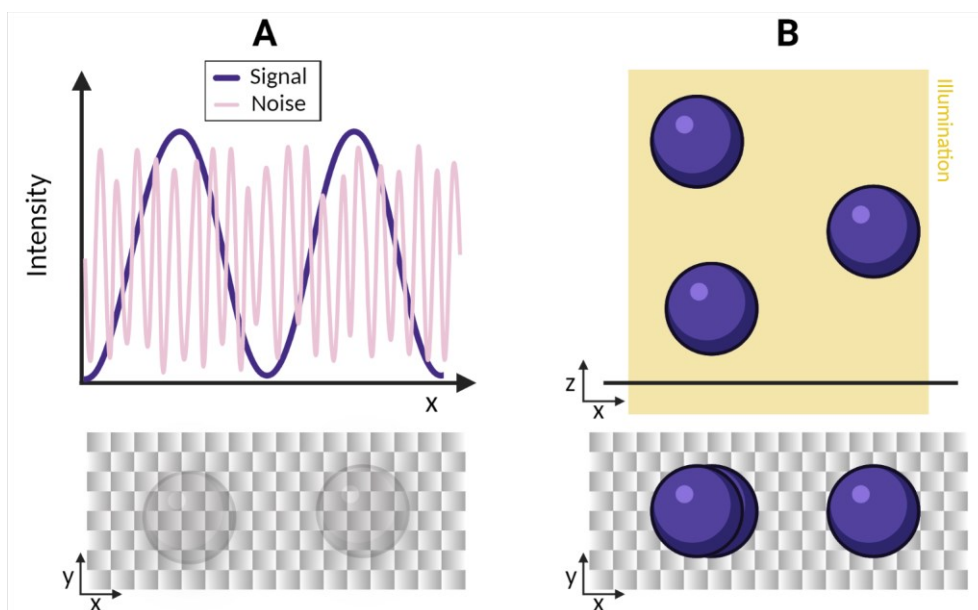


Figure 12. Effect of low image contrast on resolution. A) Effect of the similarities of the signal intensities coming from the objects of interest and the intensities of the unavoidable background noise: low signal-to-noise ratio (left) reduces the real resolving power of objects at the same distance. B) The collection of light from the full thickness of a sample can co-localize objects in the xy plane that were actually separated in the z dimension, causing a reduced spatial lateral resolution. The figure was prepared on Biorender.com

The “Trade-off Triad”. To increase the quality of the signal (generally expressed as signal-to-noise ratio, SNR), a first option may be increasing the exposure time. In this case, the sensor detects a higher real signal, without substantial increase on the intrinsic noise; however, the acquisition time for an image becomes longer, increasing the possibility of phototoxicity on live samples and decreasing the time resolution to detect active dynamics. A second option could be binning together pixels on the sensors. This method can also maintain the low noise,

while increasing the area that collects a single signal; however, as this corresponds to increasing the pixel dimension, the result is lower spatial resolution (Swift S. & Trinkle-Mulcahy L., 2012, Schermelleh L. et al., 2019). Furthermore, the temporal and spatial resolution tend to be inversely correlated as well, since a faster acquisition corresponds to a lower quality of the stored information. This leaves little to no space for image analysis, which is often fundamental to obtain super resolution information, as will be explained in § 1.3.3.3. This trade-off between the signal intensity, spatial resolution and temporal resolution is crucial for the successful application of microscopy to nanomedicine.

In the case of nanoparticles in suspension, we would ideally require: i) high temporal resolution to follow their fast Brownian motion; ii) high spatial resolution due to their nanoscale size; and possibly iii) a way to increase their SNR, as their size could be correlated to a low signal.

To image and characterize both the morphology and size of nanoparticles, one aspect we can choose to sacrifice from the trade-off triad is the temporal resolution. To achieve this, nanoparticles need immobilization. In this work I have focused on three strategies that can be implemented for imaging and characterizing immobilized nanoparticles:

- exchanging the photon beam used in light microscopy for an electron beam, switching over to electron microscopy;
- increasing the contrast of nanoparticles on background by introducing controllable bright molecules such as fluorophores, which specifically respond to light excitation and allow for the use of the new super resolution microscopy techniques;
- adjusting the light source and the detection methods to either reduce the contribution from out-of-focus light, or to measure a different property of matter such as the phase delay of light.

In practice, the first of these strategies has become the predominant one in nanomedicine research, probably because throughout history, advancement in electron microscopy has been the fastest at achieving the highest resolution required to characterize nanomedicine. Therefore, techniques such as transmission electron microscopy (TEM) and scanning electron microscopy (SEM) are currently considered the gold standards for the complementary characterization of nanoparticles (Soares S. et al., 2018), even though the recently advanced light microscopy techniques could be considered competitive.

1.3.2.2 Gold Standard Imaging Methods and Associated Challenges

The high spatial resolution achievable in electron microscopy is explainable by the nature of the electrons (described by L. de Broglie in 1925, awarded with the Nobel Prize in Physics in 1929). As for photons (Figure 8, page 18), electrons too possess a particle-wave nature, but with wavelengths much shorter than photons. Because the diffraction limit is wavelength-dependent, shorter wavelengths will correspond to smaller resolvable distances. To make use of this dual nature of electrons, a thermal source can be used to produce an electron beam (gun), which can be stabilized in high vacuum (10^{-6} Torr) and focused onto a sample. As a type of ionizing radiation, a range of secondary signals can be detected from the sample and subsequently utilized in different electron microscopy techniques (Williams D.B. & Carter C.B., 1996). After a century of developments, electron microscopy, in both transmission (TEM) and scanning (SEM) mode, is routinely performed in any laboratory that can afford such instruments. TEM offers super high resolution that can be achieved for small field of view, on thin samples embedded into electron-transparent base material. SEM provides slightly lower resolution but is less sensitive to the thickness of the specimens as it allows to scan the surface on wider fields of view (Modena M.M. et al., 2019).

In nanomedicine, these methods can be utilized for both morphology and size analysis of the dry mass of nanomaterials. The fact that these instruments work in high vacuum implies the requirement of pre-drying the specimens to image. For solid particles, such as metal nanoparticles, the need for dehydration of the specimen is not expected to affect the morphology. Furthermore, these particles are electron-dense, hence they are opaque to the electron beam and ensure a good contrast over background in the images (Grabar K.C. et al., 1997). However, for non-rigid particles such as liposomes, the process of dehydration can induce shrinkage and/or morphology changes (e.g., Figure 13A) and therefore be poorly representative of their morphology in suspension (Bibi S. et al., 2011). Furthermore, lipid-based nanocarriers, among others, can be transparent to the electron beam. This property results in the need of additional pre-treatments of the samples before imaging. In the case of TEM, it has become a standard procedure to apply negative staining (e.g., with uranyl acetate) to darken the background around the nanoparticles (Ruozi B. et al., 2011, Modena M.M. et al., 2019). Although significantly increasing the contrast, this treatment can induce additional artifacts on the images, such as faulty multi-lamellarity effects (Bibi S. et al., 2011) or deceiving

oval shapes due to partial staining (Figure 13B). In the case of SEM, prior gold/palladium coating is necessary to increase the superficial electron conduction and obtain sufficient contrast on the image. However, this coating of 5-20 nm can introduce a significant systematic error in the determination of the size of nanoparticles (Eaton P. et al., 2017).



Figure 13. Examples of artifacts in TEM imaging of liposomes. A) Squared liposomes show altered morphology as drying artifacts. B) Oval and asymmetric liposomes show altered morphology as drying and partial staining artifacts. Pilot data to paper IV.

Electron microscopy images can be analyzed to obtain a number-weighted size distribution of the nanoparticles within the imaged field of view. This can be easily achieved through different methods of segmentation and analysis, which are now widely available in most imaging platforms (Saaim K.M. et al., 2022). Nonetheless, there are some important aspects to consider when using such methods. First, the diameters of the nanoparticles that are measured in the images refer to their dry diameter, which is expected to be smaller than the hydrodynamic diameter determined with the scattering-based techniques (as described in § 1.3.1.) (Modena M.M et al., 2019). Second, although some morphology changes for known samples can easily be recognizable (e.g., Figure 13), less evident effects of the sample preparation procedures, such as vesicle shrinkage, easily pass the image quality check, possibly leading to a downwards bias in the size estimation (Bibi S. et al., 2011). Third, as number-weighted distributions, these size estimations cannot be directly compared to intensity-based distributions obtained, e.g., in DLS (Kaasalainen M. et al., 2017).

To avoid such complex sample preparations, newer techniques such as environmental SEM (ESEM) have been proposed as suitable alternatives. In ESEM, the sample is maintained at a pressure of 0.2-2 Torr in aqueous vapor. This avoids both full drying and pre-coating since the signal is amplified through the vapor. However, the limited availability of these instruments makes it difficult to implement for routine imaging (Mohammed A. & Abdullah A., 2018).

1.3.3 Fluorescence-based Imaging of Nanocarriers

1.3.3.1 Fluorescence as a Property of Matter

To achieve imaging in more realistic environments, we can focus on the most powerful tool biologists have had since the invention of the microscope: fluorescence. The fluorescence as a phenomenon is the result of a specific interaction between light (photons) and matter (here, electrons in atoms). It represents a specific emission exclusively triggered by a given excitation source (Lichtman J.W. & Conchello J.A., 2005). To describe the interaction of light with matter, the Jablonski's diagram is often utilized as one of the clearest tools (Figure 14). Once a photon interacts with an electron, the latter absorbs energy, resulting in an excited singlet state (S1 or S2), as shown by the blue arrows on Figure 14A. Here, the instability of this excited state can be resolved in three ways:

- Non radiative relaxation (green arrows): the electron returns to its ground state of energy through vibrational relaxation, which does not include far-field emission.
- Fluorescence emission (red arrow): after internal conversion, the electron collapses to its ground state, emitting a photon as a far-field electromagnetic wave.
- Intersystem crossing (yellow arrow): after internal conversion, the electron enters the forbidden triplet state (T1) in a slow transition leading to a high reactivity of the molecule. Consequently, the electron can relax to ground state through phosphorescence (orange arrow) or be forced into delayed fluorescence (violet arrows) through the excited singlet state (S1).

The fluorescence phenomenon can be described by certain physical rules. **Kasha's rule** states that the emission of photons as far-field radiations is possible only from the lowest excited state (0 of S1, in Figure 14A). For this reason, independently of the intensity of absorption, the electron will undergo non-radiative vibrational relaxation to 0 of S1, prior to fluorescence emission. There are two main corollaries deriving from this rule. First, the emission spectrum is independent of the excitation wavelength – **Vavilov rule**. Second, the vibrational relaxation results in energy loss, therefore the emitted photon wave will have lower energy than the absorbed one. In turn, the emission spectra will shift towards longer wavelengths if compared to the excitation spectra, a phenomenon known as the **Stokes shift** (Figure 14C) (Jameson D.M., 2014).

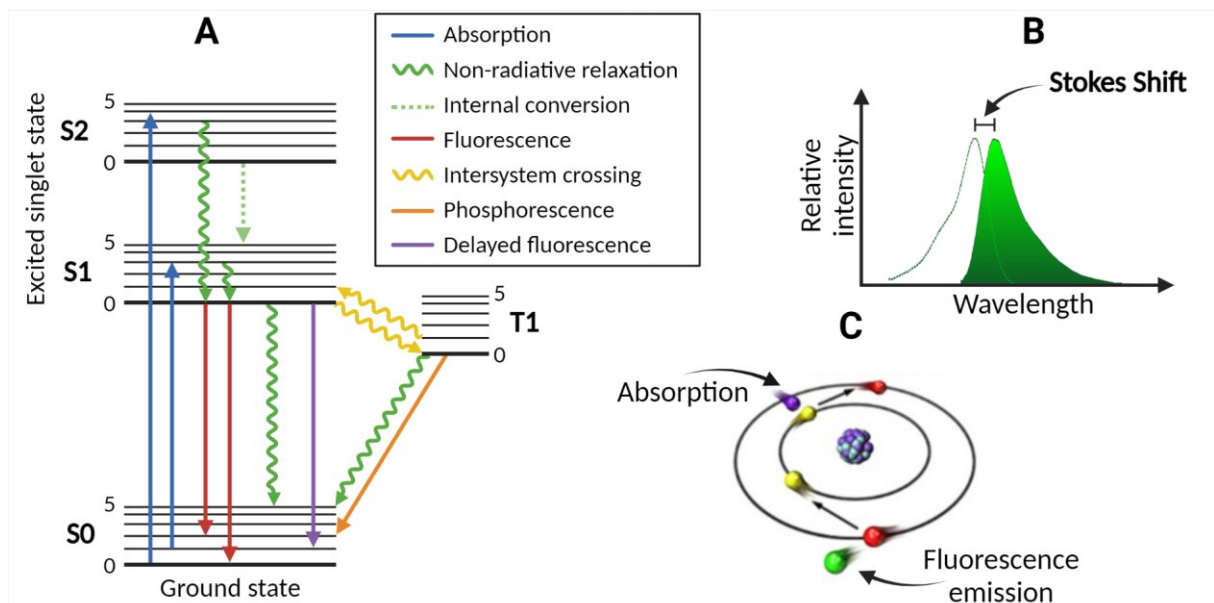


Figure 14. Interaction of light with matter. A) Jablonski's energy diagram for the visualization of the energy state of electrons. The solid arrows represent far-field radiations while the wavy arrows refer to non-radiative relaxation. The dotted arrow shows internal conversion as a lossless energy transition. B) Atomic model for the generation of a fluorescent signal. C) Excitation and emission spectra of a sample fluorophore (FITC) showing the red-shifted emission, known as the Stokes shift. Figures were independently prepared on Biorender.com as an adaptation from: <http://zeiss-campus.magnet.fsu.edu/articles/basics/fluorescence.html>.

How long the electrons stay in each state depends on the chemistry of the molecule, the environment in which the molecule is placed in, and the type of excitation used (Lichtman J.W. & Conchello J.A., 2005). Molecules that can emit a fluorescence signal are known as fluorophores. Their outermost layer of electrons determines the shape of their absorption and emission spectra, as well as their efficiency as emitters. Based on the chemistry of the molecule, it is possible to predict its fluorescence behavior to some extent. In particular, the possibility of a molecule to fluoresce has long been linked to the presence of aromatic rings, where the electrons are delocalized in a system of conjugated double bonds. In general, the higher the number of double bonds, the higher the efficiency of a fluorophore in converting the absorbed photons into fluorescence emission (Lakowicz J.R., 1999). Such efficiency is known as **quantum yield** (ϕ) of a fluorophore (Equation 12) and is expressed as a ratio of the radiative fluorescence relaxation (k_f) and the sum of radiative and non-radiative (k_{nr}) relaxation. This value, expressed in the range from 0 to 1, is the first aspect contributing to the final brightness of a fluorophore. The second aspect, known as molar **extinction coefficient** (ϵ), is accounted for in the Lambert-Beer Law (Equation 5, here expressed as 5')

and measured as a function of absorbance at a given wavelength (A_λ), molar concentration (M) and pathlength of light shone through the sample (l).

$$\Phi_f = \frac{N(\text{photons emitted})}{N(\text{photons absorbed})} = \frac{k_f}{k_f + \sum k_{nr}} \quad (12)$$

$$\varepsilon = \frac{A_\lambda}{Ml} \quad (5')$$

The higher the values for quantum yield and extinction coefficient, the brighter is the fluorophore at hand. Herewith, a third factor comes into play when choosing a fluorophore: **excited-state lifetime**. The time the electrons spend in the excited state (generally 1-10 nanoseconds) reveals the fate of the energy absorbed with the photons. Longer times reflect a higher vibrational relaxation, which in turn shows a bigger Stokes shift. This is a useful property for the detection of clean fluorescent emission without interference from the excitation source (e.g., through band-pass filters, as shown in the striped pattern in Figure 14C). However, longer excited-state times also hold higher probability of a chemical interaction between the fluorophore and molecules in the environment, possibly leading to loss of fluorescence (with quenching or photobleaching), or intersystem crossing to the forbidden triplet state (Guilbault G.G., 2020).

1.3.3.2 Use of Fluorescence in Biological Sciences

Historically, since the discovery and description of the quinine sulfate as the first small organic fluorophore (Herschel J.F.W., 1845), several molecules have been studied and exploited for their fluorescence. Biologically relevant molecules such as NAD(P)H, amino acids, vitamins and flavins were the first used to follow cellular dynamics as intrinsic fluorophores (Monici M., 2005), although now they are mostly regarded as background autofluorescence. Native fluorescent amino acids such as tryptophan (Trp), but also Phenylalanine (Phe) and tyrosine (Tyr), have been used to engineer fluorescent proteins, as genetically encoded probes, in the line of the well-characterized green fluorescent protein, GFP (Wiedenmann J. et al., 2011). Additionally, small organic molecules with aromatic systems have been studied and optimized as individual fluorophores (Terai T. & Nagano T., 2013), summarized in Figure 15 (top), or covalently bound to the macromolecules of interest (e.g., fluorescently labeled lipids), presented in Figure 15 (bottom) (Kyrychenko A., 2015).

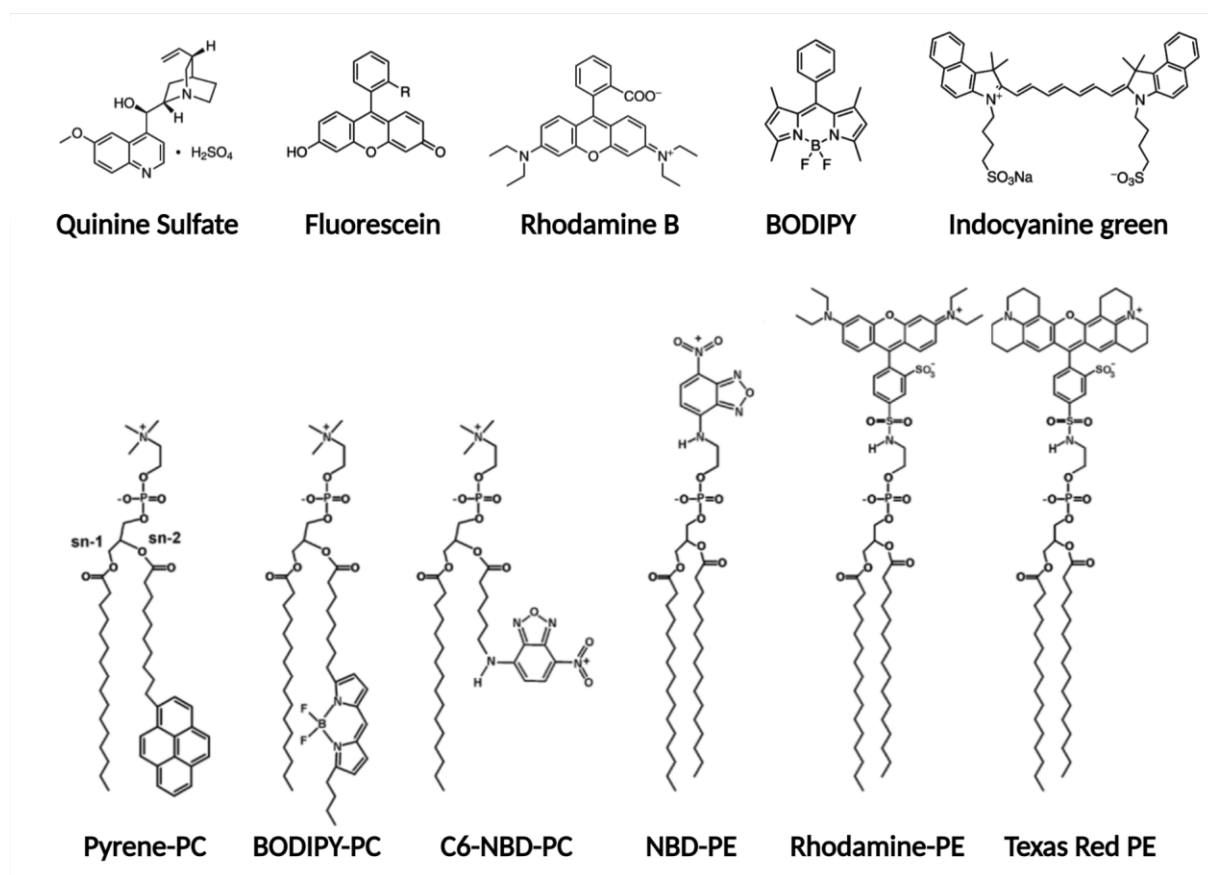


Figure 15. Examples of small organic fluorescent molecules (top) and fluorescently labeled phospholipids. Images adapted from Terai T. & Nagano T., 2013 and Kyrchenko A., 2015, with permission from Elsevier and IOP Publishing, respectively.

The predictable behavior of fluorophores in response to a specific excitation has been utilized in biological and medical sciences. Subsequently, for a known fluorophore of interest, it is possible to adjust the microscope setup to detect the range of wavelengths that are solely fluorophore specific, blocking all the non-specific scattered light. The obtained image will then exhibit a bright signal over a dark background, allowing **high contrast** imaging. Furthermore, with the same principle of blocking and re-directing specific wavelengths of light, instruments can also be tailored for sequential or even simultaneous detection of two or more colors in the visible spectra, allowing for **multi-color** imaging. When the fluorescent moieties of choice are used to label biological structures of interest (e.g., through covalent bond or domain sequestration), this **specificity of labeling** permits tracking of biological dynamics, possibly over time and space. Furthermore, the introduction of small fluorescent moieties in biological systems generally bears **low cytotoxicity**, having little effect on the cell life cycles and potentially enabling long-term experiments (Terai T. & Nagano T., 2013).

For almost a century, scientists have utilized these advantages of fluorescent molecules to investigate biological phenomena, down to cellular and sub-cellular level. Starting from the autofluorescence of natural molecules, advancing through the specific labeling developed by modifying the chemistry of small molecules, to more complex biodistribution studies, that enabled following the accumulation of fluorophores as model pharmacological treatments (Kasten F.H., 1989), fluorescence has gained more and more attention in biomedical field. However, as more and more technological developments were implemented into the microscopy field, some limitations started to become evident (Cohen B.E., 2010).

The choice of the fluorescent molecule affects the outcome of imaging experiments. The **brightness** of a label depends on its chemistry and can significantly vary in different biological environments, making quantification rather complex if not relativized with internal and external controls (Lakowicz J.R., 1999). Furthermore, the chemistry of the fluorophore and its interaction with the environment can also influence its stability. In fact, if the fluorescence emission upon excitation happens with a simultaneous chemical modification of the moiety, the fluorophore will undergo a progressive loss of fluorescence, which is known as **quenching** (if reversible) or **photobleaching** (if irreversible, as in the case of a covalent reaction with oxygen molecules in the environment). When these phenomena are predominant in the experiment, performing and quantifying long-term data becomes difficult (Lichtman J.W. & Conchello J.A., 2005).

To complicate the situation even further, it is important to consider that the biological samples often possess intrinsic fluorescent structures, which can vary in composition and distribution according to the cell cycle and stress (Surre J. et al., 2018). The emissions from this intrinsic **autofluorescence** can then be detected together with the specific signal of the structures of interest if the emission wavelengths overlap. From the instrument point of view, if the contribution from out-of-focus light is not excluded, this can decrease the contrast of the structures of interest in the focal plane, causing a lower-than-optimal contrast and higher **background noise** (Schermelleh L. et al., 2019). Furthermore, although the fluorescent labeling is in general not toxic for live imaging, the necessity to use high power sources and/or prolonged imaging times can translate into illumination-induced toxicity, known as **phototoxicity** (Laissue P.P. et al., 2017).

Although the disadvantages might sound substantial, the advancements the microscopy field have offered solutions to overcome some of the issues, exploiting these very challenges as new sources of information. New fluorophores are continuously being developed to tackle low brightness and poor physicochemical stability of the emitters (Trinh N. et al., 2020, Cong H. et al., 2020), with novel classes being increasingly implemented into practice, such as 2-photon absorbing organic dyes (Cohen B.E., 2010, Niu G. et al., 2019). Hence, brighter specific signal could be better identified over the autofluorescence of the background, while a lower illumination power could be sufficient for imaging, reducing the phototoxicity on the live samples and allowing for longer imaging timeframes (Tosheva K.L. et al., 2020). The chemical interaction of fluorophores with their environment has been harnessed to develop chemical probes and concentration indicators for different analytes. This allows non- or weakly-fluorescent molecules to emit a fluorescent signal after interacting with the molecules of interest (Terai T. & Nagano T., 2013). Similarly, the quenching of fluorophores has been exploited in super-resolution microscopy (SRM) through specific buffers to induce photoactivation and/or photo-switching (Jradi F.M. & Lavis L.D., 2019), but also in well-known techniques such as PeT (photoinduced electron transfer) or FRET (Föster resonance energy transfer) (Tian X. et al., 2021). In these techniques, the close proximity of two matching fluorophores (e.g., FRET pair) causes the first one to quench after external excitation and the second one becomes excited by the first (Zu F. et al., 2017). The total fluorescence emission in the respective channels is thus an indicator of the distance between the fluorophores. Therefore, pre-labeling two structures of interest with a FRET pair makes it possible to follow the dynamics of their interaction (Gulin-Sarfraz T. et al., 2019). In parallel, technological developments in fluorescence microscopy currently enable several approaches to reduce the background noise deriving from out-of-focus light as well as an increase of the signal-to-noise ratio (SNR) in the images (e.g., through image processing or manipulation of the light source).

1.3.3.3 Super Resolution Fluorescence Microscopy

The sensational development of light microscopy in the last 20 years is linked to the so-called super-resolution microscopy (SRM), the importance of which saw the three scientists Eric Betzig, Stefan W. Hell and William E. Moerner being awarded the Nobel Prize in Chemistry in 2014. Although Abbe's limit is still a valid physical law (Maznev A. & Wright O., 2017), these scientists and many others working in the SRM field have developed tricks to play around this

limit, allowing us to bring the advantages of light microscopy to resolutions previously possible only in electron microscopy (Schermelleh L. et al., 2019).

The first class of SRM techniques can be collectively defined as single molecule localization microscopy (**SMLM**). Here, the individual emitters which are too close to be resolved in space are resolved in time. The main requirement for these techniques is for the individual fluorescent molecules to blink, such that at any given time only some emitters are switched on, hence being sparse enough to be resolved in space. The acquisition then becomes a multi-frame imaging that is subsequently reconstructed into a single image through image processing (Figure 16) (Sage D. et al., 2019). The different methods in this class use different approaches to achieve the blinking. For example, the use of specific photoswitchable fluorophores is needed for the application of fluorescence photoactivation localization microscopy (fPALM), while special buffers are required in direct stochastic optical reconstruction microscopy (dSTORM) to induce the intermittent emission on conventional fluorophores (Li H. & Vaughan J.C., 2018). Resolutions down to molecular level can easily be achieved at the expenses of temporal resolution (for the long acquisition times required) and easiness of sample preparation (as the spatiotemporal sparsity of the emitters needs to be ensured through correct staining and blinking behavior) (Whelan D.R. & Bell T.D., 2015).

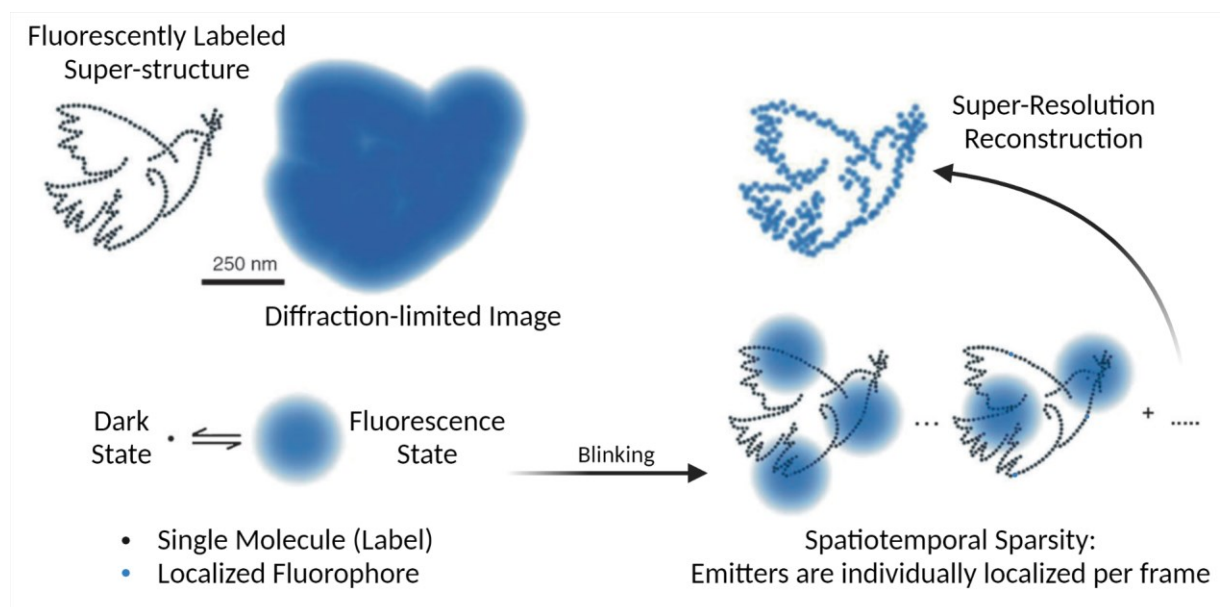


Figure 16. Visual schematics of the application of single molecule localization microscopy. The blinking of emitters gives them spatiotemporal sparsity such that a repeated acquisition of the same field of view over time enables the resolution of close objects appearing in different frames. Figure adapted from Möckl L. et al., 2014, with permission from John Wiley and Sons publisher.

Recently, a new class of methods related to SMLM has shown strong potential for biological samples with high labeling density. Collectively, these new methods are known as fluorescence fluctuation super resolution microscopy (**FF-SRM**) and they can be defined as computational algorithms for image processing of multi-frame imaging datasets (Schermelleh L. et al., 2019).

Super-resolution optical fluctuation imaging (**SOFI**) was the first one to be developed. In this algorithm, the fluorescence fluctuation per pixel is analyzed over time on a multi-frame dataset. After cumulant analysis on each pixel through all the frames, the processed image shows only the highly correlated fluctuations (e.g., removing the contributions of emitters on neighboring pixels); hence reducing the background noise, increasing the contrast, and allowing super-resolution acquisition on a standard diffraction-limited setup. Only requirements for this algorithm are: i) two different emission states for the fluorophore (e.g., on and off) and ii) this blinking must happen individually and stochastically for each emitter (Dertinger T. et al., 2009).

Super-resolution radial fluctuations imaging (**SRRF**) is an analytical method which builds on the principles of SOFI by accounting for the so-called radially transform. Herewith, the algorithm performs a sub-pixel analysis to quantify local radial symmetry. Assuming that each emitter is a symmetric point source, high local symmetry will correspond to the emitter while low local symmetry will be interpreted as background and hence suppressed, obtaining higher SNR, contrast, and resolution (Gustafsson N. et al., 2016).

Super-resolution imaging based on auto-correlation two-step deconvolution (**SACD**) is a composite algorithm built on two models, namely the Lucy-Richardson deconvolution and the multi-plane autocorrelation. The deconvolution step is performed to remove the systematic imaging error due to the PSF of the microscope, hence reducing the background noise on the image. The autocorrelation step is similar to the SOFI approach; however, because of the deconvolution pre- and post-processing, a lower number of frames can be fed to the algorithm to similarly reconstruct a super-resolved image with high degree of background suppression (Zhao W. et al., 2018)

Entropy-based super-resolution imaging (**ESI**) is an algorithm that interprets fluorescence fluctuations in terms of entropy per pixel. High entropy corresponds to high probability of an emitter of being localized within the pixel area. Hence, once accounted for the cross-entropy

among neighboring pixels, the algorithm will reconstruct the images as a probability function (Yahiatene I. et al., 2015).

Multiple signal classification algorithm (**MUSICAL**) is a statistical method which combines single value decomposition of the image stack and pattern recognition. To each of the generated patterns (eigenimages) the algorithm assigns a singular value. The higher the value the more prominent is the pattern, hence, the more probable is its correlation to the location of emitters. Lower values will then mostly refer to noise background. By selecting a threshold between high values (signals) and low values (background noise), the algorithm can analyze and compare them in the form of ratio. The subsequent incorporation of the information of the PSF allows to locate and super-resolve the position of the labeled structures of interest (Agarwal, K. & Macháň R., 2016)

The advantage of both SMLM and FF-SRM methods is the fact that they can theoretically be implemented on any fluorescence microscope at hand, as they do not require modifications to the illumination setup. On the other hand, all these methods are very heavy on image processing, which can become a disadvantage if the quality of the acquisition does not meet the requirements as the algorithms could render artefact-y images (Schermelleh L. et al., 2019). However, as the potential of these methods is experimentally reviewed in this thesis, I will postpone some more details to the dedicated section (§ 4.3.2.).

An alternative approach to improve the resolution in light microscopy is to modify the illumination setup (Tang J. et al., 2019). The conventional widefield illumination shown in Figure 17A is the simplest approach where a laser shines light of a specific wavelength through the whole thickness of the sample. In widefield mode, the light collection is also coming from the whole thickness of the sample; hence the contrast of the images can be lower if the structures of interest are well separated in z , but not in xy . Changing this illumination mode can increase the contrast in the detection of emitted light and therefore increase the effective resolution on the images. The first approach historically developed is confocal laser scanning microscopy (CLSM, Figure 17B). The light is channeled to a small spot which is moved first in xy and then in z for a point-by-point scanning of the sample. This illumination trick allows the optical sectioning of the thickness of the sample and therefore reduces the contribution of out-of-focus light into the signal detected from the focal plane (Pawley J., 2006). Figure 17C shows the total internal reflection (TIR) illumination mode. As the name says, here the light is

totally reflected away from the sample creating at the very surface of it a so-called evanescent field that can excite the fluorophores in its proximity. Although this illumination cannot penetrate through bigger thicknesses than 200-300 nm, it can provide superficial information with very high contrast and very low phototoxicity for live samples (Axelrod D., 2013).

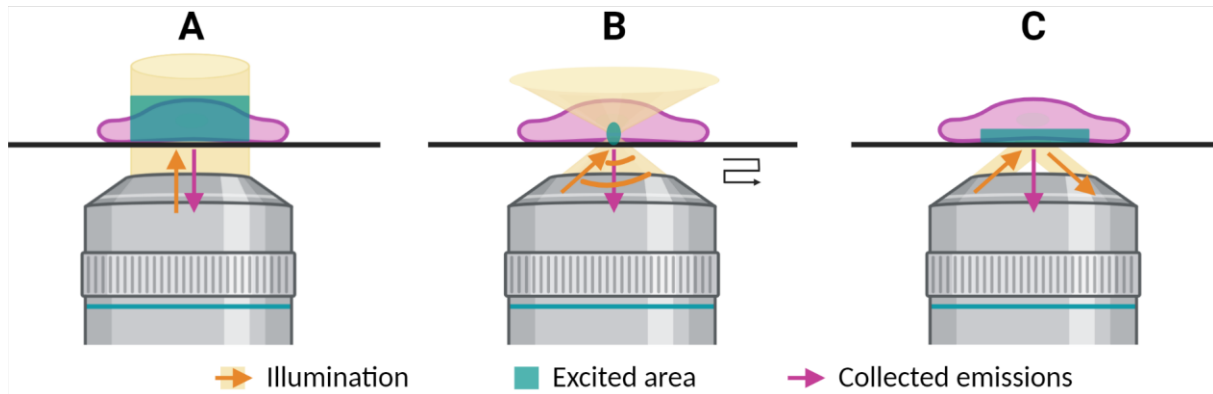


Figure 17. Mode of illumination most applied in fluorescence microscopy. A) Widefield illumination. B) Confocal laser scanning illumination (cone of light for point scanning on the sample). C) Total internal reflection mode. The figure was prepared on Biorender.com.

The modification of the light collection allowed by CLSM and TIR illumination result in increased contrast and effective resolution. However, both these modes are still considered diffraction-limited microscopy as Abbe's resolution limit of light is still the theoretical lower bound. To achieve super-resolution information, these illumination modes need to be combined with a super-resolution approach. Specifically, CLSM finds its own super-resolution method in stimulated emission depletion (STED), while the TIR illumination can be implemented in several systems for both SMLM and structure illumination microscopy (SIM) (Schermelleh L. et al., 2019).

Stimulated emission depletion (**STED**) is the direct upgrade of confocal microscopy for super-resolution applications. Here, a doughnut-shaped high-power laser is combined to a confocal laser to effectively reduce the area of the point that is illuminated at each time in the scanning (Figure 18 A). By regulating the intensity of the STED laser, it is possible to control the resolution. In fact, higher power corresponds to a smaller region of minimal intensities (center of the doughnut). The depletion laser shifts the expected emission of the fluorophores outside of the detected range, which means that the fluorophores are still excited and can undergo photobleaching. Furthermore, the high power of the STED laser can cause high phototoxicity on live samples. However, STED is the only SRM technique which does not require image processing per se, hence being the least prone to artifacts (Hell S.W. & Wichmann J., 1994).

Lastly, structured illumination microscopy (**SIM**) plays its strength on a fringe pattern of illumination, where the distance between the stripes is close to the resolution limit. The interferences deriving from the shifting and rotation of this pattern within a specific field of view allow the encoding of high frequency information (hence, smaller objects) into the detectable information. A computational trick in the frequency domain (Fourier transform) will thus allow the image reconstruction with details previously not resolvable. Hence, the resolution of an optimized SIM microscope allows to half the theoretical resolution limit, with very little requirements for the sample preparation that in turn opens the possibility to optimize live cell imaging (Wu Y. & Shroff H., 2018, Richter V. et al., 2021).

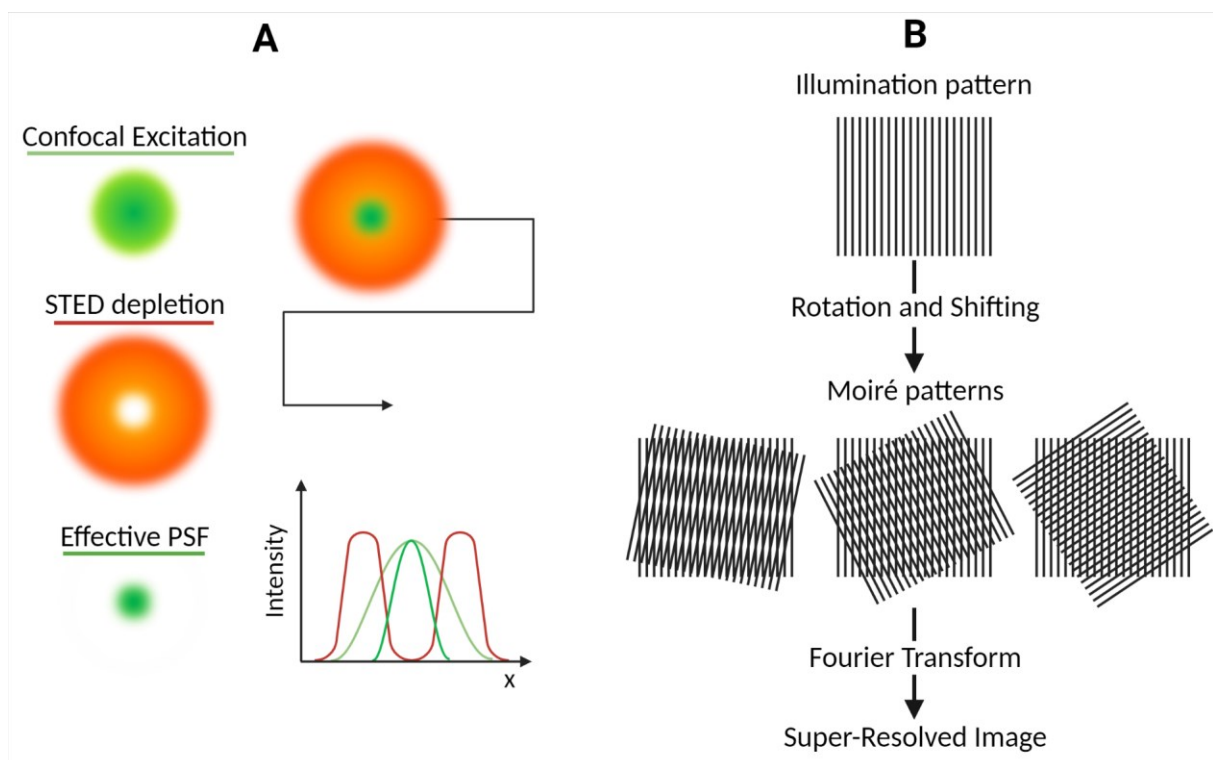


Figure 18. Super-resolution microscopy obtained by modifying the illumination on the sample. A) Stimulated emission depletion STED, based on the doughnut depletion laser. B) Structure illumination microscopy SIM, based on the stripe-pattern illumination which determines the Moiré interference. The figure was prepared on Biorender.com.

The use of these super-resolution techniques in health sciences, and nanomedicine in particular, enhances the advantages of the simple use of fluorescence allowing us to localize structures of interest down to molecular level with multi-color specificity of labeling (Pujals S. & Albertazzi L., 2019). However, as this field of microscopy is still relatively young, to be able to believe in what we see in the nanoscale, alternative techniques able to assist in method validation are needed.

1.3.4 Label-free Light Microscopy on Nanomedicine

1.3.4.1 Phase Property of Light and Light Sources

An often-disregarded property of electromagnetic waves resides in their phase information. In fact, when illuminating a sample with a light source, the information that is usually recorded is the intensity decrease due to absorption, hence the reduction in amplitude of the wave. However, objects that show low degree of absorption, such as many cell types and biomaterials, will be mostly transparent to the light. In these cases, although not significantly affected in amplitude, the light wavefront emerging from a sample is shifted in phase; hence, the analysis of this shift can help retrieving information otherwise invisible in intensity measurements (Park Y. et al., 2018)

Physically speaking, the phase of a wave (φ) is an angular description of the oscillation period (sinusoidal function), which is dependent on the position (x, y) at all times. This dependence on reference spatial coordinates makes the phase information complex to interpret as an absolute value. For this reason, experimentally, phase is always evaluated through an internal control: the light generated at the source is passed through a beam splitter where half the radiations are collected raw (reference beam), and half are first directed towards the sample (object beam). As such, the overlapping of the information carried by reference and object beams generates an interference pattern (interferogram) that is a visual representation of the phase delay that happened at the sample plane. The effect that a sample can have on the phase of light depends on the wavelength used λ , the thickness of the sample h and the difference in refractive indexes between objects n_2 and medium n_1 , as shown in Equation 13:

$$\varphi(x, y) = \frac{2\pi}{\lambda} [n_2(x, y) - n_1(x, y)] h(x, y) . \quad (13)$$

By applying this formula to the recorded interferograms, it is then possible to obtain point-by-point quantitative information about the thickness of the sample, usually visualized as a phase map. Being able to measure phase shifts of 1 mrad allows the detection of nanometric changes in thickness, even with minimal differences in the refractive index (Bhaduri B. et al., 2014). However, the trade-off triad between signal intensity, temporal resolution, and spatial resolution (§ 1.3.2.1.) can be found also when dealing with phase imaging.

The choice between temporal and spatial resolution is connected to the choice of the geometry of the instrument and the relative processing algorithm needed to extract the phase

maps from the recorded interferograms. An off-axis geometry, combined with a CCD camera, allows fast acquisition and therefore high temporal resolution, retrievable through the Fourier transfer algorithm. However, the interferograms recorded as such tend to lose the high frequency information (relative to smaller objects/details), with a consequent reduction of spatial resolution. On the other hand, if temporal resolution can be spared (e.g., for immobilized samples), the use of an on-axis geometry and the acquisition of interferograms with a higher number of frames per phase per field of view would allow the use of the phase shifting algorithm, hence maintaining higher spatial resolution (Ahmad A. et al., 2020, Balasubramani V. et al., 2021).

To lower the contribution from the background into the images, which is vital to resolve the smallest details on the structures of interest, once again it is possible to manipulate the light source to our advantage. In particular, the sensitivity of the instrument is determined by the coherence of light source, which can be assessed in time and space. High temporal coherence for an electromagnetic wave means that the wave maintains its shape and properties in time. High spatial coherence is verified when light that originated from the same point source behaves equally in all direction of propagation (Bhaduri B. et al., 2014).

Lasers are examples of light sources with both high temporal and spatial coherence, which is an advantage in many microscopy applications (e.g., fluorescence microscopy), but becomes a disadvantage when dealing with interference-based techniques such as phase imaging, as they generate high speckle and coherent noise, introducing background artifacts. Opposite to lasers, we find the white light generated by sources such as halogen lamps, where the combination of all the wavelengths in the visible spectrum and the lower stability of the emitting source makes the coherence low both in temporal and spatial terms. This light source was shown to produce a more consistent and low background (Bhaduri B. et al., 2012); however, white light carries properties of dispersion and chromatic aberrations that can make the alignment difficult to implement if not on a small field of view. A third light source often used in microscopy labs is the LED light, with a partial increase in both spatial and temporal coherence in comparison to the white light from halogen lamps. When using LED light, the consistent and low background can be mildly extended over a larger field of view, but the difficulties in alignments remain. The fourth, and newest, light source has been recently developed as a low spatial and high temporal coherence source, named pseudothermal light

source (PTLS). This source combines an easy-to-align laser diode with a rotating diffuser that purposely reduces the spatial coherence of the original source, hence reducing the speckle noise while maintaining stable illumination over wide fields of view (Ahmad A. et al., 2016).

1.3.4.2 Quantitative Phase Microscopy (QPM) in Biological Sciences

The possibility of encoding the phase information into the traditional brightfield imaging has worked as a contrast enhancer technique for almost a century, and the father of phase microscopy, Frits Zernike, was awarded the Nobel Prize in 1953 for this discovery (Zernike F., 1955). However, the technological development that now allows to detect minimal pathlength shifts, together with the possibility of quantifying such shifts (Equation 13) has guided microscopists towards the so-called quantitative phase microscopy (QPM, also known as quantitative phase imaging, and closely related to other interferometric methods such as digital holographic microscopy) (Bhaduri B. et al., 2014).

The intrinsic **quantitative** information that can be retrieved in each image is the first advantage of QPM, as it allows the point-by-point direct measurement of the thickness of a sample. Specifically, the **nanometer sensitivity** in z is the most valuable information, rather unique to this method, as most of the microscopy techniques show much lower resolution in z than in xy . The **versatility of setups** for QPM allows to adapt to the needs of the biological question, hence on-axis geometry will be chosen for static samples with fine details to resolve while off-axis geometries will be preferred to follow dynamic events over time (Mir M. et al., 2012). Furthermore, the requirements for QPM imaging are very little, if any, which translate to **easy sample preparation**. Theoretically, any support can be adapted on the microscope stage and, as for any microscope by now, a stage incubator can be predisposed to maintain an optimal temperature and atmosphere for live samples. Live imaging is in fact not only possible, but often preferable to other methods, as QPM does not require high power lasers, thus showing **low phototoxicity** on the sample (Aknoun S. et al., 2021). Last but definitely not least, QPM is a **label-free** technique which avoids all downsides of using fluorescent labeling while keeping the advantages of light microscopy (as previously discussed in § 1.3.3.2).

The potential of this technique has been harnessed in many applications for health sciences. QPM was used to follow cell-cell interaction and cell growth (Mir M. et al., 2011), membrane fluctuations on red blood cells (Popescu G. et al., 2008), motility of sperm cells for in vitro fertilization (Butola A. et al., 2020), dynamics of intracellular transport (Wang Z. et al., 2011),

phagocytosis in macrophages (Zuo C. et al., 2013), as well as changes in cell morphology after treatment with nanoparticles (Luther E. et al., 2017, Sternbæk L. et al., 2019), among many other applications (Park Y. et al., 2020). Although this wide variety of applications explored, the use of QPM for the characterization of nanoparticles has been vastly disregarded because of the two disadvantages of this method: the **diffraction-limited resolution** and the **poor sensitivity to movements in z**. As we all love a good challenge, the potential of QPM for the characterization of nanomedicine is addressed in this thesis; hence, we will get back to this in § 4.3.4.

1.3.5 Fate of Nanocarriers in Biological Environments

1.3.5.1 In Vitro Models and Cell Selection

In vitro testing is a crucial step in the development of new pharmaceuticals and nanoformulations, as it can and should be a high throughput screening tool that predicts in vivo behavior. However, this is often the limiting step in development because, even with the best of technologies available, the correlation between in vitro testing and in vivo behavior is still suboptimal (Soares S. et al., 2018). Failing in vitro predictions can bring forward unsuitable candidates doomed to fail in clinical testing but also discard valid options. In both cases, the money and time invested in animal testing, as well as the unnecessary use of animals can directly slow the drug development process (Fontana F. et al., 2021). This cascade of unwanted (and ethically controversial) research waste should be addressed already at early developmental stage.

One could argue that the importance of reliable in vitro models has never been higher. Recent years witnessed numerous novel and smarter models being developed and validated in drug development, comprising organs-on-chip (Azizipour N. et al., 2020), body-on-a-chip (Sung J.H. et al., 2019), scaffold-based 3D cell cultures (Badekila A.K. et al., 2021), or spheroids and organoids (Liu D. et al., 2021), among others. These novel models offer the possibility of following cell behavior under physiological flow (e.g., microfluidic chips) or in co-culture with multiple cell types (e.g., organoids). However, the complexity of the sample preparations and the batch-to-batch variability explain some skepticism and still limited spread of these techniques in practice. While many are working to improve in vitro models to eventually discard the use of animal experimentation (Jensen C. & Teng Y., 2020), the routine cell testing still relies on the 2D static culture on plasticware (glass-bottomed for imaging purpose). This

gold standard is far from ideal; the results can depend on the model cell line chosen and even on the pipetting style used for drug administration (Ahmad Khanbeigi R. et al., 2012). Especially when developing new formulations with rather unknown behavior, the choice of cell model will affect the testing outcome; hence, the current and most effective strategy is to test the nanocarriers on more than one cell type.

Different cells can respond differently to nanoparticles in their proximity. Furthermore, once administered in vivo, nanoparticles have high probability to encounter different cell types than the designated target (Meng H. et al., 2018). As we have seen in § 1.2.1, the RES system is involved with the clearance of nanoparticles, therefore at least one of these cells should be included in routine testing (Halamoda-Kenzaoui B. et al., 2019). Murine macrophages represent a good standard as they are generally easy to culture, they can be maintained for a long time, and they express several internalization pathways (including pinocytosis and phagocytosis) which could recognize nanoparticles, specifically or non-specifically (Ahmad Khanbeigi R. et al., 2012). However, immortalized cell lines could show biased results. Hence, it is often considered good practice to include testing on freshly isolated primary cells. Liver sinusoidal endothelial cells (LSECs) are queens of primary cells for this purpose, as their scavenger function through clathrin mediated endocytosis could be the responsible for the clearance of nanoparticles from the blood, as it is for many pharmaceutical ingredients (Sørensen K.K. et al., 2012, Szafranska K. et al., 2021). Furthermore, epithelial and endothelial cells should be included according to the administration route of choice; moreover, other cancer cells could show cell-specific behaviors and targeting possibilities. In this thesis, macrophages were chosen as main model; however, aiming to showcase the potential of different microscopy techniques for nanomedicine, the selection of alternative cell models was also driven by the compatibility with the method of choice.

1.3.5.2 Tracking Nanomedicine Fate In Vitro

When applying a nanoparticle treatment to a cell culture, all the challenges we have seen for their localization and characterization are instantly amplified. The complex medium used to sustain the cells is a new source of possible interactions, such as the well-known protein corona (Münter R. et al., 2022). These new interactions can directly affect the integrity of the nanocarrier, e.g., in the case of fluorescently labeled nanoparticles, a displacement of the fluorophore can cause loss of tracking specificity (Münter R. et al., 2018). Furthermore, the

efficacy of targeting strategies can be limited by the protein corona covering the targeting ligands and preventing their specific recognition (Fan Z. et al., 2020). Adding salt to the wound, the culture medium is an unbeatable source of background noise (and often also autofluorescence) that can compromise the use of several standard techniques.

The most straightforward approach to analyze the behavior of nanoformulations is based on indirect approaches, which can include studying the activity of the payload (e.g., effect of antimicrobials on the proliferation of bacteria, Gao W. et al. 2018) or quantifying metabolites or byproducts of the cell cycles, before and after treatment (e.g., inflammatory mediators, Giordani B. et al. 2020, Hemmingsen L.M. et al., 2021). Although highly informative on the behavior of the payload, the results from these methods are difficult to generalize for the nanocarriers since the observed effect could be due to internalization or local release (Wu L.-P. et al., 2020). Similarly to the indirect methods, where the fate of a treatment is compared to an untreated control, electron microscopy can be used to analyze changes in intracellular morphology such as organelles shape and distribution, utilizing the conventional TEM for 2D imaging (Malatesta M., 2016) or techniques of volume electron microscopy (such as serial blockface imaging or focused ion beam scanning electron microscopy, FIB-SEM, Peddie C.J. & Collison L.M., 2014).

To add specificity on the information of nanoparticles internalization, fluorescence tagging can be implemented in several techniques. Nanoformulations can be fluorescently labeled in a specific color (with careful considerations discussed in § 4.2.), while non-overlapping colors can be used for specific labeling of cellular structures of interest (e.g., nucleus, cell membrane, mitochondria, and/or lysosomes). Historically, flow cytometry (FCM) and confocal microscopy have been the go-to techniques for tracking fluorescence (Ducat E. et al., 2011).

Flow cytometry, and the complementary method of fluorescence activated cell sorting (FACS), can be considered a batch mode analysis. Once a cell suspension is injected into a flow cytometer, a finely tuned microfluidic system directs the cells into a one-by-one flow towards the so-called interrogation point. Here, the selected lasers illuminate the sample while the detector registers the total fluorescence intensity emitted by each cell, allowing population analyses from tens to hundreds of thousands of events within minutes (Bonner W. et al., 1972, Agarwal A. et al., 2020). In advanced flow cytometry systems, multiple colors can be read simultaneously, allowing the screening of dual labeling or combined treatments (Truneh A. et

al., 1987, Škalko N. et al., 1998), treatments in co-cultures (Susewind J. et al., 2016, Alhussan A. et al., 2021), or toxicity assays (Arbab A.S. et al., 2003).

Fluorescence microscopy, often performed in confocal mode (CLSM), is accounted as a single-cell method and it is often combined with flow cytometry as it can provide more detailed information of the cellular distribution of a certain fluorescent signal while analyzing a small number of cells. Although the diffraction limited resolution does not allow single-particle to single-cell imaging, this technique is widely available and can give information on treatment-dependent toxicity, intracellular accumulation, and/or colocalization with other structures of interest (Jonkman J. et al., 2020).

The monitoring of live cells is a complex challenge and introducing nanoparticles in the system adds another layer of complexity. Nonetheless, the development of novel imaging methods and the optimization of older ones is constantly widening the available options (Pantanowitz L. et al., 2019). Ultimately, the best strategy to address the limitations of the individual methods is to combine them. By introducing a reference system with coordinates in the sample, it is possible to image the same area under different instruments (e.g., fluorescence and electron microscopes) and perform correlative microscopy. The overlay of these images thus brings different types of information into the same picture. However, the sample preparation required to accommodate different imaging methods can be challenging (Loussert Fonta C. & Humbel B.M., 2015) and will be further addressed in § 4.4.4.

2 Aims

The success stories in nanomedicine research have drawn ever-growing attention and fundings to the research field. However, the expectations surrounding *magic bullet* formulations are yet to be met. To improve in vitro predictions and reduce failures at later stages of developments, the field is urging for improvement and standardization of methods. For this reason, the main aim of this thesis was to comprehend the nanocarriers features by updating the toolbox of methods enabling us to understand the properties and behavior of nanocarriers in biological environments. To gain a deeper insight on back-to-basics research, liposomes were chosen as model nanocarriers for their versatility, biocompatibility, and clinical relevance. The specific aims, divided by project focuses, are:

Paper I

- To formulate and characterize trackable liposomes using fluorescently labeled lipids.
- To assess how fluorophore and nanoformulations affect each other's properties.
- To evaluate the biological activity of labeled and unlabeled formulations.
- To derive the internalization profile of nanocarriers using their fluorescence signal.

Paper II

- To explore and optimize the use of fluorescence-fluctuation based super resolution microscopy techniques for biologically relevant samples, namely nanocarriers, fixed cells, live cells, and tissues.
- To assesses the reliability of size estimation, reduction of background noise and resolution of fluorescently labeled immobilized liposomes.

Paper III

- To explore the downsides of conventional batch-mode characterization of liposomes (e.g., DLS) and fluorescent labeling.
- To validate quantitative phase microscopy (QPM) as an alternative label-free method for the characterization of nanoparticles.

Paper IV

- To combine the strength of fluorescence and electron microscopy and recognize potential downsides.
- To showcase the use of correlative microscopy for nanomedicine research.

3 Summary of Papers

3.1 Paper I

Following the Fate of Dye-Containing Liposomes in vitro

Following the fate of liposomes in vitro should help us to predict and screen the efficacy of delivery as well as cytotoxicity of nanoformulations at early stages of development, allowing early optimization interventions. However, due to their small size and dynamic nature, liposomes are difficult to track per se in biological environments. For this reason, in paper I, the focus was put on formulating trackable liposomes through the incorporation of fluorescently labeled phospholipids in liposomal bilayers. Incorporating the fluorescent moieties into liposomes, especially when they are chemically linked to the lipid structural units of the vesicles, provides a powerful tool for tracking the nanocarriers, even possibly individually. However, to be able to infer any fluorescence-based result to the nanocarrier itself, a deep insight on the behavior of the labeled formulations is necessary.

In this work, two lipid dyes were chosen among the marketed dyes, specifically Cy5-DSPE (C) as a surface lipid dye – for its labeled polar head, and TopFluor®-PC (T) as a lipid dye – for its labeled hydrophobic tail. Each dye was individually incorporated in the bilayer in four different concentrations and the size of liposomes adjusted to approximately 150-200 nm. To assess if and how the presence of a fluorophore affects the properties of the nanocarrier, size and zeta-potential were evaluated in comparison to the unlabeled control, over 60 days and at different storage temperatures, namely 4 °C (fridge) and 25 °C (RT). While no variations could be seen for the formulations stored in the fridge, the increased storage temperature showed a direct effect on the stability of all labeled formulations, where at the 30 days endpoint a thick sediment was found. Furthermore, as expected, the trend of increased negativity of the zeta-potential over time, due to low degree of lipid oxidation, was more evident for the formulations containing a surface lipid dye (C), especially in high concentration.

To assess how the formulation affects the fluorescence stability of the dyes, all labeled formulations were aliquoted and stored at 4, 25 and 37 °C. The quantitative fluorimetry was performed daily over the course of a week. The surface lipid dye (C) showed significant decrease in fluorescence emission, more relevant for lower concentrations of dye and for higher storage temperatures, while the lipid dye (T) exhibited higher fluorescence stability

during both fridge and RT storage. Interestingly, the T-labeled liposomes with higher concentrations of dye showed lower fluorescence stability at 37 °C, hinting at a saturation of the bilayer that causes more fluorescent moieties to be exposed to the water-based medium. Based on the behaviors observed, the choice of suspension medium for the liposomes was inferred to directly affect the fluorescence stability of the dyes. In fact, media rich in strong electron acceptors will faster inactivate the fluorescent moieties by removing their delocalized electrons, which are responsible for the fluorescence emission itself.

Finally, to assess the potential cytotoxicity and pharmacological response of the labeled formulations in comparison to their unlabeled control, high throughput in vitro treatments of murine macrophages RAW 264.7 and keratinocytes HaCaT were performed. No variations were observed between labeled and non-labeled formulations in terms of cell proliferation. Furthermore, after treating LPS-inflamed macrophages with liposomes, a concentration-dependent reduction in NO production was observed for all the formulations, with limited variations of behavior between labeled and unlabeled liposomes.

The T-labeled formulation with lowest concentration of fluorescent dye (T1) was then selected for the investigation of internalization profiles. Internalization was quantified at different endpoints within 24 h of treatment utilizing flow cytometry; the quantitative population analysis was validated by visualizing the positive live cells in flow imaging. After 4-6 h, almost all cells were found positive for internalization; however, a linear increase of fluorescence intensity was observed, showing no saturation withing the timeframe of the experiment. Fluorescent images revealed that the fluorophore was condensed into intracellular organelles, such as phagosomes and phagolysosomes, and not uniformly distributed in the cytosol. This visual information, combined with the non-saturation of internalization, suggested that the phagocytosis was the most probable internalization pathway.

Although this work did not give definitive mechanistic proof, it showed that combining different techniques, especially the powerful fluorescence-based ones, can be useful in the screening phase of formulation optimization. However, it is only a robust characterization of how fluorescent moiety and nanocarrier affect each other's properties that validates these kinds of findings. We therefore identified the time, temperature, medium, choice of dye, dye concentration and localization in the bilayer as main experimental conditions that can affect the outcome of internalization experiments.

3.2 Paper II (Manuscript)

Fluorescence Fluctuations-Based Super-Resolution Microscopy Techniques: An Experimental Comparative Study

The development of super-resolution microscopy (SRM) has driven fluorescence microscopy into the nanoscale world, finding applications in all kinds of fields, from material to biological sciences. An emerging class of SRM techniques is based on image processing and referred to as fluorescence fluctuations-based super resolution microscopy (FF-SRM). The methods comprise computational algorithms which reconstruct a single super-resolved image by analyzing the fluctuations of fluorescence signal across sequential frames in multi-frame (video-like) imaging datasets. Although validated on fluorescence beads and some optimized samples, these methods have remained widely unchallenged regarding their possible application for biologically relevant specimens, with commonly used staining techniques.

In this paper, the focus was put on assessing the performance of five of these FF-SRM methods, namely super-resolution optical fluorescence imaging (SOFI), entropy-based super-resolution imaging (ESI), multiple signal classification algorithm (MUSICAL), super-resolution imaging with autocorrelation two-step deconvolution (SACD), and super-resolution radial fluctuations (SRRF). Being computational algorithm, and often referred to as statistical imaging, all FF-SRM methods require the input of several parameters prior to image reconstruction. The performance of the individual methods was assessed throughout a relevant range of values for several crucial parameters, namely number of frames (#fs), order of processing (method-specific for SOFI, ESI, and SACD), threshold (method-specific for MUSICAL), additional options/settings (method-specific for SRRF), and Haar wavelet kernel (HAWK) pre-processing (additional algorithm for the enhancement of data sparsity).

The methods were utilized to characterize four biologically relevant samples with increasing complexity. First, liposomes were chosen as a sub-diffraction nanoparticle sample, with expected higher variability than fluorescence beads in terms of both uniformity of labeling and size distribution of the particles. Second, fixed cells were selected as easiest biological sample for the analysis of super-resolution cellular ultrastructures such as filopodia and actin filaments (macrophages). Third, tissue samples were used as model for densely labeled thick samples (here, from placenta and heart tissue). And finally, live cells were imaged to observe

the highly dynamic organelle motion (here, in cardiomyoblast transiently transfected to fluorescently tag mitochondria and endoplasmic reticulum).

A common aspect of all four biologically relevant samples is the absence of a ground truth, which, even in the simplest case of liposomes, corresponds only to possible particle size range, without any information on the actual size of the particles in the field of view. Hence, to tackle the challenging aspects of these samples, simulation studies were performed to assist the experimental image processing, explain the results obtained, and eventually predict the optimal imaging and processing conditions to choose on the different samples and techniques.

The performance of the different techniques, with different parameter selection, in the different samples, was visually assessed in terms of i) background signal, ii) recognizable/repeated patterns of unlike biological origin (reconstruction artifacts), and iii) resolution enhancement for closely localized structures. In spite of the rather wide range of conditions considered in the project, all methods visually underperformed in most cases. Size estimations demonstrated high variability in a technique-dependent manner (more than sample-dependent). Moreover, several background artifacts were recognized and described. However, the potential of these techniques is not to be underestimated as the current state-of-the-art requires a manual choice and input of parameters, which can introduce user-dependent biases. A more comprehensive pre-analysis (e.g., based on artificial intelligence) for the automatic determination of the most suitable image processing would optimize the image processing, possibly predicting the suitability of a given multi-frame acquisition for a specific FF-SRM method.

3.3 Paper III

Characterization of Liposomes Using Quantitative Phase Microscopy (QPM)

The behavior of liposomes in biological environment depends closely on their physicochemical properties, such as their size, membrane fluidity and surface charge. Being small and almost transparent dynamic vesicles, liposomes are very complex to detect and especially image. Recurring to the use of fluorophores can help the visualization aspects; however, fluorescent molecules are known for their high sensitivity to the experimental conditions and possible loss of tracking specificity over time (e.g., leakage and photobleaching). To tackle the downsides of conventional and fluorescence-based techniques, the focus of this paper was put on the assessment of quantitative phase microscopy (QPM) as a complementary label-free technique for the visualization and characterization of liposomes.

Liposomes of three different sizes (N1 – 1 μm , N3 – 200 nm and N4 – 100 nm as aimed diameters) were considered for the validation. Dynamic light scattering (DLS) was used as a conventional characterization technique for the estimation of size distribution of liposomes in suspension, as a function of backscattered light and speed of the Brownian movement. Single particle optical sensing (SPOS) was used for such estimation in the case of liposomes outside the available DLS range of detection (0.01-1 μm). For imaging purpose, liposomes were immobilized on PLL-coated silicon wafers within an adherent PDMS frame. A coverslip was sealed on top to prevent evaporation and therefore to allow imaging in non-dried conditions. A fluorescent phospholipid (14:0-06:0 NBD-PC, N) was included for validation purposes of the newly developed QPM setup. The combination of the low-spatial and high-temporal coherence of the light source (pseudothermal light source – PTL), the on-axis geometry of the microscope and the corresponding phase shifting algorithm used for image reconstruction allowed for the preservation of high spatial resolution.

First, the method was used to localize immobilized liposomes, showing direct correlation with the fluorescence images taken in parallel. In particular, the technique was proven effective not only in the detection of sub-diffraction sized liposomes, but also in distinguishing the sizes from N3 and N4, respectively close to and below the resolution limit of light. Furthermore, prolonged phase and fluorescence imaging showed the potential of QPM over fluorescence for long-term tracking of liposomes. The persistent laser illumination of the sample induced a

complete photobleaching, while little to no changes were seen in the phase map retrieved in QPM, confirming the integrity of the vesicles.

Full field of view images were then recorded for the N3 – 200 nm sample, comparing the retrieved phase map with the correspondent fluorescence image. The phase map showed high capability of locating liposomes, even the smallest ones, with little to no fluorophore incorporated, difficult to locate in fluorescence. The refractive index difference between liposomes and medium was set to 0.4, and the thickness of each liposome within the field of view was plotted into a number-weighted size distribution, which resulted in a peak at around 100 nm diameter size. The underestimation of the QPM distribution, in comparison to the DLS one, was expected for several reasons. First, intensity-based distributions (DLS) tend to show an upwards bias in size estimation as bigger particles contribute more to the overall scattering detected. Second, the QPM distributions tend to show a downwards bias in size estimation for the possible loss of high frequency information (smaller details) in the light detection. Third, the size estimated in DLS refers to the hydrodynamic radius, which in the case of charged particles can include a strongly stabilized layer of medium on the surface. Furthermore, the choice of refractive index difference used for the size estimation was in itself an estimate, which can be a source of error, as demonstrated in a simulation of size variance as a function of refractive index.

The successful immobilization of liposomes and the QPM imaging in their hydrated state, which was firstly achieved in this work, confirmed the potential of this technique to compare formulation morphology (e.g., sphericity) and vesicle size in early stages of development. The independence of phase measurements from fluorescence signals further endorses the applicability of this technique to track the liposome integrity over time. Furthermore, it was postulated that for known vesicle sizes the analysis of refractive index variations could be implemented to visualize the composition of nanoformulations and their interactions with the environment.

3.4 Paper IV (Manuscript)

Correlative microscopy provides insights on localization, internalization, and subcellular trafficking of liposomes

To predict the behavior of nanocarriers within relevant biological environments prior to actual *in vivo* experiments, one should perform reliable characterization of those nanocarriers, follow their localization *in vitro*, especially their intracellular trafficking, while understanding the cellular response/toxicity as a consequence of the nanocarrier treatment. The aim of this work was to optimize an integrated methodology that allows to gather this bulk of information on the same specimens. Hence, correlative microscopy was the chosen approach due to its potential to localize a fluorescently labeled nanocarrier (by fluorescence microscopy) and to visualize the cellular response to treatment, in terms of organelle morphology and stress (by electron microscopy). Confocal laser scanning microscopy (CLSM) was the fluorescence-based technique of choice, while for the electron microscopy side of the experiment, different samples were imaged utilizing different techniques, namely scanning electron microscopy (SEM), focused ion beam SEM (FIB-SEM), and transmission electron microscopy (TEM).

First, a final formulation of liposomes in dry form was used for correlative CLSM-SEM. Fluorescently labeled liposomes were incorporated in nanofibers. For such specimen (dry form), only the step of confocal imaging was added to the conventional characterization performed through SEM; hence, without further need of sample preparation. By applying 50% transparency on the fluorescence image, a perfect overlay as a direct linear correlation was obtained, with no distortions required. A partial integrity of liposomes could be thus verified, as a fluorescence gradient in intensity decrease could be detected surrounding the brightest spots.

For biological specimens, PEGylated and non-PEGylated liposomes were compared in terms of their internalization and cellular response, on macrophages and glioblastoma cells, at 4 and 24 h of treatment incubation. Confocal microscopy, with airy scan detection and fixed settings, was first performed on all conditions and controls. Clear differences in internalization behavior were seen depending on the conditions. Macrophages displayed, already after 4 h, a higher overall internalization, slightly reduced in the case of PEGylated liposomes. Interestingly, glioblastoma cells exhibited the opposite trend, with PEGylated liposomes being more internalized vesicles. At the 24 h endpoint the intensities were reduced and rather diffused

for both macrophages and glioblastoma, possibly suggesting degradation taking place. However, in the case of non-PEGylated liposomes exposed to glioblastoma cells, possible signs of exocytosis could be seen instead.

The glioblastoma samples were further imaged in FIB-SEM to obtain volumetric correlative information, while macrophages were resin embedded, sectioned, and imaged in TEM, as their thickness is incompatible with reasonable imaging times (each cell could take up to a week of image acquisition). The signs of cell stress could be seen through the presence of huge intracellular bodies of irregular shape, suggesting massive degradation mechanisms in place. Furthermore, the mitochondrial morphology exhibited altered shape and unexpected lipid accumulations.

Further confirmations of these findings may be obtained through on-section correlative light and electron microscopy, i.e., performing the confocal imaging step after the laborious sample preparation for electron microscopy. However, although yielding a higher performance regarding the correlation itself, the effect that this harsh processing would have on the liposomal localization would have to be separately assessed.

4 Results and Discussion

In this section, I present and discuss the main results obtained throughout this project, contextualizing the different findings in the relevant literature. I structure the results according to the methods used, together with some methodological considerations.

4.1 Choice and Preparation of Nanocarriers

Lipid-based nanocarriers were chosen as model formulations for their biocompatibility, biosafety, and clinical relevance (Gadekar V. et al., 2021). Among them, liposomes were used throughout the project (Paper I to IV) because of their versatility and non-rigid structure. Their vesicular nature serves as a model for non-rigid nanoparticles which generally are more difficult to stabilize for imaging purposes.

Different preparation methods were used according to the properties of the lipid ingredients and the required characteristics of the nanocarrier. Initially, all lipids and hydrophobic ingredients were deposited as a thin film in low pressure rotary evaporation. This allowed for a uniform dispersion in the solvent of choice. The film was then directly re-dispersed in a water-based medium (e.g., water or phosphate buffer) to obtain multi-lamellar/multi-vesicular structures, according to the film hydration method (Xiang B. & Cao D.-Y., 2021).

When considering intravenous administration, the target size of liposomes was deemed acceptable when < 200 nm, aiming for 100 nm whenever possible. To ensure these sizes, three size reduction methods were considered and compared in terms of PDI and entrapment of the molecule of interest (Figure 23). Of the three methods, two are widely available and commonly used in nanomedicine laboratories, namely extrusion and probe sonication. The first method consists of a sequential extrusion of the multi-lamellar/multi-vesicular suspension obtained after film hydration. This sieving causes the liposomal membranes to be rearranged into smaller and smaller vesicles at each passage, with a consequential reduction in PDI to a monodispersed system (often $\text{PDI} < 0.1$) (Ong S.G. et al., 2016). The second method consists of introducing a sonication probe deep into the sample. The direct contact of the probe and the sample enables high-energy radiations to penetrate the suspension and stimulate rearrangements of the lipid bilayers into smaller vesicles (Paini M. et al., 2015). Despite being fast and easy to perform, probe sonication induces local temperature increase which cannot be finely tuned and can represent an issue in the case of temperature-sensitive

ingredients. Furthermore, sterility cannot be ensured and possible metal contaminations from the probe are known (Khadke S. et al., 2018). The third method, microfluidization, is the link between small- and large-scale production. Devices such as the Microfluidizer LM20 (Microfluidics International Corporation, Westwood, Massachusetts) can process 20 to 300 mL of liposomal suspensions, in few seconds per pass. This technology is a form of high-pressure homogenization as it pushes the formulation through a diamond chamber of microchannels, where the high pressure and the shear forces between the liposomal membranes and the walls of the channels cause the lipid rearrangement and size reduction (Mayhew E. et al., 1984, Barnadas-Rodríguez R. & Sabés M., 2001). Notwithstanding the high throughput of this technology, to be effective it requires both high volumes and high initial concentrations of lipids (Yadav K.S. & Kale K., 2020), which can be costly to achieve for optimization purposes. Hence, for lab-scale production of highly concentrated liposomes, alternative methods such as the dual asymmetric centrifugation (DAC) are more advisable (Massing U. et al., 2008), maintaining the scalability potential and several advantages of the small-scale production (Ingebrigtsen S.G. et al. 2017).

Figure 23 presents the comparison between the same formulation of liposomes processed through the hand-extrusion, probe sonication and microfluidization to a final size of 100-200 nm. Soy phosphatidylcholine (SPC, 20 mg/mL) was used for the formulation of simple liposomes, as commonly reported in literature (Jøraholmen M.W. et al., 2020, Hemmingsen L.M. et al., 2021), and rhodamine B was chosen as fluorescent dye (4 mg/mL). Although often used as a bilayer marker (Ternullo S. et al., 2017), the partial water solubility of rhodamine B can explain its distribution in the hydrophilic liposomal compartment (Kuznetsova D.A. et al., 2021), especially when used in high concentrations. To remove the untrapped molecules, membrane dialysis was performed prior to quantifications.

The microfluidization technique was associated, on average, to higher polydispersity values, lower entrapment than the extruded formulation, and lower reproducibility. The increased number of passes of the formulation through the microfluidizer chamber resulted in a progressive decrease in the polydispersity index (PDI) (Figure 23B); however, a drastic decrease of the entrapment was also noted (Figure 23D). These trends were found coherent with sonication experiments previously described in literature (Jøraholmen M.W. et al., 2014). Furthermore, the high polydispersity and the intra-batch variability of the microfluidized

samples can be attributed to the low initial concentration of all ingredients, which causes the shear forces in the chamber to be non-uniform (Barnadas-Rodríguez R. & Sabés M., 2001).

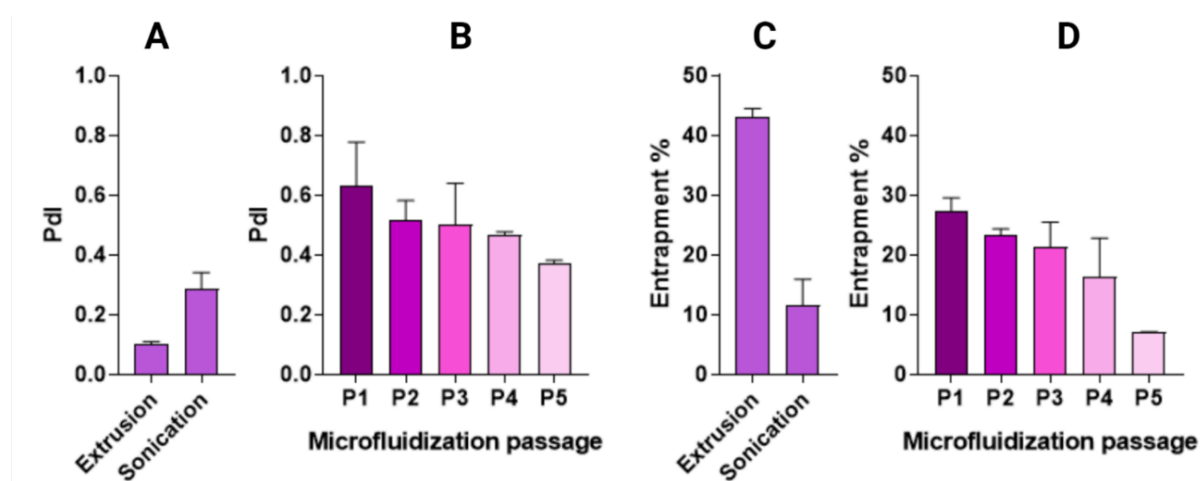


Figure 23. Comparison of size reduction methods (hand-extrusion, sonication and microfluidization) in terms of Pdl (A,B) and entrapment (C,D). The same initial formulation was used for all the cases: 20 mg/mL of soy phosphatidylcholine (SPC) and 4 mg/mL of rhodamine B. The label “extrusion” refers to a sample processing of 4 x 800 nm + 4 x 400 nm + 4 x 200 nm + 4 x 100 nm. The label “sonication” refers to a sample processing of 10x3 seconds. B and D specifically refer to the total amount of passes (P) through the microfluidizer. Pilot data not included in the manuscripts.

To maintain the lipid concentration within an optimal range for optimization purposes, the focus was kept on the hand extrusion method, combined with short sonication in case the smallest vesicle sizes could not be achieved with the former technique. Furthermore, the localization of rhodamine B at the high concentrations of interest was found to carry poor labeling specificity. Its presence in the bilayer, hydrophilic core, and possibly in the dispersant medium (consequence of the osmotic equilibration through the liposomal membrane) was found inadequate for single-particle imaging experiments, and thus the focus was shifted onto covalently labeled phospholipids.

4.2 Formulation of Trackable Liposomes

Including a fluorescent molecule in the formulation of liposomes can be a powerful tool for their characterization and trackability, especially when covalently attached to lipid moieties. The high contrast, the possibility to obtain multi-color imaging, the generally low cytotoxicity and the labeling specificity are the main advantages (Terai T. & Nagano T., 2013). However, different labeling strategies can lead to different results, even for the same nanocarrier (Snipstad S. et al., 2017). Brightness, quantum yield and fluorescence lifetime of a specific

fluorophore can influence not only the applicability of certain methods (e.g., where high-power lasers are required), but also any quantitative analysis on the images (Lichtman J.W. & Conchello J.-A., 2005). Furthermore, the affinity of certain fluorescent molecules for other macromolecules present in biological environments may induce fluorophore leakage from the nanocarrier (Münter R. et al., 2018, Snipstad S. et al., 2017). For these reasons, the deep characterization of labeled nanoparticles is a fundamental step to ensure the specificity of tracking.

Four fluorescently labeled lipids were selected over the course of the project, with a fluorescent molecule covalently bound to the lipid head (for C and R) or tail (for T and N), as shown in Figure 24.

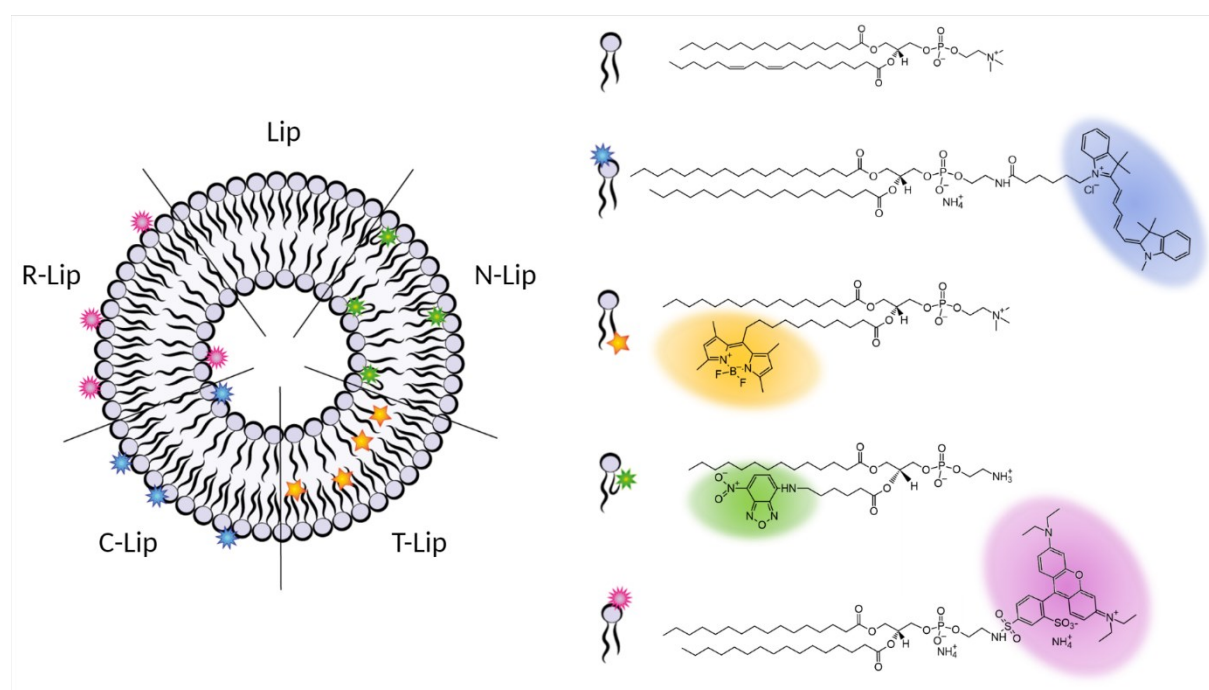


Figure 24. Fluorescently labeled formulations and chemical structures of the lipids used in the project. From the top) Sample phosphatidylcholine lipid in SPC as main lipid ingredient in liposomes, C-lipid: Cyanine5-labeled phosphatidylethanolamine. T-lipid: TopFluor®-labeled phosphatidylcholine. N-lipid: NBD-labeled phosphatidylcholine. R-lipid: Rhodamine-labeled phosphatidylethanolamine. Abbreviation: Lip: liposomal formulation. The figure was prepared with Adobe Illustrator CS6. Molecules were drawn using ACD/ChemSketch 2019 2.1.

The similarity of these molecules to the main lipid ingredient (soy phosphatidylcholine, SPC) ensured the best description of the liposomal bilayer. However, the presence of the fluorescent moieties inside the bilayer, or on its surface, can influence the properties of the unlabeled nanocarriers, specifically the processing required to achieve the size target and final

surface charge of the particles. Table 1 shows a direct comparison between an unlabeled control (Lip) and four labeled formulations, where each fluorophore was individually incorporated in liposomes.

Table 1. Comparison of formulations with different lipid labeling at the concentrations of 10 mg/mL SPC and 0.03 mg/mL of fluorescent lipid. Processing, size, Pdl and ζ -potential are indicated for each formulation. Lip refers to the unlabeled control. The percentage in parenthesis in the size column refers to the intensity-weighted most relevant peak. Data obtained in the optimization steps for paper I, II and IV.

	Processing	Size [nm]	Pdl	ζ -potential [mV]
Lip	Sonication (8 x 15 s) + Extrusion (4 x 400,200,100 nm)	135±20 (88%)	0.23±0.02	-1.4±5
T-Lip	Sonication (8 x 15 s) + Extrusion (4 x 400,200,100 nm)	158±40 (96%)	0.16±0.01	-3.6±4
C-Lip	Sonication (8 x 15 s) + Extrusion (4 x 400,200,100 nm)	161±42 (89%)	0.24±0.01	-1.2±5
N-Lip	Extrusion (4 x 400,200,100 nm)	122±20 (100%)	0.12±0.01	-7.2±3
R-Lip	Extrusion (4 x 400,200,100 nm)	152±22 (100%)	0.08±0.01	-31±7

In terms of processing, when utilizing the T and C fluorophores, a sonication step prior to extrusion needed to be included to achieve the wanted sizes (< 200 nm). The T-lipid exhibits a multi-ring structure which places itself inside the bilayer, simulating a cholesterol effect of stiffening the membranes (Regan D. et al., 2019). Therefore, the extrusion through the 100 nm membrane sieving size was difficult to perform and resulted in ineffective size reduction. Similarly, the incorporation of the C-lipid resulted in difficulties in size reduction, although as surface lipid label an interference with the bilayer itself is not expected. This behavior is comparable to the one known for some polymer coatings (e.g., PEG and chitosan, Jøraholmen M.W. et al., 2014). The incorporation of the N-lipid in liposomes resulted in rather opposite behavior. The hand extrusion achieved the best size reduction, even more easily than the unlabeled control, such that the sonication step was removed as it merely increased the polydispersity of the system, without an effective influence on its size reduction. The backflip of the fluorescent moiety towards the polar head of the N-lipid molecule explains a certain degree of disruption in the bilayer, hence increasing its fluidity (Kay J.G. et al., 2012). Lastly, the R-lipid was successfully incorporated in liposomes, which were easily reduced in size

without the need of a sonication step. Although rhodamine (in R-Lip) and cyanine (in C-Lip) have a similar molecular weight, the steric volume of the rhodamine is not as elongated, preventing it from reaching the high degree of organized (Rokitskaya T.I. et al., 2018).

In terms of surface charge, the effect that the presence of fluorescence moieties has on the liposomes is dependent on the nature of the molecule, its position in/on the bilayer, and its concentration. The SPC unlabeled liposomes tend to exhibit neutral (or slightly negative) ζ -potential as the polar heads show zwitterionic behavior in aqueous media (Khandelia H. & Mouritsen O.G., 2009). At the tested concentrations of labeled lipid (0.01 to 0.1 mg/mL), the T- and C-lipid molecules did not demonstrate a relevant change in the ζ -potential of the formulations. The N-lipid contributed to a slight increase in negativity (likely due to the backflip of the fluorescent moiety towards the surface of the bilayer; Kay J.G. et al., 2012), and the R-lipid was associated with a high increase in negativity (possibly caused by the deprotonated state of the rhodamine moiety on the surface, Kuznetsova D.A. et al., 2021). The surface charge of nanoparticles has long been linked to their internalization and behavior in biological environments (Fröhlich E., 2012, Kamali S.M. et al., 2021); therefore, the choice of fluorescent molecule and its concentration are fundamental to disguise the fluorescent dyes in the formulation and fully describe its behavior.

Since the presence of a fluorescence marker can affect the properties and behavior of a formulation, the formulation can also affect the expected properties of the fluorophore, particularly its fluorescence stability. Figure 25 (top row) shows the progressive loss of fluorescence the formulations demonstrate over time (5 days) and storage temperature (4 °C, usual fridge storage, 25 °C, room temperature for handling formulations, and 37 °C, usual temperature for cell work incubation). This behavior of overall decreased fluorescence when increasing the storage temperature would not be expected when observing the fluorescent behavior of the fluorescent lipids freely dissolved in their native organic solvent (Figure 25, bottom row). In fact, the conjugated system of electron delocalization, typical of fluorescent moieties, tends to interact differently with non-polar organic solvents, such as methanol, and polar ones, such as water or saline buffers. As the aromatic delocalization is often responsible for the emission of fluorescence signals, chemical disruptions can cause significant a loss of fluorescence (Stennett E.M. et al., 2014).

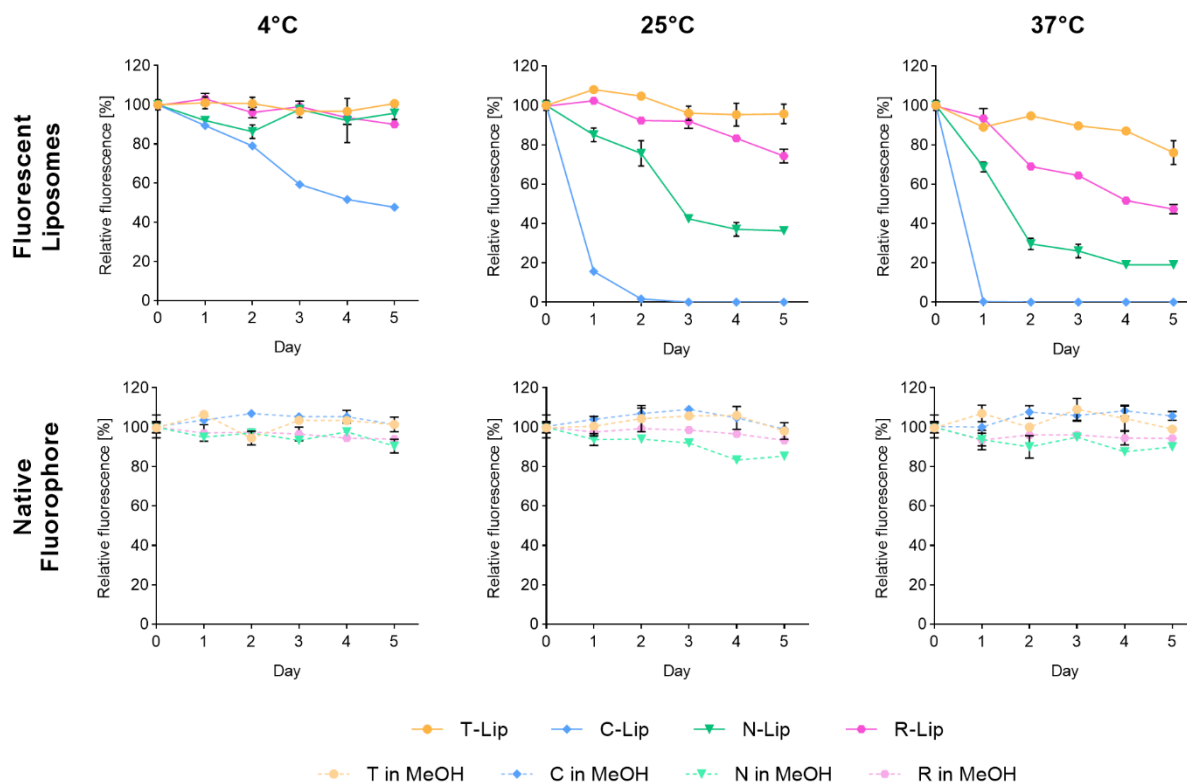


Figure 25: Fluorescence stability of liposomal formulation (Top) over time (5 days) and at three different storage temperatures (4, 25 and 37°C), compared to the native fluorescent lipid dissolved in methanol (Bottom). The temperature exhibited a direct effect on the fluorescence stability of the fluorophores in liposomes to an extent that depends on the formulation itself. All fluorescent lipids freely dissolved in methanol showed no evident reduction in fluorescent intensity over the course of the experiment. Data merged from paper I, and pilot data for paper II, III and IV.

In terms of fluorescence stability, it is not surprising to see that the fluorescent moiety that is tightly packed inside the bilayer (T, yellow) is the most stable over time and temperature range, closely followed by R (pink) and N (green). Both the R and N fluorescent moieties directly interact with the medium, as the first is a surface lipid label and the second shows backflip towards the surface. The explanation of the higher stability of R over N is found in the chemistry of the molecules themselves, as the rhodamine contains a bigger aromatic system that can ensure delocalization even after partial interruption/disruption (Demchenko A.P., 2020). In this experiment, the C-lipid (blue) showed the highest incompatibility with the medium, and a dramatic decrease of fluorescence in the formulation, even at the lowest storage temperature. In water, and especially in buffer, the cyanine itself can easily undergo covalent modifications, which can quickly bleach the fluorophore (Valdes-Aguilera O. et al., 1987). This progressive loss of fluorescence can be interpreted as a massive loss in specificity

of tracking, and in early stages of formulation development this could easily lead to false negative in targeting experiments. However, the knowledge of this phenomenon can be utilized in specific methods and/or labeling strategies. For example, the fact that cyanines display low fluorescence in water makes them perfect candidates for labeling hydrophobic compartments such as the cell membrane (e.g., DiD, Dil or DiO), as the untrapped fluorophore will not significantly contribute to the background noise (Terasaki M. & Jaffe L.A., 2004). Furthermore, surface labeling of structures, such as that in the C-Lip formulations prepared in this project, can be considered for highly specialized chemical imaging methods such as FRET (Yang G. et al., 2021) and SMLM (Matikonda S.S. et al., 2020).

4.3 Characterization of Liposomes

4.3.1 Conventional Characterization

There is always a good reason for a technique to become gold standard in the field. Scattering-based analyses of nanocarriers in suspension are high throughput, fast and easy methods that can be implemented potentially in any lab (Maguire C.M. et al., 2017). However, it is important to separate what can be interpreted from these results from what cannot (Bhattacharjee S., 2016). Figure 26 shows the output of a size analysis of the same sample through DLS (Zetasizer Nano – ZS, Malvern, Oxford, UK) and NTA (Zetaview® NTA, Particle Metrix GmbH, Germany). The direct data output of DLS is an intensity-based distribution (green), while for NTA the direct output is a number-based distribution. The consequence of this very first difference in data output is that results can be complex to compare. The software of both DLS and NTA devices offer the possibility of converting distributions from intensity-weighted to number- (black) and volume-weighted (blue), and from number-weighted to volume-weighted distributions. Although two of these options appear to be a common ground between the two techniques, at each conversion of a fitted distribution the measurement error is enhanced, with the biggest effect in the conversion of intensity to number (Eaton P. et al., 2017). Furthermore, as previously introduced (§ 1.3.1.2), DLS and NTA are subjected to different errors (Gioria S. et al., 2018). Converting each distribution to the volume-weighted one results in the propagation of different kinds of errors, which can drift the distributions farther apart, as seen in Figure 26 (data table).

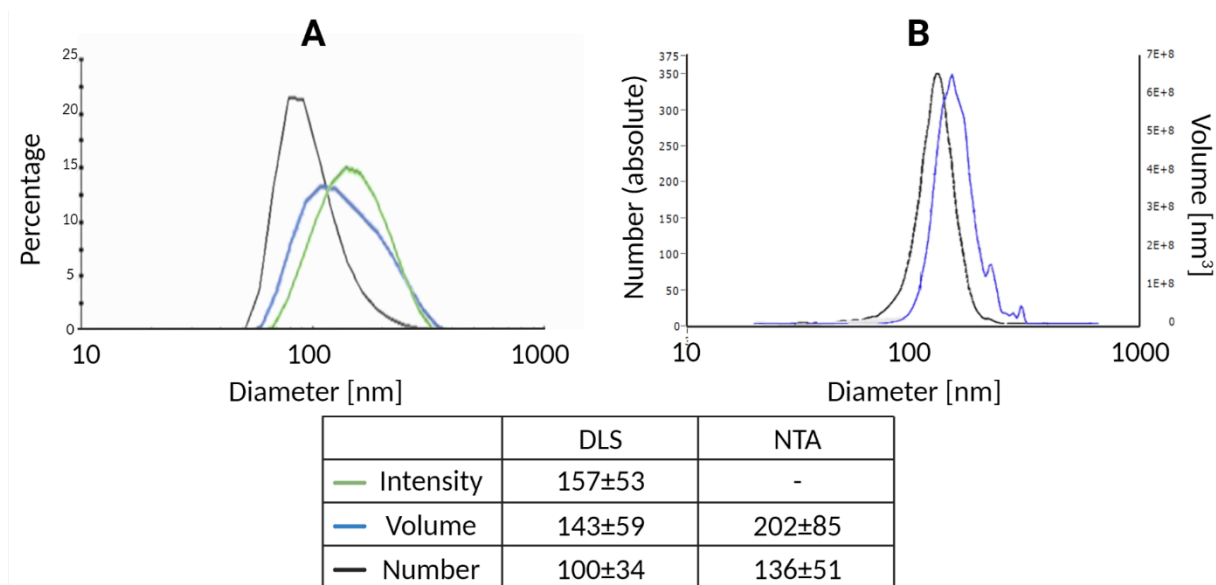


Figure 26. Direct comparison of data output from A) dynamic light scattering (DLS), and B) nanoparticle tracking analysis (NTA) size measurements for an unlabeled formulation of liposomes (Lip). The data table shows the mean \pm st.dev calculated from each fitted curve. Pilot data for paper IV.

Although software development is constantly improving to account for the intrinsic errors of the measurements (Stetefeld J. et al., 2016), the chosen strategy to deal with results from different techniques was to keep the mathematical analysis to the minimum. Hence, in this project, if not otherwise specified, DLS data was expressed as intensity-weighted distribution (mean \pm st.dev) of the hydrodynamic diameter and used as a reference for validation of the new techniques.

4.3.2 Nanoparticle Immobilization for Imaging

To image nanoparticles with the highest spatial resolution, the samples require immobilization. The standard immobilization method consists of drying and fixing the particles on a polymer base (Ruozi B. et al., 2011). This is necessary when aiming for electron microscopy, as the measurements are generally performed in high vacuum. Although easy and fast, this method becomes difficult to perform and interpret for non-solid particles, such as liposomes (Bibi S. et al., 2011). Figure 27 shows the two alternative strategies utilized throughout the project, with the immobilization on agarose patch (Figure 27A) and poly-L-lysine, PLL (Figure 27B), optimized in paper II and III, respectively. Both tricks are based on previous cell work; sperm cells have been successfully immobilized on agarose for super resolution imaging (Opstad I.S. et al., 2018) and PLL is a positively charged biocompatible

polymer which is commonly used to achieve cell adhesion on non-ideal supports (e.g., glass and metal). In the first case, a patch of solid agarose prepared in thin sheets (approx. 2 mm) was laid on top of the liposome suspension, which was previously pipetted directly onto a coverslip, for imaging on an inverted microscope. In the second case, it was the liposome suspension to be applied on top of the PLL coating, consequently sealed with a coverslip, for imaging on a modified upright microscope. After setting the sample on stage, few minutes of equilibration time were allowed for the liposomes to be stably immobilized prior to imaging.

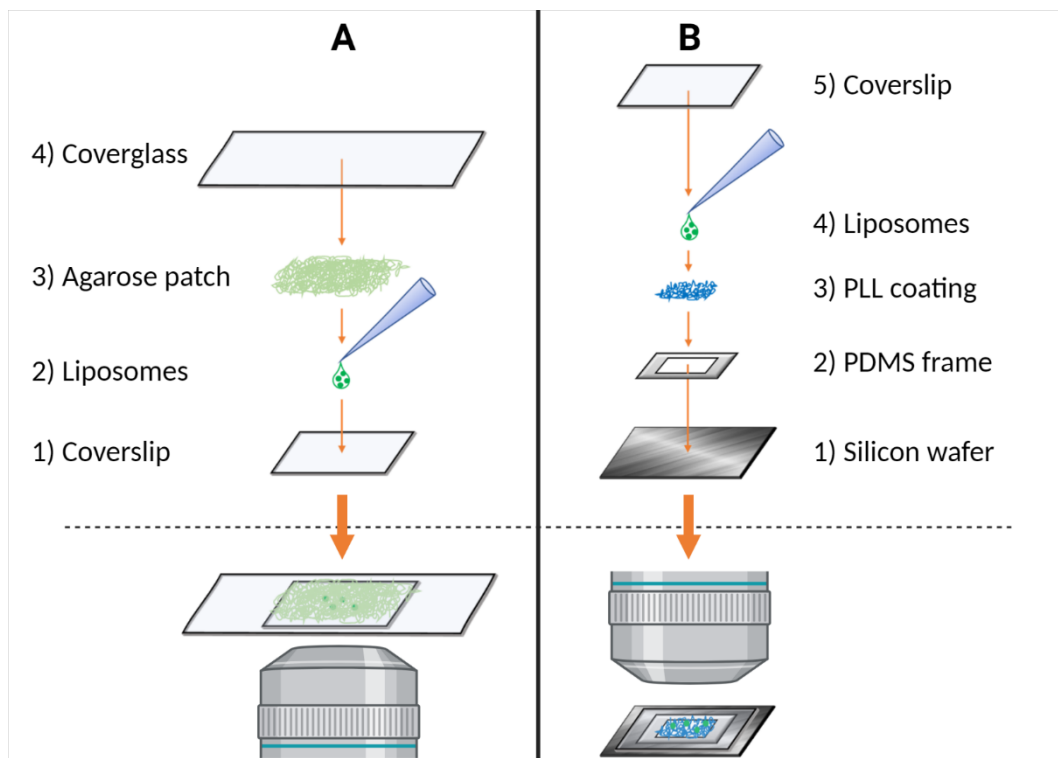


Figure 27. Schematics of sample preparation to immobilize nanoparticles for imaging. A) Immobilization on agarose patch (paper II). B) Immobilization on Poly-L-Lysine, PLL (paper III). The figure was prepared on Biorender.com.

4.3.3 Fluorescence-Based Characterization

The inclusion of a fluorescent label into a nanoparticle formulation for tracking purposes can be exploited also for the characterization of the nanocarrier itself. Several methods that use fluorescence to measure the size of nanocarriers have been already established, such as spectroscopic techniques (Zhou J. et al., 2020), fluorescence-based NTA (Dlugolecka M. et al., 2021), flow cytometry (Simonsen J.B. et al., 2019) and single particle imaging (Mortensen K.I. et al. 2018). Within this last category, the sub-diffraction sizes of nanocarriers require the use of super-resolution approaches, such as SMLM, SIM, and STED (Schermelleh L. et al., 2019). Although new fluorescence microscopy techniques are always first tested utilizing

fluorescence beads, which can themselves be classified as nanoparticles, the information obtained, and/or the optimizations of the methods cannot be directly translated to real formulations used in nanomedicine. Fluorescence beads are specifically designed for validating and calibrating imaging techniques in ideal conditions, as they are solid particles in monodisperse systems with homogeneous fluorescence, but also with close to no other practical use. In nanomedicine, to follow complex formulations of nanoparticles, the addition of a fluorophore should not significantly affect the intrinsic properties of the unlabeled carrier. Hence, contrary to fluorescent beads, the fluorescent moiety is usually not the star of the show. Common suboptimal conditions in these samples are non-uniform distribution of the labeling (Andrian T. et al., 2021) and/or the chemical instability of the fluorophore in the formulation, which can be responsible for reduced brightness and photo-instability (as seen in § 4.2, paper I). These very suboptimal properties of real formulations make nanoparticles a good sample to test the performance of super resolution imaging techniques, bridging the ideal case of fluorescent beads to more complex biological samples (e.g., fixed cells, live cells and tissues). This still uncharted territory for the newly developed fluorescence fluctuation super resolution microscopy techniques (FF-SRM) was investigated in paper II by comparing the performance of 5 different methods, namely ESI (Yahiatene I. et al., 2015), SOFI (Dertinger T. et al., 2009), SRRF (Gustafsson N. et al., 2016), SACD (Zhao W. et al., 2018), and MUSICAL (Agarwal, K. & Macháň R., 2016), with or without HAWK image pre-processing (Marsh R.J. et al., 2018).

Fluorescently labeled liposomes are a good example of real nanoformulations; relatively little can be precisely known before actual imaging. The hydrodynamic diameter described by DLS distributions is the only estimation of a size range for the set of particles, where the accuracy depends on the sample polydispersity (Bhattacharjee S., 2016) and with no precise size estimate for each individual particle. Fluorescently labeled lipids are included in the initial mixture of lipids and are therefore randomly interspersed among the individual liposomes. Additionally, the fluorophores are chosen among the currently used (Münter R. et al., 2018) and not according to the ideal requirements of a given microscopy technique.

N-labeled liposomes (green fluorescent) were immobilized on agarose patch, which was a good background noise model as it possesses a low degree of green autofluorescence. Figure 28 shows the data overview of the two samples of interest of about 100 nm (DLS: 117 ± 30 nm,

A) and about 250 (DLS: 240 ± 80 nm, B). The 1st frame closeup (bottom-left corners) shows that the background signal is much more comparable to the liposomes signal in the case of smaller particles (A), where the same total concentration of fluorophore is distributed over a larger number of particles, making the overall signal/particle lower. The standard deviation closeup (STD, bottom-right corners) is a visual 2D projection of the signal deviation per pixel across the image stack (200 frames) and it gives an initial indication on the fluctuations of the fluorescence per pixel. Again, the dotted background seen in sample A anticipates that the fluctuations of the background fluorescence might significantly interfere with the image processing, while for sample B the fluctuations deriving from the liposomes demonstrate a clear difference over the background. As all figures are shown with linear autocorrection of brightness and contrast (B&C, performed automatically in ImageJ), these differences in the quality of the image stack are less evident from the simple sum images.

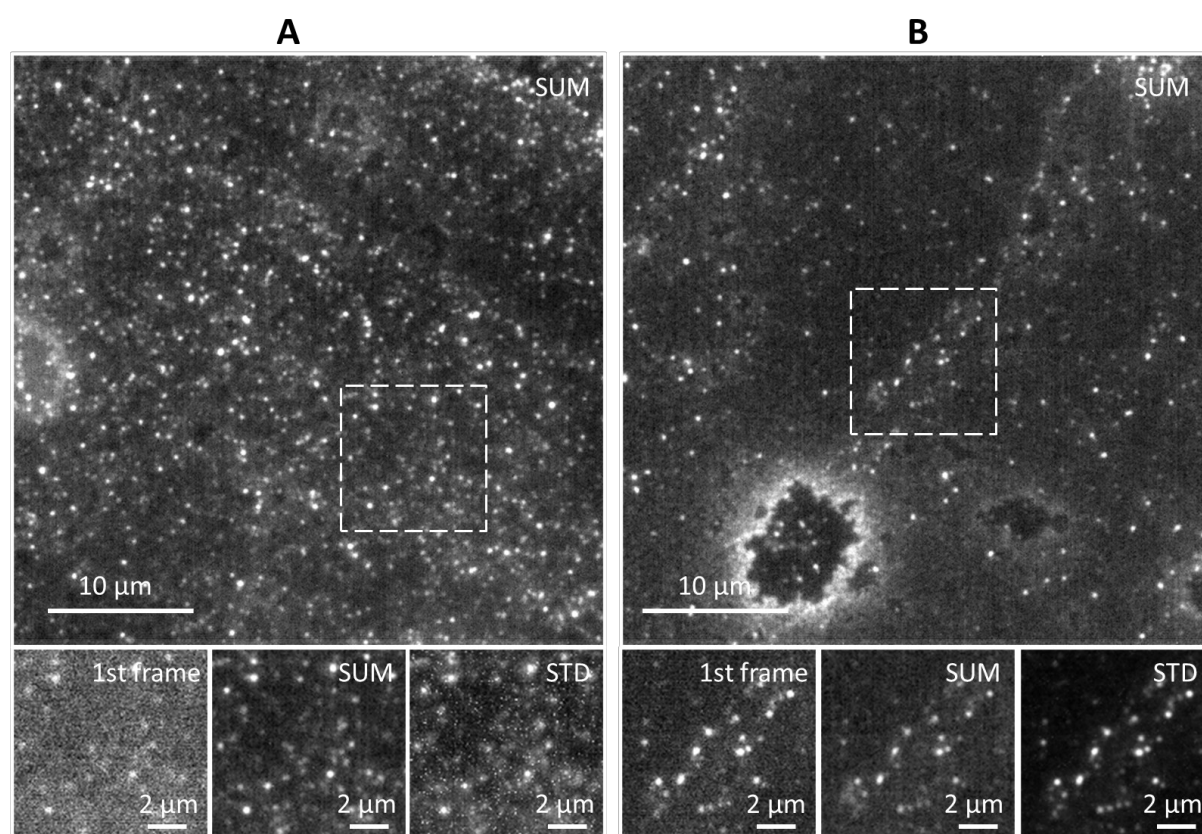
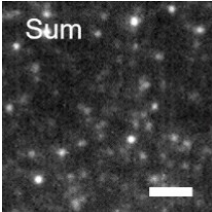
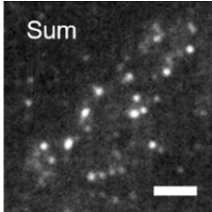
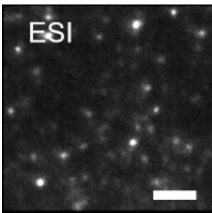
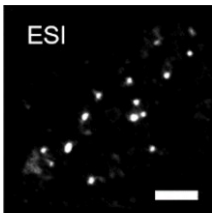
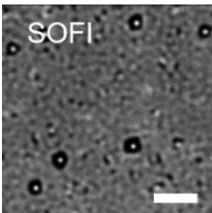
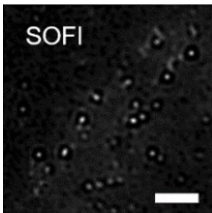
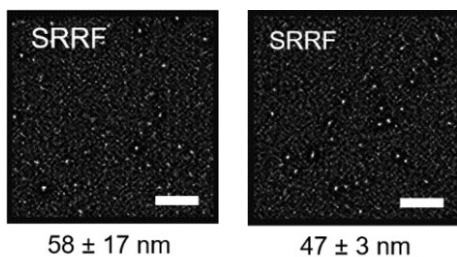


Figure 28. Dataset overview for immobilized liposomes of size A) around 100 nm and B) around 250 nm. From the full field of view (top) a region of interest (ROI) was selected for further image processing. On the bottom row the 1st frame, sum image projection and standard deviation (STD) image projection are presented for each sample. All images underwent autocorrection of brightness and contrast by selecting the Auto function on ImageJ.

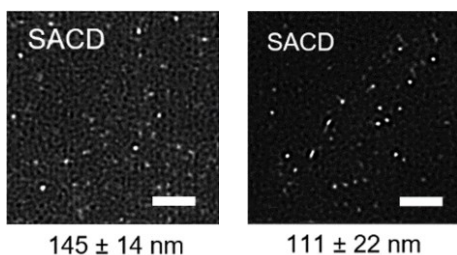
After screening for several reconstruction parameters for the different algorithms, Table 2 shows the best reconstructed images for both samples, with a technique-specific description of the images. To give all the techniques the same opportunity to shine and reconstruct an image that *looks good*, the visualization is hereby based on the linear autocorrection of brightness and contrast (auto function in ImageJ). In the special case of ESI, a further non-linear gamma adjustment ($\gamma=0.5$) was used, prior to B&C adjustment, to achieve higher contrast on the image, as typically done in microscopy for better visualization of dark images (Georgieva V. et al., 2019). However, all quantitative analyses (e.g., size determination and resolution profiles) were performed on raw reconstructed images, with no B&C adjustments and especially no gamma corrections, whilst ensuring no pixel saturation.

Table 2. Size characterization of liposomes based on FF-SRM image reconstruction algorithms. For each algorithm, the best reconstructed image is presented for the diffraction-limited sample (A) and the one at the resolution limit (B).

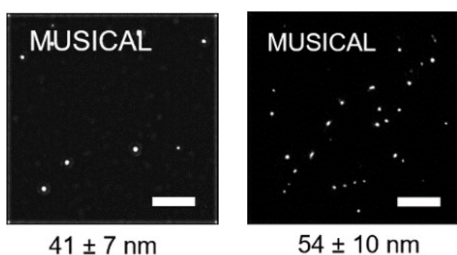
Approx. 100 nm A	Approx. 250 nm B	Technique-specific comments
 <p>Sum 323 ± 29 nm</p>	 <p>Sum 325 ± 74 nm</p>	<p>The sum image is a projection in 2D of the sum of the intensities per pixel throughout the stack acquired at the microscope, without any image processing. As expected, the sample below resolution (A) and close to the resolution limit of light (B) do not appear significantly different and their sizes (full width half max, FWHM) are widely overestimated in both cases.</p>
 <p>ESI 196 ± 16 nm</p>	 <p>ESI 183 ± 19 nm</p>	<p>The performance on background suppression for ESI shows dependance on the sample, as it is more effective for bigger particles (B). The smaller the particles, the more similar is the fluctuation of their signals to the background fluorescence. Reading this in terms of entropy, the algorithm reconstructs the image with less-defined edges of the liposomes.</p>
 <p>SOFI 201 ± 27 nm</p>	 <p>SOFI 184 ± 19 nm</p>	<p>SOFI shows different background suppression on the different samples. The autocorrelation function, characteristic of this algorithm, recognizes fluctuations at high intensity as point emitters (surrounded with a dark donut). If the fluctuations in the background are recognized as signals, they will be reconstructed as high-density of emitters (grey areas, A).</p>



In both cases, SRRF shows an artefactual background, excluding the very proximity of the liposome signal (high intensity signal surrounded by a dark donut). The symmetry of the emitter signal, which is assumed by the algorithm, is also recognized in the agarose background fluorescence, and reconstructed as a series of low intensity point emitters.



The Lucy-Richardson deconvolution, which in SACD is combined with the SOFI-like autocorrelation function, demonstrates a higher-than-SOFI degree of background suppression. However, a mesh-like artifact in the background could still be recognized, and only slightly lowered when reducing the number of processed frames (especially in the case of sample B).



MUSICAL shows excellent background suppression, due to the complete removal of out-of-focus signals. In fact, this algorithm first decomposes the acquired image stack into individual patterns. Hence, once selected a threshold, only the liposomes perfectly lying in the same plane will be recognized as prominent patterns and maintained in the reconstructed image.

Considering the overall performance of the FF-SRM techniques, they all provided efficient reconstruction and localization of the liposomes in the focal plane, with possible increased resolution for particles closely localized. However, from the quantitative point of view, the size estimation (from the FWHM of the image line profile) showed rather unexpected size values in comparison to the ranges obtained in DLS. The sizes determined from the images appear to be technique-dependent more than sample-dependent. Furthermore, when changing the parameters of the image processing, a considerable degree of variation was found on the size measurements of the same particle, making it complex to identify the most accurate estimation (if not by choosing the set of parameters that renders the image that visually *looks better*).

To reliably use this set of statistical imaging techniques, the selection of the technique-specific parameters is fundamental. However, for all the techniques, the selection currently needs to be manually performed, which makes the image processing laborious and can induce operator-based biases. The introduction of a pre-analysis for the automatic determination of

the most suitable parameters could be the key to match in practice the great potential that these techniques have shown in the last decades. In the meantime, it is worth having a closer look into label-free imaging to circumvent some of the disadvantages related to the fluorophore (e.g., chemical instability and photobleaching).

4.3.4 Label-Free Characterization

The development of any microscopy technique is continuously attempting to improve contrast, as the lack of contrast results in failure to achieve the theoretical highest resolution (Schermelleh L. et al., 2019). In nanomedicine, choosing not to use fluorescent molecules for light microscopy means removing the biggest source of contrast. For example, in the case of liposomes, the transparency of the lipid bilayers and the sub-diffraction sizes of the vesicles makes them invisible in common light microscopy. This challenge was visualized through coherent laser imaging of a liposome sample of approx. 120 nm (Figure 29A), where the scattering signal from the liposomes could not be localized over the background. To increase the contrast, it was then necessary to modify the illumination setup, such as shown in Figure 29B, where a partially coherent light source (PTLS with low spatial and high temporal coherence) was used to reduce the known speckle noise caused by the coherent laser source (Ahmad A. et al., 2019).

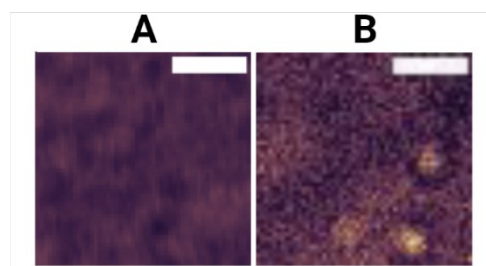


Figure 29. Label-free imaging of immobilized liposomes performed with A) epi-illumination with coherent laser source (660 nm), or B) dynamic speckle illumination with partially coherent pseudo-thermal light source (PTLS, 660 nm). The scale bars refer to 2 μm . Raw images from (Jayakumar N., et al., 2021).

Being able to localize the liposomal vesicles over the noisy background is the first step towards their characterization. However, the images obtained as such are still strongly subjected to the diffraction limit of light (Jayakumar N., et al., 2021). To obtain quantitative information on the sample, the partially coherent PTLS was used in quantitative phase microscopy (QPM), switching the focus of the detection from intensity of the scattered light to phase delay of the light reflected through the sample (Paper III). By using the Linnick interferometer in reflection

mode, in a nearly on-axis geometry, it was possible to maintain high spatial resolution, encoded in the recorded interferogram (Figure 30A). In the case of immobilized liposomes (not needing high temporal resolution), it was possible to acquire 5 frames per phase per image, and utilize the phase-shifting algorithm for high-resolution phase recovery (Figure 30B,C). Finally, the obtained phase map could be translated into a thickness map (as phase and thickness are directly proportional), giving the possibility to measure the size of liposomes in terms of height.

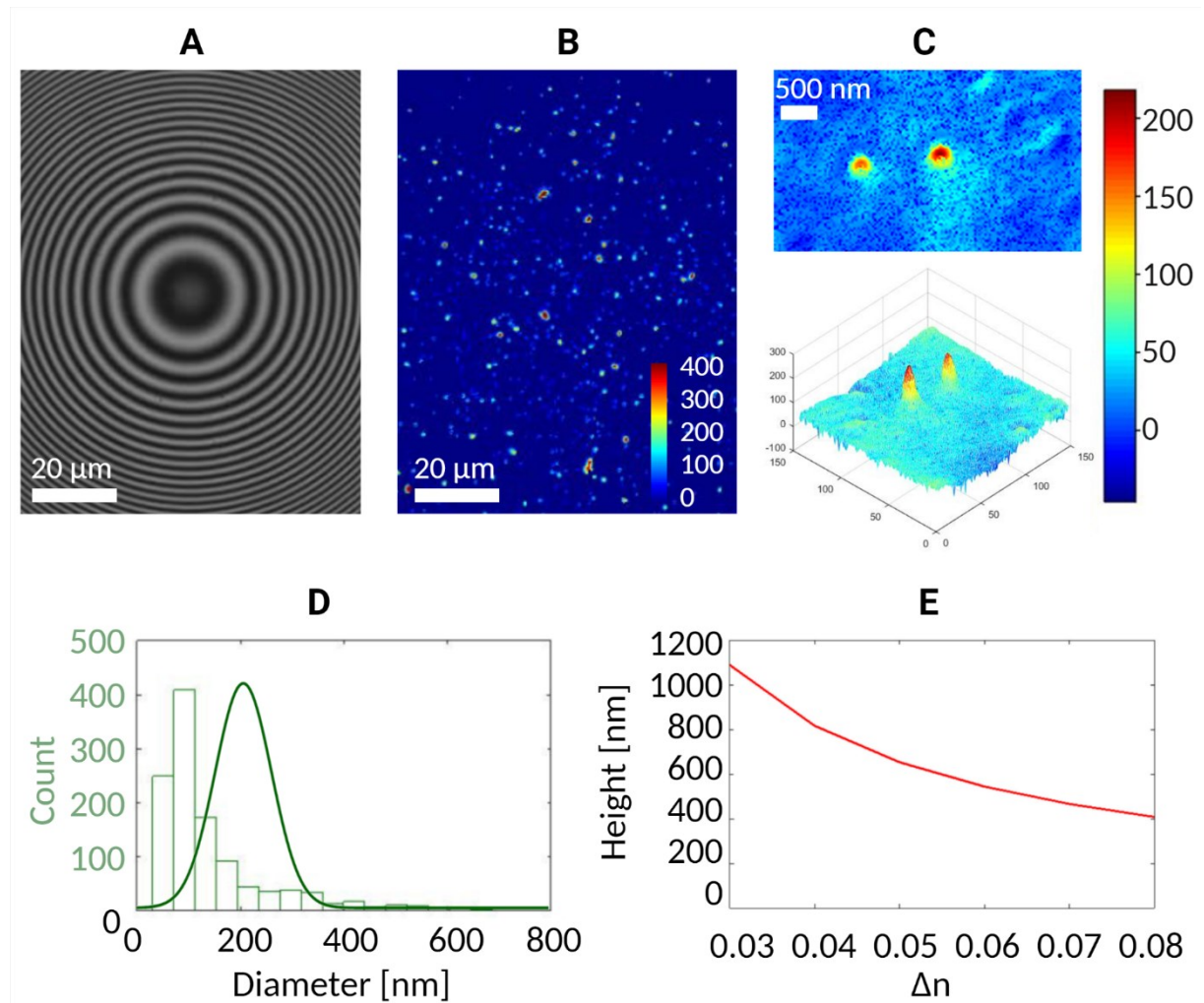


Figure 30. Quantitative phase microscopy on liposomes (N3 – 200 nm sample, paper III). A) Example of raw interferogram recorded at the QPM microscope. B) Phase map retrieved from a large field of view. C) Phase maps prior to numerical background suppression shown in top view (top) and lateral tridimensional view (bottom) to visualize the height of liposomes. D) Overlay of the size distribution obtained from QPM images (light green) and the one obtained in DLS (dark green). E) Simulation of the variation in liposome size (in terms of height) according to the refractive index difference Δn chosen.

A noticeable size underestimation was noticed in the number-weighted distribution derived from the QPM data in comparison to the range measured in DLS (Figure 30D). When comparing a number- and an intensity-weighted distribution, a perfect overlap is never expected (§4.3.1). However, three causes were identified as possibly contributing to the QPM underestimation, namely i) choice of refractive index, ii) comparison of particle diameter (QPM) vs hydrodynamic diameter (DLS), and iii) loss of high-frequency information in the recording of the interferogram. To retrieve the height measurements, the required factor is the refractive index difference between the object of interest and the surrounding medium Δn . Figure 30E shows a simulation of how deeply the value given to this factor can affect the size determination in terms of height. On the nano and molecular level, which is the case of the samples analyzed in this work, the refractive index for the different components of the system becomes an estimation, which could be the first source of error. Second, although the particles are immobilized in their hydrated state, the diameter measured in QPM is refractive-index dependent, therefore it refers to the actual particle diameter and does not include the hydration layers. Third, although the modification to the light source in this PTLs-QPM permits high contrast imaging and localization of nano-objects, QPM is not a proper super-resolution technique as both light source and detection are still diffraction limited. Considering this, some degree of loss of high-frequency information (referring to the smaller details) is expected in the detection of the interferogram (Butola A. et al., 2020).

Overall, these label-free results show many similarities with the fluorescence-based determinations (§4.3.4); both strategies are faced with the same limitations of low contrast and diffraction limit of light. However, QPM exhibited superior capability of localizing and following the integrity of liposomes over time, in comparison to the quick loss of fluorescence signal under laser illumination. As for the FF-SRM techniques, to reach the full potential of QPM at the current state-of-the-art, calibration systems with available ground truth could be set in place to quantify the underestimation and correct for it. Furthermore, further increasing the contrast on the images could still provide better localization for a more reliable estimation of the distribution. E.g., Figure 31 compares a fluorescence-based imaging method (in TIR mode, A), a wide-field PTLs imaging (B) and a decoupling of illumination and detection with on-chip label-free optical microscopy (cELS, C), where the latter identifies more individual signals over a significantly suppressed background (Jayakumar N. et al., 2021)

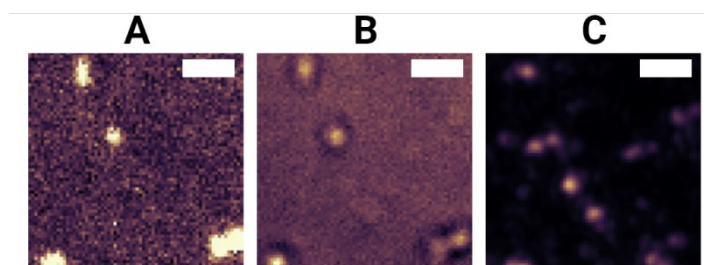


Figure 31. Imaging of immobilized liposomes performed in A) fluorescence TIR mode (488 nm laser), B) dynamic speckle illumination with partially coherent pseudo-thermal light source (PTLS, 660 nm), and C) decoupled illumination and detection system through chip-based evanescent light scattering (cELS). The scale bars refer to 2 μm . Raw images from (Jayakumar N. et al., 2021).

4.3.5 Combination of Fluorescence and Label-Free Imaging

The availability of both fluorescence-based and label-free methods, and their continuous technological developments, open doors for the combination of these powerful tools for the determination of different properties within the same sample. For nanomedicine purposes, the field of correlative microscopy is very young and still of limited accessibility because of the challenges related to the sample preparation and optical imaging of diffraction-limited low-scattering objects (e.g., liposomes). A recent paper from Andrian T. et al. (2021) has first demonstrated the correlation of super-resolution microscopy (specifically, SMLM) and TEM images for the determination of heterogeneity in nanoparticles labeling and ligand distribution, on a single-nanoparticle level. The implementation of these kinds of studies in early stages of development can bring highly specific information on the outcomes of the preparation methods, which can be significantly more informative than bulk analyses and averaged results.

Figure 32 shows an example of correlative microscopy for nanomedicine purposes (paper IV), utilizing widely available instruments (confocal microscope and SEM microscope). This example refers to a liposomes-in-nanofibers formulation, where a primary carrier (liposomes) is incorporated into a secondary vehicle (polymeric nanofibers), which acts as a scaffold for the easy-to-handle topical administration of drugs. In the technological optimization of these nanoformulations, SEM imaging is the conventional method used for the visualization of the fiber morphology (Širc J. et al., 2012). By adding a fluorescent labeling on the primary nanocarrier, it is then possible to obtain an indication on the uniformity of the distribution of liposomes throughout the nanofibers (Chandrawati R. et al., 2017). Hence, simply mounting

the formulation on a coordinate system for imaging (e.g., MatTek dishes with #1.5 gridded coverslip), a direct correlated image can be obtained without the need for non-linear distortions in either of the original microscopy images (CLSM: Figure 32A, and SEM: Figure 32B).

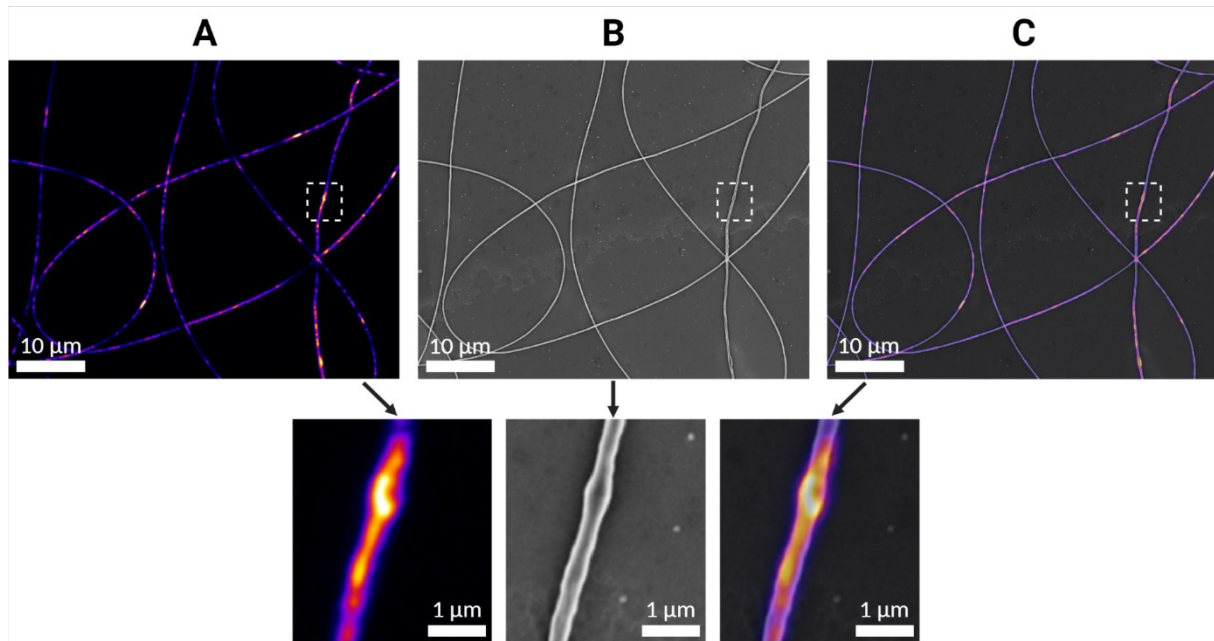


Figure 32. Direct correlation of confocal imaging and SEM imaging on a liposomes-in-nanofibers formulation. A) Confocal image performed in airyscan mode and visualized with the intensity-based fire lookup table (LUT), available in ImageJ. B) SEM image. C) Correlated overlay of images A and B, with no distortions applied. The bottom row shows blow-ups from the top images. Data from paper IV.

The examined specimen of liposomes-in-nanofibers revealed that the presence of liposomes in the spinning solution did not affect the integrity of the nanofibers (as previously shown in literature (Zylberberg C. & Matosevic S., 2017)), although bigger-than-expected fibers could be identified in the sample. As for the liposomes, a clear non-uniform distribution could be recognized. In fact, the confocal imaging in airyscan mode allowed to distinguish areas with high fluorescence intensity (brighter spots in Figure 32A), low intensity (blue areas), and zero intensity (black areas, corresponding to both the background where no fibers were present, but also to some areas within the fibers). This gradient of fluorescence intensities could be interpreted as a partial integrity of the liposomes in the fibers, which is consistent with earlier studies on liposomes-in-nanofibers preparations by needle-free electrospinning (Mickova A. et al., 2012).

As nanofibers are intrinsically dried formulations, liposomes-in-nanofibers represent a perfect specimen for correlative microscopy and could potentially be benchmarked for the calibration of such experiments. Furthermore, the combination of information on the nanofibers morphology (SEM) and liposomes localization/agglomeration (confocal) is particularly important in the technological development of liposomes-in-nanofibers formulations. The integrity of both liposomes and nanofibers directly affects the kinetics of API release and therefore can be a predictor of the treatment outcome (Luraghi A. et al., 2021). Hence, this methodology could provide quick and easy insights on the efficiency of the preparation method when screening e.g., for different polymers, concentrations of the different ingredients, or other environmental parameters.

4.4 Internalization of Liposomes

4.4.1 Indirect Approaches

Indirect approaches refer to the various methods which follow the cellular response to a certain treatment in comparison to an untreated control, whilst allowing to screen a large number of conditions, e.g., different formulations in different concentrations (Collins A.R. et al., 2017).

A first approach is to test cell proliferation with and without treatment, which can promptly allow to define the therapeutic range of a formulated API and/or measure the degree of cytotoxicity of the formulations (Ternullo S. et al., 2018). Figure 33A presents an example of how the proliferation study was used to ensure that inclusion of fluorescently labeled phospholipids within the liposomal bilayers does not impair liposomes safety. No significant difference was noted between the untreated control, the unlabeled liposomes and the fluorescently labeled formulations, even at increasing lipid concentration (1-50 $\mu\text{g}/\text{mL}$).

A second approach to evaluate the cellular response to treatments is to measure cellular metabolites of interest. In the case of macrophages, the elected cell line for this study, the inflammatory response to the environment is a signature biological activity. Hence, the nitric oxide (NO) production is a good indicator of the cellular performance under inflammatory stress (Jøraholmen M.W. et al., 2017). Furthermore, as lipid-based formulations, liposomes are known to have a positive effect in reducing the inflammatory response on activated (LPS-triggered) macrophages (Giordani B. et al., 2020, Hemmingsen L.M. et al., 2021). Therefore,

the NO production of activated cells becomes an indirect measure of how the presence of the liposomal fluorophore affects the biological activity of the unlabeled liposomes. Figure 33B shows an example of such comparison, where it is possible to see a higher variation of performance for both N- and R-labeled formulations, possibly due to the fluidity of the bilayer in N-Lip (Kay J.G. et al., 2012) and the negative surface charge in R-Lip (Fröhlich E., 2012). The T-labeled formulations exhibited a higher degree of overall disguise and therefore were further investigated in terms of uptake through fluorescence-based batch-mode analyses.

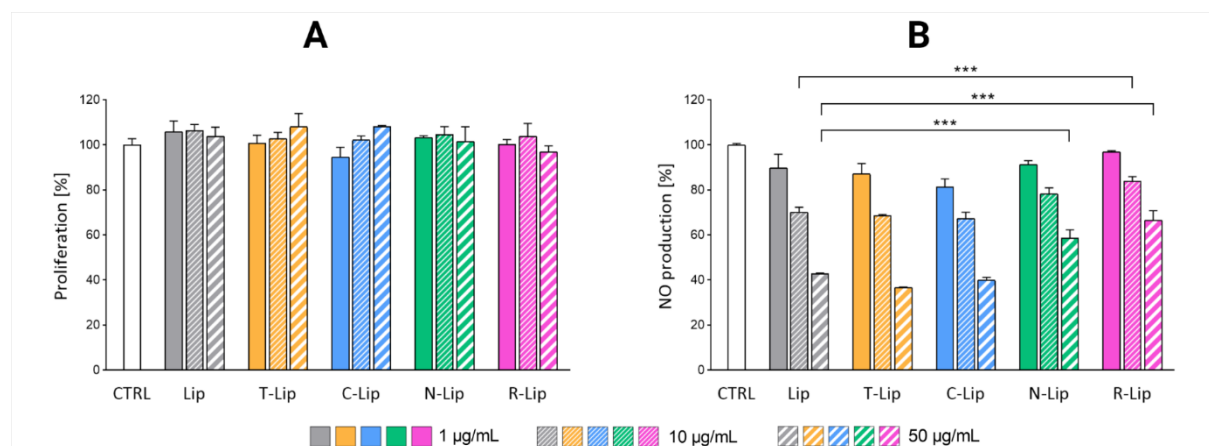


Figure 33. Biological activity of fluorescently labeled liposomal formulations in comparison to untreated cell control and unlabeled liposomes. Murine macrophages RAW264.7 were used as model cell line. CTRL refers to the untreated cell control. Lip refers to the unlabeled formulation of liposomes. The labeled formulations comprise 10 mg/mL of SPC and 0.03 mg/mL of labeled lipid, prior to dilution to the final lipid concentrations of 1, 10 or 50 µg/mL as indicated in the legend. A) Cell proliferation assay performed with the Cell Counting Kit-8 (from Sigma Aldrich Chemie). B) NO production on LPS-activated cells, measured with the Griess reagent. Data merged from paper I, and pilot data for paper II, III.

4.4.2 Fluorescence-Based Batch-Mode Approach

Flow cytometry (FCM) is considered one of the fluorescence-based techniques with highest possible throughput. In a matter of minutes, hundreds of thousands of cells are individually screened in terms of i) forward scattering (FSC), ii) side scattering (SSC), and iii) specific total fluorescent emission (Collins A.R. et al., 2017). When the cell flow passes in front of the laser (interrogation point), each cell will show a contribution in FSC and SSC according to its dimensions. Bigger objects exhibit bigger forward scattering, while smaller objects are associated with more relevant side scattering. In the case of macrophages, both values of FSC and SSC were considerably high, such that an additional filter to dim the scattered light was

added to avoid saturation of the detector. This earlier reported behavior (Wayne E.C. et al., 2019) was expected due to the big cellular dimensions (20-30 μm), which resulted in high FSC. In addition, the complexity of the cells in terms of small organelles and granules was detected as high SSC. This analysis, in terms of FSC and SSC, can be used to identify and select/gate the cell population of interest, as these values are reproducible among different samples and experiments. Furthermore, in addition to the scattering analysis, up to four different fluorescent labels can be individually quantified as a total emission per cell (Adan A. et al., 2017).

Figure 34 presents an example of FCM results, with the specific detection of the T fluorophore (from the T-Lip treatment) and propidium iodide (PI), a dead-cell marker. Specifically, Figure 34A displays the scatterplot of fluorescence readings from a negative control, freshly stained with PI. This fluorescent marker intercalates DNA, forming a complex that emits a bright orange signal ($\lambda_{em} = 617 \text{ nm}$). However, the double positive charge on the molecule makes it strictly membrane-impermeable, implying that live cells will not internalize the molecule. This intrinsic property of the molecule allows for the visual separation of two clouds in the population analysis, where the one shifted upwards (high PI intensity in quadrant Q1) marks all dead cells with damaged plasma membranes (King M.A., 2000). The y-axis histograms exhibit two recognizable features of the PI labeling. First, the peak corresponding to the live-cell population (marked as 1 in the figure below), is slightly shifted upwards from the zero level. This phenomenon is due to unspecific binding of fluorophores to the cell membrane, often reported in immunolabeling and experienced in practice with any sort of fluorescent treatment (Ahlers M. et al., 1991). Second, the peak corresponding to the dead-cell population (peak 2), is a double peak, which inherently distinguishes the cells that died before and after DNA replication in the S phase of the cell cycle (King M.A., 2000).

Once gates and quadrants of interest are specified, the same population analysis is repeated on all the samples and can be visually overlaid as shown in Figure 34B. In respect to the untreated control (gray), the cells that were exposed to T-labeled liposomes (orange) exhibited a shift to the right of the cloud and corresponding top histogram (high T intensity in Q3). The extent of this shift is an indication of the liposomes' internalization; the brighter the cell signals, the bigger the associated shift (Collins A.R. et al., 2017).

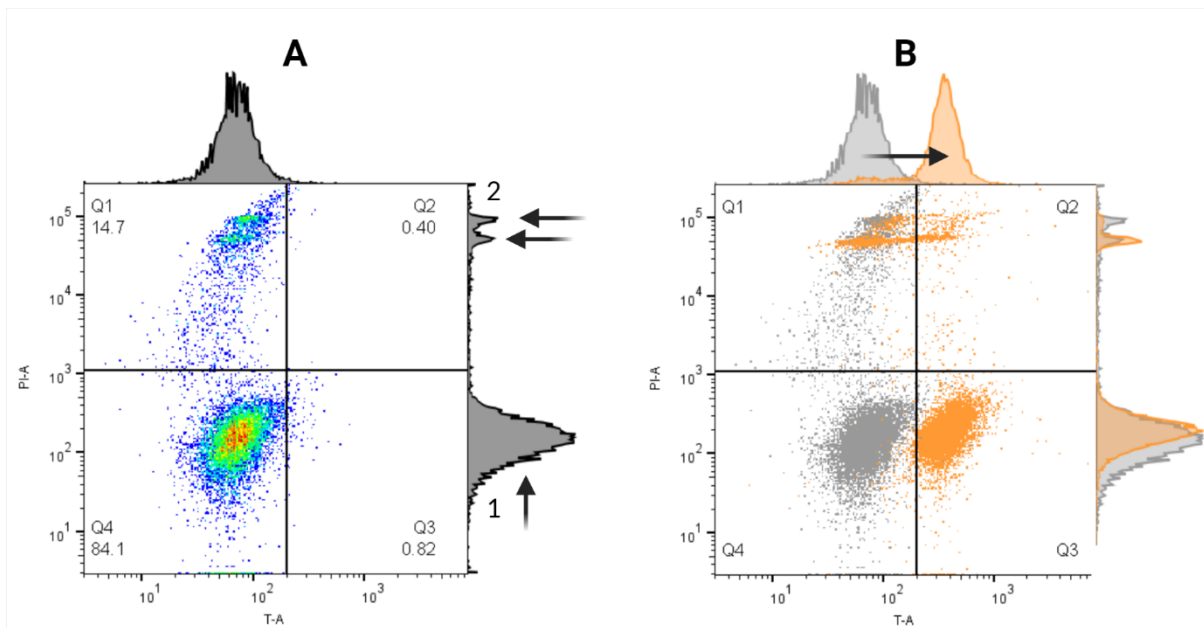


Figure 34. Data visualization of flow cytometry population readings. This 2-color analysis shows, simultaneously, live cells (with low intensity of the propidium iodide PI channel, y-axis) and cells which have internalized the nanoparticle of interest (with high intensity on the T channel, x-axis). Each dot represents an event; hence, a single cell at the interrogation point. A) Full population analysis on untreated cells (negative control). The color code on the cloud of events is a density map, where red corresponds to the peak on the count histograms on both axes (here shown on the top and right borders). B) Overlay of full population analyses of untreated (gray) and treated cells (here treatment with T-labeled liposomes for 18 h, orange). The figure was prepared on FlowJo™ v10 software (BD biosciences) utilizing sample data from paper I.

The presence of dead cells in all analyzed samples can be explained by the experimental choices. The cell line utilized for the experiment was murine immortalized macrophages RAW264.7, a well-known adherent cell line (Kuriyama T. et al., 2021). After seeding in 6-well plates, cells were grown overnight to 80% confluent monolayer before applying the stepwise treatments. At the final endpoint, cells were washed and re-suspended in low volume of phosphate buffer (1 mL) by gentle scraping on the plastic bottom. The cell suspensions were consequently stored in ice bath for the remaining processing and transportation time. Each step of the sample preparation represents a disturbance in the cell growth:

- Prolonged culture in confluence and temporary suspension in DPBS are both causes for nutrients depletion in cell growth; nonetheless, these procedures allowed for high concentration of cells per sample and low background fluorescence, which are requirements for efficient analyses in flow cytometry (Kalina T., 2020).

- The storage on ice (short-term hypothermic preservation) reduces the cell metabolism; moreover, its extent of reversibility is often incomplete, with time and temperature dependence (Rubinsky B., 2003), but it allows buffer time to process all the samples and transport them to the flow cytometer.
- The scraping method has been shown to induce physical stress on the cells (Kuriyama T. et al., 2021). However, with adherent cells such as macrophages, which did not respond to the available trypsin-based method, the use of cell scrapers was considered the most suitable alternative to allow fast processing of a high number of samples, reducing the time of DPBS suspension and storage in ice.

As Figure 35A indicates, the percentage of live cells did not significantly vary between controls and treatments, in agreement with the proliferation assay done in parallel (§4.4.1). Hence, the cloud of dead cells was considered to be linked to the experimental procedure and excluded in the gating tree for quantification purposes.

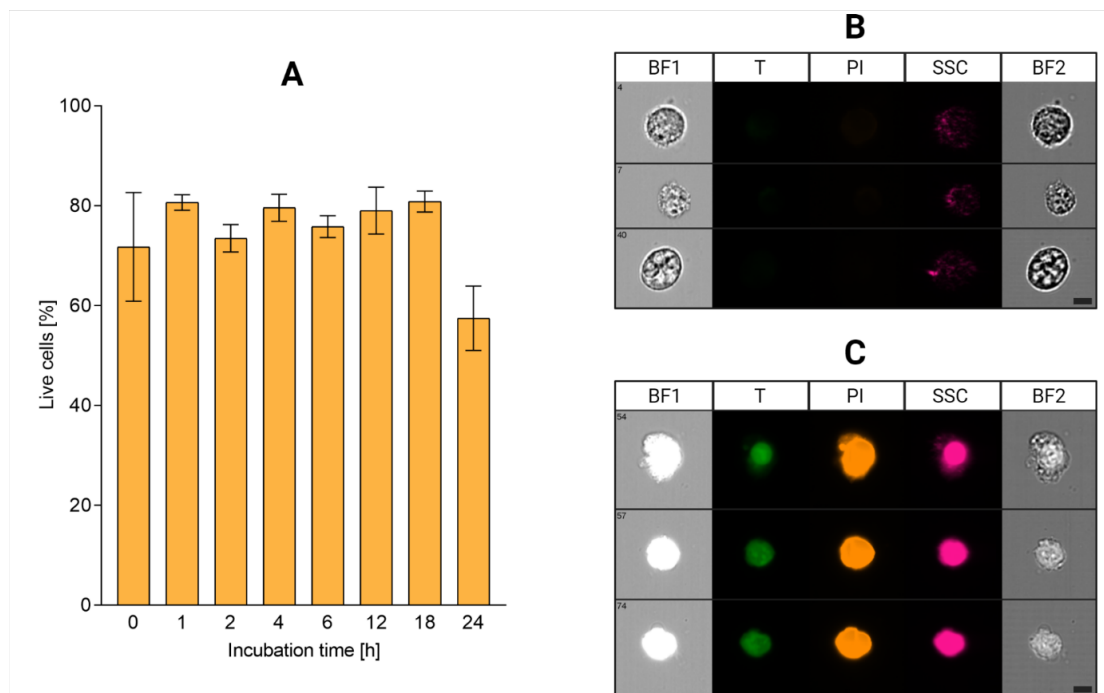


Figure 35. Live and dead cells analysis. A) Quantitative population analysis of PI-negative cells in the different samples analyzed in flow cytometry (n=3). B,C) Qualitative analyses in flow imaging of untreated live and dead cells, respectively. BF1 and BF2 are bright fields of the available cameras. T (Ch02, 528/65) is the channel for the visualization of T-labeled liposomes. PI (Ch04, 610/30) marks dead cells. SSC (Ch6, 762/35) is a visual representation of the side scattering from the granularity of the cells (note: this is not a fluorescence channel; the bright pink is a pseudo-color solely assigned for visualization purposes). The scale bars correspond to 7 μ m. Data from paper I.

Further analyses on the cell suspension were then performed in flow imaging to obtain additional qualitative information about the fluorophore distribution (Figure 35B and 35C). Both available cameras were activated to record bright fields (BF1 and BF2) of the single cells at the interrogation point. Furthermore, the fluorescence channel of interest (T: Ch02, 528/65), the PI-channel (PI: Ch04, 610/30) and the side scattering channel (SSC: Ch6, 762/35) were activated to detect, respectively, the internalization of liposomes, the internalization of PI (dead cells) and the granularity of the cells (typical of macrophages). Interestingly, dead cells (with bright PI fluorescence, orange) would often show a bright signal in the green fluorescence channel as well (Figure 35C). This phenomenon corroborated the decision of gating out dead cells for the quantitative analysis. In fact, dead macrophages have been shown to have higher green autofluorescence intensity than the correspondent live cells (Kozlova A.A. et al., 2020), in a manner that is independent on the fluorophore of interest.

The internalization kinetic in live cells was then analyzed through cell count and fluorescence intensity obtaining two different curve shapes (Figure 36). In the first 2 h of incubation, a notably small shift in the fluorescence spectra of the population showed a low number of cells having internalized liposomes (Figure 36A) and little to no change in the overall fluorescence intensity of the population (Figure 36B). This behavior, previously reported in the literature for plain neutral liposomes (Raz A. et al., 1981), was explain as unspecific binding and early internalization. Between 4 and 6 h, most live cells were screened positive to the T-label, with a sharp rise in the count curve in Figure 36A, while showing increasing fluorescence intensity of the population as a linear trend in figure 36B. The delayed start and the non-saturation of internalization capacity, in the observation period, pointed at a correlation with phagocytosis pathways, previously acknowledged in literature (Ahsan F. et al., 2002, Manzanares D. & Cena V., 2020). Qualitative analyses in flow imaging confirmed these internalization profiles, confirming a non-uniform distribution of the fluorophore in organelles, such as phagosomes and phagolysosomes, where the recognition of liposomes is known to be facilitated by the presence of a phospholipid receptor (Conrad K.S. et al., 2017).

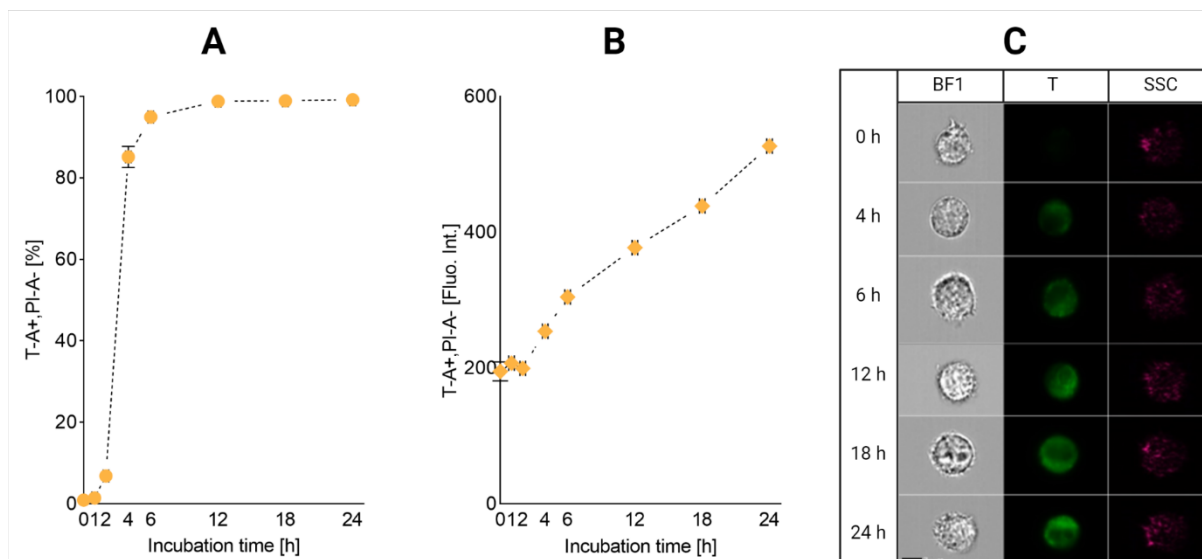


Figure 36. Internalization of T-labeled liposomes. A) Internalization profile as count of live cells that have internalized fluorophore. B) Internalization profile as peak fluorescence intensity in the T channel on the population analysis of live cells. C) Visualization of the internalization in flow imaging. One representative live cell is shown for the incubation times of 0 h (negative control), 4, 6, 12, 18 and 24 h. BF1 is bright field (Channel Ch01 in the instrument), T (Ch02, 528/65) shows the granular internalization of T-labeled liposomes, and SSC (Ch6, 762/35) is a visualization of the side scattering. The scale corresponds to 7 μm . Data from paper I.

In this case, flow imaging served as a qualitative validation of the population analysis performed in FCM, as an alternative method to the conventional confocal microscopy. The short acquisition time and the wide-field image detection allowed to circumvent some issues encountered with the fluorophore of choice (T). In fact, despite having shown the highest long-term stability to the aqueous environment (§4.2), the T-label was quickly associated to poor photostability under laser illumination. As a consequence, significant photobleaching was detected through the acquisition of image stacks, making it progressively more complex to identify the specific signals over the autofluorescence of macrophages (particularly relevant in the green channel, Kozlova A.A. et al., 2020).

To further investigate the intracellular fate of liposomes in more conventional microscopy setups, a change of fluorophore was considered, shifting the focus towards higher photostability and emission in a different channel. Rhodamine B was chosen as the second in line in terms of stability to the environment, its orange emission ($\lambda_{em} = 583 \text{ nm}$), and favorable photochemistry (Grimm J.B. et al., 2020).

4.4.3 Fluorescence-Based Single-Cell Approach

To follow the internalization of liposomes in cells, the ideal scenario includes live-cell imaging. However, the need for high temporal resolution to image fast dynamics requires short acquisition times, which are often not compatible with scanning techniques such as the conventional CLSM (Lemon W.C. & McDole K., 2020). Furthermore, the real dynamics of nanocarrier interaction with the cell membranes are particularly difficult to visualize in fluorescence microscopy, as most fluorescent probes have been shown to deeply affect the functionality of the membranes (Specht E.A. et al., 2017). Figure 37 displays an example of live-cell imaging of an unstained cell, after 30 min incubation with R-labeled liposomes. A 10-frame video acquisition was performed in fast confocal scanning of a small ROI at the edge of a cell. A single z plane was chosen to avoid further delays in the acquisition time of a z-stack and the scan speed was adjusted to obtain acquisition time of 2 s per frame. Both characteristic motion artifacts of scanning imaging can be recognized in the short span of 20 seconds. The line-like structures, visible on the right side of each frame (area outside the cell), are the visual representation of the fast Brownian motion of liposomes in suspension. In fact, with such small objects, by the time the confocal reading scans back the same area, the liposome has moved and therefore its intensity will be shifted. On the other hand, the ring-like structures, well visible for example at 00.18-00.20 seconds, represent the PSF of out of focus structures, referring to the movement of objects on the z-direction. Interestingly, liposomes interacting with cells exhibit a slower motion which enables their clear localization in the frame. In fact, according to the Stokes-Einstein equation, when increasing the viscosity of the medium (e.g., cytoplasm of cells), the diffusion of particles slows down proportionally to their radius (Florence A.T., 2012a). This explains a certain use of confocal live imaging for the description of intracellular trafficking (Watson P. et al., 2005, Foroozandeh P. & Aziz A.A., 2018). However, with this kind of dataset for unstained cells, it was not possible to determine whether the round-like signals came from internalized vesicles or simply referred to surface contact of liposomes with the cell membranes. Furthermore, the diffraction-limited imaging does not allow to resolve whether these signals come from a single vesicle or are the co-localization of more nanocarriers, e.g., pre- or post-internalization.

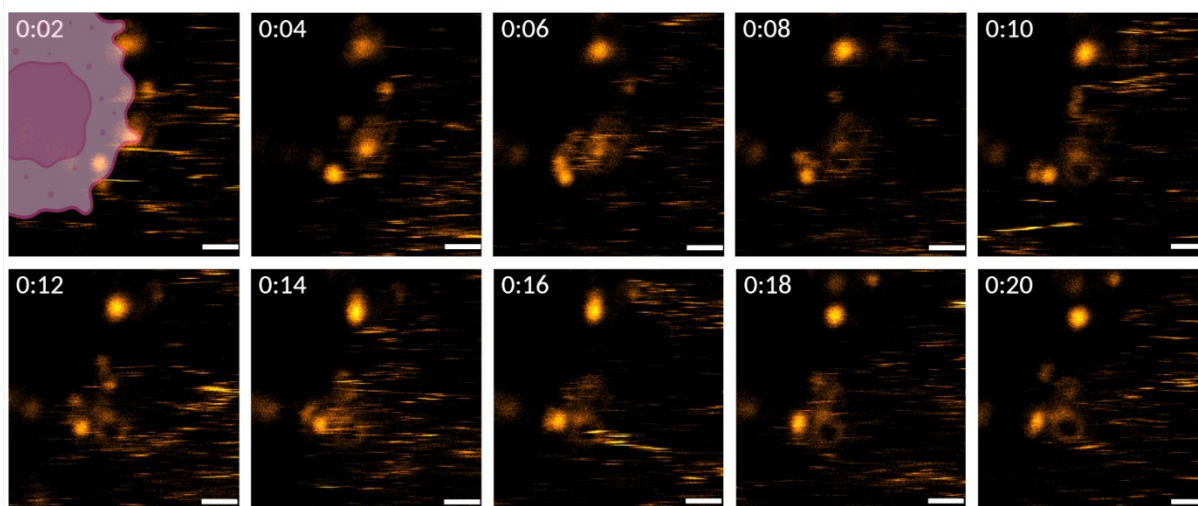


Figure 37. Live cell imaging of unstained cell sample (A549, human lung cancer cells) after 30 min of incubation with T-labeled liposomes. The region of interest was chosen as a single z-plane at the right edge of a cell (as shown with the cell drawing in the first frame). The scan speed was adjusted to a frame acquisition time of 2 seconds. Note: the cell localization was confirmed with post staining. The video-acquisition was processed with ImageJ and the figures were assembled using Biorender.com.

Super-resolution imaging was widely considered throughout the project, especially through STED and SIM. Both techniques require relatively long acquisition times and, although not impossible, are complex to implement on live cell imaging (Lemon W.C. & McDole K., 2020). The high laser power required on STED easily induces phototoxicity on cells, other than photobleaching of common dyes, if not properly adjusted for small areas and specific conditions (Kilian N. et al., 2018). The illumination pattern utilized in SIM partially solves the problem of phototoxicity (such that SIM is still considered the go-to super-resolution techniques for live-cell imaging, Sandmeyer A. et al., 2021). However, the need for repeated frame acquisition (while shifting and rotating the illumination pattern) and the finely tuned z-stacking is often correlated with photobleaching of the fluorophores, which is a major cause of artifact reconstruction if not recognized and (if possible) corrected for (Fan J. et al., 2019). The fluorescently labeled lipids which were stabilized in liposomes throughout this project were found chemically unsuitable for either of these techniques, as they are prone to photobleaching in SIM and incompatible with the fluorescence depletion mechanism on which STED is based.

The focus was therefore put on optimizing the confocal imaging. After verifying that cell fixation does not compromise the samples readings in fluorescence, cells were imaged in

airyscan detection mode (which is considered a pseudo-SRM, Huff J., 2015), with pixel oversampling (hence, aiming for the theoretical resolution of 200 nm). Figure 38 shows the type of information obtainable with confocal datasets. With the highest available magnification (60x/1.4 oil immersion objective), 20-40 cells can be imaged in one field of view, and the average intensity projection can show the overlay of the different colors to address possible co-localization of different structures of interest. By maintaining constant the acquisition parameters (e.g., laser power, scan speed, and pinhole size), and the B&C adjustments on the different channels, it is then possible to visually compare the overall intensities between untreated and treated samples. Furthermore, a 3D rendering of the confocal stack can give volumetric information on the stained structures on interest, although the evident lower z resolution which can become challenging to interpret.

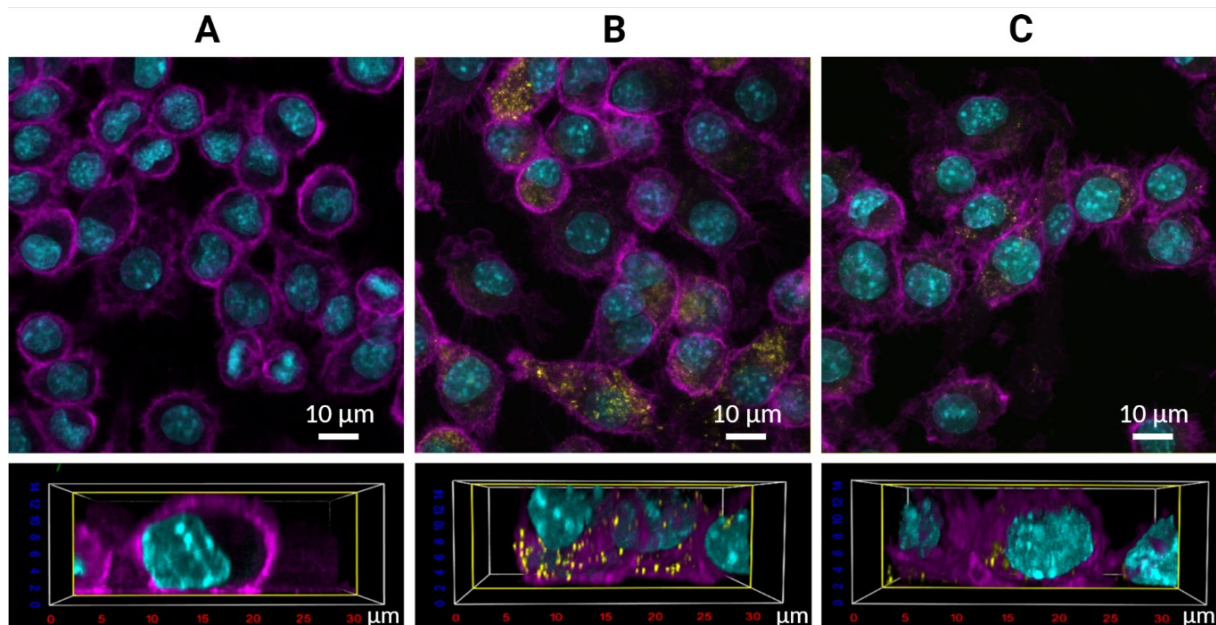


Figure 38. Examples of confocal stacks in xy multi-channel intensity projection (top) and 3D volumetric rendering (bottom). The cells are murine macrophages RAW264.7. The magenta color refers membrane staining (WGA640), the cyan color highlights the nucleus (stained with Hoechst 33342) and the yellow localizes the rhodamine-lipid signal. A) Untreated control. B) 24 h treatment endpoint with T-labeled plain liposomes. C) 24 h treatment endpoint with PEGylated T-labeled liposomes. Data from paper IV.

To combine the specificity of the fluorescent information with more general knowledge on the cell morphology and stress condition, correlative light and electron microscopy was pursued as ultimate approach.

4.4.4 Combination of Fluorescence and Label-Free Imaging

First rule of thumb to perform correlative microscopy is to prepare the sample on a coordinate system, such that a specific area can be imaged in two different microscopes. Figure 39 represents the development of a grid of coordinates for correlative microscopy (CLSM and SEM), utilizing a cell culture as a sample. The easiest approach that can be implemented on any sample and lab is to scratch the surface of the sample using a sterile pipette tip (Figure 39A). Although easy and fast to perform, this method showed poor reproducibility as the visibility of the lines depended on the density of the plated sample (i.e., cell confluence). A second direct approach was to adhere the copper finder grid (routinely utilized for correlative CLSM-TEM) on the bottom of the plastic/glass support and apply a PLL coating on top of the grid, prior to addition of the sample (Figure 39B). Although quick, easy, and reproducible, the PLL coating could not completely isolate the copper, which showed significant cytotoxicity on live samples (Cortizo M.C. & Lorenzo de Mele M.F., 2004). To maintain the coordinate system typical of the copper finder grid without leaving residual copper into the sample, the grid was used as a mask on the support. On the first attempt, a thick carbon coating was applied to the glass support prior to grid removal (Figure 39C), which showed good biocompatibility (Barkhudarov E.M. et al., 2020) but low visibility of the coordinates and low contrast in SEM. On the second attempt, methacrylate glue was used for grid printing onto glass support, removing the grid prior to full solidification of the methacrylate (Figure 39D). This was considered the most successful grid print and used further for correlative experiments. However, the poor reproducibility of the print and the need to use a new TEM grid mask for each sample required reverting back to commercially available gridded MatTek dishes.

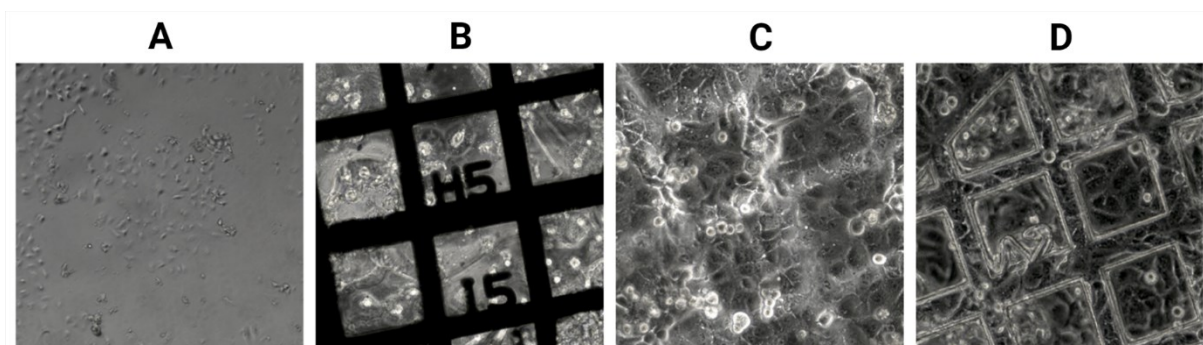


Figure 39. Optimization of a coordinate system for correlative CLSM-SEM imaging. A) Tip printing by scratching the surface of a cell culture. B) Copper finder grid (used for CLSM-TEM correlation) embedded in PLL coating. C) Carbon coating using the finder grid as mask. D) Methacrylate grid print using the finder grid as mask. Pilot data to Paper IV.

A successful example of CLSM-SEM correlation on methacrylate grid is shown in Figure 40, focusing on nuclear staining and T-labeled liposomes internalization. The peculiar combination of these techniques, only seldom found in literature (de Waal G.M. et al., 2018, Luckner M. & Wanner G., 2018, Jeong D. & Kim D., 2022), allows for the simultaneous visualization of the specific signals from the internalized liposomes and the surface morphology/condition of the cells. In the example shown, the roughness of the membrane was higher in the liposome-treated sample (Figure 40B) when compared to the untreated control (Figure 40A). Furthermore, the co-incubation of liposomes (red) with cell-penetrating peptides (unstained) showed the expected increase in liposomal internalization (Khan M.M. et al., 2021) and was linked to more evident membrane roughness (Figure 40C).

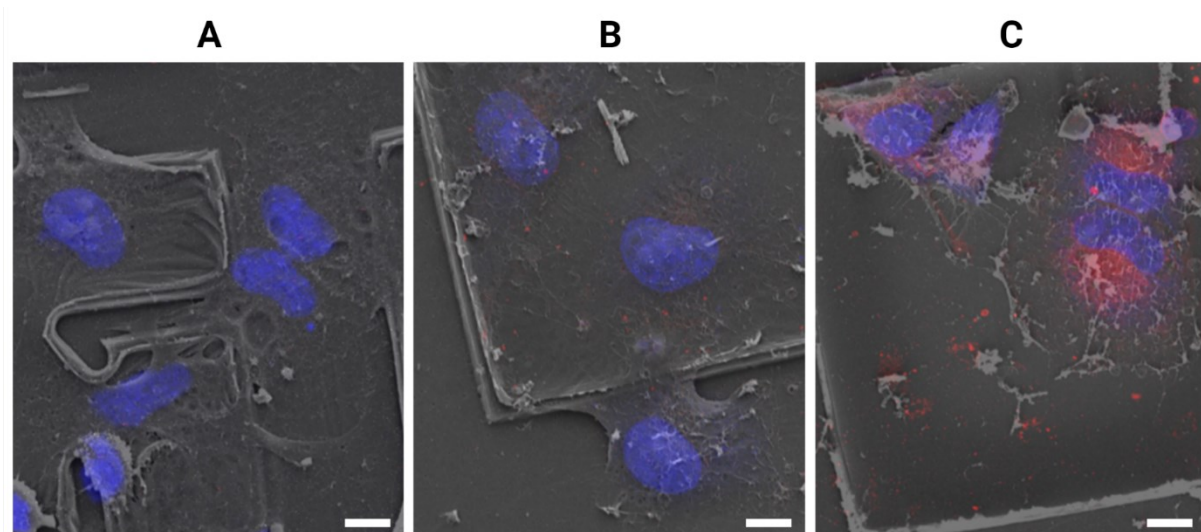


Figure 40. Example of CLSM-SEM on methacrylate printed grid. The blue color refers to DAPI nuclear staining while the red refers to the internalization of T-labeled liposomes. The correlation was performed by overlay with 50% transparency using the coordinates visible both in SEM and in the transmission image recorded with the confocal stack. A) Untreated control of human lung carcinoma A549. B) 24 h endpoint after T-Lip treatment. C) 24 h endpoint after co-treatment of T-Lip and cell-penetrating peptides. The scale bar refers to 10 μm . Pilot data to paper IV.

A final remark is now due. When resorting to electron microscopy in imaging protocols, sample preparation becomes particularly important to optimize and assess, as the fixation, dehydration, and even the imaging itself can induce artifacts in the specimen, especially if biological (Loussert Fonta, C. & Humbel B.M., 2015). Figure 41 shows examples of such artifacts, namely membrane bubbles (Figure 41A, fixation artifact), cell shrinkage and distortion (Figure 41B, fixation/drying artifact), stitching mismatch (Figure 41C, imaging

artifact due to tile acquisition in TEM), and charging artifacts (Figure 41D, imaging line artifact typical of thick samples imaged in SEM).

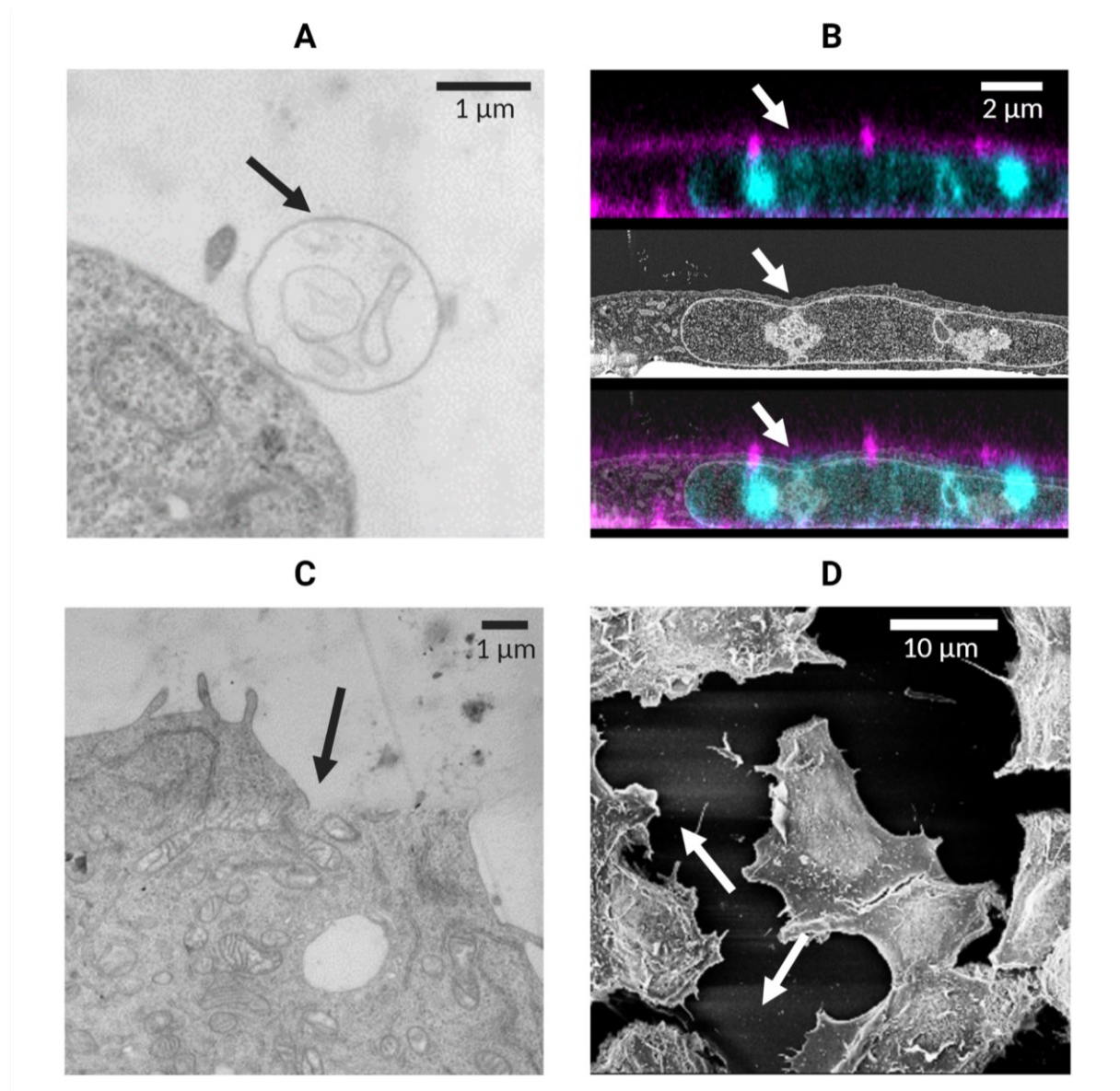


Figure 41. Examples of image artifacts. A) Membrane bubbles as fixation artifact. B) Cell shrinkage and distortions as fixation/drying artifact. C) Stitching mismatch as imaging artifact in TEM tile acquisition. D) Charging artifacts as typical SEM imaging artifact of gold/palladium-coated thick samples.

Considering the harsh processing that biological samples often require to be suitable for electron microscopy, the presence of some of these artifacts can never be fully eliminated. However, as for any method, the knowledge on its limitations is most valuable, not only to avoid false claims but also to confirm the truth.

5 Conclusions

This work actively expands the toolbox of available techniques for the characterization and tracking of nanocarriers, specifically considering advanced microscopy methods.

The use of fluorescence, often applied for nanocarrier tracking, was here harnessed for the characterization of nanocarriers, first in terms of physicochemical stability of the fluorescently labeled formulation (paper I), and then in terms of size estimation based on the image analysis of the fluorescence fluctuations in the sample (paper II). Furthermore, label-free imaging (here, quantitative phase microscopy) was first applied for the localization and characterization of sub-diffraction liposomes (paper III). The performance of the new techniques was compared to well established standards, indicating that the information obtained through new methods is complementary to the conventional methods. Finally, fluorescence-based and label-free imaging (here, confocal microscopy and scanning electron microscopy, respectively) were directly correlated to determine the integrity of liposomes in a dry secondary vehicle (nanofibers) used for topical administration (paper IV).

The internalization of liposomes in cells was followed by flow cytometry, as a high throughput technique, to derive the internalization kinetic and screen the relevant incubation endpoints (paper I). To determine the intracellular localization, both flow imaging and confocal microscopy were utilized. Furthermore, to contemporary assess the cell response to treatment in terms of organelles stress, transmission electron microscopy was used on the same samples imaged in confocal microscopy. Finally, volume correlation was attempted to directly correlate the fluorescence-based information on liposomal localization with the cellular ultrastructure morphology imaged in electron microscopy, discussing the benefits and limitations of the methods involved (paper IV).

6 Future Perspectives

Within the aim of expanding the toolbox of available methods for nanomedicine development, the results presented in this work are encouraging. The exponential method development, happening in different fields, can provide strong support for the characterization and in vitro testing of nanomedicine formulations, to better face in vivo challenges and clinical translation.

As this work modeled nanomedicine of vesicular nature, these results could first be transferred to other types of nanocarriers, especially to more rigid structures. In fact, the higher stability of these samples for imaging could potentially allow further morphological investigations, which are particularly relevant for the newer generations of nanomedicine.

To be able to reliably predict the in vivo fate of nanomedicine from in vitro settings, the implementation of the emerging technologies of organoids and organs-on-chip could be considered for more comprehensive preclinical studies. In fact, these cell culture models would allow for nanomedicine testing in co-culture and/or under flow conditions. The methods applied in this thesis could enable the evaluation of both nanocarrier and cellular state before and after treatment.

Furthermore, the expected next development in microscopy is based on the photonic chip technology, which is translating potent microscopes into small and widely affordable chips. As this thesis shows the important role of microscopy in understanding nanomedicine, achieving widespread availability of advanced microscopy would set the path for both scale-up within industrial settings and personalized medicine in hospital settings.

Each step brings us closer to the future; advanced microscopy offers us the lenses to see it.

7 References

- Abildgaard, J. T., Chung, A. S., Tokish, J. M., & Hattrup, S. J. (2019). Clinical Efficacy of Liposomal Bupivacaine: A Systematic Review of Prospective, Randomized Controlled Trials in Orthopaedic Surgery. *JBJS Rev*, 7(7), e8. doi:10.2106/JBJS.RVW.18.00192
- Adan, A., Alizada, G., Kiraz, Y., Baran, Y., & Nalbant, A. (2017). Flow cytometry: basic principles and applications. *Crit Rev Biotechnol*, 37(2), 163-176. doi:10.3109/07388551.2015.1128876
- Agarwal, A. (2020). A Review of FACS: Fluorescence Activated Cell Sorting System. *Biosci Biotechnol Res Commun*, 13(14), 436-439. doi:10.21786/bbrc/13.14/98
- Ahlers, M., Blankenburg, R., Haas, H., Möbius, D., Möhwald, H., Müller, W., . . . Siegmund, H. U. (1991). Protein interactions with ordered lipid films: Specific and unspecific binding. *Adv Mat*, 3(1), 39-46. doi:10.1002/adma.19910030108
- Ahmad, A., Dubey, V., Butola, A., Tinguely, J. C., Ahluwalia, B. S., & Mehta, D. S. (2020). Sub-nanometer height sensitivity by phase shifting interference microscopy under environmental fluctuations. *Opt Express*, 28(7), 9340-9358. doi:10.1364/OE.384259
- Ahmad, A., Dubey, V., Singh, G., Singh, V., & Mehta, D. S. (2016). Quantitative phase imaging of biological cells using spatially low and temporally high coherent light source. *Opt Lett*, 41(7), 1554-1557. doi:10.1364/OL.41.001554
- Ahmad, A., Mahanty, T., Dubey, V., Butola, A., Ahluwalia, B. S., & Mehta, D. S. (2019). Effect on the longitudinal coherence properties of a pseudothermal light source as a function of source size and temporal coherence. *Opt Lett*, 44(7), 1817-1820. doi:10.1364/OL.44.001817
- Ahmad Khanbeigi, R., Kumar, A., Sadouki, F., Lorenz, C., Forbes, B., Dailey, L. A., & Collins, H. (2012). The delivered dose: Applying particokinetics to in vitro investigations of nanoparticle internalization by macrophages. *J Control Release*, 162(2), 259-266. doi:10.1016/j.jconrel.2012.07.019
- Ahsan, F. (2002). Targeting to macrophages: role of physicochemical properties of particulate carriers—liposomes and microspheres—on the phagocytosis by macrophages. *J Control Release*, 79(1-3), 29-40. doi:10.1016/s0168-3659(01)00549-1
- Albanese, A., Tang, P. S., & Chan, W. C. (2012). The effect of nanoparticle size, shape, and surface chemistry on biological systems. *Annu Rev Biomed Eng*, 14, 1-16. doi:10.1146/annurev-bioeng-071811-150124
- Alhussan, A., Smazynski, J., & Chithrani, D. (2021). *Gold Nanoparticles Uptake in Monoculture vs Co-culture of Pancreatic Cancer Cells*. Paper presented at the 7th World Congress on New Technologies, Prague, Czech Republic (Virtual).
- Ameta, S. K., Rai, A. K., Hiran, D., Ameta, R., & Ameta, S. C. (2020). Use of nanomaterials in food science. In M. Ghorbanpour, P. Bhargava, A. Varma, & D. Choudhary (Eds.), *Biogenic Nano-Particles and their Use in Agro-ecosystems* (pp. 457). Singapore: Springer.
- Amoabediny, G., Haghirsadat, F., Naderinezhad, S., Helder, M. N., Akhouni Kharanaghi, E., Mohammadnejad Arough, J., & Zandieh-Doulabi, B. (2017). Overview of preparation methods of polymeric and lipid-based (niosome, solid lipid, liposome) nanoparticles: A comprehensive review. *Int J Polym Mater Polym Biomater*, 67(6), 383-400. doi:10.1080/00914037.2017.1332623

- Andrian, T., Delcanale, P., Pujals, S., & Albertazzi, L. (2021). Correlating Super-Resolution Microscopy and Transmission Electron Microscopy Reveals Multiparametric Heterogeneity in Nanoparticles. *Nano Lett*, 21(12), 5360-5368. doi:10.1021/acs.nanolett.1c01666
- Ansari, M. T., Ramlan, T. A., Jamaluddin, N. N., Zamri, N., Salfi, R., Khan, A., . . . Hasnain, M. S. (2020). Lipid-based Nanocarriers for Cancer and Tumor Treatment. *Curr Pharm Des*, 26(34), 4272-4276. doi:10.2174/1381612826666200720235752
- Antimisiaris, S. G., Marazioti, A., Kannavou, M., Natsaridis, E., Gkartziou, F., Kogkos, G., & Mourtas, S. (2021). Overcoming barriers by local drug delivery with liposomes. *Adv Drug Deliv Rev*, 174, 53-86. doi:10.1016/j.addr.2021.01.019
- Arbab, A. S., Bashaw, L. A., Miller, B. R., Jordan, E. K., Lewis, B. K., Kalish, H., & Frank, J. A. (2003). Characterization of biophysical and metabolic properties of cells labeled with superparamagnetic iron oxide nanoparticles and transfection agent for cellular MR imaging. *Radiology*, 229(3), 838-846. doi:10.1148/radiol.2293021215
- Axelrod, D. (2013). Evanescent excitation and emission in fluorescence microscopy. *Biophys J*, 104(7), 1401-1409. doi:10.1016/j.bpj.2013.02.044
- Azizipour, N., Avazpour, R., Rosenzweig, D. H., Sawan, M., & Ajji, A. (2020). Evolution of Biochip Technology: A Review from Lab-on-a-Chip to Organ-on-a-Chip. *Micromachines*, 11(6), 599. doi:10.3390/mi11060599
- Baboci, L., Capolla, S., Di Cintio, F., Colombo, F., Mauro, P., Dal Bo, M., . . . Macor, P. (2020). The Dual Role of the Liver in Nanomedicine as an Actor in the Elimination of Nanostructures or a Therapeutic Target. *J Oncol*, 2020, 4638192. doi:10.1155/2020/4638192
- Badekila, A. K., Kini, S., & Jaiswal, A. K. (2021). Fabrication techniques of biomimetic scaffolds in three-dimensional cell culture: A review. *J Cell Physiol*, 236(2), 741-762. doi:10.1002/jcp.29935
- Balasubramani, V., Kujawinska, M., Allier, C., Anand, V., Cheng, C. J., Depeursinge, C., . . . Ziemczonok, M. (2021). Roadmap on Digital Holography-Based Quantitative Phase Imaging. *J Imaging*, 7(12), 252. doi:10.3390/jimaging7120252
- Bangham, A. D., & Horne, R. (1964). Negative staining of phospholipids and their structural modification by surface-active agents as observed in the electron microscope. *J Mol Biol*, 8(5), 660-IN610. doi:10.1016/S0022-2836(64)80115-7
- Barkhudarov, E. M., Kossyi, I. A., Anpilov, A. M., Ivashkin, P. I., Artem'ev, K. V., Moryakov, I. V., . . . Smirnova, V. V. (2020). New nanostructured carbon coating inhibits bacterial growth, but does not influence on animal cells. *Nanomaterials*, 10(11), 2130. doi:10.3390/nano10112130
- Barnadas Rodriguez, R., & Sabes Xamani, M. (2003). Liposomes prepared by high-pressure homogenizers. *Methods Enzymol*, 367, 28-46. doi:10.1016/s0076-6879(03)67004-7
- Bassetti, M., Vena, A., Russo, A., & Peghin, M. (2020). Inhaled Liposomal Antimicrobial Delivery in Lung Infections. *Drugs*, 80(13), 1309-1318. doi:10.1007/s40265-020-01359-z
- Bertrand, N., & Leroux, J. C. (2012). The journey of a drug-carrier in the body: an anatomophysiological perspective. *J Control Release*, 161(2), 152-163. doi:10.1016/j.jconrel.2011.09.098

- Bhaduri, B., Edwards, C., Pham, H., Zhou, R., Nguyen, T. H., Goddard, L. L., & Popescu, G. (2014). Diffraction phase microscopy: principles and applications in materials and life sciences. *Adv Opt Photonics*, 6(1), 57-119. doi:10.1364/aop.6.000057
- Bhaduri, B., Pham, H., Mir, M., & Popescu, G. (2012). Diffraction phase microscopy with white light. *Opt Lett*, 37(6), 1094-1096. doi:10.1364/OL.37.001094
- Bhattacharjee, S. (2016). DLS and zeta potential - What they are and what they are not? *J Control Release*, 235, 337-351. doi:10.1016/j.jconrel.2016.06.017
- Bibi, S., Kaur, R., Henriksen-Lacey, M., McNeil, S. E., Wilkhu, J., Lattmann, E., . . . Perrie, Y. (2011). Microscopy imaging of liposomes: from coverslips to environmental SEM. *Int J Pharm*, 417(1-2), 138-150. doi:10.1016/j.ijpharm.2010.12.021
- Bonner, W. A., Hulett, H. R., Sweet, R. G., & Herzenberg, L. A. (1972). Fluorescence activated cell sorting. *Rev Sci Instrum*, 43(3), 404-409. doi:10.1063/1.1685647
- Boucrot, E., Ferreira, A. P., Almeida-Souza, L., Debard, S., Vallis, Y., Howard, G., . . . McMahon, H. T. (2015). Endophilin marks and controls a clathrin-independent endocytic pathway. *Nature*, 517(7535), 460-465. doi:10.1038/nature14067
- Bunker, A., Magarkar, A., & Viitala, T. (2016). Rational design of liposomal drug delivery systems, a review: Combined experimental and computational studies of lipid membranes, liposomes and their PEGylation. *Biochim Biophys Acta*, 1858(10), 2334-2352. doi:10.1016/j.bbamem.2016.02.025
- Butola, A., Popova, D., Prasad, D. K., Ahmad, A., Habib, A., Tinguely, J. C., . . . Ahluwalia, B. S. (2020). High spatially sensitive quantitative phase imaging assisted with deep neural network for classification of human spermatozoa under stressed condition. *Sci Rep*, 10(1), 13118. doi:10.1038/s41598-020-69857-4
- Chandrawati, R., Olesen, M. T., Marini, T. C., Bisra, G., Guex, A. G., de Oliveira, M. G., . . . Stevens, M. M. (2017). Enzyme prodrug therapy engineered into electrospun fibers with embedded liposomes for controlled, localized synthesis of therapeutics. *Adv Healthc Mater*, 6(17), 1700385. doi:10.1002/adhm.201700385
- Chatzikleantous, D., O'Hagan, D. T., & Adamo, R. (2021). Lipid-Based Nanoparticles for Delivery of Vaccine Adjuvants and Antigens: Toward Multicomponent Vaccines. *Mol Pharm*, 18(8), 2867-2888. doi:10.1021/acs.molpharmaceut.1c00447
- Chuang, S.-Y., Lin, C.-H., Huang, T.-H., & Fang, J.-Y. (2018). Lipid-based nanoparticles as a potential delivery approach in the treatment of rheumatoid arthritis. *Nanomaterials*, 8(1), 42. doi:10.3390/nano8010042
- Cohen, B. E. (2010). Biological imaging: Beyond fluorescence. *Nature*, 467(7314), 407-408. doi:10.1038/467407a
- Collins, A. R., Annangi, B., Rubio, L., Marcos, R., Dorn, M., Merker, C., . . . Dusinska, M. (2017). High throughput toxicity screening and intracellular detection of nanomaterials. *Wiley Interdiscip Rev Nanomed Nanobiotechnol*, 9(1), e1413. doi:10.1002/wnan.1413
- Cong, H., Wang, K., Zhou, Z., Yang, J., Piao, Y., Yu, B., . . . Zhou, Z. (2020). Tuning the Brightness and Photostability of Organic Dots for Multivalent Targeted Cancer Imaging and Surgery. *ACS Nano*, 14(5), 5887-5900. doi:10.1021/acsnano.0c01034
- Conrad, K. S., Cheng, T. W., Ysselstein, D., Heybrock, S., Hoth, L. R., Chrnyk, B. A., . . . Ehlers, M. D. (2017). Lysosomal integral membrane protein-2 as a phospholipid receptor revealed

- by biophysical and cellular studies. *Nat Commun*, 8(1), 1908. doi:10.1038/s41467-017-02044-8
- Cortizo, M. C., & Fernandez Lorenzo de Mele, M. (2004). Cytotoxicity of copper ions released from metal: variation with the exposure period and concentration gradients. *Biol Trace Elem Res*, 102(1-3), 129-141. doi:10.1385/bter:102:1-3:129
- Crommelin, D. J. A., van Hoogevest, P., & Storm, G. (2020). The role of liposomes in clinical nanomedicine development. What now? Now what? *J Control Release*, 318, 256-263. doi:10.1016/j.jconrel.2019.12.023
- Dai, Q., Bertleff-Zieschang, N., Braunger, J. A., Bjornmalm, M., Cortez-Jugo, C., & Caruso, F. (2018). Particle Targeting in Complex Biological Media. *Adv Healthc Mater*, 7(1), 1700575. doi:10.1002/adhm.201700575
- Danaei, M., Dehghankhold, M., Ataei, S., Hasanzadeh Davarani, F., Javanmard, R., Dokhani, A., . . . Mozafari, M. R. (2018). Impact of Particle Size and Polydispersity Index on the Clinical Applications of Lipidic Nanocarrier Systems. *Pharmaceutics*, 10(2), 57. doi:10.3390/pharmaceutics10020057
- de Waal, G. M., Engelbrecht, L., Davis, T., de Villiers, W. J. S., Kell, D. B., & Pretorius, E. (2018). Correlative Light-Electron Microscopy detects lipopolysaccharide and its association with fibrin fibres in Parkinson's Disease, Alzheimer's Disease and Type 2 Diabetes Mellitus. *Sci Rep*, 8(1), 16798. doi:10.1038/s41598-018-35009-y
- Demchenko, A. P. (2020). Photobleaching of organic fluorophores: quantitative characterization, mechanisms, protection. *Methods Appl Fluoresc*, 8(2), 022001. doi:10.1088/2050-6120/ab7365
- DeRose, J. A., & Doppler, M. (2018). Guidelines for understanding magnification in the modern digital microscope era. *Micros Today*, 26(4), 20-33. doi:10.1017/S1551929518000688
- Dertinger, T., Colyer, R., Iyer, G., Weiss, S., & Enderlein, J. (2009). Fast, background-free, 3D super-resolution optical fluctuation imaging (SOFI). *Proc Natl Acad Sci U S A*, 106(52), 22287-22292. doi:10.1073/pnas.0907866106
- Dhaval, M., Vaghela, P., Patel, K., Sojitra, K., Patel, M., Patel, S., . . . Parmar, R. (2021). Lipid-based emulsion drug delivery systems - a comprehensive review. *Drug Deliv Transl Res*. doi:10.1007/s13346-021-01071-9
- Dlugolecka, M., Szymanski, J., Zareba, L., Homoncik, Z., Domagala-Kulawik, J., Polubiec-Kownacka, M., & Czystowska-Kuzmicz, M. (2021). Characterization of Extracellular Vesicles from Bronchoalveolar Lavage Fluid and Plasma of Patients with Lung Lesions Using Fluorescence Nanoparticle Tracking Analysis. *Cells*, 10(12), 3473. doi:10.3390/cells10123473
- Ducat, E., Evrard, B., Peulen, O., & Piel, G. (2011). Cellular uptake of liposomes monitored by confocal microscopy and flow cytometry. *J Drug Deliv Sci Technol*, 21(6), 469-477. doi:10.1016/s1773-2247(11)50076-0
- Duong, V. A., Nguyen, T. T., & Maeng, H. J. (2020). Preparation of Solid Lipid Nanoparticles and Nanostructured Lipid Carriers for Drug Delivery and the Effects of Preparation Parameters of Solvent Injection Method. *Molecules*, 25(20), 4781. doi:10.3390/molecules25204781

- Eaton, P., Quaresma, P., Soares, C., Neves, C., de Almeida, M. P., Pereira, E., & West, P. (2017). A direct comparison of experimental methods to measure dimensions of synthetic nanoparticles. *Ultramicroscopy*, *182*, 179-190. doi:10.1016/j.ultramic.2017.07.001
- Emad, N. A., Ahmed, B., Alhalimi, A., Alzobaidi, N., & Al-Kubati, S. S. (2021). Recent progress in nanocarriers for direct nose to brain drug delivery. *J Drug Deliv Sci Technol*, *64*, 102642. doi:10.1016/j.jddst.2021.102642
- Fan, J., Huang, X., Li, L., Tan, S., & Chen, L. (2019). A protocol for structured illumination microscopy with minimal reconstruction artifacts. *Biophys Rep*, *5*(2), 80-90. doi:10.1007/s41048-019-0081-7
- Fan, Z., Zhu, P., Zhu, Y., Wu, K., Li, C. Y., & Cheng, H. (2020). Engineering long-circulating nanomaterial delivery systems. *Curr Opin Biotechnol*, *66*, 131-139. doi:10.1016/j.copbio.2020.07.006
- Faouzi, A., & Roullin, V. G. (2021). Think big, start small: how nanomedicine could alleviate the burden of rare CNS diseases. *Pharmaceuticals*, *14*(2), 109. doi:10.3390/ph14020109
- Ferreira, M., Ogren, M., Dias, J. N. R., Silva, M., Gil, S., Tavares, L., . . . Aguiar, S. I. (2021). Liposomes as Antibiotic Delivery Systems: A Promising Nanotechnological Strategy against Antimicrobial Resistance. *Molecules*, *26*(7), 2047. doi:10.3390/molecules26072047
- Feynman, R. (1991). There's plenty of room at the bottom. *Science*, *254*(5036), 1300-1301.
- Florence, A. T. (2012a). Reductionism and complexity in nanoparticle-vectored drug targeting. *J Control Release*, *161*(2), 399-402. doi:10.1016/j.jconrel.2011.11.005
- Florence, A. T. (2012b). "Targeting" nanoparticles: the constraints of physical laws and physical barriers. *J Control Release*, *164*(2), 115-124. doi:10.1016/j.jconrel.2012.03.022
- Fontana, F., Figueiredo, P., Martins, J. P., & Santos, H. A. (2021). Requirements for Animal Experiments: Problems and Challenges. *Small*, *17*(15), e2004182. doi:10.1002/smll.202004182
- Fontana, F., Figueiredo, P., Zhang, P., Hirvonen, J. T., Liu, D., & Santos, H. A. (2018). Production of pure drug nanocrystals and nano co-crystals by confinement methods. *Adv Drug Deliv Rev*, *131*, 3-21. doi:10.1016/j.addr.2018.05.002
- Foroozandeh, P., & Aziz, A. A. (2018). Insight into cellular uptake and intracellular trafficking of nanoparticles. *Nanoscale Res Lett*, *13*(1), 1-12. doi:10.1186/s11671-018-2728-6
- Foulkes, R., Man, E., Thind, J., Yeung, S., Joy, A., & Hoskins, C. (2020). The regulation of nanomaterials and nanomedicines for clinical application: current and future perspectives. *Biomater Sci*, *8*(17), 4653-4664. doi:10.1039/d0bm00558d
- Freitas, C., & Müller, R. H. (1998). Spray-drying of solid lipid nanoparticles (SLNTM). *Eur J Pharm Biopharm*, *46*(2), 145-151. doi:10.1016/S0939-6411(97)00172-0
- Freitas, R. A., Jr. (2005). What is nanomedicine? *Nanomedicine*, *1*(1), 2-9. doi:10.1016/j.nano.2004.11.003
- Fröhlich, E. (2012). The role of surface charge in cellular uptake and cytotoxicity of medical nanoparticles. *Int J Nanomedicine*, *7*, 5577-5591. doi:10.2147/IJN.S36111
- Fu, X., Cai, J., Zhang, X., Li, W. D., Ge, H., & Hu, Y. (2018). Top-down fabrication of shape-controlled, monodisperse nanoparticles for biomedical applications. *Adv Drug Deliv Rev*, *132*, 169-187. doi:10.1016/j.addr.2018.07.006

- Fytianos, G., Rahdar, A., & Kyzas, G. Z. (2020). Nanomaterials in Cosmetics: Recent Updates. *Nanomaterials*, *10*(5), 979. doi:10.3390/nano10050979
- Gadekar, V., Borade, Y., Kannaujia, S., Rajpoot, K., Anup, N., Tambe, V., . . . Tekade, R. K. (2021). Nanomedicines accessible in the market for clinical interventions. *J Control Release*, *330*, 372-397. doi:10.1016/j.jconrel.2020.12.034
- Gao, W., Chen, Y., Zhang, Y., Zhang, Q., & Zhang, L. (2018). Nanoparticle-based local antimicrobial drug delivery. *Adv Drug Deliv Rev*, *127*, 46-57. doi:10.1016/j.addr.2017.09.015
- Georgieva, V., Petrov, P., Mironov, R., & Mihaylova, A. (2019). *An approach for microscopy image restoration*. Paper presented at the Proceedings of the Eighth International Conference on Telecommunications and Remote Sensing.
- Germain, M., Caputo, F., Metcalfe, S., Tosi, G., Spring, K., Aslund, A. K. O., . . . Schmid, R. (2020). Delivering the power of nanomedicine to patients today. *J Control Release*, *326*, 164-171. doi:10.1016/j.jconrel.2020.07.007
- Giordani, B., Basnet, P., Mishchenko, E., Luppi, B., & Skalko-Basnet, N. (2019). Utilizing Liposomal Quercetin and Gallic Acid in Localized Treatment of Vaginal Candida Infections. *Pharmaceutics*, *12*(1), 9. doi:10.3390/pharmaceutics12010009
- Gioria, S., Caputo, F., Urbán, P., Maguire, C. M., Bremer-Hoffmann, S., Prina-Mello, A., . . . Mehn, D. (2018). Are existing standard methods suitable for the evaluation of nanomedicines: some case studies. *Nanomedicine*, *13*(5), 539-554. doi:10.2217/nnm-2017-0338
- Grabar, K. C., Brown, K. R., Keating, C. D., Stranick, S. J., Tang, S. L., & Natan, M. J. (1997). Nanoscale characterization of gold colloid monolayers: a comparison of four techniques. *Anal Chem*, *69*(3), 471-477. doi:10.1021/ac9605962
- Gregoriadis, G. (1973). Drug entrapment in liposomes. *FEBS Lett*, *36*(3), 292-296. doi:10.1016/0014-5793(73)80394-1
- Grimm, J. B., Tkachuk, A. N., Xie, L., Choi, H., Mohar, B., Falco, N., . . . Lavis, L. D. (2020). A general method to optimize and functionalize red-shifted rhodamine dyes. *Nat Methods*, *17*(8), 815-821. doi:10.1038/s41592-020-0909-6
- Guilbault, G. G. (2020). *Practical fluorescence*. In G. G. Guilbault (Ed.), *Modern monographs in analytical chemistry*. 2nd Edition, New York: CRC Press.
- Guimarães, D., Cavaco-Paulo, A., & Nogueira, E. (2021). Design of liposomes as drug delivery system for therapeutic applications. *Int J Pharm*, *601*, 120571. doi:10.1016/j.ijpharm.2021.120571
- Gulin-Sarfraz, T., Pryazhnikov, E., Zhang, J., Khiroug, L., & Rosenholm, J. M. (2019). Chemical and photonic interactions in vitro and in vivo between fluorescent tracer and nanoparticle-based scavenger for enhanced molecular imaging. *Mater Today Bio*, *2*, 100010. doi:10.1016/j.mtbio.2019.100010
- Gustafsson, N., Culley, S., Ashdown, G., Owen, D. M., Pereira, P. M., & Henriques, R. (2016). Fast live-cell conventional fluorophore nanoscopy with ImageJ through super-resolution radial fluctuations. *Nat Commun*, *7*(1), 12471. doi:10.1038/ncomms12471

- Haddadzadegan, S., Dorkoosh, F., & Bernkop-Schnurch, A. (2022). Oral delivery of therapeutic peptides and proteins: Technology landscape of lipid-based nanocarriers. *Adv Drug Deliv Rev*, *182*, 114097. doi:10.1016/j.addr.2021.114097
- Halamoda-Kenzaoui, B., Baconnier, S., Bastogne, T., Bazile, D., Boisseau, P., Borchard, G., . . . Bremer-Hoffmann, S. (2019). Bridging communities in the field of nanomedicine. *Regul Toxicol Pharmacol*, *106*, 187-196. doi:10.1016/j.yrtph.2019.04.011
- Hamza, E. K., & Jaafar, S. N. (2022). Nanotechnology Application for Wireless Communication System. In *Nanotechnology for Electronic Applications* (Eds. Mubarak, Gopi, Balakrishnan) (pp. 115-130) Singapore: Springer.
- Hassan, P. A., Rana, S., & Verma, G. (2015). Making sense of Brownian motion: colloid characterization by dynamic light scattering. *Langmuir*, *31*(1), 3-12. doi:10.1021/la501789z
- Hell, S. W., & Wichmann, J. (1994). Breaking the diffraction resolution limit by stimulated emission: stimulated-emission-depletion fluorescence microscopy. *Opt Lett*, *19*(11), 780-782. doi:10.1364/ol.19.000780
- Hemmingsen, L. M., Giordani, B., Pettersen, A. K., Vitali, B., Basnet, P., & Skalko-Basnet, N. (2021). Liposomes-in-chitosan hydrogel boosts potential of chlorhexidine in biofilm eradication in vitro. *Carbohydr Polym*, *262*, 117939. doi:10.1016/j.carbpol.2021.117939
- Herschel, J. F. W. (1845). On a case of superficial colour presented by a homogeneous liquid internally colourless. *Philos Trans R Soc Lond*(135), 143-145. doi:10.1098/rstl.1845.0004
- Hua, S., & Wu, S. Y. (2013). The use of lipid-based nanocarriers for targeted pain therapies. *Front Pharmacol*, *4*, 143. doi:10.3389/fphar.2013.00143
- Huda, S., Alam, M. A., & Sharma, P. K. (2020). Smart nanocarriers-based drug delivery for cancer therapy: an innovative and developing strategy. *J Drug Deliv Sci Technol*, 102018.
- Huff, J. (2015). The Airyscan detector from ZEISS: confocal imaging with improved signal-to-noise ratio and super-resolution. *Nat Methods*, *12*(12), i-ii. doi:10.1038/nmeth.f.388
- Ingebrigtsen, S. G., Didriksen, A., Johannessen, M., Skalko-Basnet, N., & Holsaeter, A. M. (2017). Old drug, new wrapping - A possible comeback for chloramphenicol? *Int J Pharm*, *526*(1-2), 538-546. doi:10.1016/j.ijpharm.2017.05.025
- Ishida, T., Harashima, H., & Kiwada, H. (2002). Liposome clearance. *Biosci Rep*, *22*(2), 197-224. doi:10.1023/a:1020134521778
- Jaganan, K., & Singh, M. (2021). Nanomedicine for Neurodegenerative Disorders: Focus on Alzheimer's and Parkinson's Diseases. *Int J Mol Sci*, *22*(16), 9082. doi:10.3390/ijms22169082
- Jameson, D. M. (2014). *Introduction to fluorescence*. Boca Raton CRC Press.
- Jarzębski, M., Bellich, B., Białopiotrowicz, T., Śliwa, T., Kościński, J., & Cesàro, A. (2017). Particle tracking analysis in food and hydrocolloids investigations. *Food Hydrocoll*, *68*, 90-101. doi:10.1016/j.foodhyd.2016.09.037
- Jash, A., Ubeyitogullari, A., & Rizvi, S. S. H. (2021). Liposomes for oral delivery of protein and peptide-based therapeutics: challenges, formulation strategies, and advances. *J Mater Chem B*, *9*(24), 4773-4792. doi:10.1039/d1tb00126d
- Jayakumar, N., Dullo, F. T., Dubey, V., Ahmad, A. A., Cauzzo, J., Guerreiro, E. M., . . . Ahluwalia, B. S. (2021). Label-free chip-based evanescent light scattering super-resolution

- and superior-contrast optical microscopy (cELS). *arXiv preprint arXiv:2108.10575*. doi:10.48550/arXiv.2108.10575
- Jensen, G. M., & Hodgson, D. F. (2020). Opportunities and challenges in commercial pharmaceutical liposome applications. *Adv Drug Deliv Rev*, 154-155, 2-12. doi:10.1016/j.addr.2020.07.016
- Jeong, D., & Kim, D. (2022). Recent Developments in Correlative Super-Resolution Fluorescence Microscopy and Electron Microscopy. *Mol Cells*, 45(1), 41-50. doi:10.14348/molcells.2021.5011
- Jonkman, J., Brown, C. M., Wright, G. D., Anderson, K. I., & North, A. J. (2020). Tutorial: guidance for quantitative confocal microscopy. *Nat Protoc*, 15(5), 1585-1611. doi:10.1038/s41596-020-0313-9
- Jøraholmen, M. W., Basnet, P., Acharya, G., & Skalko-Basnet, N. (2017). PEGylated liposomes for topical vaginal therapy improve delivery of interferon alpha. *Eur J Pharm Biopharm*, 113, 132-139. doi:10.1016/j.ejpb.2016.12.029
- Jøraholmen, M. W., Johannessen, M., Gravningen, K., Puolakkainen, M., Acharya, G., Basnet, P., & Skalko-Basnet, N. (2020). Liposomes-In-Hydrogel Delivery System Enhances the Potential of Resveratrol in Combating Vaginal Chlamydia Infection. *Pharmaceutics*, 12(12). doi:10.3390/pharmaceutics12121203
- Jøraholmen, M. W., Vanic, Z., Tho, I., & Skalko-Basnet, N. (2014). Chitosan-coated liposomes for topical vaginal therapy: assuring localized drug effect. *Int J Pharm*, 472(1-2), 94-101. doi:10.1016/j.ijpharm.2014.06.016
- Jradi, F. M., & Lavis, L. D. (2019). Chemistry of Photosensitive Fluorophores for Single-Molecule Localization Microscopy. *ACS Chem Biol*, 14(6), 1077-1090. doi:10.1021/acscchembio.9b00197
- Kaasalainen, M., Aseyev, V., von Haartman, E., Karaman, D. S., Makila, E., Tenhu, H., . . . Salonen, J. (2017). Size, Stability, and Porosity of Mesoporous Nanoparticles Characterized with Light Scattering. *Nanoscale Res Lett*, 12(1), 74. doi:10.1186/s11671-017-1853-y
- Kalina, T. (2020). Reproducibility of flow cytometry through standardization: opportunities and challenges. *Cytometry A*, 97(2), 137-147. doi:10.1002/cyto.a.23901
- Kamali Shahri, S. M., Sharifi, S., & Mahmoudi, M. (2021). Interdependency of influential parameters in therapeutic nanomedicine. *Expert Opin Drug Deliv*, 18(10), 1379-1394. doi:10.1080/17425247.2021.1921732
- Kargozar, S., & Mozafari, M. (2018). Nanotechnology and Nanomedicine: Start small, think big. *Mat Today-Proc*, 5(7), 15492-15500. doi:DOI 10.1016/j.matpr.2018.04.155
- Kasten, F. H. (1989). The Origins of Modern Fluorescence Microscopy and Fluorescent Probes. In E. Kohen and J.G. Hirschberg (Ed.), *Cell Structure and Function by Microspectrofluorometry* (pp. 3-50) San Diego: Academic Press.
- Kay, J. G., Koivusalo, M., Ma, X., Wohland, T., & Grinstein, S. (2012). Phosphatidylserine dynamics in cellular membranes. *Mol Biol Cell*, 23(11), 2198-2212. doi:10.1091/mbc.E11-11-0936
- Khadke, S., Stone, P., Rozhin, A., Kroonen, J., & Perrie, Y. (2018). Point of use production of liposomal solubilised products. *Int J Pharm*, 537(1-2), 1-8. doi:10.1016/j.ijpharm.2017.12.012

- Khan, K. U., Minhas, M. U., Badshah, S. F., Suhail, M., Ahmad, A., & Ijaz, S. (2022). Overview of nanoparticulate strategies for solubility enhancement of poorly soluble drugs. *Life Sci*, 291, 120301. doi:10.1016/j.lfs.2022.120301
- Khan, M. M., Filipczak, N., & Torchilin, V. P. (2021). Cell penetrating peptides: A versatile vector for co-delivery of drug and genes in cancer. *J Control Release*, 330, 1220-1228. doi:10.1016/j.jconrel.2020.11.028
- Kilian, N., Goryaynov, A., Lessard, M. D., Hooker, G., Toomre, D., Rothman, J. E., & Bewersdorf, J. (2018). Assessing photodamage in live-cell STED microscopy. *Nat Methods*, 15(10), 755-756. doi:10.1038/s41592-018-0145-5
- Kim, A., Ng, W. B., Bernt, W., & Cho, N. J. (2019). Validation of Size Estimation of Nanoparticle Tracking Analysis on Polydisperse Macromolecule Assembly. *Sci Rep*, 9(1), 2639. doi:10.1038/s41598-019-38915-x
- King, M. A. (2000). Detection of dead cells and measurement of cell killing by flow cytometry. *J Immunol Methods*, 243(1-2), 155-166. doi:10.1016/s0022-1759(00)00232-5
- Kozlova, A. A., Verkhovskii, R. A., Ermakov, A. V., & Bratashov, D. N. (2020). Changes in Autofluorescence Level of Live and Dead Cells for Mouse Cell Lines. *J Fluoresc*, 30(6), 1483-1489. doi:10.1007/s10895-020-02611-1
- Kuriyama, T., Fukuma, Y., Imashiro, C., Kabayama, K., Kurashina, Y., & Takemura, K. (2021). Detachment of RAW264. 7 macrophages from a culture dish using ultrasound excited by a Langevin transducer. *J Biosci Bioeng*, 131(3), 320-325. doi:10.1016/j.jbiosc.2020.11.003
- Kuznetsova, D. A., Vasileva, L. A., Gaynanova, G. A., Pavlov, R. V., Sapunova, A. S., Voloshina, A. D., . . . Sinyashin, O. G. (2021). Comparative study of cationic liposomes modified with triphenylphosphonium and imidazolium surfactants for mitochondrial delivery. *J Mol Liq*, 330. doi:10.1016/j.molliq.2021.115703
- Kyrychenko, A. (2015). Using fluorescence for studies of biological membranes: a review. *Methods Appl Fluoresc*, 3(4), 042003. doi:10.1088/2050-6120/3/4/042003
- Laissue, P. P., Alghamdi, R. A., Tomancak, P., Reynaud, E. G., & Shroff, H. (2017). Assessing phototoxicity in live fluorescence imaging. *Nat Methods*, 14(7), 657-661. doi:10.1038/nmeth.4344
- Lakowicz, J. R. (1999). Introduction to fluorescence. In J. R. Lakowicz (Ed.), *Principles of fluorescence spectroscopy* (pp. 1-23). Boston: Springer.
- Lakshminarayan, R., Wunder, C., Becken, U., Howes, M. T., Benzing, C., Arumugam, S., . . . Johannes, L. (2014). Galectin-3 drives glycosphingolipid-dependent biogenesis of clathrin-independent carriers. *Nat Cell Biol* 16(6), 592-603. doi:10.1038/ncb2970
- Lammers, T., & Ferrari, M. (2020). The success of nanomedicine. *Nano Today*, 31. doi:10.1016/j.nantod.2020.100853
- Large, D. E., Abdelmessih, R. G., Fink, E. A., & Auguste, D. T. (2021). Liposome composition in drug delivery design, synthesis, characterization, and clinical application. *Adv Drug Deliv Rev*, 176, 113851. doi:10.1016/j.addr.2021.113851
- Lemon, W. C., & McDole, K. (2020). Live-cell imaging in the era of too many microscopes. *Curr Opin Cell Biol*, 66, 34-42. doi:10.1016/j.ceb.2020.04.008

- Li, H., & Vaughan, J. C. (2018). Switchable Fluorophores for Single-Molecule Localization Microscopy. *Chem Rev*, *118*(18), 9412-9454. doi:10.1021/acs.chemrev.7b00767
- Li, X., Liu, W., Sun, L., Aifantis, K. E., Yu, B., Fan, Y., . . . Watari, F. (2015). Effects of physicochemical properties of nanomaterials on their toxicity. *J Biomed Mater Res A*, *103*(7), 2499-2507. doi:10.1002/jbm.a.35384
- Lichtman, J. W., & Conchello, J. A. (2005). Fluorescence microscopy. *Nat Methods*, *2*(12), 910-919. doi:10.1038/nmeth817
- Lim, J. P., & Gleeson, P. A. (2011). Macropinocytosis: an endocytic pathway for internalising large gulps. *Immunol Cell Biol*, *89*(8), 836-843. doi:10.1038/icb.2011.20
- Liu, D., Chen, S., & Win Naing, M. (2021). A review of manufacturing capabilities of cell spheroid generation technologies and future development. *Biotechnol Bioeng*, *118*(2), 542-554. doi:10.1002/bit.27620
- Loussert Fonta, C., & Humbel, B. M. (2015). Correlative microscopy. *Arch Biochem Biophys*, *581*, 98-110. doi:10.1016/j.abb.2015.05.017
- Luckner, M., & Wanner, G. (2018). Precise and economic FIB/SEM for CLEM: with 2 nm voxels through mitosis. *Histochem Cell Biol*, *150*(2), 149-170. doi:10.1007/s00418-018-1681-x
- Luraghi, A., Peri, F., & Moroni, L. (2021). Electrospinning for drug delivery applications: A review. *J Control Release*, *334*, 463-484. doi:10.1016/j.jconrel.2021.03.033
- Luther, E., Mendes, L. P., Pan, J., Costa, D. F., & Torchilin, V. P. (2017). Applications of label-free, quantitative phase holographic imaging cytometry to the development of multi-specific nanoscale pharmaceutical formulations. *Cytometry A*, *91*(5), 412-423. doi:10.1002/cyto.a.23102
- Maguire, C. M., Rosslein, M., Wick, P., & Prina-Mello, A. (2018). Characterisation of particles in solution - a perspective on light scattering and comparative technologies. *Sci Technol Adv Mater*, *19*(1), 732-745. doi:10.1080/14686996.2018.1517587
- Maguire, C. M., Sillence, K., Roesslein, M., Hannell, C., Suarez, G., Sauvain, J.-J., . . . El Yamani, N. (2017). Benchmark of nanoparticle tracking analysis on measuring nanoparticle sizing and concentration. *J Micro Nano-Manuf*, *5*(4). doi:10.1115/1.4037124
- Mahmoudi, M. (2021). The need for robust characterization of nanomaterials for nanomedicine applications. *Nat Commun*, *12*(1), 5246. doi:10.1038/s41467-021-25584-6
- Malatesta, M. (2016). Transmission electron microscopy for nanomedicine: novel applications for long-established techniques. *Eur J Histochem*, *60*(4), 2751. doi:10.4081/ejh.2016.2751
- Mäntele, W., & Deniz, E. (2017). UV–VIS absorption spectroscopy: Lambert-Beer reloaded. *Spectrochim Acta A Mol Biomol Spectrosc*, *173*, 965-968. doi:10.1016/j.saa.2016.09.037
- Manzanares, D., & Cena, V. (2020). Endocytosis: The Nanoparticle and Submicron Nanocompounds Gateway into the Cell. *Pharmaceutics*, *12*(4). doi:10.3390/pharmaceutics12040371
- Martins, J. P., das Neves, J., de la Fuente, M., Celia, C., Florindo, H., Gunday-Tureli, N., . . . Santos, H. A. (2020). The solid progress of nanomedicine. *Drug Deliv Transl Res*, *10*(3), 726-729. doi:10.1007/s13346-020-00743-2

- Massing, U., Cicko, S., & Zirolì, V. (2008). Dual asymmetric centrifugation (DAC)--a new technique for liposome preparation. *J Control Release*, *125*(1), 16-24. doi:10.1016/j.jconrel.2007.09.010
- Mayhew, E., Lazo, R., Vail, W. J., King, J., & Green, A. M. (1984). Characterization of liposomes prepared using a microemulsifier. *Biochim Biophys Acta Biomembr*, *775*(2), 169-174. doi:10.1016/0005-2736(84)90167-6
- Maznev, A. A., & Wright, O. B. (2017). Upholding the diffraction limit in the focusing of light and sound. *Wave Motion*, *68*, 182-189. doi:10.1016/j.wavemoti.2016.09.012
- Melo, M., Nunes, R., Sarmiento, B., & das Neves, J. (2018). Rectal administration of nanosystems: from drug delivery to diagnostics. *Mater Today Chem*, *10*, 128-141. doi:10.1016/j.mtchem.2018.09.001
- Meng, H., Leong, W., Leong, K. W., Chen, C., & Zhao, Y. (2018). Walking the line: The fate of nanomaterials at biological barriers. *Biomaterials*, *174*, 41-53. doi:10.1016/j.biomaterials.2018.04.056
- Merza, K. S., Al-Attabi, H. D., Abbas, Z. M., & Yusr, H. A. (2012). Comparative study on methods for preparation of gold nanoparticles. *Green Sustain Chem*, *2*(1), 26-28. doi:10.4236/gsc.2012.21005
- Michaelides, E. E. (2015). Brownian movement and thermophoresis of nanoparticles in liquids. *Int J Heat Mass Transf*, *81*, 179-187. doi:j.ijheatmasstransfer.2014.10.019
- Mickova, A., Buzgo, M., Benada, O., Rampichova, M., Fisar, Z., Filova, E., . . . Amler, E. (2012). Core/shell nanofibers with embedded liposomes as a drug delivery system. *Biomacromolecules*, *13*(4), 952-962. doi:10.1021/bm2018118
- Mir, M., Bhaduri, B., Wang, R., Zhu, R., & Popescu, G. (2012). *Quantitative phase imaging* (Vol. 57) Amsterdam: Elsevier
- Mishra, D. K., Shandilya, R., & Mishra, P. K. (2018). Lipid based nanocarriers: a translational perspective. *Nanomedicine*, *14*(7), 2023-2050. doi:10.1016/j.nano.2018.05.021
- Möckl, L., Lamb, D. C., & Brauchle, C. (2014). Super-resolved fluorescence microscopy: Nobel Prize in Chemistry 2014 for Eric Betzig, Stefan Hell, and William E. Moerner. *Angew Chem Int Ed Engl*, *53*(51), 13972-13977. doi:10.1002/anie.201410265
- Modena, M. M., Rühle, B., Burg, T. P., & Wuttke, S. (2019). Nanoparticle characterization: what to measure? *Advanced Materials*, *31*(32), 1901556. doi:10.1002/adma.201901556
- Mohamed, M., Alaaeldin, E., Hussein, A., & A Sarhan, H. (2020). Liposomes and PEGylated liposomes as drug delivery system. *J Adv Biomed Pharmaceut Sci*, *3*(2), 80-88. doi:10.21608/JABPS.2020.22937.1068
- Mohammed, A., & Abdullah, A. (2018). *Scanning electron microscopy (SEM): A review*. Paper presented at the Proceedings of the 2018 International Conference on Hydraulics and Pneumatics—HERVEX, Băile Govora, Romania.
- Monici, M. (2005). Cell and tissue autofluorescence research and diagnostic applications. In *Biotechnology Annual Review* (Vol. 11, pp. 227-256) Biotechnol Annu Rev, *11*, 227-56. Doi: 10.1016/S1387-2656(05)11007-2

- Mortensen, K. I., Tassone, C., Ehrlich, N., Andresen, T. L., & Flyvbjerg, H. (2018). How To Characterize Individual Nanosize Liposomes with Simple Self-Calibrating Fluorescence Microscopy. *Nano Lett*, *18*(5), 2844-2851. doi:10.1021/acs.nanolett.7b05312
- Mostafavi Yazdi, S. J., & Baqersad, J. (2022). Mechanical modeling and characterization of human skin: A review. *J Biomech*, *130*, 110864. doi:10.1016/j.jbiomech.2021.110864
- Münter, R., Kristensen, K., Pedersbaek, D., Larsen, J. B., Simonsen, J. B., & Andresen, T. L. (2018). Dissociation of fluorescently labeled lipids from liposomes in biological environments challenges the interpretation of uptake studies. *Nanoscale*, *10*(48), 22720-22724. doi:10.1039/c8nr07755j
- Münter, R., Stavnsbjerg, C., Christensen, E., Thomsen, M. E., Stensballe, A., Hansen, A. E., . . . Andresen, T. L. (2022). Unravelling Heterogeneities in Complement and Antibody Opsonization of Individual Liposomes as a Function of Surface Architecture. *Small*, e2106529. doi:10.1002/smll.202106529
- Murphy, D. B., & Davidson, M. W. (2012). *Fundamentals of Light Microscopy and Electronic Imaging* (2nd Edition ed.) New Jersey: Wiley-Blackwell.
- Mydin, R. B. S. M. N., & Moshawih, S. (2019). Nanoparticles in Nanomedicine Application: Lipid-Based Nanoparticles and Their Safety Concerns. In S. Siddiquee, G. J. H. Melvin, & M. M. Rahman (Eds.), *Nanotechnology: Applications in Energy, Drug and Food* (pp. 227-232). Cham: Springer International Publishing.
- Niedergang, F., & Grinstein, S. (2018). How to build a phagosome: new concepts for an old process. *Curr Opin Cell Biol*, *50*, 57-63. doi:10.1016/j.ceb.2018.01.009
- Niu, G., Zhang, R., Gu, Y., Wang, J., Ma, C., Kwok, R. T. K., . . . Tang, B. Z. (2019). Highly photostable two-photon NIR AIEgens with tunable organelle specificity and deep tissue penetration. *Biomaterials*, *208*, 72-82. doi:10.1016/j.biomaterials.2019.04.002
- Obuobi, S., Ngoc Phung, A., Julin, K., Johannessen, M., & Skalko-Basnet, N. (2022). Biofilm Responsive Zwitterionic Antimicrobial Nanoparticles to Treat Cutaneous Infection. *Biomacromolecules*, *23*(1), 303-315. doi:10.1021/acs.biomac.1c01274
- Ong, S. G., Chitneni, M., Lee, K. S., Ming, L. C., & Yuen, K. H. (2016). Evaluation of Extrusion Technique for Nanosizing Liposomes. *Pharmaceutics*, *8*(4). doi:10.3390/pharmaceutics8040036
- Opstad, I. S., Popova, D. A., Acharya, G., Basnet, P., & Ahluwalia, B. S. (2018). Live-cell imaging of human spermatozoa using structured illumination microscopy. *Biomed Opt Express*, *9*(12), 5939-5945. doi:10.1364/BOE.9.005939
- Ouyang, B., Poon, W., Zhang, Y. N., Lin, Z. P., Kingston, B. R., Tavares, A. J., . . . Chan, W. C. W. (2020). The dose threshold for nanoparticle tumour delivery. *Nat Mater*, *19*(12), 1362-1371. doi:10.1038/s41563-020-0755-z
- Paini, M., Daly, S. R., Aliakbarian, B., Fathi, A., Tehrany, E. A., Perego, P., . . . Valtchev, P. (2015). An efficient liposome based method for antioxidants encapsulation. *Colloids Surf B Biointerfaces*, *136*, 1067-1072. doi:10.1016/j.colsurfb.2015.10.038
- Pantanowitz, L., Preffer, F., & Wilbur, D. C. (2019). Advanced imaging technology applications in cytology. *Diagn Cytopathol*, *47*(1), 5-14. doi:10.1002/dc.23898
- Park, H., Otte, A., & Park, K. (2022). Evolution of drug delivery systems: From 1950 to 2020 and beyond. *J Control Release*, *342*, 53-65. doi:10.1016/j.jconrel.2021.12.030

- Park, K. (2019). The beginning of the end of the nanomedicine hype. *J Control Release*, 305, 221-222. doi:10.1016/j.jconrel.2019.05.044
- Park, Y., Depeursinge, C., & Popescu, G. (2018). Quantitative phase imaging in biomedicine. *Nat Photonics*, 12(10), 578-589. doi:10.1038/s41566-018-0253-x
- Pawley, J. (2006). *Handbook of biological confocal microscopy* (3 ed. Vol. 236). New York: Springer Science & Business Media.
- Pecora, R. (2000). Dynamic Light Scattering Measurement of Nanometer Particles in Liquids. *J Nanoparticle Res*, 2(2), 123-131. doi:10.1023/a:1010067107182
- Peddie, C. J., & Collinson, L. M. (2014). Exploring the third dimension: volume electron microscopy comes of age. *Micron*, 61, 9-19. doi:10.1016/j.micron.2014.01.009
- Piston, D. W. (1998). Choosing objective lenses: the importance of numerical aperture and magnification in digital optical microscopy. *Biol Bull*, 195(1), 1-4. doi:10.2307/1542768
- Poovi, G., & Damodharan, N. (2018). Lipid nanoparticles: A challenging approach for oral delivery of BCS Class-II drugs. *Future J of Pharm Sci*, 4(2), 191-205. doi:10.1016/j.fjps.2018.04.001
- Popescu, G., Park, Y., Choi, W., Dasari, R. R., Feld, M. S., & Badizadegan, K. (2008). Imaging red blood cell dynamics by quantitative phase microscopy. *Blood Cells Mol Dis*, 41(1), 10-16. doi:10.1016/j.bcmd.2008.01.010
- Pujals, S., & Albertazzi, L. (2019). Super-resolution Microscopy for Nanomedicine Research. *ACS Nano*, 13(9), 9707-9712. doi:10.1021/acsnano.9b05289
- Qi, P., Cao, M., Song, L., Chen, C., Liu, M., Li, N., . . . Zhao, J. (2016). The biological activity of cationic liposomes in drug delivery and toxicity test in animal models. *Environ Toxicol Pharmacol*, 47, 159-164. doi:10.1016/j.etap.2016.09.015
- Radhakrishna, M., Govindh, M. V., & Veni, P. K. (2021). A review on image processing sensor. *J Phys Conf Ser*, 1714, 012055.
- Raz, A., Bucana, C., Fogler, W. E., Poste, G., & Fidler, I. J. (1981). Biochemical, morphological, and ultrastructural studies on the uptake of liposomes by murine macrophages. *Cancer Res*, 41(2), 487-494.
- Regan, D., Williams, J., Borri, P., & Langbein, W. (2019). Lipid Bilayer Thickness Measured by Quantitative DIC Reveals Phase Transitions and Effects of Substrate Hydrophilicity. *Langmuir*, 35(43), 13805-13814. doi:10.1021/acs.langmuir.9b02538
- Rennick, J. J., Johnston, A. P. R., & Parton, R. G. (2021). Key principles and methods for studying the endocytosis of biological and nanoparticle therapeutics. *Nat Nanotechnol*, 16(3), 266-276. doi:10.1038/s41565-021-00858-8
- Richter, V., Lanzerstorfer, P., Weghuber, J., & Schneckenburger, H. (2021). Probing small distances in live cell imaging. *Photonics*, 8(6), 176. doi:10.3390/photonics8060176
- Rubinsky, B. (2003). Principles of low temperature cell preservation. *Heart Fail Rev*, 8(3), 277-284. doi:10.1023/a:1024734003814
- Ruozi, B., Belletti, D., Tombesi, A., Tosi, G., Bondioli, L., Forni, F., & Vandelli, M. A. (2011). AFM, ESEM, TEM, and CLSM in liposomal characterization: a comparative study. *Int J Nanomedicine*, 6, 557-563. doi:10.2147/IJN.S14615

- Saaim, K. M., Afridi, S. K., Nisar, M., & Islam, S. (2022). In search of best automated model: Explaining nanoparticle TEM image segmentation. *Ultramicroscopy*, *233*, 113437. doi:10.1016/j.ultramic.2021.113437
- Sage, D., Pham, T. A., Babcock, H., Lukes, T., Pengo, T., Chao, J., . . . Holden, S. (2019). Super-resolution fight club: assessment of 2D and 3D single-molecule localization microscopy software. *Nat Methods*, *16*(5), 387-395. doi:10.1038/s41592-019-0364-4
- Saleh, T. A. (2020). Nanomaterials: Classification, properties, and environmental toxicities. *Environmental Technology & Innovation*, *20*, 101067. doi:10.1016/j.eti.2020.101067
- Sandmeyer, A., Lachetta, M., Sandmeyer, H., Hübner, W., Huser, T., & Müller, M. (2021). Cost-effective live cell structured illumination microscopy with video-rate imaging. *ACS Photonics*, *8*(6), 1639-1648. doi:10.1021/acsp Photonics.0c01937
- Sato, Y., Nakamura, T., Yamada, Y., & Harashima, H. (2021). The nanomedicine rush: New strategies for unmet medical needs based on innovative nano DDS. *J Control Release*, *330*, 305-316. doi:10.1016/j.jconrel.2020.12.032
- Schermelleh, L., Ferrand, A., Huser, T., Eggeling, C., Sauer, M., Biehlmaier, O., & Drummen, G. P. C. (2019). Super-resolution microscopy demystified. *Nat Cell Biol*, *21*(1), 72-84. doi:10.1038/s41556-018-0251-8
- Selby, L. I., Cortez-Jugo, C. M., Such, G. K., & Johnston, A. P. R. (2017). Nanoescapology: progress toward understanding the endosomal escape of polymeric nanoparticles. *Wiley Interdiscip Rev Nanomed Nanobiotechnol*, *9*(5), e1452. doi:10.1002/wnan.1452
- Simonsen, J. B., Larsen, J. B., Hempel, C., Eng, N., Fossum, A., & Andresen, T. L. (2019). Unique Calibrators Derived from Fluorescence-Activated Nanoparticle Sorting for Flow Cytometric Size Estimation of Artificial Vesicles: Possibilities and Limitations. *Cytometry A*, *95*(8), 917-924. doi:10.1002/cyto.a.23797
- Širc, J., Hobzova, R., Kostina, N., Munzarová, M., Jukličková, M., Lhotka, M., . . . Michálek, J. (2012). Morphological characterization of nanofibers: methods and application in practice. *J Nanomater*, *2012*. doi:10.1155/2012/327369
- Skalko, N., Peschka, R., Altenschmidt, U., Lung, A., & Schubert, R. (1998). pH-sensitive liposomes for receptor-mediated delivery to chicken hepatoma (LMH) cells. *FEBS Lett*, *434*(3), 351-356. doi:10.1016/s0014-5793(98)00984-3
- Skotland, T., Iversen, T. G., & Sandvig, K. (2021). Cellular uptake of nanoparticles: Involvement of caveolae? *Precis Nanomed*, *4*, 782-786. doi:10.33218/001c.22201
- Snipstad, S., Hak, S., Baghirov, H., Sulheim, E., Morch, Y., Lelu, S., . . . Aslund, A. K. O. (2017). Labeling nanoparticles: Dye leakage and altered cellular uptake. *Cytometry A*, *91*(8), 760-766. doi:10.1002/cyto.a.22853
- Soares, S., Sousa, J., Pais, A., & Vitorino, C. (2018). Nanomedicine: Principles, Properties, and Regulatory Issues. *Front Chem*, *6*, 360. doi:10.3389/fchem.2018.00360
- Sørensen, K. K., McCourt, P., Berg, T., Crossley, C., Le Couteur, D., Wake, K., & Smedsrod, B. (2012). The scavenger endothelial cell: a new player in homeostasis and immunity. *Am J Physiol Regul Integr Comp Physiol*, *303*(12), R1217-1230. doi:10.1152/ajpregu.00686.2011
- Souto, E. B., Dias-Ferreira, J., Lopez-Machado, A., Ettcheto, M., Cano, A., Camins Espuny, A., . . . Sanchez-Lopez, E. (2019). Advanced Formulation Approaches for Ocular Drug Delivery:

- State-Of-The-Art and Recent Patents. *Pharmaceutics*, 11(9), 460.
doi:10.3390/pharmaceutics11090460
- Specht, E. A., Braselmann, E., & Palmer, A. E. (2017). A Critical and Comparative Review of Fluorescent Tools for Live-Cell Imaging. *Annu Rev Physiol*, 79(1), 93-117.
doi:10.1146/annurev-physiol-022516-034055
- Stennett, E. M., Ciuba, M. A., & Levitus, M. (2014). Photophysical processes in single molecule organic fluorescent probes. *Chem Soc Rev*, 43(4), 1057-1075.
doi:10.1039/c3cs60211g
- Sternbæk, L., Kimani Wamaitha, M., Gawlitzka, K., Janicke, B., Alm, K., & Wingren Gjørloff, A. (2019). Digital holographic microscopy: Macrophage uptake of nanoprobe. *Imaging and Microscopy*(1), 21-23.
- Stetefeld, J., McKenna, S. A., & Patel, T. R. (2016). Dynamic light scattering: a practical guide and applications in biomedical sciences. *Biophys Rev*, 8(4), 409-427. doi:10.1007/s12551-016-0218-6
- Strebhardt, K., & Ullrich, A. (2008). Paul Ehrlich's magic bullet concept: 100 years of progress. *Nat Rev Cancer*, 8(6), 473-480. doi:10.1038/nrc2394
- Sung, J. H., Wang, Y. I., Narasimhan Sriram, N., Jackson, M., Long, C., Hickman, J. J., & Shuler, M. L. (2019). Recent Advances in Body-on-a-Chip Systems. *Anal Chem*, 91(1), 330-351.
doi:10.1021/acs.analchem.8b05293
- Surre, J., Saint-Ruf, C., Collin, V., Orenge, S., Ramjeet, M., & Matic, I. (2018). Strong increase in the autofluorescence of cells signals struggle for survival. *Sci Rep*, 8(1), 12088.
doi:10.1038/s41598-018-30623-2
- Susewind, J., de Souza Carvalho-Wodarz, C., Repnik, U., Collnot, E. M., Schneider-Daum, N., Griffiths, G. W., & Lehr, C. M. (2016). A 3D co-culture of three human cell lines to model the inflamed intestinal mucosa for safety testing of nanomaterials. *Nanotoxicology*, 10(1), 53-62. doi:10.3109/17435390.2015.1008065
- Swift, S., & Trinkle-Mulcahy, L. (2012). To bin or not to bin. *infocus Magazine*, 4-14.
doi:10.22443/rms.inf.1.82
- Swinehart, D. F. (1962). The Beer-Lambert Law. *J Chem Educ*, 39(7), 333.
doi:10.1021/ed039p333
- Szafranska, K., Kruse, L. D., Holte, C. F., McCourt, P., & Zapotoczny, B. (2021). The wHole Story About Fenestrations in LSEC. *Front Physiol*, 12, 735573.
doi:10.3389/fphys.2021.735573
- Tang, J., Ren, J., & Han, K. Y. (2019). Fluorescence imaging with tailored light. *Nanophotonics*, 8(12), 2111-2128. doi:10.1515/nanoph-2019-0227
- Terai, T., & Nagano, T. (2013). Small-molecule fluorophores and fluorescent probes for bioimaging. *Pflugers Arch*, 465(3), 347-359. doi:10.1007/s00424-013-1234-z
- Terasaki, M., & Jaffe, L. A. (2004). Labeling of cell membranes and compartments for live cell fluorescence microscopy. *Methods Cell Biol*, 74, 469-489. doi:10.1016/s0091-679x(04)74019-4
- Ternullo, S., Basnet, P., Holsaeter, A. M., Flaten, G. E., de Weerd, L., & Skalko-Basnet, N. (2018). Deformable liposomes for skin therapy with human epidermal growth factor: The

- effect of liposomal surface charge. *Eur J Pharm Sci*, 125, 163-171. doi:10.1016/j.ejps.2018.10.005
- Ternullo, S., de Weerd, L., Holsaeter, A. M., Flaten, G. E., & Skalko-Basnet, N. (2017). Going skin deep: A direct comparison of penetration potential of lipid-based nanovesicles on the isolated perfused human skin flap model. *Eur J Pharm Biopharm*, 121, 14-23. doi:10.1016/j.ejpb.2017.09.006
- Tewabe, A., Abate, A., Tamrie, M., Seyfu, A., & Abdela Siraj, E. (2021). Targeted Drug Delivery - From Magic Bullet to Nanomedicine: Principles, Challenges, and Future Perspectives. *J Multidiscip Healthc*, 14, 1711-1724. doi:10.2147/JMDH.S313968
- Thorn, K. (2016). A quick guide to light microscopy in cell biology. *Mol Biol Cell*, 27(2), 219-222. doi:10.1091/mbc.E15-02-0088
- Thottacherry, J. J., Kosmalska, A. J., Kumar, A., Vishen, A. S., Elosegui-Artola, A., Pradhan, S., . . . Mayor, S. (2018). Mechanochemical feedback control of dynamin independent endocytosis modulates membrane tension in adherent cells. *Nat Commun*, 9(1), 4217. doi:10.1038/s41467-018-06738-5
- Tian, X., Murfin, L. C., Wu, L., Lewis, S. E., & James, T. D. (2021). Fluorescent small organic probes for biosensing. *Chem Sci*, 12(10), 3406-3426. doi:10.1039/d0sc06928k
- Tosheva, K. L., Yuan, Y., Matos Pereira, P., Culley, S., & Henriques, R. (2020). Between life and death: strategies to reduce phototoxicity in super-resolution microscopy. *J Phys D Appl Phys*, 53(16), 163001. doi:10.1088/1361-6463/ab6b95
- Trinh, N., Jolliffe, K. A., & New, E. J. (2020). Dual-Functionalisation of Fluorophores for the Preparation of Targeted and Selective Probes. *Angew Chem Int Ed Engl*, 59(46), 20290-20301. doi:10.1002/anie.202007673
- Truneh, A., Machy, P., & Horan, P. K. (1987). Antibody-bearing liposomes as multicolor immunofluorescence markers for flow cytometry and imaging. *J Immunol Methods*, 100(1-2), 59-71. doi:10.1016/0022-1759(87)90173-6
- Ulrich, A. S. (2002). Biophysical aspects of using liposomes as delivery vehicles. *Biosci Rep*, 22(2), 129-150. doi:10.1023/a:1020178304031
- Valdes-Aguilera, O., Cincotta, L., Foley, J., & Kochevar, I. E. (1987). Photobleaching of a cyanine dye in solution and in membranes. *Photochem Photobiol*, 45(3), 337-344. doi:10.1111/j.1751-1097.1987.tb05384.x
- van de Hulst, H. (2012). *Light Scattering by Small Particles*. New York: Dover Publications; Illustrated edition.
- Van Leeuwen, S. R., & Baranoski, G. V. G. (2018). Elucidating the contribution of Rayleigh scattering to the bluish appearance of veins. *J Biomed Opt*, 23(2), 1-17. doi:10.1117/1.JBO.23.2.025001
- Vanić, Ž., & Škalko-Basnet, N. (2017). Nanoformulations for vaginal therapy. In Rai, M. and dos Santos C. A. (Eds) *Nanotechnology Applied To Pharmaceutical Technology* (pp. 183-221) Cham, Springer.
- Vu, M. N., Kelly, H. G., Kent, S. J., & Wheatley, A. K. (2021). Current and future nanoparticle vaccines for COVID-19. *EBioMedicine*, 74, 103699. doi:10.1016/j.ebiom.2021.103699

- Wang, Y., & Kohane, D. S. (2017). External triggering and triggered targeting strategies for drug delivery. *Nat Rev Mater*, 2(6), 17020. doi:10.1038/natrevmats.2017.20
- Wang, Z., Millet, L., Chan, V., Ding, H., Gillette, M. U., Bashir, R., & Popescu, G. (2011). Label-free intracellular transport measured by spatial light interference microscopy. *J Biomed Opt*, 16(2), 026019. doi:10.1117/1.3549204
- Watson, P., Jones, A. T., & Stephens, D. J. (2005). Intracellular trafficking pathways and drug delivery: fluorescence imaging of living and fixed cells. *Adv Drug Deliv Rev*, 57(1), 43-61. doi:10.1016/j.addr.2004.05.003
- Wayne, E. C., Long, C., Haney, M. J., Batrakova, E. V., Leisner, T. M., Parise, L. V., & Kabanov, A. V. (2019). Targeted Delivery of siRNA Lipoplexes to Cancer Cells Using Macrophage Transient Horizontal Gene Transfer. *Adv Sci (Weinh)*, 6(21), 1900582. doi:10.1002/advs.201900582
- Wei, Y., Quan, L., Zhou, C., & Zhan, Q. (2018). Factors relating to the biodistribution & clearance of nanoparticles & their effects on in vivo application. *Nanomedicine*, 13(12), 1495-1512. doi:doi.org/10.2217/nnm-2018-0040
- Whelan, D. R., & Bell, T. D. (2015). Image artifacts in single molecule localization microscopy: why optimization of sample preparation protocols matters. *Sci Rep*, 5(1), 7924. doi:10.1038/srep07924
- Wiedenmann, J., D'Angelo, C., & Nienhaus, G. U. (2011). Fluorescent proteins: Nature's colorful gifts for live cell imaging. In *Fluorescent Proteins II* (pp. 3-33): Springer.
- Williams, D. B., & Carter, C. B. (1996). The Transmission Electron Microscope. In *Transmission Electron Microscopy* (pp. 3-17). Boston: Springer US.
- Wu, I. Y., Skalko-Basnet, N., & di Cagno, M. P. (2017). Influence of the environmental tonicity perturbations on the release of model compounds from large unilamellar vesicles (LUVs): A mechanistic investigation. *Colloids Surf B Biointerfaces*, 157, 65-71. doi:10.1016/j.colsurfb.2017.05.062
- Wu, L. P., Wang, D., & Li, Z. (2020). Grand challenges in nanomedicine. *Mater Sci Eng C Mater Biol Appl*, 106, 110302. doi:10.1016/j.msec.2019.110302
- Wu, Q., Miao, W. S., Zhang, Y. D., Gao, H. J., & Hui, D. (2020). Mechanical properties of nanomaterials: A review. *Nanotechnol Rev*, 9(1), 259-273. doi:10.1515/ntrev-2020-0021
- Wu, Y., & Shroff, H. (2018). Faster, sharper, and deeper: structured illumination microscopy for biological imaging. *Nat Methods*, 15(12), 1011-1019. doi:10.1038/s41592-018-0211-z
- Xiang, B., & Cao, D.-Y. (2021). Preparation of drug liposomes by thin-film hydration and homogenization. In W.-L. Lu & X.-R. Qi (Eds.), *Liposome-based drug delivery systems* (pp. 25-35). Singapore: Springer Nature.
- Yadav, K. S., & Kale, K. (2020). High Pressure Homogenizer in Pharmaceuticals: Understanding Its Critical Processing Parameters and Applications. *J Pharm Innov*, 15(4), 690-701. doi:10.1007/s12247-019-09413-4
- Yahiatene, I., Hennig, S., Müller, M., & Huser, T. (2015). Entropy-Based Super-Resolution Imaging (ESI): From Disorder to Fine Detail. *ACS Photonics*, 2(8), 1049-1056. doi:10.1021/acsp Photonics.5b00307

- Yang, G., Liu, Y., Teng, J., & Zhao, C. X. (2021). FRET Ratiometric Nanoprobes for Nanoparticle Monitoring. *Biosensors*, *11*(12), 505. doi:10.3390/bios11120505
- Zahednezhad, F., Saadat, M., Valizadeh, H., Zakeri-Milani, P., & Baradaran, B. (2019). Liposome and immune system interplay: Challenges and potentials. *J Control Release*, *305*, 194-209. doi:10.1016/j.jconrel.2019.05.030
- Zernike, F. (1955). How I discovered phase contrast. *Science*, *121*(3141), 345-349. doi:10.1126/science.121.3141.345
- Zhao, W., Liu, J., Kong, C., Zhao, Y., Guo, C., Liu, C., . . . Li, H. (2018). Faster super-resolution imaging with auto-correlation two-step deconvolution. *arXiv preprint*. doi:10.48550/arXiv.1809.07410
- Zhou, J., Chizhik, A. I., Chu, S., & Jin, D. (2020). Single-particle spectroscopy for functional nanomaterials. *Nature*, *579*(7797), 41-50. doi:10.1038/s41586-020-2048-8
- Zuo, C., Chen, Q., Qu, W., & Asundi, A. (2013). Noninterferometric single-shot quantitative phase microscopy. *Opt Lett*, *38*(18), 3538-3541. doi:10.1364/OL.38.003538
- Zylberberg, C., & Matosevic, S. (2016). Pharmaceutical liposomal drug delivery: a review of new delivery systems and a look at the regulatory landscape. *Drug Deliv*, *23*(9), 3319-3329. doi:10.1080/10717544.2016.1177136
- Zylberberg, C., & Matosevic, S. (2017). Bioengineered liposome-scaffold composites as therapeutic delivery systems. *Ther Deliv*, *8*(6), 425-445. doi:10.4155/tde-2017-0014

Paper 1



Article

Following the Fate of Dye-Containing Liposomes In Vitro

Jennifer Cauzzo ¹, Mona Nystad ^{2,3}, Ann Mari Holsæter ¹, Purusotam Basnet ^{2,4}
and Nataša Škalko-Basnet ^{1,*}

¹ Drug Transport and Delivery Research Group, Department of Pharmacy, Faculty of Health Sciences, University of Tromsø The Arctic University of Norway, N-9037 Tromsø, Norway; jennifer.cauzzo@uit.no (J.C.); ann-mari.holsater@uit.no (A.M.H.)

² Women's Health and Perinatology Research Group, Department of Clinical Medicine, Faculty of Health Sciences, University of Tromsø The Arctic University of Norway, N-9037 Tromsø, Norway; mona.nystad@uit.no (M.N.); purusotam.basnet@uit.no (P.B.)

³ Department of Medical Genetics, University Hospital of North Norway, N-9038 Tromsø, Norway

⁴ Department of Obstetrics and Gynecology, University Hospital of North Norway, N-9038 Tromsø, Norway

* Correspondence: natasa.skalko-basnet@uit.no

Received: 18 June 2020; Accepted: 7 July 2020; Published: 9 July 2020



Abstract: The rather limited success of translation from basic research to clinical application has been highlighted as a major issue in the nanomedicine field. To identify the factors influencing the applicability of nanosystems as drug carriers and potential nanomedicine, we focused on following their fate through fluorescence-based assays, namely flow cytometry and imaging. These methods are often used to follow the nanocarrier internalization and targeting; however, the validity of the obtained results strictly depends on how much the nanosystem's fate can be inferred from the fate of fluorescent dyes. To evaluate the parameters that affect the physicochemical and biological stability of the labeled nanosystems, we studied the versatility of two lipid dyes, TopFluor[®]-PC and Cy5-DSPE, in conventional liposomes utilizing well-defined in vitro assays. Our results suggest that the dye can affect the major characteristics of the system, such as vesicle size and zeta-potential. However, a nanocarrier can also affect the dye properties. Medium, temperature, time, fluorophore localization and its concentration, as well as their interplay, affect the outcome of tracing experiments. Therefore, an in-depth characterization of the labeled nanosystem should be fundamental to understand the conditions that validate the results within the screening process in optimization of nanocarrier.

Keywords: liposomes; nanomedicine; cellular uptake; fluorescent dye; stability

1. Introduction

Nanomedicine has been proposed as the superior approach within advanced drug therapy, able to respond to the ever growing demands of various diseases. However, the past decades did not fully confirm its translational significance [1,2]. The reasons for this limited success rate are numerous and often interconnected, however, the heterogeneous physicochemical characteristics of nanomedicine formulations have a large influence on their biological performance [3]. In general, cellular uptake of drug-containing nanocarriers, including liposomes, will determine both the efficacy of drug delivery and toxic effects of carrier-associated drugs or active molecules. Liposomes made of natural phospholipids offer reassuring safety profiles [4] and become one of the most studied nanomedicines. Their versatility offers opportunities to tailor their features to enhance specific interactions with the target site. Optimizing liposomal features involves predicting/controlling their fate in vivo. The first step in optimization should, therefore, focus on determining the cellular uptake

in rather simple in vitro conditions. There are various methods to follow and quantify the cellular uptake; probably, the most commonly applied methods are flow cytometry and imaging [5]. The fate of nanocarriers is often followed by tracing one or more fluorescent dyes associated with carriers. Based on the results, the formulations will be modified/tailored to achieve the desired cellular uptake. However, it is important to consider that the findings are based on two assumptions: i) the dye does not alter the interactions of nanocarriers with cells/tissues; ii) the dye encapsulated/incorporated in the nanocarrier is stable and remains associated with the carrier throughout the process. Unfortunately, these assumptions are not always correct [6]. Rodriguez-Lorenzo et al. [7] first described the possibility of the dye affecting the properties of the carrier, regarding gold nanoparticles. The change in surface charge due to the covalent link of a fluorescent dye had great effect on the cellular internalization. Considering liposomes as nanocarriers, liposomes are most often labeled by the fluorescent dye lipids incorporated within liposomal bilayers. Recently, Münter et al. [8] validated the assumption that dye remains associated with the liposomes throughout the experiment and found that the choice of labeled lipid can influence the conclusions on uptake of liposomes, as well as their localization within the cell. Many of the commonly used lipid dyes dissociate prior or upon exposure to biological environment. Moreover, the dye dissociations are not detected in the commonly applied in vitro assays used to determine dye leakage. For both (i) dye-induced modification of cellular fate and (ii) dye leakage, the dye loses its primary function of tracking the system behavior; as a result, the fate of the dye is followed rather than the fate of the dye-labeled nanocarrier.

Rather than searching for an ever superior nanomedicine formulation, we propose to go back to basics and start rechecking the widely accepted dogmas. In an attempt to do so, we have focused on following the fate of liposomes as a model nanosized system in in vitro cell culture settings. Therefore, as the first step, we assessed the system's stability in respect to both the effect that the dye might have on the physicochemical properties of the carrier, as well as the effect that the formulation might have on the dye stability. Finally, we investigated the biological properties of the new labeled nanocarrier.

Our hypothesis was that the dye-labeled nanocarrier can be considered as a new system, which needs to be compared to the dye-free delivery system and the free dye. To confirm our hypothesis, we chose to label our liposomes using fluorophores that resemble the chemical structure of the phospholipids building liposomes, and investigated their interference on the intrinsic behavior of the bilayer. Hence, we selected two commonly used fluorescent lipids [9], namely 1-palmitoyl-2-(dipyrrometheneboron difluoride)undecanoyl-sn-glycero-3-phosphocholine (TopFluor[®]-PC, T) and 1,2-distearoyl-sn-glycero-3-phosphoethanolamine-N-(Cyanine 5) (Cy5-DSPE, C) [6,8] as labels for our nanocarrier. Both dyes in four different ratios were individually incorporated in liposomes, and their stability, as well as impact on in vitro liposomal cellular uptake, were evaluated and compared.

2. Results

2.1. Liposome Characterization and Stability

Composition, vesicle size, ζ -potential and fluorescence spectra for all freshly prepared formulations (Day 0) are summarized in Figure 1 and Table 1. The liposomes comprising the lipid dye (T, TopFluor[®]-PC) are presented as T1, T2, T3 and T4 (Lip-T), with increasing concentration of dye (T1 the lowest and T4 the highest ratio). Similarly, the liposomes comprising the surface lipid dye (C, Cy5-DSPE) are referred to as C1, C2, C3 and C4 (Lip-C), respectively. The T dye (MW= 909.97) is a fatty acid-labeled phospholipid that is expected to accommodate its fluorescent moiety within the bilayer, without significantly altering its structure [10,11]. The C dye (MW= 1266.20) is a headgroup-labeled phospholipid that is expected to expose the fluorescent moiety on the surface (Figure 1).

All labeled liposomes were in the size range below 200 nm, to assure that vesicles could be administered intravenously [12]. Since NICOMP distributions permit the presentation of bimodal size distributions (vesicle populations), rather than conventional Gaussian distributions, we set up the

internal quality parameters to be i) polydispersity index (PdI) below 0.25 and ii) vesicle intensity above 80% for the most representative size peak. Both parameters, therefore, indicate the clear dominance of one vesicle population over the other. The Gaussian ζ -potential distribution estimated the surface charge to be mostly neutral for all formulations, confirming that the presence of either dye was not significantly interfering with the surface property of the liposomes. Furthermore, all liposomal suspensions were visually inspected before any analysis to assure that no precipitates were detected. The low values of polydispersity index indicated that all labeled liposomes were rather homogenous in size, with the majority of the vesicles of very similar size. Moreover, the incorporation of dye within the liposome did not affect the vesicle size (Table 1).

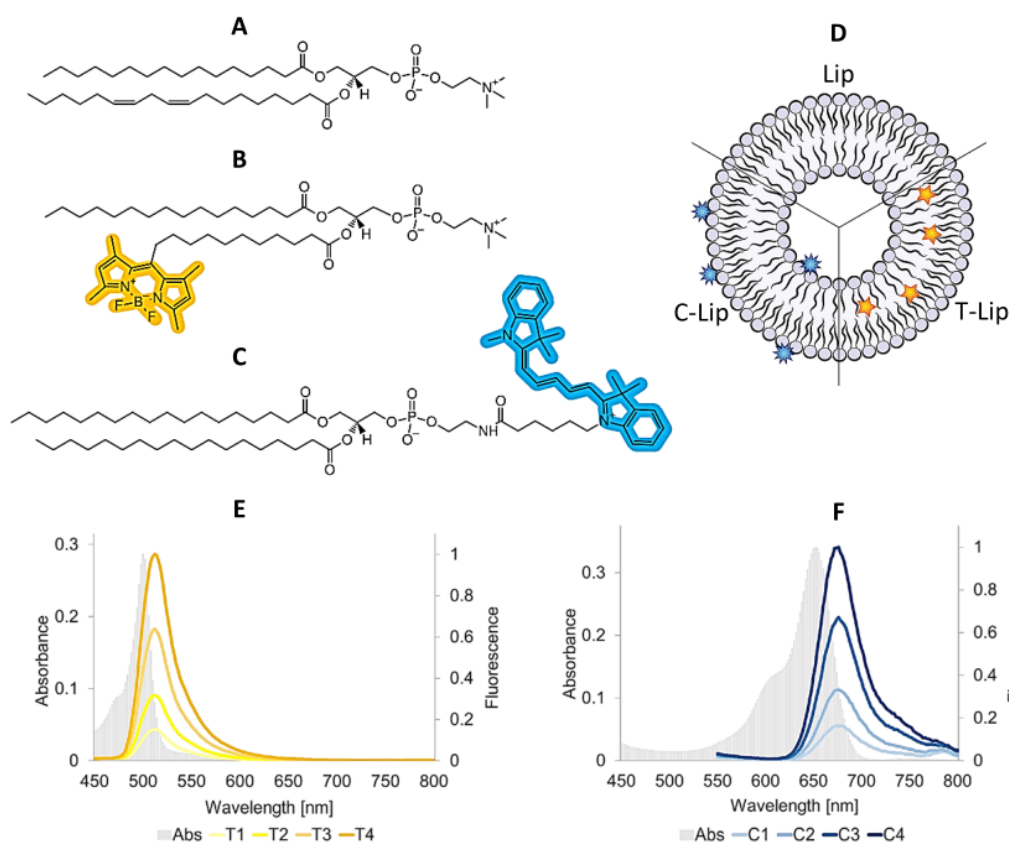


Figure 1. Molecular formulae of the lipid ingredients, postulated dye localization in the liposomal bilayer and fluorescence spectra of all dye-containing liposomal formulations (Day 0). The molecular formula of the most representative lipid in soy phosphatidylcholine (SPC) is provided (panel A) for comparison with the structures of the labeled phospholipids C and T (panel B and C, respectively). ACD/ChemSketch (Freeware) 2019 2.1 was used to draw the molecules and highlight the fluorescent moieties. All lipids ingredients are insoluble in water and highly soluble in methanol (respectively, >10000 and <1 mass parts of solvent required to dissolve 1 mass part of solute; according to Pharmacopeia's definition). The liposome model (panel D) shows the expected localization of the labeled phospholipids according to their chemical structure and previous studies [10,11]. Panel E and F show the spectra for T-Lip and C-Lip formulations. The gray background spectrum represents the absorbance (primary y-axis), the solid colored lines refer to the fluorescent emission for all labeled formulations after normalization on the maximum values for T4 and C4 (secondary y-axis). Abbreviations: Lip refers to empty liposomes; T-Lip and C-Lip to the labeled formulations.

Table 1. Characteristics of freshly prepared liposomal suspensions.

Type of Liposomes	Fluorescent Dye		Vesicle Size		ζ -Potential	
	T [mg/mL]	C [mg/mL]	Peak 1 [nm (%)]	Peak 2 [nm (%)]	PdI	[mV]
Lip	-	-	135 ± 1 (88%)	38 ± 1 (12%)	0.23 ± 0.01	-1.4 ± 0.1
T1	0.015	-	167 ± 2 (95%)	39 ± 11 (5%)	0.17 ± 0.01	-2.0 ± 0.2
T2	0.030	-	158 ± 7 (96%)	35 ± 12 (4%)	0.16 ± 0.01	-3.6 ± 0.3
T3	0.060	-	160 ± 4 (95%)	35 ± 4 (5%)	0.20 ± 0.04	-1.2 ± 0.1
T4	0.120	-	168 ± 4 (89%)	42 ± 3 (11%)	0.22 ± 0.01	-1.8 ± 0.0
C1	-	0.015	163 ± 8 (94%)	35 ± 1 (6%)	0.21 ± 0.01	-1.2 ± 0.1
C2	-	0.030	161 ± 4 (89%)	40 ± 1 (11%)	0.24 ± 0.01	-1.2 ± 0.1
C3	-	0.060	156 ± 1 (93%)	37 ± 1 (7%)	0.22 ± 0.01	-2.0 ± 0.1
C4	-	0.120	157 ± 7 (89%)	39 ± 8 (11%)	0.22 ± 0.01	-1.5 ± 0.1

Values are expressed as mean ± SEM ($n = 2$). To describe the bimodal size distribution, the intensity-weighted percentage of each population peak is indicated in brackets. The vesicle size was measured after dilution in isotonic buffer, whereas ζ -potential after dilution in distilled water. The concentration of neutral (zwitterionic) SPC (>94% purity) was 10 mg/mL. Abbreviations: SPC refers to soy phosphatidylcholine; T represents TopFluor lipid dye whereas C represents Cy5-DSPE surface lipid dye; PdI is polydispersity index; SEM, standard error of the mean.

The next step was to determine the vesicle stability to assure that the experiments, performed with either fresh or week-old labeled liposomes, would not differ due to the freshness of their preparation. As evident in Figure 2A, no significant variations in size were detected (over 60 days) in liposomal suspension stored at 4 °C. Despite the initially neutral ζ -potential, the rather small size and narrow polydispersity of the liposomal suspension assured the stable size distribution over the tested timeframe. However, a progressive lowering of the ζ -potential over time was identified for all formulations, more evidently for the C-containing liposomes, suggesting that this increased surface charge could help stabilize the suspension at the later time points [12]. As expected, the long-term storage at 25 °C (Figure 2B) resulted in great instability of all dye-containing formulations as compared to their respective no-dye control. We were able to follow the size distributions for formulations stored at 25 °C for only 15 days; when measuring the formulations stored for 30 days, a dense sediment was observed in the vials and the suspension was not stable enough throughout the duration of the measurements. We could only measure the dye-free liposomes which were stable in size. Although the stability issue for storage at room temperature was expected, it also indicated that leaving the samples at room temperature could affect the vesicle aggregation and consequently, the cellular uptake, and it is one of the parameters which needs to be considered in the experiments.

After identifying the stability issue with dye-containing liposomes, we went a step further to evaluate the effect of storage temperature on the stability of the dye-containing formulations, focusing on the stability of fluorescence, namely the loss of fluorescence over time. As shown in Figure 3, the overall fluorescence stability of all T-containing formulations in buffer was higher than the corresponding C-containing liposomes. The trend was observed at all tested storage temperatures (4, 25 and 37 °C). Nevertheless, when the same dyes were dissolved in methanol and their stability was tested under the same storage conditions, the dyes remained stable. The medium of the liposomal suspension, thus, directly affected the fluorescence stability of the fluorophores in the formulations, and the degree of instability was dependent on the fluorophore and its localization in the bilayer. In our case, the greater instability of the C-lip formulations supports the expected localization of the fluorescent moiety onto the surface, as the carbocyanine group is known to be prone to photobleaching in buffer [13] when not protected by the lipid bilayer [14]. This finding has a significant impact and should raise concerns when explaining the biological fate of liposomes based on the measured intensities of liposome-associated dyes.

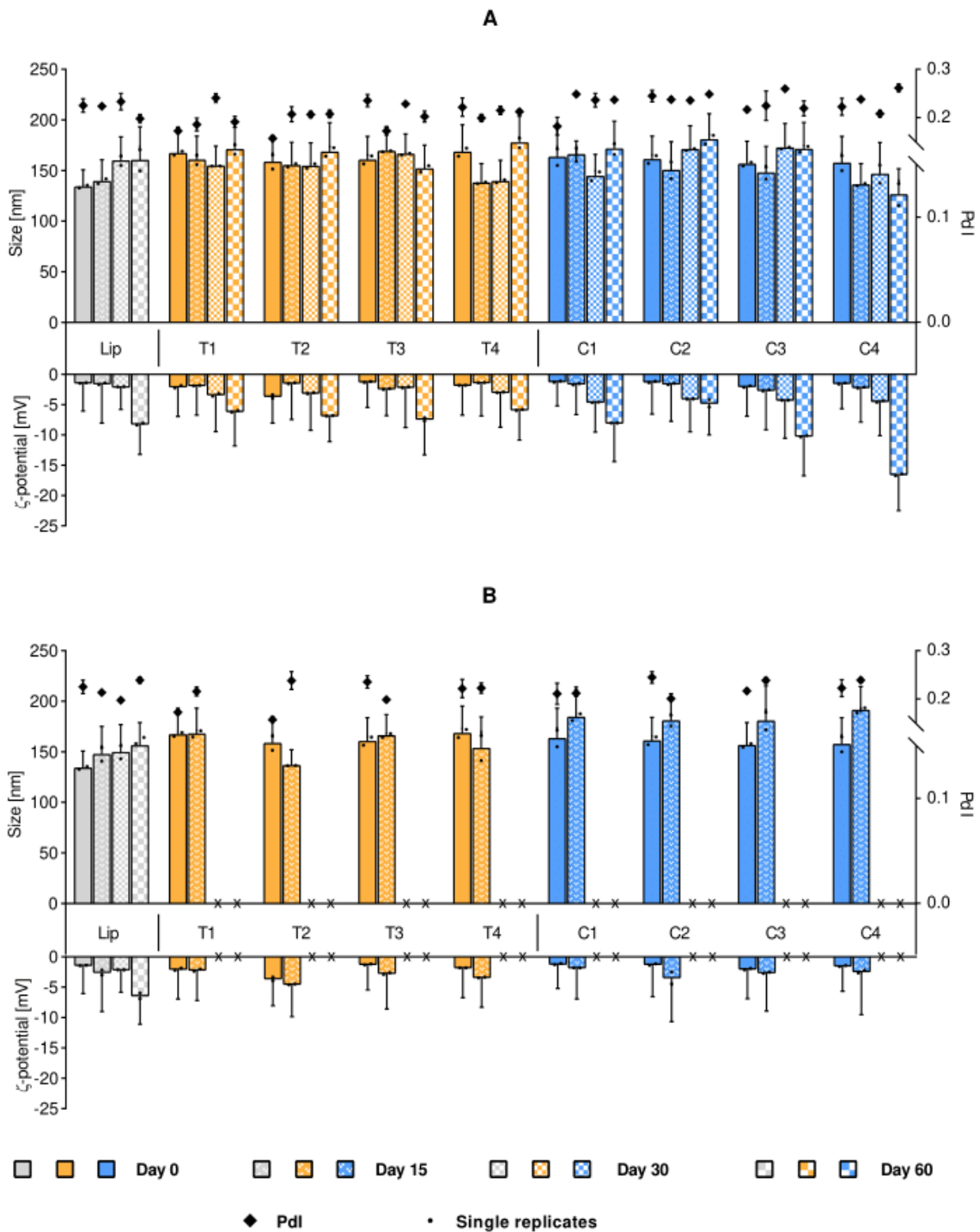


Figure 2. Stability of liposomal suspensions upon storage at 4 °C (panel A) and 25 °C (panel B). The stability is expressed as changes in original liposomal size and ζ -potential. Each bar cluster represents a suspension over time (Day 0, 15, 30 and 60, when measurable). The size is presented on the positive y-axis, where the bars refer to the main peak (primary y-axis), together with the associated SD (half width of the peaks) and the mean of the single replicates (small dots, $n = 2$). The diamonds correspond to the PDI (secondary y-axis) mean, with associated SD. The ζ -potential stability is displayed on the negative y-axis, with corresponding SD and single replicates. Isotonic phosphate buffer was used in pre-dilutions for size measurements, while distilled water was used for the ζ -potential determination. Abbreviations: Lip refers to empty liposomes (gray); T (yellow) and C (blue) refer to the lipid dye and the surface lipid dye, respectively; PDI is the polydispersity index; SD is the standard deviation.

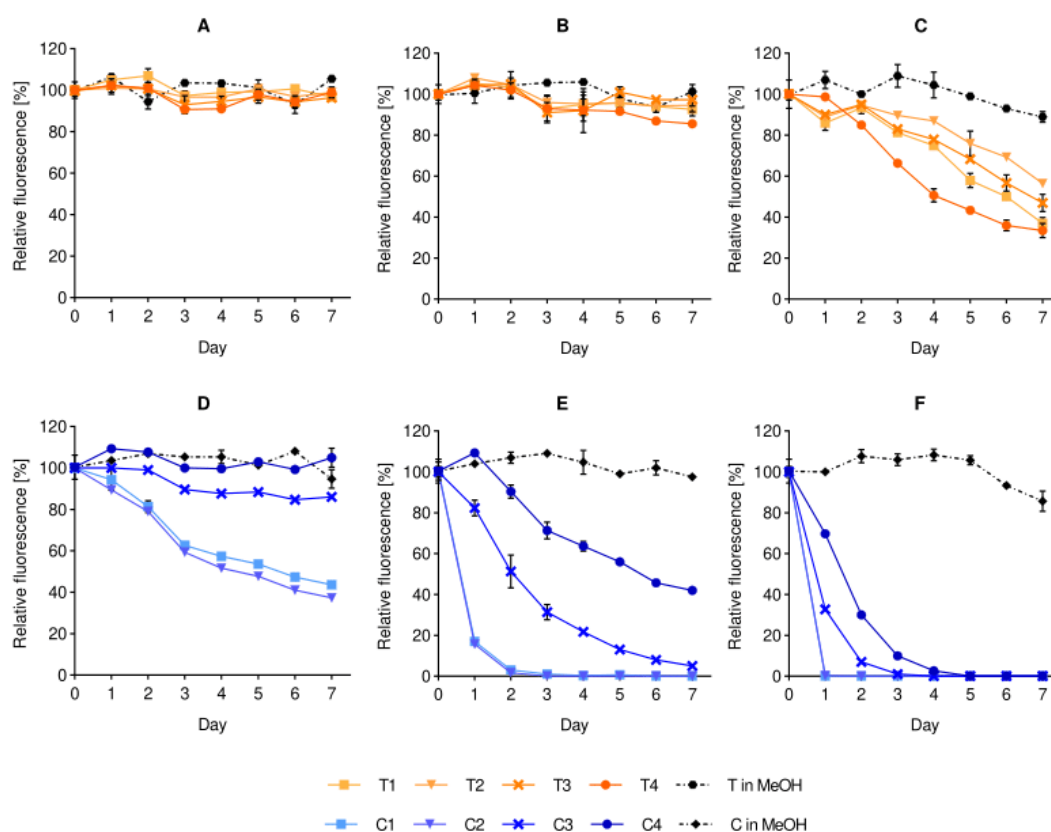


Figure 3. Effect of storage temperature on the fluorescence stability of liposomal dyes. The stability of T-containing formulations (panels A–C) and C-containing formulations (panels D–F) are compared to their respective dye solutions in methanol after daily sampling at the temperatures of 4 °C (A,D), 25 °C (B,E) and 37 °C (C,F). All formulations were pre-diluted in isotonic buffer to fit in the detectable range of the instrument. The fluorescence is expressed as mean (%) \pm SD ($n = 3$), where 100% is the initial fluorescence value of each formulation (Day 0). Abbreviations: T refers to the lipid dye; C to the surface lipid dye; MeOH is short for methanol; SD is standard deviation.

2.2. Biological Activity In Vitro

Another important parameter to be considered when choosing the dye to be incorporated in liposomes is the potential toxicity and pharmacological response of dye-in-liposomes. We tested the cytotoxicity and anti-inflammatory responses of all liposomal suspensions.

2.2.1. Cytotoxicity

Cytotoxicity of labeled liposomes were studied on macrophages (RAW 264.7) and keratinocytes (HaCaT) at lipid concentrations of 1, 10 and 50 $\mu\text{g/mL}$. None of the formulations exhibited any cytotoxic effect on the selected cell lines up to the lipid concentration of 50 $\mu\text{g/mL}$. Moreover, the behavior of the dye-containing liposomes did not significantly differ from the control represented by dye-free liposomes (Figure 4). The colorimetric reduction in the tetrazolium salt WST-8 was used as an indicator of cell viability, since this reaction requires an active dehydrogenase catalysis to be completed [15]. Hence, cell proliferation was expressed as a function of this enzymatic activity, setting 100% as the viability of the untreated control. Overall cell growth after the treatment was similar to the untreated controls, however, a tendency of increased keratinocytes proliferation was noticed for cells treated with liposomes in increasing lipid concentrations (Figure 4B).

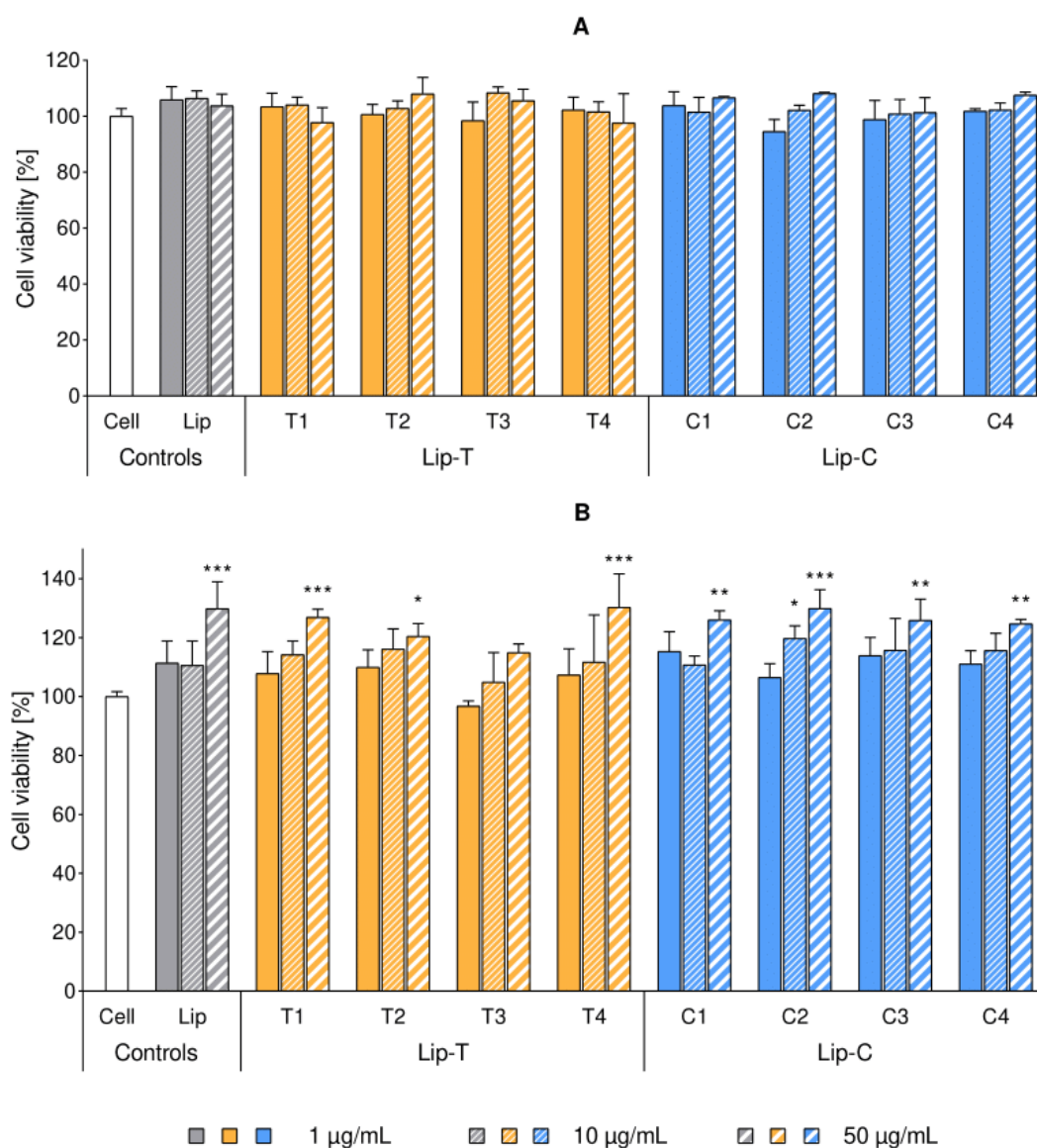


Figure 4. Cytotoxicity of liposomal suspensions tested on RAW 264.7 macrophages (panel A) and HaCaT keratinocytes (panel B). Cell proliferation was expressed in percentage, referencing the untreated control (mean \pm SD, $n = 3$). Each cluster refers to the same liposome formulation, applied in three different concentrations indicated in the legend. Concentration values correspond to the concentration of lipids per well (1, 10 and 50 $\mu\text{g/mL}$, complete RPMI-1640). Stars of significance indicate the increased proliferation over cell control (white bar): * $p < 0.05$; ** $p < 0.01$; *** $p < 0.001$. All dye-containing liposomes affected the cell proliferation in a similar manner as empty liposomes. Abbreviations: Lip refers to liposomes; T and C refer to the lipid dye and the surface lipid dye, respectively; Lip-T and Lip-C denote the dye-containing formulation; SD is standard deviation.

2.2.2. Anti-Inflammatory Assay

Anti-inflammatory responses related to liposomal formulations were expressed by measuring the inhibition on nitric oxide (NO) production in LPS-induced macrophages. The anti-inflammatory activity was expressed as percentage of NO production inhibition calculated with respect to control (untreated cells as shown in Figure 5, white bar).

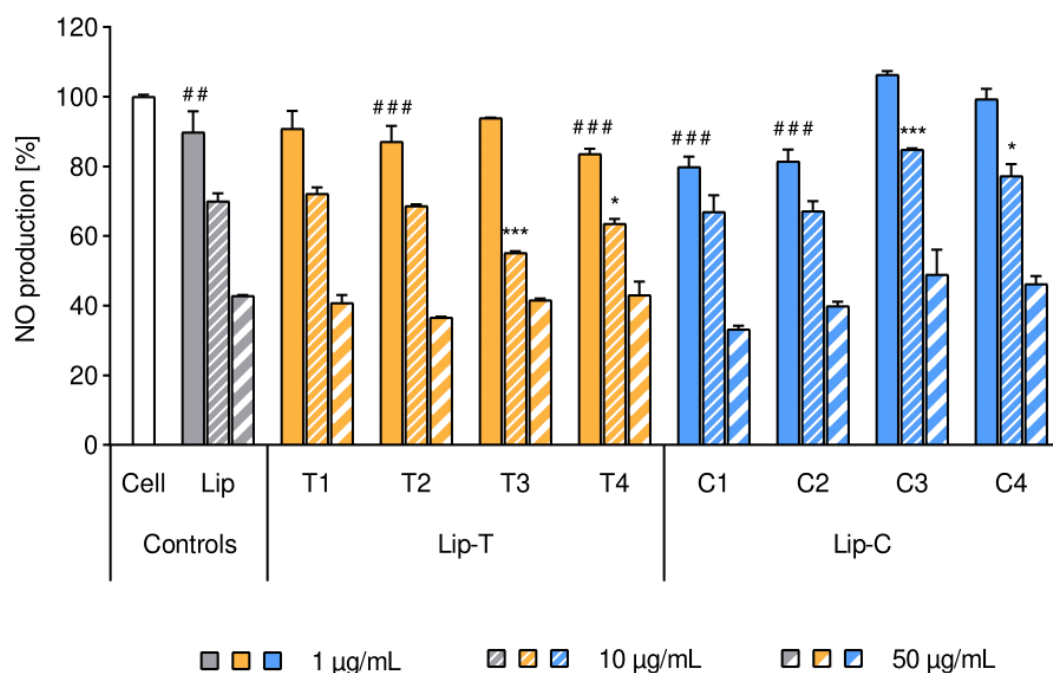


Figure 5. Effect of liposomes on the intrinsic inflammatory activity of RAW 264.7 macrophages. Intrinsic nitric oxide production was expressed in percentage from 0% (non-inflamed cells) to 100% (1 µg/mL LPS-inflamed cell as control, white bar). Bars represent mean \pm SD ($n = 3$) and separate clusters refer to different liposomes in three concentrations of lipids (1, 10 and 50 µg/mL per well). Tags of significance show deviance from the cell control (white bar) for all the lowest lipid concentration applied (1 µg/mL): #: $p < 0.05$; ###: $p < 0.001$. All liposomes at the lipid concentration of 10 and 50 µg/mL showed the highest significance of $p < 0.001$ (not marked in the figure). Stars of significance indicate deviance from the respective empty liposome control (Lip, gray cluster): *: $p < 0.05$; ***: $p < 0.001$. Abbreviations: Lip refers to liposomes; Lip-T and Lip-C refer to the dye-containing liposomes with T (lipid dye) and C (surface lipid dye) respectively; NO is nitric oxide; SD is standard deviation.

All liposomal formulations showed lipid concentration-dependent inhibition of NO production in LPS-activated macrophage (Figure 5) and the results were in agreement with the literature [16,17]. Liposomal formulations at the concentration of 50 µg/mL inhibited approximately 50% of NO production as compared to the non-treated control.

After the cells were exposed to liposomal suspensions, an evident reduction in the inflammatory activity was measured and validated by a significant concentration-dependency ($p < 0.01$). As Figure 5 shows, within each cluster, the increasing lipid concentration resulted in a decreased NO production. The pattern for the anti-inflammatory effect of non-labeled liposomes was similar to the fluorescently-labeled liposomes (Figure 5). Slight deviations (mostly not on significant level) were observed for both dye-containing liposomes when liposomes comprised higher dye to lipid ratios (T3, T4 and C3, C4, respectively).

2.2.3. Flow Cytometry and Imaging

After confirming the safety and retained biological activity of the liposomal suspensions, we proceeded to follow their cellular uptake. Based on the stability data, we have selected the T1 liposomes as model dye-in-liposomes suspension. T1 liposomes comprise the lowest dye-to-lipid ratio, which would be highly advantageous considering both cost and possible interference. Liposomal uptake was quantified and imaged by flow cytometry at different time points over 24 h. According to the number of cells screened as T-positive (T-A +), the uptake was proven in almost all cells within the

first 6 h of incubation (Figure 6A). On the other hand, the total uptake—quantified as mean peak of fluorescence—did not reach a plateau in the 24 h of analysis, thus, indicating that no saturation took place in the tested timeframe (Figure 6B).

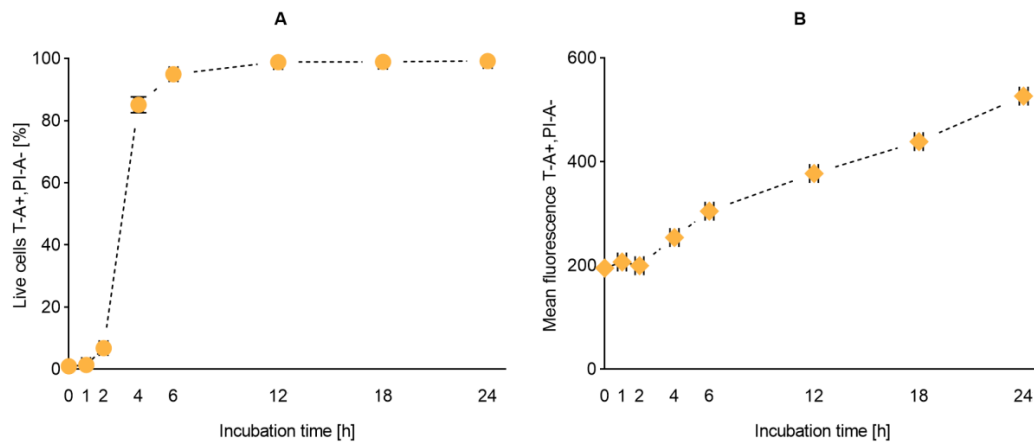


Figure 6. Uptake of T1 liposomes by RAW 264.7 macrophages. Liposomal uptake was expressed as percentage of fluoresce-activated live cells (panel A) and mean fluorescence (panel B). Each point represents mean \pm SD on the y-axis ($n = 3$). A standard error of ± 5 min was given as default on the incubation time for the practical handling of the samples. Abbreviations: T refers to the lipid dye; T-A+, PI-A- represent the gate for fluorescence-activated live cells; SD is standard deviation.

The flow imaging analysis confirmed the cellular uptake, indicating a non-homogeneous distribution of the fluorescent signal within the cell. As expected, the highly lipophilic dye neither was able to reach the nucleus nor did it dissolve uniformly in the cytoplasm (Figure 7).

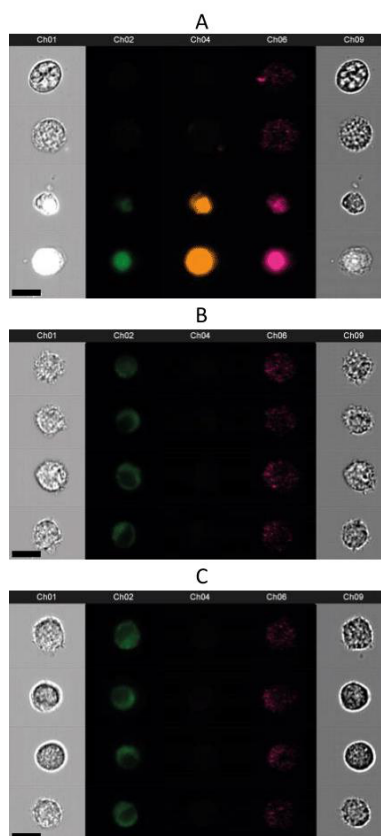


Figure 7. Cont.

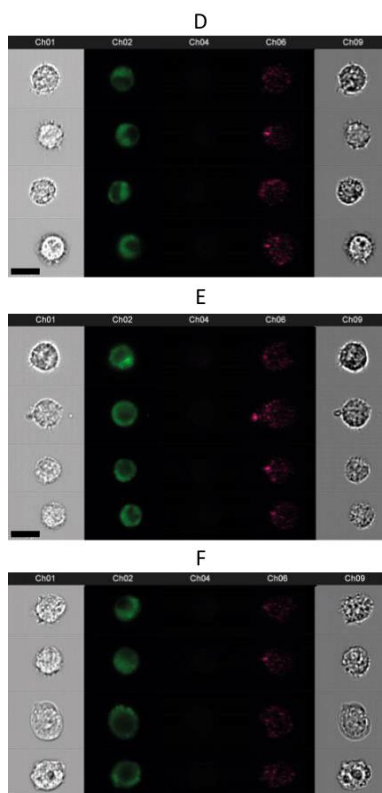


Figure 7. Uptake of T1 liposomes by RAW 264.7 macrophages presented by flow imaging. Four representative pictures are selected for the incubation time of 4 (panel **B**), 6 (**C**), 12 (**D**), 18 (**E**) and 24 h (**F**) after adjusting auto-fluorescence on the negative control (**A**: two upper rows). Ch01 and Ch09 exhibit bright field images, Ch02 detects the fluorophore T, Ch4 represents the PI fluorescence and Ch6 visually expresses the side scattering. A ch04-positive control is included for comparison (**A**: two bottom rows). The scale bar (black bar, bottom right) is 15 μm . Abbreviations: Ch refers to channel; PI to Propidium Iodide; T to the lipid dye.

3. Discussion

Nanomedicine was expected to offer means to revolutionize diagnostics and targeted drug therapies, while improving the cost-effectiveness of health care. Although many of the promises remain to be fulfilled, success stories, even limited in numbers, confirmed its potential. Therefore, focus on addressing the challenges and current limitations might lead to a faster translation from laboratory into clinic [2,18]. There are various means to approach the challenges, from in vitro conditions to more complex in vivo studies. Recently, the intracellular delivery of nanomaterials as well as nanomaterial-associated drugs have attracted increasing attention due to the ever growing interest in subcellular drug targeting [19]. To be able to confirm the intracellular fate of nanoparticles, and optimize their properties to achieve subcellular delivery, we aimed to focus on a rather simple yet often neglected interplay between the nanocarrier and the dye used to follow its fate. To do so, we selected a simple liposomal composition based on the neutral (zwitterionic) phospholipid phosphatidylcholine. Vesicular size, surface charge and modifications, as well as lipid composition, are widely known to affect the liposome internalization rate and mechanism, with a consequent effect on intracellular dispatch [20–24]. However, it is the interplay of these features that determines the biological outcome. Thus, this work intended to provide deeper insight on the effects a fluorophore associated with liposomes can have on the dye-in-liposome system.

To avoid the known effect of size on the internalization behavior [25], all liposomal suspensions were thereby prepared to be of similar size, namely below 200 nm (Table 1). Plain (dye-free) liposomes remained stable in size over a period of 60 days when stored at 4 $^{\circ}\text{C}$ (Figure 2). The zeta-potential,

originally slightly negative or neutral for both plain and dye-in-liposomes, indicated that neither of the dyes was interfering with the surface charge of the liposome (Table 1). However, the surface charge changed, exhibiting an increased negativity as observed over time at 4 °C storage, and potentially prolonging the stability of the suspension.

The findings were in agreement with previously reported low degree of lipid oxidation. Plain conventional liposomes are known to exhibit a slight oxidation tendency over time [26], which has been correlated to a decrease in zeta-potential [27]. Oxidation is indeed known to cause rearrangements of atoms and ions with steric changes of the orientation of lipid polar heads; the computational analysis even proposed the possibility of complete chain reversal of the oxidized phospholipids [28]. Since the zeta-potential measures the interaction of the liposomal surface with counter-ions in the medium, changes in the orientation of the choline zwitterion would result in different ζ -average values [29,30].

In this dynamic model, the presence of a fluorophore in the bilayer thus affects the behavior of the system according to its chemistry and location (Figure 1). The lipid dye (T) exhibited a low superficial interference and better stability against ionic changes in the environment, since this fluorescent moiety is known to reside stably within the core of the lipid bilayer [10]. The surface lipid dye (C), although not charged per se, exhibited a more relevant deviation from the control. This may be explained by the presence of an aromatic group with delocalized charge for interaction with the medium [14].

Interestingly, the characterization of all labeled formulations stored at 25 °C indicated a denser sedimentation over time in comparison to the plain liposomes control. This temperature-dependent physicochemical instability corresponded to the fluorescence instability of the dye in the formulations. The storage at higher temperatures (25 and 37 °C) yielded a progressive decrease in fluorescent signal for all of the dye-containing liposomes. This decrease was not observed to the same extent in the controls, namely the dyes dissolved in methanol, suggesting a direct effect of the medium on the fluorescence stability of the formulation. In the case of the carbocyanine derivative (C), the lower stability in the intact formulation is explained by its known quenching and lower fluorescence in phosphate-buffered saline PBS [13]. When comparing the observed behavior with previously published works on correspondent hydrophilic cyanines, our results are similar to the findings on cyanines freely dissolved in PBS, compared to the cyanines inside the bilayer [14,31]. Although we do not have precise evidence, the findings further corroborate the postulation on the surface localization of the fluorescent moiety in our C dye (Figure 1D). On the contrary, the lipid dye (T) showed a limited reduction in fluorescent signal over time and with increased temperature, which suggested an overall better fluorescence stability, in agreement with published research [11,32]. Remarkably, for both dyes, the fluorophore concentration did affect the (in)stability of the formulation. It was expected that the higher the dye-to-lipid ratio was, the greater the chance to retain a relevant fluorescent signal after storage/incubation would be. This was not verified for the lipid dye (T) as the highest ratio dye-to-lipid exhibited a higher loss of fluorescence signal over time. Hence, the bilayer exerts a physicochemical protection on the fluorophore from the environment (here, in T1, T2 and T3) but a spatial saturation (here, reached in T4) can reduce this protective effect, increasing the exposure of the fluorescent moieties [14,28].

The small radical NO was used as an indicator of the inflammatory response in macrophages as it is a potent inflammatory mediator [33]. Specifically, the LPS used in the present study activated the conversion of L-arginine into L-citrulline with the production of NO as a major byproduct. This unstable radical was quickly converted into NO_3^- and NO_2^- , molecule that the Griess reagent can quantify through a colorimetric reaction. Hence, the quantification of the colored product was first correlated to the NO initial concentration through a NaNO_2 standard curve, and then, correlated to the inflammatory activity of the macrophages [34].

The presence of dye within liposomes did not affect their cytotoxicity, as indicated in Figure 4. Moreover, no difference in cell proliferation was detected when the cells were treated either with dye-containing or dye-free liposomes. Our findings were in full agreement with earlier studies involving keratinocytes with a concentration-dependent increase in cellular proliferation [15]. Keratinocytes are

responsible for the maintenance of the skin barrier where extracellular lipids play a major role [35] and are, therefore, a good model to test potential toxicity. As a second type of cells, we selected macrophages due to their role in interacting with nanocarriers and wide variety of inflammatory diseases [36]. We could not detect liposome-induced proliferative effects in non-inflamed cells (Figure 4A), however, we confirmed a concentration-dependent reduction in NO production after liposomal treatment of LPS-inflamed cells (Figure 5) [16,17]. Although no toxicity was determined for the dye-containing liposomes, we observed larger variability in the readings for NO production in activated macrophages. This was more pronounced for the surface lipid dye (C) and at the highest labeling ratios.

T1 was selected as most suitable formulation for a time-course internalization assay. Our rationale was that if we could successfully follow the fate of liposomes with the least dye content, we would limit possible interference of the dye with biological processes. A weaker fluorescent signal was already registered in the first two hours of incubation, as expected for neutral plain liposomes [37], but almost all cells were screened as positive to the fluorophore after 6 h. In spite of the sharp rising in the number of cells that had internalized liposomes within 2 and 6 h, the progressive linear increase in mean fluorescence confirmed that the internalization capacity of the macrophages was not saturated. These internalization profiles were confirmed in flow imaging and, as expected, the fluorophore did not uniformly distribute in the cytosol and was condensed to intracellular organelles, such as phagosomes and phagolysosomes. Phagocytosis has long been considered the main internalization pathway for liposomes encountering macrophages [20]. Moreover, the presence of a protein phospholipid receptor on the lysosomal membrane is known to facilitate the liposomal recognition by these organelles [38].

When characterizing a labeled nanoscale system such as dye-in-liposomes, the interplay of the different components and the environment can affect not only the leakage of the dye, but also the final biological activities of the system. Therefore, fluorophores that have shown lower tendency to detach from their system (e.g., Cy5-DSPE, [8]) could have unwanted biological effects and/or higher instability of the fluorescent signal, which could explain lack of internalization [6] as possible false-negative results. On the contrary, higher physicochemical stability of the components in the nanosystem (e.g., TopFluor[®]-PC [32]) can then show higher leakage of the fluorophore, with a consequent loss of tracking confidence over time [8].

To summarize, a deep characterization of the nanosystems can be performed by addressing the interplay between its different components. In fact, not only the presence of the dye can affect the physicochemical properties of the system (such as size and zeta potential), the different components within the system can also affect the properties of the dye. Additionally, the fluorescent signal and behavior of the fluorophore in a system can affect both its physicochemical, as well as its biological properties, modulated by a consequent variation of the experimental conditions.

A trade-off has to be considered when choosing a fluorescent dye for a formulation. As a general consideration, time and temperature are the first in line to affect the system stability. Only then, once the effect of different sizes and zeta-potentials are removed, can the steric organization on the nanoscale and the compatibility of the fluorophores with the medium become the predictors of the usability of the system. Leakage information will then be fundamental when designing experiments over selected time frames. This full assessment is necessary for the validation of fluorescence-based assays in the screening of targeting efficiency not only to avoid false-positive results but also not to disregard false-negative promising strategies.

4. Materials and Methods

4.1. Materials

Soy phosphatidylcholine (Lipoid S100, SPC) was generously provided by Lipoid GmbH (Ludwigshafen, Germany). The 1-palmitoyl-2-(dipyrrometheneboron difluoride)undecanoyl-sn-glycero-3-phosphocholine (TopFluor[®]-PC, T) and 1,2-distearoyl-sn-glycero-3-phosphoethanolamine-N-(Cyanine 5) (18:0 Cy5-PE, C) were purchased

from Avanti Polar Lipids, AL, USA. Methanol, naphthylethylenediamine, potassium phosphate monobasic, sodium chloride, sodium phosphate dibasic dodecahydrate, sulfanilamide, phosphoric acid (H_3PO_4), RPMI-1640 medium, Dulbecco's phosphate buffer, lipopolysaccharide (LPS, Escherichia coli, 055:B5) and propidium iodide (PI) were obtained from Sigma-Aldrich, Steinheim, Germany.

4.2. Liposome Preparation

The film hydration method was used to prepare liposomes in aqueous medium [39]. Briefly, lipids were dissolved in methanol in a round-bottomed flask. To form a thin lipid film, low-pressure rotary evaporation was performed on a Büchi Rotavapor R-124 with vacuum pump V-700 (Büchi Labortechnik, Flawil, Switzerland). The film was then resuspended in 8 mL of isotonic phosphate buffer (pH 7.4, 290 mOsm) by hand-shaking and 10 min bath sonication (Branson[®] ultrasonic 5510, Vlierberg, Holland). A concentration of 10 mg/mL of neutral SPC S100 (with over 94% of pure phosphatidylcholine from soybean) was used for all formulations. Fluorescent dyes (T and C) were separately incorporated in the initial lipid mixture at the concentrations of 0.015, 0.030, 0.060 and 0.120 mg/mL, respectively.

The effective size reduction of the multilamellar dispersions was achieved by combining 2 min sonication (Ultrasonic processor 500 W, Sigma-Aldrich, MO, USA) and a stepwise hand extrusion through Nucleopore[®] polycarbonate membranes (with sieving sizes of 400 and 200 nm, respectively). Overnight stabilization was allowed in between the steps and prior to the characterization. All liposomal suspension were then stored in the fridge (4 °C) and at room temperature (25 °C), respectively.

4.3. Liposome Characterization

4.3.1. Size Analysis

Photon correlation spectroscopy was used for the size distribution analysis of liposomes in suspension, as previously described [40]. Submicron particle sizer model 370 (Nicomp Santa Barbara, CA, USA) was set on the vesicle mode and intensity-weighted distribution. All suspensions were diluted in isotonic phosphate buffer to obtain a particle intensity of 400–500 kHz for 15 min/cycle. The sample measurement was repeated on day 0, 15, 30 and 60 to follow the size stability dependency on the storage temperature (4 or 25 °C).

4.3.2. Zeta-Potential Analysis

The zeta-potential distribution was derived from a Gaussian distribution analysis of the electrophoretic mobility, as an indication of liposomal surface charge [39]. Laser Doppler Electrophoresis was applied utilizing a Malvern Zetasizer Nano—ZS (Malvern, Oxford, UK) in the General Purpose mode. All suspensions were diluted 1:20 in deionized water and measured after 15 min equilibration time. Deionized water was chosen over buffer and tap water to ensure the reliability of the measurements, as the presence of the fluorophore tends to interfere with the instrument sensitivity [41]. To further stabilize the measurements, individual runs were performed with a 1 min pause in between to allow the electrodes not to be overheated for high mobility samples. Stability measurements were conducted on day 0, 15, 30 and 60, respectively.

4.4. Fluorescence Analysis

Fluorescence stability of all dye-containing formulations was assessed as a function of storage temperature. All suspension were diluted 1:100 in isotonic phosphate buffer and stored separately in the fridge (4 °C), at room temperature (RT, 25 °C) and in the incubator (Termaks, Bergen, Norway) at 37 °C. Sampling for top fluorescence intensity reading was performed with a recurrence of 24 h for 7 days (Tecan SPARK spectrofluorometer, Tecan, Switzerland). Gain and wavelength (λ) of excitation (ex) and emission (em) were optimized on the full scan of the formulations, on Day 0, and maintained throughout the experiment (T: $\lambda_{ex} = 430$ nm, $\lambda_{em} = 510$ nm, C: $\lambda_{ex} = 600$ nm, $\lambda_{em} = 665$ nm; gain = 90). The same procedure was used to read each dye's own stability in methanol.

4.5. Biological Activity In Vitro

Murine macrophages RAW 264.7 (ATCC[®] TIB-71TM, ATCC, Manassas, USA) and human immortalized keratinocytes HaCaT (ATCC, Manassas, USA) were cultured in flasks and incubated at 37 °C with 5% CO₂. RPMI-1640 medium was used to culture the cells, supplemented with the addition of 10% (v/v) fetal bovine serum and antibiotics (penicillin-streptomycin). Complete medium was also used to pre-dilute all liposomal formulations right before treating the cells [15,39].

4.5.1. Cytotoxicity Assay

Cell toxicity of all formulations was evaluated using the Cell Counting Kit-8 (Sigma-Aldrich Chemie) as a function of dehydrogenase activity, directly proportional to cell viability in macrophages (RAW 264.7) and keratinocytes (HaCaT) [15]. To 90 µL/well of cell suspension (1×10^5 cells/mL, pre-incubated overnight in 96 wells), 10 µL of either medium (control) or liposomes were added. Three concentrations of liposomes (1, 10 and 50 µg/mL of lipids), each in triplicates, were exposed to the cells to observe the cytotoxic effect. At the 24 h endpoint, CCK-8 reagent (10 µL/well) was applied and plates were further incubated for 4 h. The detection of the absorbance was set on 450 nm and referenced at 650 nm (Tecan SPARK spectrophotometer, Tecan, Switzerland).

4.5.2. Anti-Inflammatory Activity

The anti-inflammatory effects of all liposomal formulations were analyzed on LPS-activated macrophages (RAW 264.7) by measuring the inhibition on the nitric oxide production [39]. Cells were cultured in RPMI-1640 supplemented medium until the formation of a confluent monolayer. The homogenous cell suspension (5×10^5 cells/mL) was plated into a 24-well plate (1 mL/well) and incubated for 24 h. The old medium was replaced with 990 µL of LPS-containing medium (1 µg/mL of LPS) in order to induce inflammation. All formulations (10 µL each) were applied in triplicates for three different concentration of lipids (1, 10 and 50 µg/mL per well, respectively). After 24 h incubation, the anti-inflammatory response was quantified by measuring NO production in the medium by the cells with the Greiss reagent (1% sulfanilamide, 0.1% naphthylethylenediamine, 2.5% H₃PO₄). Spectrophotometric endpoint measurements were performed at 540 nm and evaluated through a NaNO₂ standard curve (Single Cuvette UV Vis Spectrophotometer, SpectraMax 190 with SoftMax Pro v5 software, Molecular devices, CA, USA).

4.5.3. Flow Cytometry

The time dependency of liposomal uptake in macrophages was quantified by flow cytometry (FACSAria[™] with FACSDiva software version 8.0.1, BD Biosciences, San Jose, CA, USA) Macrophages (RAW 264.7) were seeded on 6-well plates 24 h prior to the treatment (3 mL/well). Liposomes (T1) were freshly pre-diluted in complete RPMI-1640 (50 µg/mL per well) and the suspension was used to change the medium in each well. At the endpoints of 1, 2, 4, 6, 12, 18 and 24 h, cells were washed with Dulbecco's phosphate buffer and suspended in 800 µL of fresh RPMI-1640 by pipetting. Propidium iodide (PI) was added to the filtered cell suspensions to single out live cells, which were gated as PI-negative (PI-A-). Ten thousand events were recorded and liposomal uptake was measured on the correspondent channel (T-A) after adjusting for cell/medium auto-fluorescence of the untreated control [42].

4.5.4. Flow Imaging

Fluorescence-activated cell sorting was performed on the T-A+, PI-A- population, which was concentrated and visualized with a flow imaging system (ImageStreamX[®] with IDEAS software version 6, Amnis, Seattle, WA, USA). Cells were gated in the forward vs. side scattering diagram to exclude the signal from running calibration beads. Live cells were then located as low Channel 4 intensity (Ch4, 610/30 nm) and 100 pictures were recorded with 60X magnification and max sensitivity. Both cameras

were activated to obtain bright field images and confirm the presence of a cell in the stream (Ch1 and Ch9). Furthermore, side scattering was recorded to confirm the granularity of macrophages (Ch6, 762/35). The liposome uptake was imaged in green fluorescence (Ch02, 528/65 nm) after 4, 6, 12, 18 and 24 h. Untreated live and dead cells were also imaged, as negative and positive controls, respectively, to adjust for auto-fluorescence and validate the gating tree [43].

4.6. Statistical Analysis

One-way ANOVA with Bonferroni's multiple comparisons post test was used to assess statistical significance. Significance was assigned for p value < 0.05 (GraphPad Prism version 8.1.2 for Windows, GraphPad Software, La Jolla CA, USA).

5. Conclusions

A thorough physicochemical and biological characterization of dye-containing nanosystems is required to fully benefit from the enormous potential of the fluorescence-based techniques in tracing the fate of nanocarriers. When introducing a fluorescent dye, the individual properties of both free dye and unlabeled nanocarrier, as well as their stability and behavior, can be affected by the experimental conditions, namely medium, temperature, time, dye localization and concentration. Therefore, deeper characterization of the dye-containing nanocarriers can assure the interpretation accuracy of the fluorescence-based assays. This can be considered the key to success in optimizing new drug delivery systems.

Author Contributions: Conceptualization, J.C., A.M.H. and N.Š.-B.; Data curation, J.C., M.N., and P.B.; Formal analysis, J.C.; Funding acquisition, N.Š.-B.; Investigation, J.C.; Methodology, J.C., M.N. and P.B.; Project administration, N.Š.-B.; Resources, N.Š.-B.; Supervision, A.M.H. and N.Š.-B.; Validation, J.C.; Visualization, J.C.; Writing—original draft, J.C. and N.Š.-B.; Writing—review and editing, all authors. All authors have read and agreed to the published version of the manuscript.

Funding: This project has received funding from the European Union's Horizon 2020 research and innovation programme under the Marie Skłodowska-Curie grant agreement No. 766181. The publication charges for this article have been funded by a grant from the publication fund of UiT The Arctic University of Norway.

Acknowledgments: The authors would like to thank Roy A. Lyså for the technical support at the imaging facilities, Lipoid GmbH (Ludwigshafen, Germany) for providing the lipid used to prepare liposomes and UiT The Arctic University of Norway for publishing fund.

Conflicts of Interest: The authors declare no conflict of interest.

Abbreviations

C	1,2-distearoyl-sn-glycero-3-phosphoethanolamine-N-(Cyanine 5) (18:0 Cy5-PE), surface lipid dye
CCK-8	Cell Counting Kit-8 (Sigma-Aldrich Chemie)
MW	Molecular weight
NO	Nitric oxide
PdI	Polydispersity index
PI	Propidium iodide
RT	Room temperature, 25 °C
SPC	Soy phosphatidylcholine (Lipoid S100)
T	1-palmitoyl-2-(dipyrrometheneborondifluoride)undecanoyl-sn-glycero-3-phosphocholine (TopFluor®-PC), lipid dye
	Water-soluble tetrazolium salt, main
WST-8	reagents of the Cell Counting Kit-8 (Sigma-Aldrich Chemie, Patent No. WO97/38985); [2-(2-methoxy-4-nitrophenyl)-3-(4-nitrophenyl)-5-(2,4-disulfophenyl)-2H-tetrazolium, monosodium salt]

References

1. Park, K. The beginning of the end of the nanomedicine hype. *J. Control. Release* **2019**, *305*, 221–222. [[CrossRef](#)]
2. Martins, J.P.; das Neves, J.; de la Fuente, M.; Celia, C.; Florindo, H.; Gunday-Tureli, N.; Popat, A.; Santos, J.L.; Sousa, F.; Schmid, R.; et al. The solid progress of nanomedicine. *Drug Deliv. Transl. Res.* **2020**, *10*, 726–729. [[CrossRef](#)] [[PubMed](#)]
3. Greish, K.; Mathur, A.; Bakhiet, M.; Taurin, S. Nanomedicine: Is it lost in translation? *Ther. Deliv.* **2018**, *9*, 269–285. [[CrossRef](#)]
4. Le, N.T.T.; Cao, V.D.; Nguyen, T.N.Q.; Le, T.T.H.; Tran, T.T.; Hoang Thi, T.T. Soy Lecithin-Derived Liposomal Delivery Systems: Surface Modification and Current Applications. *Int. J. Mol. Sci.* **2019**, *20*, 4706. [[CrossRef](#)]
5. Ducat, E.; Evrard, B.; Peulen, O.; Piel, G. Cellular uptake of liposomes monitored by confocal microscopy and flow cytometry. *J. Drug Deliv. Sci. Technol.* **2011**, *21*, 469–477. [[CrossRef](#)]
6. Snipstad, S.; Har, S.; Baghirov, E.; Sulheim, E.; Mørch, Y.; Lélou, S.; von Haartman, E.; Bäck, M.; Nilsson, K.P.R.; Klymchenko, A.S.; et al. Labelling nanoparticles: Dye leakage and altered cellular uptake. *Cytometry Part A* **2017**, *91A*, 760–766. [[CrossRef](#)]
7. Rodriguez-Lorenzo, L.; Fytianos, K.; Blank, F.; Von Garnier, C.; Rothen-Rutishauser, B.; Petri-Fink, A. Fluorescence-Encoded Gold Nanoparticles: Library Design and Modulation of Cellular Uptake into Dendritic Cells. *Small* **2014**, *10*, 1341–1350. [[CrossRef](#)] [[PubMed](#)]
8. Münter, R.; Kristensen, K.; Pedersbæk, D.; Bruun Larsen, J.; Simonsen, J.J.; Andersen, T.L. Dissociation of fluorescently labeled lipids from liposomes in biological environments challenges the interpretation of uptake studies. *Nanoscale* **2018**, *10*, 22720–22724. [[CrossRef](#)]
9. Kleusch, C.; Hersch, N.; Hoffmann, B.; Merkel, R.; Csiszar, A. Fluorescent lipids: Functional parts of fusogenic liposomes and tools for cell membrane labeling and visualization. *Molecules* **2012**, *17*, 1055–1073. [[CrossRef](#)] [[PubMed](#)]
10. Kay, J.G.; Koivusalo, M.; Ma, X.; Wohland, T.; Grinstein, S. Phosphatidylserine dynamics in cellular membranes. *Mol. Biol. Cell* **2012**, *23*, 2198–2212. [[CrossRef](#)] [[PubMed](#)]
11. Regan, D.; Williams, J.; Borri, P.; Langbein, W. Lipid bilayer thickness measured by quantitative DIC reveals phase transitions and effects of substrate hydrophilicity. *Langmuir* **2019**, *35*, 13805–13814. [[CrossRef](#)] [[PubMed](#)]
12. Sercombe, L.; Veerati, T.; Moheimani, F.; Wu, S.Y.; Sood, A.K.; Hua, S. Advances and Challenges of Liposome Assisted Drug Delivery. *Front. Pharmacol.* **2015**, *6*, 286. [[CrossRef](#)] [[PubMed](#)]
13. Claassen, E. Post-formation fluorescent labelling of liposomal membranes: In Vivo detection, localisation and kinetics. *J. Immunol. Methods* **1992**, *147*, 231–240. [[CrossRef](#)]
14. Valdes-Aguilera, O.; Cincotta, L.; Foley, J.; Kochevar, I. Photobleaching of a cyanine dye in solution and in membranes. *J. Photochem. Photobiol.* **1987**, *45*, 337–344. [[CrossRef](#)] [[PubMed](#)]
15. Ternullo, S.; Basnet, P.; Holsaeter, A.M.; Flaten, G.E.; de Weerd, L.; Škalko-Basnet, N. Deformable liposomes for skin therapy with human epidermal growth factor: The effect of liposomal surface charge. *Eur. J. Pharm. Sci.* **2018**, *125*, 163–171. [[CrossRef](#)]
16. Giordani, B.; Basnet, P.; Mishchenko, E.; Luppi, B.; Škalko-Basnet, N. Utilizing Liposomal Quercetin and Gallic Acid in Localized Treatment of Vaginal Candida Infections. *Pharmaceutics* **2020**, *12*, 9. [[CrossRef](#)]
17. Basnet, P.; Hussain, H.; Tho, I.; Skalko-Basnet, N. Liposomal delivery system enhances anti-inflammatory properties of curcumin. *J. Pharm. Sci.* **2012**, *101*, 598–609. [[CrossRef](#)]
18. Wu, L.-P.; Wang, D.; Li, Z. Grand challenges in nanomedicine. *Mater. Sci. Eng. C* **2020**, *106*, 110302. [[CrossRef](#)]
19. Azevedo, C.; Macedo, M.H.; Sarmiento, B. Strategies for the enhanced intracellular delivery of nanometrials. *Drug Discov. Today* **2018**, *23*, 944–959. [[CrossRef](#)] [[PubMed](#)]
20. Ahsan, F.; Rivas, I.P.; Khan, M.A.; Suárez, A.I.T. Targeting to macrophages: Role of physicochemical properties of particulate carriers—liposomes and microspheres—on the phagocytosis by macrophages. *J. Control. Release* **2002**, *79*, 29–40. [[CrossRef](#)]
21. Kelly, C.; Jefferies, C.; Cryan, S.A. Targeted liposomal drug delivery to monocytes and macrophages. *J. Drug Deliv.* **2011**, 1–11. [[CrossRef](#)] [[PubMed](#)]
22. Signorell, R.D.; Luciani, P.; Brambilla, D.; Leroux, J.-C. Pharmacokinetics of lipid-drug conjugates loaded into liposomes. *Eur. J. Pharm. Biopharm.* **2018**, *128*, 188–199. [[CrossRef](#)] [[PubMed](#)]
23. Nag, O.K.; Delehanty, J.B. Active Cellular and Subcellular Targeting of Nanoparticles for Drug Delivery. *Pharmaceutics* **2019**, *11*, 543. [[CrossRef](#)] [[PubMed](#)]

24. Manzanares, D.; Cena, V. Endocytosis: The Nanoparticle and Submicron Nanocompounds Gateway into the Cell. *Pharmaceutics* **2020**, *12*, 371. [[CrossRef](#)]
25. Hoshyar, N.; Gray, S.; Han, H.; Bao, G. The effect of nanoparticle size on in vivo pharmacokinetics and cellular interactions. *Nanomedicine* **2016**, *11*, 673–692. [[CrossRef](#)] [[PubMed](#)]
26. Guldiken, B.; Gibis, M.; Boyacioglu, D.; Capanoglu, E.; Weiss, J. Physical and chemical stability of anthocyanin-rich black carrot extract-loaded liposomes during storage. *Food Res. Int.* **2018**, *108*, 491–497. [[CrossRef](#)] [[PubMed](#)]
27. Mosca, M.; Ceglie, A.; Ambrosone, L. Effect of membrane composition on lipid oxidation in liposomes. *Chem. Phys. Lipids* **2011**, *164*, 158–165. [[CrossRef](#)]
28. Khandelia, H.; Mouritsen, O.G. Lipid gymnastics: Evidence of complete acyl chain reversal in oxidized phospholipids from molecular simulations. *Biophys. J.* **2009**, *96*, 2734–2743. [[CrossRef](#)]
29. Makino, K.; Yamada, T.; Kimura, M.; Oka, T.; Ohshima, H.; Kondo, T. Temperature- and ionic strength-induced conformational changes in the lipid head group region of liposomes as suggested by zeta potential data. *Biophys. Chem.* **1991**, *41*, 175–183. [[CrossRef](#)]
30. Mozuraityte, R.; Rustad, T.; Storror, I. Oxidation of cod phospholipids in liposomes: Effects of salts, pH and zeta potential. *Eur. J. Lipid Sci. Technol.* **2006**, *108*, 944–950. [[CrossRef](#)]
31. Texier, I.; Goutayer, M.; Da Silva, A.; Guyon, L.; Djaker, N.; Jossierand, V.; Neumann, E.; Bibette, J.; Vinet, F. Cyanine-loaded lipid nanoparticles for improved in vivo fluorescence imaging. *J. Biomed. Opt.* **2009**, *14*, 1–11. [[CrossRef](#)] [[PubMed](#)]
32. Draffehn, S.R.; Kumke, M.U. Monitoring the collapse of pH-sensitive liposomal nanocarriers and environmental pH simultaneously: A fluorescence-based approach. *Mol. Pharm.* **2016**, *13*, 1608–1617. [[CrossRef](#)] [[PubMed](#)]
33. Bredt, D.S.; Snyder, S.H. Nitric oxide: A physiologic messenger molecule. *Annu. Rev. Biochem.* **1994**, *63*, 175–195. [[CrossRef](#)] [[PubMed](#)]
34. Tsikas, D. Methods of quantitative analysis of the nitric oxide metabolites nitrite and nitrate in human biological fluids. *Free Radic. Res.* **2005**, *39*, 797–815. [[CrossRef](#)] [[PubMed](#)]
35. Feingold, K.R. Thematic review series: Skin lipids. The role of epidermal lipids in cutaneous permeability barrier homeostasis. *J. Lipid Res.* **2007**, *48*, 2531–2546. [[CrossRef](#)]
36. He, W.; Kapate, N.; Shields IV, C.V.; Mitragotri, S. Drug delivery to macrophages: A review of targeting drugs and drug carriers to macrophages for inflammatory diseases. *Adv. Drug Deliv. Rev.* **2019**. (Epub ahead of print). [[CrossRef](#)]
37. Raz, A.; Bucana, C.; Fogler, W.E.; Poste, G.; Fidler, I.J. Biochemical, morphological, and ultrastructural studies on the uptake of liposomes by murine macrophages. *Cancer Res.* **1981**, *41*, 487–494.
38. Conrad, K.S.; Cheng, T.W.; Ysselstein, D.; Heybrock, S.; Hoth, L.R.; Chrunky, B.A.; Am Ende, C.W.; Krainc, D.; Schwake, M.; Saftig, P.; et al. Lysosomal integral membrane protein-2 as a phospholipid receptor revealed by biophysical and cellular studies. *Nat. Commun.* **2017**, *8*, 1908. [[CrossRef](#)]
39. Jørholm, M.W.; Basnet, P.; Acharya, G.; Škalko-Basnet, N. PEGylated liposomes for topical vaginal therapy improve delivery of interferon alpha. *Eur. J. Pharm. Biopharm.* **2017**, *113*, 132–139. [[CrossRef](#)]
40. Ternullo, S.; de Weerd, L.; Holsaeter, A.M.; Flaten, G.E.; Skalko-Basnet, N. Going skin deep: A direct comparison of penetration potential of lipid-based nanovesicles on the isolated perfused human skin flap model. *Eur. J. Pharm. Biopharm.* **2017**, *121*, 14–23. [[CrossRef](#)]
41. Wu, I.Y.; Skalko-Basnet, N.; di Cagno, M.P. Influence of the environmental tonicity perturbations on the release of model compounds from large unilamellar vesicles (LUVs): A mechanistic investigation. *Colloids. Surf. B* **2017**, *157*, 65–71. [[CrossRef](#)] [[PubMed](#)]
42. Bellavance, M.A.; Poirier, M.B.; Fortin, D. Uptake and intracellular release kinetics of liposome formulations in glioma cells. *Int. J. Pharm.* **2010**, *395*, 251–259. [[CrossRef](#)] [[PubMed](#)]
43. Wayne, E.C.; Long, C.; Haney, M.J.; Batrakova, E.V.; Leisner, T.M.; Parise, L.V.; Kabanov, A.V. Targeted Delivery of siRNA Lipoplexes to Cancer Cells Using Macrophage Transient Horizontal Gene Transfer. *Adv. Sci.* **2019**, *6*, 1900582. [[CrossRef](#)] [[PubMed](#)]



Paper 2

Fluorescence fluctuations-based super-resolution microscopy techniques: an experimental comparative study

Ida S. Opstad ^{1†#}, Sebastian Acuña ^{1#}, Luís Enrique Villegas Hernandez ^{1#}, Jennifer Cauzzo ², Nataša Škalko-Basnet ², Balpreet S. Ahluwalia ^{1,3}, Krishna Agarwal ^{1*}

¹Nanoscopy Research Group, Department of Physics and Technology, UiT – The Arctic University of Norway, Tromsø, Norway.

²Drug Transport and Delivery Research Group, Department of Pharmacy, UiT – The Arctic University of Norway, Tromsø, Norway.

³Department of Clinical Science, Intervention and Technology – CLINTEC Karolinska Institute, Sweden.

Correspondence: † ida.s.opstad@uit.no, * uthkrishth@gmail.com.

These authors contributed equally to the study

Abstract

Fluorescence fluctuations-based super-resolution microscopy (FF-SRM) is an emerging field promising low-cost and live-cell compatible imaging beyond the resolution of conventional optical microscopy. A comprehensive overview on how the nature of fluctuations, label density, out-of-focus light, subcellular dynamics, and the sample itself influence the reconstruction in FF-SRM is crucial to design appropriate biological experiments. We have experimentally compared several of the recently developed FF-SRM techniques (namely ESI, bSOFI, SRRF, SACD, MUSICAL and HAWK) on widefield fluorescence image sequences of a diverse set of samples (namely liposomes, tissues, fixed and living cells), and on three-dimensional simulated data where the ground truth is available. The simulated microscopy data showed that the different techniques have different requirements for signal fluctuation to achieve their optimal performance. While different levels of signal fluctuations had little effect on the SRRF, ESI and SACD images, image reconstructions from both bSOFI and MUSICAL displayed a substantial improvement in their noise rejection, z-sectioning, and overall super-resolution capabilities.

Teaser

We compare the performance of novel super-resolution imaging methods on challenging but realistic microscopy data.

Abbreviations

(b)SOFI: (balanced) super-resolution optical fluorescence imaging

ESI: entropy-based super-resolution imaging

FF-SRM: fluorescence fluctuations-based super-resolution microscopy

HAWK: Haar wavelet kernel

MUSICAL: multiple signal classification algorithm

TIRFM: total internal reflection fluorescence microscopy

SACD: super-resolution imaging with autocorrelation two-step deconvolution

SBR: signal-to-background ratio

SIM: structured illumination microscopy

SNR: signal-to-noise ratio

SMLM: single molecule localization microscopy

SRM: super-resolution microscopy

SRRF: super-resolution radial fluctuations

SRM: Super-resolution microscopy

STED: stimulated emission depletion microscopy

2D/3D: two/three-dimensional

Introduction

Super-resolution microscopy (SRM) has revolutionized the field of microscopy, allowing visualization of nanoscale sub-cellular details smaller than the diffraction limit of optical microscopy. The spectrum of techniques in SRM is spanned by single molecule localization microscopy (SMLM), stimulated emission depletion microscopy (STED) and structured illumination microscopy (SIM). All SRM techniques require an expensive high-end acquisition system, expert sample preparation and system operation. Live-cell imaging is demonstrated for all of these SRM techniques [1] but remains quite challenging especially because of two reasons. Firstly, the fast dynamics of many cellular processes, in combination with relatively weak fluorescent signal, render the acquisition of sufficient signal-to-noise ratio (SNR) challenging for most analytical tasks. We make the distinction between image *noise* resulting from the camera electronics and photon arrival statistics, and image *background* resulting from e.g., out-of-focus sample features and unbounded dye molecules. Both image noise and

background signal cause reduced image contrast and often similar analytical challenges but are inherently distinct phenomena.

Secondly, the cellular functions and morphology are sensitive to small changes in the cellular biochemical environment that can be significantly altered by introducing fluorescent probes, imaging buffers and excitation light exposure. As a consequence, SIM is arguably the best SRM technique for living samples currently available due to its comparatively fast widefield and volumetric acquisition together with lesser requirements on fluorophore photophysical properties and illumination intensities. However, under sub-optimal acquisition conditions such as fast-moving samples, low signal-to-background ratio (SBR) and/or significant photobleaching, SIM reconstruction is often unreliable and prone to artifacts. Furthermore, the SIM imaging systems are not commonly available, likely due to their cost and complexity, and the requirement for trained personnel for system maintenance and operation. Recent development of SIM encompasses both algorithmic improvements enabling successful reconstruction under less favorable signal and noise conditions [2,3] and efforts towards reducing the system overall cost and complexity [4,5].

There is a new set of techniques, namely fluorescence fluctuations-based super-resolution microscopy (FF-SRM) techniques that, like SMLM, use the photokinetics of fluorescence emission, but do not rely on the external introduction of spatiotemporal sparsity via the chemical environment and high-power laser modulation. This is an interesting avenue for bio-image analysis, possibly with the potential of democratizing SRM by greatly reduced system cost, and overall live-cell capabilities of high-resolution microscopy. The core phenomenon utilized in FF-SRM is the stochasticity of the number of photons emitted by fluorescent labels over time. These techniques use statistical analysis as the core mechanism to super-resolve the fluorescent molecule distribution, where each molecule independently contributes to fluctuations in the measured fluorescence intensity. FF-SRM in the context of super-resolution fluorescence microscopy techniques is presented in Figure 1.

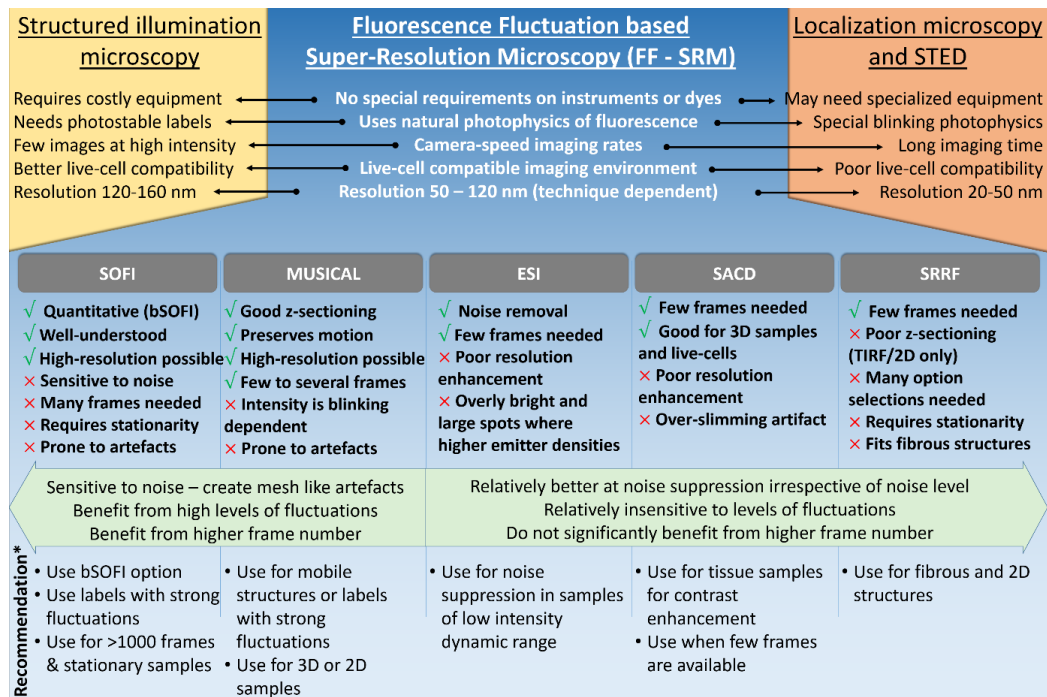


Figure 1. Summary and overview. Comparison to other super-resolution microscopy techniques and summary of our observations and recommendations for FF-SRM.

Although the development of FF-SRM techniques is fairly recent, several techniques have been proposed in the short duration of a few years. Each of these techniques differs in the treatment of the raw data and statistical approach used. Some of them are super-resolution optical fluorescence imaging (SOFI) [6] and balanced SOFI (bSOFI) [7], entropy-based super-resolution imaging (ESI) [8], super-resolution radial fluctuations (SRRF) [9], multiple signal classification algorithm (MUSICAL) [10], super-resolution imaging with autocorrelation two-step deconvolution (SACD) [11], Bayesian analysis of blinking and bleaching (3B) [12], and sparsity based super-resolution correlation optical microscopy (SPARCOM) [13]. Additionally, the data pre-processing technique Haar wavelet kernel (HAWK) analysis has been developed as a tool to enable SRM of higher-density emitter data for both SMLM and FF-SRM, thus ‘enabling high-speed, artifact-free super-resolution imaging of live cells’ [14]. As evaluated and benchmarked in the original papers (by using reference examples from single molecule localization microscopy dataset and simulation examples), they provide a resolution in the range of 50-120 nm. Notably, all of the above-mentioned FF-SRM techniques use two-dimensional (2D) PSF considerations only (not 3D), and the simulated emitters lie perfectly in the focal plane, except for the noteworthy exception shown by Solomon et al. [13], where also emitters at 1 μm distance from the focal plane were considered. Development for 3D SOFI has been demonstrated by Yeh and Waller in combination with speckle illumination [15], and by

Purohit et al. in combination with a specialized phase plate for the encoding of emitter axial position [16]. Furthermore, a detailed analysis of the artifacts of high order SOFI and discussions on how it can affect bSOFI reconstructions together with some proposed solution have been provided by Yi et al. [17,18]. The FF-SRM methods applied in this review ((b)SOFI, ESI, SRRF, MUSICAL, SACD and HAWK) together with their reconstruction parameters are further described in the Methods section under *Nanoscopy algorithms and their parameters*.

When imaging real three-dimensional samples for biological or biomedical applications, the reliability of the reconstruction is of more significance than any of the quantitative merits such as the image resolution or contrast. This is especially because common resolution assessment methods applied in microscopy can confuse reconstruction artifacts as high-resolution image content. We are not aware of any comprehensive study of how these methods perform on real biological samples in comparison to each other and under various conditions of intensity fluctuation.

Each of the methods has been demonstrated on experimental data of samples that have been arguably designed to illustrate the best characteristics of their own method or on SMLM benchmark data in which case all the methods benefit from the spatio-temporal sparsity in the fluorescence. A comparative study of these techniques on a wide variety of data is important to understand the opportunities and potential pitfalls of the different methods. The aim is not to identify a winner technique or criticize another, but to create an understanding and appreciation of the realistic aspects that will help application scientists in designing their studies better and deriving reliable interpretations using any of these approaches. Moreover, such a comparative study will contribute to setting the right expectations and assigning suitable confidence in the biological interpretations derived from these methods.

In order to do so, an in-depth analysis is needed on the sample and imaging conditions and how they affect the performances of the different FF-SRM methods. For example, how the sample and label density, out-of-focus signal, nature of fluctuations, and sub-cellular dynamics affect the reconstructions would be insightful for the experimental design and choice of technique. To this end, we have undertaken a first large-scale experimental study of FF-SRM techniques covering the following aspects:

1. We present an extensive study encompassing nanoparticles (liposomes), actin and membrane in fixed cells and tissues, and mitochondria and the endoplasmic reticulum (ER) in living cells.
2. We tested all the methods on exactly the same data, thereby performing the first unbiased comparative analysis of the performances of the techniques. In most situations, factors such as fluctuation density, number of frames, and a variety of relevant conditions for imaging or processing the data are considered. The control parameters of each method are tuned within reasonable limits to identify the best performance of the method and the related algorithmic settings.
3. We elucidate the performances of the techniques through three-dimensional (3D) simulation examples that closely emulate the sample conditions. We explain how and why the actual samples challenge the fluctuations-based techniques beyond the scope of design. We consider effects such as out-of-focus light, density of labeling, temporal density of photon emission, practical noise models and the number of frames used for reconstruction.
4. We elucidate the favorable conditions for methods and highlight the challenges that must be addressed in the algorithmic development of these FF-SRM techniques towards making them reliable tools in biomedical research.

Results

Optimal Data

For the right type of data, all the tested FF-SRM techniques perform well. This is illustrated in Figure 2 with a comparison to both the conventional image (sum of frames) and the SMLM algorithm STORM. This is a type of data where SRM methods are most often benchmarked and evaluated: 2D distribution of cytoskeletal strands. The emission is sparse but of good quality (i.e. high SBR). During the acquisition time of 1 frame, most of the emitters are in the dark state, but during the course of the acquisition of the entire data sequence used for analysis, most fluorescent molecules have emitted signal at least once. This characterizes what in this manuscript is often called a high fluctuation level. The signal variance during an image sequence is high. On the contrary, if all emitters were emitting the same across all time points, the variance would be zero and no resolution improvement would be obtainable from the image sequence.

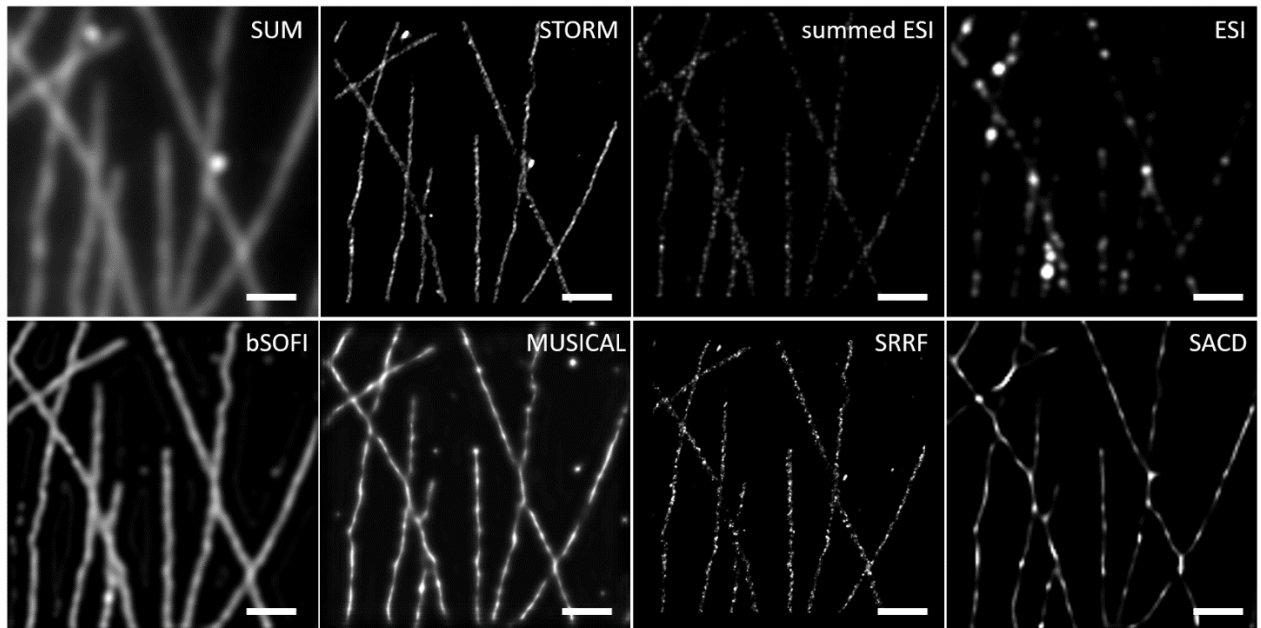


Fig. 2. Results on optimal data. The panels display reconstruction results on experimental 2D data for SMLM. The data set consisted of 15000 images of a sparsely emitting sample of microtubules. All images were used in the reconstructions, except for MUSICAL and SACD, where only 1500 images were used (due to their higher requirements on memory and processing time). The scale bars are $1\mu\text{m}$.

For the rest of this manuscript, we will consider realistic data which may be sub-optimal in the above-mentioned terms due to various inevitable characteristics of biological samples and studies: The samples extend in three dimensions and have signal fluctuations as obtained by using conventional fluorescence microscopy and common labels for microscopy. In some cases, the labeled structures may be dynamic, for example in living cell or suspended sample. We consider these samples to much more realistically represent the challenges and conditions encountered in actual biological studies, and unfortunately, also far away from the conditions usually used for technological benchmarking.

Simulated Data

To obtain fair and definitive answers about the different methods' performance, simulated samples with known ground truth were generated. Two different 3D test samples with varying levels of intensity fluctuations were generated and processed using ESI, SRRF, SACD, SOFI and MUSICAL. The ground truth emitter locations with axial color coding as a distance from the focal plane are displayed in the upper panels of Figure 3, while their corresponding microscopy images are displayed in the panels below (simulating 510 nm emission wavelength and 1.42 NA microscope objective).

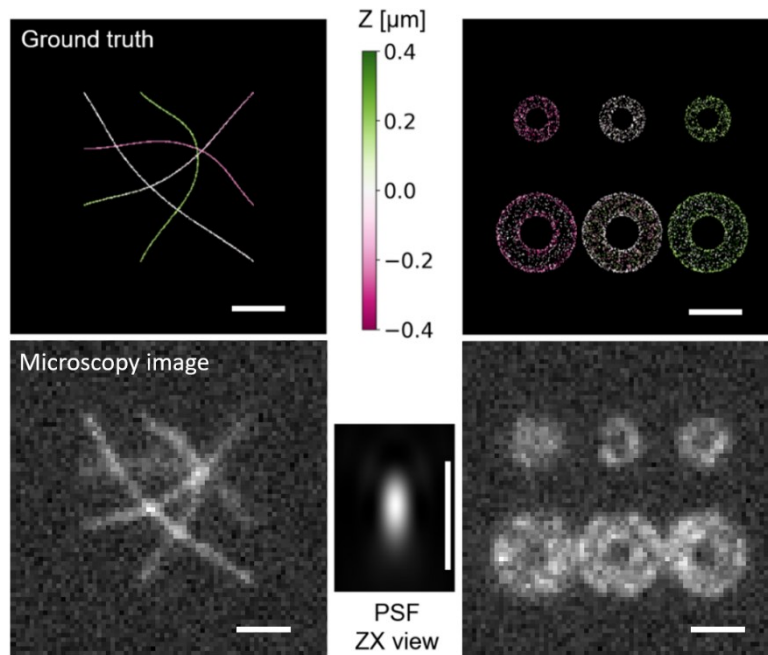


Fig. 3. Synthetic image data. The top row displays the simulated data's ground truth with color coded z-position compared to the focal plane ($Z=0$). The bottom row shows the corresponding microscopy images (single frames) after noise addition and the simulated PSF (orthogonal view) using 1.42NA and emission wavelength 510 nm. The Abbe resolution limits under these conditions are laterally 180 nm and axially 506 nm. The scale bars are 1 μm .

The biological relevance and structural details of the two samples are as follows:

1. **Actin strands.** There are four non-intersecting actin strands. Three strands are parallel with the coverglass in different z-planes, one in the focal plane and two of them above and below the focal plane by 0.4 μm respectively. The fourth actin strand is inclined and positioned across several z-planes, having one end 0.2 μm below and the other 0.2 μm above the focal plane. None of the strands are physically touching, but their (projected) microscopy image has overlapping signal in the regions where their lateral positioning is the same. These overlapping regions are where the algorithms' performance is of particular interest.
2. **Tori (hollow doughnuts).** The upper row of tori corresponds to tubes of 200 nm diameter, while the lower row has tubes of 400 nm diameter. Both rows have tori centered at three different z-positions. The tori in the lower row are resolvable using conventional microscopy, while the tori in the upper row are not. These structures were chosen to emulate significant cellular organelles like mitochondria and the endoplasmic reticulum (ER) which are outlined by 3D tubular membranes. To resolve

both the inner and outer peripheries, the FF-SRM methods must exhibit a good z-sectioning, recognition of small intensity differences but only minor lateral resolution improvement compared to the diffraction limit of optical microscopy.

A higher number of frames for the reconstructions (5000 frames) were used for ESI and SOFI compared to the other techniques (16 to 100 frames). This was due to negative results of initial testing, their capability of fast computations for larger stack sizes, together with the much higher frame number indicated by the methods' original publications.

We will especially consider three aspects of the reconstructions: i) background signal and effect of noise, ii) reconstruction quality and artifacts, iii) the effect of out-of-focus objects and z-sectioning abilities.

Actin Strand Simulations

The best results achieved from a variation of tested parameters by the five FF-SRM methods are displayed in Figure 4 in the case of simulated 3D actin strands for different levels of intensity fluctuations. A higher level of intensity fluctuations was achieved via sparser fluorescence emission from individual molecules on a densely labelled sample. Measured in terms of image frames, the emitter on time was for all samples kept at 1, while the different fluctuation levels were generated by varying the emitter off time between 3, 9 and 19, the longer the off time, the higher the fluctuation level (and image stack standard deviation). The simulations are further described in the supplementary information.

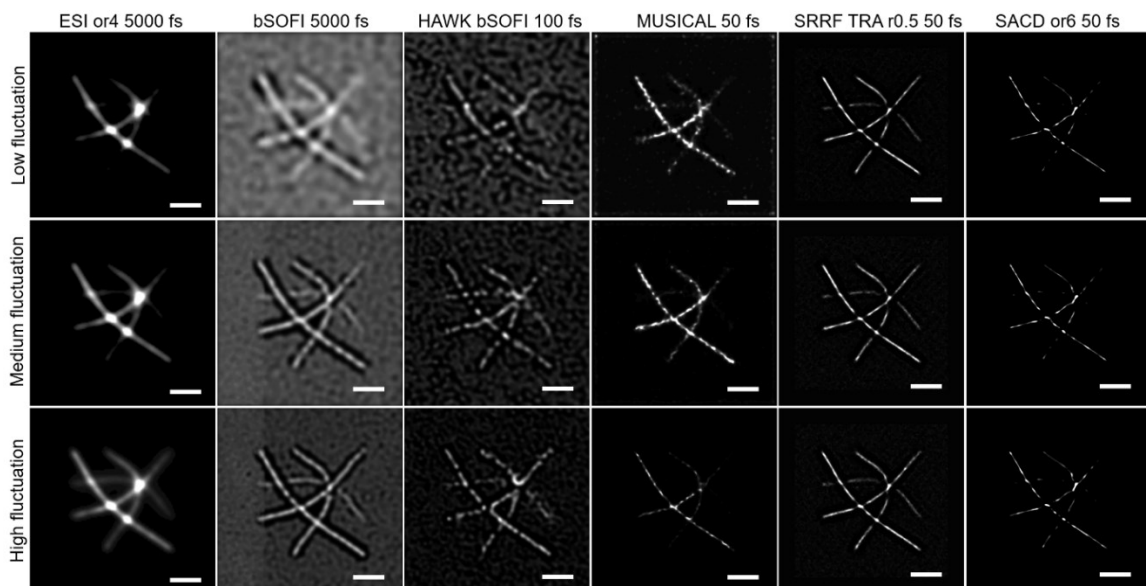


Fig. 4. Results on simulated actin strands. FF-SRM reconstructions of simulated actin strands for three different levels of fluctuations for all five tested methods. Note that only

one of the strands lies completely in the focal plane. The bSOFI and MUSCIAL images are clearly improved for higher fluctuation levels, while the ESI, SRRF and SACD images display no improvement for higher levels of fluctuations. The headers indicate method and some details about the reconstruction parameters: fs: number of frames; or: order; TRA r0.5: temporal radiality average with SRRF ring radius 0.5. The ESI images are intensity adjusted using $\gamma = 0.5$ intensity adjusted, while all other panels have linearly adjusted intensities. The scale bars are 1 μm

The noise present in the simulated microscopy images (Figure 3) appears not to pose a challenge to ESI, SRRF or SACD. The structural representations are accurate except at the intersections of the actin strands (or their projected images). Specifically, in the case of ESI the joints are excessively large and bright (the images are non-linearly intensity adjusted to also allow for visualization of the dimmer structures), and in the case of SRRF and SACD, the strands are completely missing close to the intersections. The performance of ESI, SRRF and SACD appears also largely unaffected by the varying level of fluorescence fluctuations, except for an additional out-of-focus strand appearing in the ESI images at higher levels of fluorescence fluctuations. SRRF does not exclude out-of-focus signal, while SACD does, both independently of the level of intensity fluctuations. This is very different from the results of SOFI and MUSICAL; whose performance was highly dependent on signal fluctuation level. As opposed to ESI, MUSICAL rejects more out-of-focus structures the higher the level of intensity fluctuations, and the reconstruction of the in-focus sample area are notably better. SOFI and MUSICAL do not appear to have the same issues close to the intersection points as ESI, SRRF and SACD, but SOFI is badly affected by the noise, which results in a dominating background signal that could be difficult to distinguish from the image objects. HAWK preprocessing alleviated the background issue of SOFI, especially for the highest level of fluorescence fluctuations. No improvement was found using HAWK for the other techniques. Further results using additional reconstruction parameters and other image stack sizes are found in Suppl. Figure S1 together with a more elaborate discussion on the performance of the different techniques and their artifacts under varying conditions.

Mitochondria/tori simulations

Although useful insights can be derived from simple examples like crossing actin strands, they are too simplistic to reveal how the techniques might perform on more complex biological structures such as 3D tubes.

The results for the simulated tori are summarized in Figure 5 for two different fluctuation levels and for each case one torus centered at perfect focus and one 200 nm above the focal plane. These tori correspond to the upper right and middle torus of Figure 3. Results for the complete sample are available in the SI together with results using additional reconstruction parameters (Suppl. Figures S2-S4).

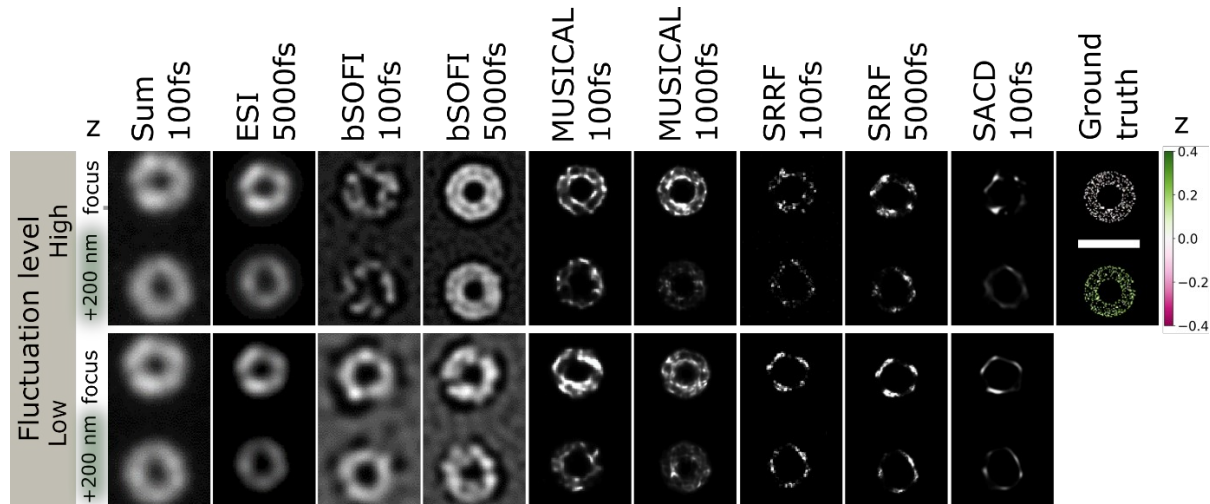


Fig. 5. Results on simulated mitochondria/tori. Reconstructions of tori (tubes of diameter 200 nm) for high (top row) and low signal fluctuation (bottom row), for a torus centered at the focal plane and 200 nm above focus. The tube shape emulates cellular structures like mitochondria and the ER. The scale bar in the ground truth image is 1 μm , and the color bar describes the emitters' axial positions in μm . Only MUSICAL manages to resolve the outer rings for 100 frames (in-focus torus at high fluctuation level), while SOFI provided good reconstruction using 5000 frames, but only for the high fluctuation level and still with significant background artifacts, likely cause by the simulated noise addition. Using 1000 frames, MUSICAL could resolve parts of the inner and outer circles also for the low fluctuation level. Although a dip in intensity is visible between the inner and outer tori boundaries, the structures are also characterized by seemingly aleatory sharp intensity patterns, likely arising from the stochastic behavior and fairly low density (~ 24 nm surface density) of emitters. The ESI ($\gamma = 0.5$ intensity adjusted), SRRF and SACD results show only a single circle for each torus (for any number of frames or parameters tested), but also with complete noise removal. The circles are in the case of SRRF and SACD significantly slimmer than the ground truth 'double circle', which illustrates a typical reconstruction artifact with these techniques that can be difficult to spot when the ground truth is not available.

As also noted for the actin strand example, ESI, SRRF and SACD eliminate noise and appear insensitive to fluctuation level as well as the 200 nm shift from the focal plane. Compared to the ground truth structures, which no longer are single lines, none of these techniques can make out the double rings (or 3D tubes). SRRF and SACD reconstruct rings way too slim

compared to the actual structures. This reconstruction artifact would not be noticeable using the actin strand example alone.

SOFI, as for the simulated actin strands, is sensitive to noise which gives some artifacts in the background but is able to reconstruct the tubes for the case of 5000 frames and a high fluctuation level (but does not work for 100 frames or low level of fluctuations). For a high level of signal fluctuations, MUSICAL is able to discern the double ring of the in-focus torus for only 100 frames, but better for 1000 frames and then also for the low fluctuation level. MUSICAL does not show any background artifacts from the noise for these cases, but the tori themselves are characterized by seemingly aleatory sharp intensity patterns, likely arising from the stochastic behavior and fairly low density (~ 24 nm surface density) of emitters. Such sharp and random patterns unrelated to the underlying biological structure, could be misleading and cause false conclusions when considering unknown biological samples.

These simulation examples have revealed some strengths and weaknesses with all five FF-SRM techniques under scrutiny. We will in the following consider their performance on actual experimental data and see how the results compare to the ones from the simulated data.

As also noted for the actin strand example, ESI, SRRF and SACD eliminate noise and appear insensitive to fluctuation level as well as the 200 nm shift from the focal plane. Compared to the ground truth structures, which no longer are single lines, none of these techniques can make out the double rings (or 3D tubes). SRRF and SACD reconstruct rings way too slim compared to the actual structures. This reconstruction artifact would not be noticeable using the actin strand example alone.

SOFI, as for the simulated actin strands, is sensitive to noise which gives some artifacts in the background but is able to reconstruct the tubes for the case of 5000 frames and a high fluctuation level (but fails for 100 frames or low level of fluctuations). For a high level of signal fluctuations, MUSICAL is able to discern the double ring of the in-focus torus for only 100 frames, but better for 1000 frames and then also for the low fluctuation level. MUSICAL does not show any background artifacts from the noise for these cases.

These simulation examples have revealed some strengths and weaknesses with all five FF-SRM techniques under scrutiny. We will in the following consider their performance on actual experimental data and see how the results compare to the ones from the simulated data.

Liposomes

Nanoparticles (NPs), including lipid-based nanoparticles, are widely studied as a mean to overcome the limitations of free drugs and active molecules when faced with biological barriers. Due to their versatility, biocompatibility, and ability to tailor their physicochemical features, lipid-based NPs are the most common class of FDA-approved nanomedicines [19]. Liposomes in particular are spherical structures comprising at least one lipid bilayer surrounding a core aqueous compartment. The small size, agile and delicate nature of liposomes make their characterization by microscopy challenging and a non-standard procedure. We tested three different sample preparations for liposomes with integrated fluorescence (NBD with excitation and emission maxima 476 nm and 537) directly on microscopy cover glasses: free-floating in suspension, dried-on, and small droplets immobilized under a patch of solid agarose gel.

The samples were imaged in fast time-lapse mode using standard epi-fluorescence microscopy. The free-floating liposomes were, as expected, moving too fast in especially axial direction for acquisition of multiple time point videos of the particles. The dried liposome suspensions appeared to be destroyed, while the suspensions of liposomes covered by solid agarose appeared intact and stationary over the course of 200-300 time points. Hence, only the samples with liposomes immobilized via agarose were considered for further analysis.

We tested the five FF-SRM methods' ability to accurately reveal liposome size from two different known size distributions: 100 nm and 250 nm, respectively. To this end, we first assessed the optimal number of frames to be used for the analysis (Suppl. Figure S5-S6). When not clear which number of frames were best, 100 frames were used, which in most cases was found to provide the optimal tradeoff between fluctuation data (i.e., number of frames) and (rapid) photobleaching together with potential instability of the supporting agarose. The autofluorescence of the agarose patch was also found to photobleach faster than the fluorophores for the first 100-200 frames, possibly beneficial to some of the FF-SRM methods.

Figure 6 shows the results evaluated as best for both the 100 and 250 nm liposomes for the five FF-SRM methods (additional results are available in Suppl. Figures S5-S7). From these images, five FWHM measurements for each case were measured, with the resulting mean and standard deviation displayed under the panels of the respective reconstructions. Notably, the estimated size depends on the FF-SRM method used, and seemingly not on the underlying

liposome size distribution. Each technique gives a different result, but the same technique gives a similar result (< 35 nm difference on the mean value) for the two significantly different size distributions (about 100 nm and 250 nm). When the same number of frames were used for the two size distributions for SOFI and SACD (different #fs was found best for the two different size distribution for these cases), the difference was even smaller (1 nm for SACD and 2 nm for bSOFI), see captions of Figure 6 and Suppl. Figure S5. The measured sizes were suspiciously similar for the two different size distributions also for the three other techniques: ESI 196 nm and 183 nm, MUSICAL 41 nm and 54 nm, and SRRF 58 nm and 47 nm. The individual measurements and chosen liposomes are shown in Suppl. Figure S8.

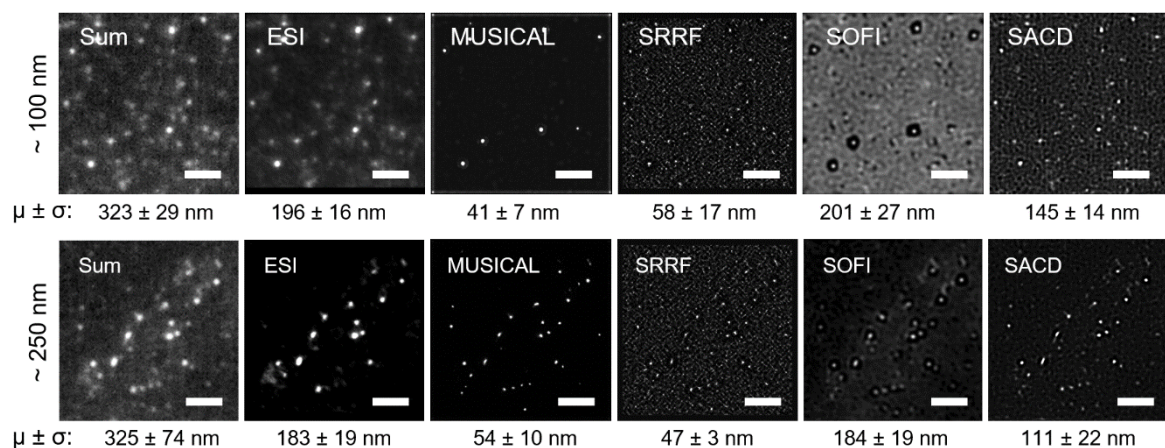


Fig. 6. Results on liposome nanoparticles. Reconstruction results for liposomes of about 100 nm (upper row) and 250 nm (bottom row) size distributions for the five different methods: ESI order 4 (100 fs), MUSICAL (100 fs) threshold -0.21 (100 nm) and -0.57 (250 nm), SRRF TRAC ring radius 0.5 (100 fs), bSOFI (100 fs for 100 nm and 200 fs for 250 nm), and SACD order 2 (100 fs for 100 nm and 25 fs for 250 nm). The mean value and standard deviation from measuring liposome FWHMs (Gaussian fit) are stated below the panels. Notably, the measured sizes depend on FF-SRM method (and their parameters) and seemingly not on the liposome size distribution. When 100 fs were used for both size distributions for SACD and SOFI, the mean values were 145 nm and 146 nm for SACD, and 201 nm and 203 nm for bSOFI. Equally problematic are the ESI, MUSICAL and SRRF results, giving similar particle sizes for the two very different size distributions. Note: Images are shown with autocorrection in brightness and contrast and for ESI and additional gamma 0.5 correction was applied; however, all quantitative measurements were performed on the raw (reconstructed) images.

This small ensemble study illustrates some of the challenges with these FF-SRM methods. Although we cannot completely exclude the possibility that one of these techniques provides the right answer for all measured lipid particles (as the ground truth is not available), the size measurements seem completely off and unlikely to be correct for either technique. Changing

any reconstruction parameters of the individual techniques also changed the measurements. For example, on the ~250 nm sample, using 25 frames for SACD gave 111 nm mean value for the FWHM, while using 100 fs resulted in mean of 146 nm. Similarly, SOFI with 100 fs gave 203 nm, while using 200 fs gave 184 nm mean value for the FWHM measurements. Better signal of the larger liposomes also appears to improve the localization, resulting in smaller size estimates (for all methods except MUSICAL, which still shows smaller estimates).

The agarose patch appears to have caused notably background artifacts in the reconstruction for SRRF, SOFI and SACD, but not as significantly for ESI or MUSICAL for these particular samples. This problem would likely be alleviated if a more stable fluorophore were available. This was however not the case for this sample, as fluorescent molecules in general are challenging to stably incorporate into liposomes [20].

The achieved image resolutions were estimated via line profiles over a sample area with an elongated spot, indicating the presence of at least two closely separated liposomes (Suppl. Figure S9). The MUSICAL, SRRF and SACD images show clear dips between two (or more) peaks, but the high prevalence of reconstruction artifacts in especially the SRRF and SACD images (likely caused by the agarose autofluorescence) render these measurements unreliable.

For future experiments, it might be of interest to ensure that the liposomes are arranged as a flat, monolayer sample that remains stably in perfect focus during image acquisition. Even small deviations from focus could alter the liposome size measurements. The use of total internal reflection fluorescence microscopy (TIRFM) would also likely help reducing the effects of agarose unevenness, autofluorescence and out-of-focus signal. These points could also be used as a general consideration for size profiling applications that use FF-SRM for particles of dimensions close to or smaller than the resolution limit.

Although quantitative analysis does not seem promising from this initial approach, it might be possible via calibration of the individual techniques' parameters on known size distributions to obtain more reliable size estimates. Especially the integration of more photostable fluorophores into the liposomes would be a game changer. As we saw from the simulation examples for the SOFI images, reliable reconstruction was not achieved for ~100 frames, but for 5000 frames with a high level of intensity fluctuations.

We will now proceed to samples where often the *qualitative* information is of considerable interest, namely biological tissues and cells.

Fixed Cells and Tissues

The five different FF-SRM methods were tested on fixed cell cultures (macrophages) and tissues (placenta and heart cryo-sections) using the commonly applied fluorescent probes CellMask Orange (membrane marker) and Phalloidin-ATTO647N (labeling filamentous actin), as before, illuminated using incoherent wide-field illumination for standard epi-fluorescence microscopy. The results were evaluated from a broad range of different reconstruction parameters for the different methods and the results considered best for each method are displayed in Figure 7 and Suppl. Figure S10 for the case of placenta tissue, and Suppl. Fig S12 for fixed cells. Results using additional reconstruction parameters/options and a data overview are available in Suppl. Figures S11-S15.

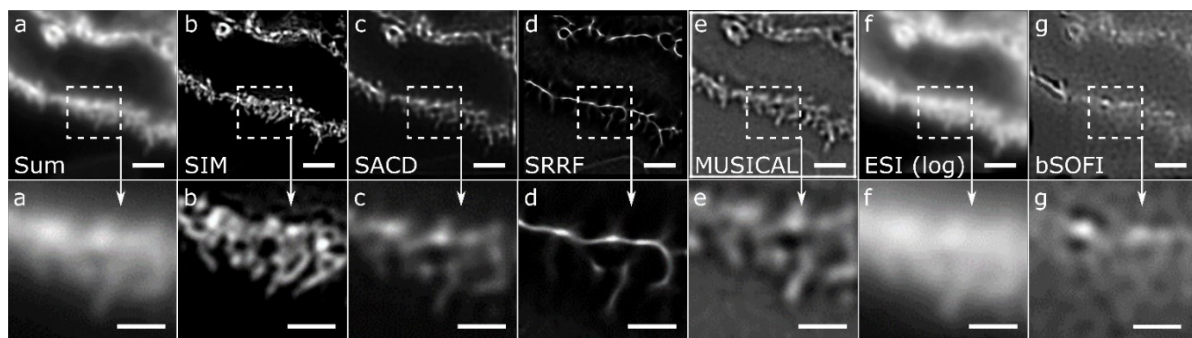


Figure 7. Results on placenta tissue section. FF-SRM reconstructions of 1 μm -thick cryo-preserved placental tissue section fluorescently labelled with Phalloidin-ATTO647N for identification of F-actin. The regions indicated in the upper panels are shown magnified below revealing the microvilli brush-border of a chorionic villus. (a) The summed image of 500 frames; (b) a single z-plane 3D SIM image; (c) SACD using 50 frames and order 2; (d) SRRF using 500 frames along with TRA option and radius 0.5; (e) MUSICAL using 200 frames and threshold -0.33267; (f) ESI order 4 using 500 frames (log intensity adjusted); (g) bSOFI using 500 frames. The scale bars are 2 μm on the upper-row panels and 1 μm in the lower-row panels.

The results for the different FF-SRM methods applied to the same sample are strikingly different. Comparing with the sum and the ‘reference’ SIM image (providing resolution doubling compared to the diffraction limit) of Figure 7, only SACD and MUSICAL give a minor improvement in detail visibility over conventional microscopy. The ESI image appears similar to the sum image, the SRRF image generates thin lines partly corresponding to the SIM image, while the SOFI image is a complete mesh of artifacts.

Results on ultrathin tissue sections (100 nm thickness) and TIRFM data gave similar discouraging results (Suppl. Figures S16-S18). This clearly indicates that out-of-focus signal need not be the main reason for the methods' lack of reliable reconstruction.

Comparing with the simulation results presented earlier, the results indicate that the high background intensities and in general poor performance of both MUSICAL and SOFI could be explained by the photo-physical properties of the fluorescent labels used, and that these problems could be countered by experimentally introducing a higher level of fluorescence intensity fluctuation (e.g., using different fluorophores or imaging conditions). Also using longer sequences (>400 frames) might have improved the results, this data is however not available.

Living Cells and Dynamics

One major motivation for performing FF-SRM instead of other nanoscopy techniques is the opportunity for data acquisition under live-cell friendly environment. In this section, we consider epi-fluorescence time-lapse data of living cells. Because of the dynamic and delicate nature of living cells, fewer frames and lower illumination intensities were used for these data sequences.

The different FF-SRM methods were applied to three different test samples: mitochondrial outer membrane and ER where little to no dynamics were visible in the conventional image stack (64 frames), and a 100 frames image sequence of mitochondria undergoing fast dynamics. The results on mitochondria for stationary and fast dynamics are displayed in Figure 8, while the results for ER and additional HAWK results for mitochondria are displayed in Suppl. Figure S19.

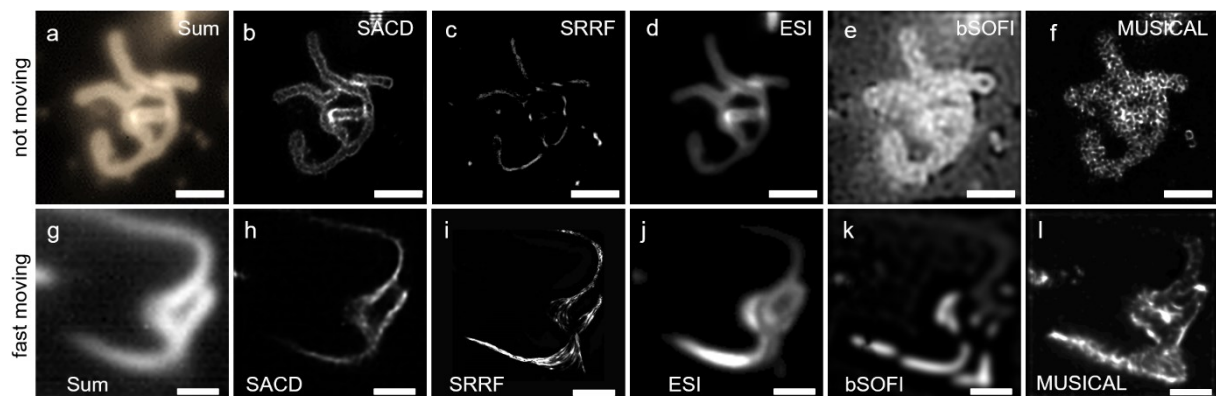


Fig. 8. Results on mitochondria in living cells. Reconstructions on live-cell data of mitochondrial outer membrane (OMP25- mCherry). Top row: stationary organelles (scale

bars: 2 μm); bottom row: fast moving mitochondria (scale bars: 1 μm). The mitochondrial dynamics introduce a new type of signal fluctuation that is not accounted for by any of the FF-SRM algorithms and introduces different artifacts compared to those of stationary objects. The object dynamics has a clearly different effect on all the five different methods. Interestingly, the mitochondrial outer membrane appears much better reconstructed by MUSICAL in the case of dynamic mitochondria (fine structure seemingly characterized by the actually labelled outer mitochondrial membrane) compared to the stationary mitochondria (fine structure characterized by mesh artifacts).

As seen for the fixed samples, all the different methods gave vastly different pictures when applied to the same image sequence. For the stationary sample, the reconstructions show similar patterns as seen for the fixed cells and tissues: ESI provides noise removal and structure slimming, but no real resolution improvement. MUSICAL provides a dominating artefact network over the entire object area. SRRF fits thin single lines to the wider tubular structure. SACD impresses with sturdily recognizing and reconstructing the outer mitochondrial membrane. The great improvement over the simulation results on the tori seen in Figure 5, can be explained by the real mitochondria (in this particular sample) are wider ($\sim 250\text{-}500\text{nm}$) than the 200 nm tubes of the tori, and not beyond the resolution limit of SACD. This can be also seen from Suppl. Figure S3, where SACD results on the entire tori simulation sample is shown. Here, the SACD images of the larger tori (400 nm tubes) show two concentric circles, while the smaller tubes (200 nm) are represented as thin mono-circles. Notably, the mitochondrial outer membrane is discernible in some places in the raw data, and especially for the summed image.

HAWK preprocessing resulted in an overall noisy and degraded image, but also a more discernible outer membrane in the case of ESI, MUSICAL and SRRF. The ER sample displayed similar patterns of reconstruction artifacts as for the mitochondria but is also a significantly difficult sample to evaluate as this tubular membrane network could take on almost any shape (shown in Suppl. Figure S19).

For the highly dynamic sample, ESI appears similar to the sum image, SACD similar to a strongly deconvolved sum image, while SOFI has deleted parts of the moving structure, presumably because dynamics give less pixel-wise signal correlation. SRRF appears to fit a different thin line for every time-point, resulting in a fine grid of multiple lines. The MUSICAL image of mitochondria looks strikingly different from the one in the previous figure, with sharp contours of the outer membrane instead of the dominating artefact network seen in the

previous figure and for the results on fixed cells. Although the sample motion introduces a new type of artifact as compared to the stationary sample, the signal fluctuations introduced by the mitochondrial dynamics also appear to be exploited by the MUSICAL algorithm as shown in the article by Sekh et al. [21] for the investigation of nanoscale dynamics.

Discussion

We have processed datasets from a broad range of samples and applied to them the fluctuation nanoscopy techniques (b)SOFI, ESI, MUSICAL SRRF and SACD, trying out many different reconstruction parameters along the way. Figure 1 presented a summary of our observations, which are discussed in detail below. We reiterate that the discussion below is meant to facilitate an application scientist in designing better studies, acquiring better data, and setting the right expectations from the different methods for the data at their hand. While each method has its significant strengths, the gap between their technical development and practical application may be bridged through the following insights.

Observations regarding SOFI and MUSICAL: The simulations revealed that only two of the techniques, namely SOFI and MUSICAL, required a high level of intensity fluctuations to achieve their optimal results. Also, only these techniques were able to resolve the more challenging 3D tube-like structures of 200 nm diameter, simulating membrane-bound cellular organelles like mitochondria and the ER. The SOFI images displayed dominating artifacts in presence of noise, but for data of high level of fluorescence signal fluctuations and thousands of time-point image sequences displayed reliable reconstruction even for the 3D samples. HAWK lowered SOFI's sensitivity to noise and greatly improved the SOFI reconstructions for few raw images (~100), but only for a high level of fluorescence intensity fluctuations. In the case of short image sequences with a high level of intensity fluctuations, MUSICAL performed the best. MUSICAL also showed an additional ability to exploit signal fluctuations arising from sample dynamics. For fixed cells and tissues, the disappointing performance of SOFI and MUSICAL was shown to be due to a too low level of signal fluctuations in our experimental data. This was especially inferred from the results on simulated data, where SOFI and MUSICAL displayed poor performance for low fluctuation levels, but good performance for higher fluctuation levels. Additionally, SOFI and MUSICAL performed poorly in the case of slow-moving (or stationary) structures in living cells, both producing a dominating circular mesh. This can be explained by a low level of intensity fluctuations, but importantly, also the use of

short image sequences (to assure sample stationarity). However, in the case of the fast-moving sample, MUSICAL was able to exploit the fluctuations induced by the sample dynamics, producing a significantly better results than seen for the slow-moving structures.

Observations regarding ESI, SRRF and SACD: Although ESI displayed faithful noise removal and was possibly the technique the least prone to artifacts, it did not present super-resolution capabilities for our data. SRRF had also significant noise-reduction capabilities for all fluctuation levels but did not reveal the true underlying structures where the ground truth (beyond the diffraction limit) was available. Both SRRF and SACD were shown to produce ‘over-slimming’ of structures, rather than revealing the true nanoscopic details in the case of the 3D simulations of doughnuts. In the case of low signal fluctuations and ‘ultra-short’ image sequences (16 frames), SACD had the decidedly best performance of 3D structures close to the resolution limit (like the mitochondrial outer membrane), although its tendency towards producing over-slimming artifacts must be kept in mind while analyzing SACD imaging results. We noted that for fixed cells and tissues, the performance of ESI, SRRF and SACD are generally better than for SOFI and MUSICAL in the sense that the images overall look closer to the actual samples with less obvious artifacts, even though they did not display super-resolving abilities. This is in agreement with our simulated 3D examples in the case of low fluctuations, where we did notice better robustness of these techniques irrespective of the super-resolution ability. Nonetheless, these techniques might generate subtle artefacts that are difficult to spot. The possible influence of these subtle artifacts in the analysis of bio-images needs further investigation. SACD showed a good ability in producing reliable reconstructions for structural details close to the diffraction limit, as evident from the live-cell data of slow-moving mitochondria. None of them however could withstand the challenge of fast-moving mitochondria.

General observations that apply to all the FF-SRM techniques tested: The simulated 3D examples do provide some important insights into the performance of these methods. A significant one is that FF-SRM methods can perform well for actin or other fiber-like structures, and these might be good examples for studying resolution. However, these results may not be suitable for setting the expectations regarding the performance of these methods for more complex 3D samples such as mitochondria and the ER. Two more important insights from

simulations are regarding (a) the effect of out-of-focus structures and level of fluctuations on the reconstructions and (b) the artefacts arising from noise and overlapping structures.

Our results showed an overall poor performance of all FF-SRM methods for the tested conditions for liposomes, fixed cells, and tissues. We noted that even if the samples are ultrathin or optical sectioning is not a challenge, FF-SRM often underperform in the case of low fluctuation levels, high background signal and/or insufficient data (number of frames). The measured sizes of liposomes from different known size distributions, revealed that the measured FWHM depend more on chosen FF-SRM technique than on nanoparticle size. Further experimental optimization and calibration of the individual methods reconstruction parameters would be needed before trustworthy nanoparticle size measurements can be carried out using FF-SRM. Or potentially, instead of using the techniques for size estimation, they can be used for localizing these particles as an initial guess for other size optimization approaches. They may also be used for count-based analytics with better accuracy than size-based analytics, if relevant.

The use of dense labelling and photo-stable fluorophores that are optimal for other nanoscopy techniques led to unreliable reconstructions and image artifacts in the case of fixed cells and tissues. Nonetheless, acquiring a large number of frames, using better-suited dyes, and introducing a higher level of fluctuations through use of imaging buffers, might assist these techniques in performing better. Depending on the resolution requirements and system availability, it might be preferable to use SRM techniques like SIM, STED or localization microscopy for fixed cells and tissues, as the considerations related to live-cell imaging do not apply for these samples.

The many different parameters offered by some of the techniques could be a potential strength allowing for super-resolution imaging for a broader range of samples and imaging conditions. It is however problematic that, to our knowledge, there are no clear guidelines for when the different parameters should be used, leaving the user with difficult and subjective choices about what might be 'the best' reconstruction. Usually, the ground truth is not available for bio-image data, which only complicates the path to derive good guidelines for parameter selection.

Live-cell compatibility is advertised by all evaluated FF-SRM methods. Still, and somewhat unfortunately, stationarity of the imaged objects (during the course of the analyzed image

sequence) is also assumed by the FF-SRM algorithms (all apart from MUSICAL). Our computational experiments on highly dynamic samples displayed very different effects of the sample dynamics on the reconstructed images depending on the FF-SRM method used. Notably, the MUSICAL algorithm appeared to exploit the signal fluctuations introduced via the sample dynamics, offering a greatly improved reconstruction of the mitochondrial outer membrane as compared to the stationary samples. On the other hand, less dynamic samples resulted in unreliable reconstructions using MUSICAL since they contribute mesh like artifacts arising from noise and localized motion-induced fluctuation.

A considerable challenge for real samples, and especially for living samples, is the complete lack of ground truth. We can use what is known about the samples (e.g., the mitochondrial outer membrane is labelled) and our knowledge and experience with the different methods to aid our evaluation (e.g., circular mesh is a sign of improper MUSICAL reconstruction), the results will still be somewhat subjective and only useful until a certain point. If, for example, all the different methods showed different patterns of membrane domain proteins (only) in a plausible outer mitochondrial membrane area, we would have great difficulty in determining which one, if any of them, provided the correct picture of the membrane protein distribution. Therefore, simulations will be extremely important in the future development and evaluation of FF-SRM methods. They must, however, encompass sufficient complexity to be representative of real image data of dynamic and 3D biological systems [21]. This is not an easy task, but neither an impossible task in the current era of open science, global collaboration, and ever-expanding computational resources.

Summary and Outlook

We have seen that reliable reconstruction can be achieved for certain imaging conditions revealed via simulations of microscopy experiments. There are however still some challenges ahead for the young field of FF-SRM on the way towards reliable super-resolution image reconstructions from image sequences of densely fluctuating fluorophores for deriving useful biological inferences.

SOFI and MUSICAL were shown to have a different and superior ability to work with intensity fluctuations compared to other techniques. Both exhibited greatly improved reconstructions with longer image sequences and with higher rate of signal fluctuations. Lamentably, they also displayed the highest level of image degradation compared to the raw image data when the

necessary requirements of the image data (like signal fluctuations) were not present. ESI, SRRF and SACD on the other hand, showed little to no improvement with the length of the image sequences and level of intensity fluctuation, but for all conditions gave less obvious artifacts and image structures that were usually more robustly in accordance with the conventional image data. As shown by simulations, the artifacts are still present and severe when considering details beyond the diffraction limit.

Choosing the right reconstruction parameters poses an additional challenge and introduces unwanted user subjectivity to the super-resolution images. The future development of these techniques should therefore encompass ‘parameter-free reconstruction’, intelligent pre-analysis of the data allowing for automatic selection of the optimal reconstruction parameters and feedback to the users about reconstruction quality and potential deficiencies of the image data. Examples of feedback include poor signal fluctuations, low SBR, sample is moving, sample appears out-of-focus, more frames needed, etc. The general lack of ground truth for living, dynamic samples is a substantial analytical challenge. Therefore, realistic 3D simulations of living cells (with known ground truth) will be important in the future development of these techniques.

We hope that this first comparative study of FF-SRM techniques highlighting the strengths and weaknesses of the different techniques will accelerate the arrival of a reliable and democratic nanoscopy technique suitable for a broad range of samples, likely combining strengths from the already suggested approaches. The potential rewards of true and reliable optical nanoscopy via conventional image sequences of ‘any sample’ together with the promising glints of reconstruction successes suggest that the many challenges along the way will be worth the effort.

Materials and Methods

Experimental design

The objective of the study was to evaluate the performance of FF-SRM methods for a diverse set of samples where resolution beyond the optical diffraction limit would be of significant interest: liposomes, live and fixed cells, and tissues. The samples were chosen from availability, local expertise, and research interest. The synthetic/simulated samples were created in accordance with relevant biological structures (mitochondria and actin strands) as

a means to accurately control experimental conditions and to better understand the effect on image reconstruction of different sample conditions by changing one parameter at the time (e.g. fluctuation level, focal plane, or sample geometry). Simulations also provided a powerful way of obtaining absolute ground truth for the evaluation of the results.

Nanoscopy Algorithms and their Parameters

ESI, *Entropy-Based Super-Resolution Imaging*, estimates the likelihood of emitter molecule presence by calculating the local and cross-pixel (information-theory) entropy throughout the image sequence. The entropy can be thought of as the expectation value of the information content. The ImageJ-plugin used for analysis was retrieved from the software link available from the original publication [8].

Parameters: *number of images* in the output, number of *bins* for entropy, the *order* of the centralized moments. In addition, the plugin automatically uses maximum and minimum intensity in the image. The *number of images* can be useful when having long data sequences (thousands of frames) available for repeated ESI application on sub-stacks. The 0th *order* is not applicable (vanishes), the 2nd order is the variance, the 3rd and 4th order is related to the distribution shape and symmetry, and above 4th order does 'not have an obvious correlation the distribution itself' [8]. The *order n*, has a similar effect of raising the microscope PSF to the *n*th order, leading to a \sqrt{n} -fold narrowing of the approximated Gaussian signal. The default *order* value is 4, and that is what is used in this work unless otherwise stated. The *bins* were set to 100, and, unless otherwise stated, 1 image in output (as fairly short data sequences were used).

bSOFI, *balanced super-resolution optical fluctuation imaging* [7], is an improved SOFI implementation that achieves 'balanced' image contrast based on the emitters actually present, in contrast to the nonlinear response to brightness and blinking seen by the original SOFI auto- and cross-cumulant analysis [6]. The theoretical resolution improvement is \sqrt{n} , where *n* cumulant order. Mainly results using bSOFI has been addressed in this work. The analysis was performed in MATLAB using software copyright © 2012 Marcel Leutenegger et al, École Polytechnique Fédérale de Lausanne, under the GNU General Public License. No parameters are user defined.

SRRF, *super-resolution radial fluctuations* [9] is similar to SOFI but in addition assumes radially of emitters. There is also a long range of additional options available in the SRRF plugin, that can be seen as different algorithms. The theoretical or expected resolution improvement depends on the reconstruction options, with the highest possible resolution improvement being by the *temporal radially auto-cumulant* (TRAC) order 4 option, which is similar to SOFI order 4, so a possible $\sqrt{n} = 2$ -fold resolution improvement. Other possible options include the *temporal radially average* (TRA) and *temporal radially pairwise product mean* (TRPPM).

For the analysis presented in this work, multiple options were tried, primarily the 'default parameters' implying ring radius 0.5 with 6 axes, TRAC 2, with intensity weighing and 'minimize SRRF pattering'. When something different than default is indicated in the results, like TRAC 2, 3, or 4, it means the 'Advanced Settings' are activated with additional 'Gradient Smoothing' and 'Gradient weighting', together with the option indicated and the other default settings (like ring radius).

The images presented in the results, were the options yielding the best results out of the options tried. It should be noted, however, that it could be better options that were not tried out. Trying all possible combinations of parameter for SRRF analysis is beyond the scope of this work. The ImageJ-plugin used for the analysis was retrieved from link in the original publication [9].

SACD, *super-resolution method based on autocorrelation two-step deconvolution* [11], is (also) inspired by SOFI, but in addition to signal autocorrelation performs a (Lucy-Richardson) deconvolution step before and after the autocorrelation analysis. The autocorrelation analysis is based on an algorithm they call *multi-plane autocorrelation* (MPAC), to counter a typical lack of image frames for autocorrelation analysis by also correlating combination of frames in multiple steps (or planes). It is especially developed for live-cell imaging under the conditions of low signal and few input frames (e.g., they use 16 frames in their article).

The reconstructions made using SACD was performed in MATLAB environment using the source code following link in the original publication. The tiff files were converted to mat-format in MATLAB prior to the SACD computation. After reconstruction, the data was converted to tiff files using the MATLAB *save* function.

Parameters: *number of deconvolution iteration steps*. 10 steps were used for the results presented. 20 steps were tried for some computations, but no significant improvement was found. *Magnification*: image upscaling by Fourier interpolation. 8 were used for the results presented. *Power of PSF* for the second deconvolution step: PSF powers were tried in the range 2-6. *Orders of MPAC used*: 2,3,4,5 and 6. The PSF order was the same as for the MPAC for the presented results. The order used for particular results is indicated in the figures. Optical parameters for PSF calculation: *wavelength, numerical aperture and pixel size*. These were in accordance with the particular sample dataset being processed.

MUSICAL, *Multiple Signal Classification Algorithm* [10], calculates higher resolution through singular value decomposition and the resulting eigenimages. Each eigenimage represents a particular pattern found in the image stack, and the associated singular value describes how significant or likely the pattern is. The larger the singular value of an eigenimage, the more likely this is to be an underlying image feature rather than resulting from noise or background signal. This way, by selecting a *threshold* for what are signal and what are noise (or unlikely) image features, the MUSICAL image is computed by taking the ratio of an independent estimate for both the signal and the noise. This ratio is for the final image intensity value taken to the power of the parameter *alpha* (usually 4). The computations are done on sub-images whose size depends on the imaging system's PSF taken into account.

The MUSICAL image and singular value computations were done in ImageJ using a plugin and macro for multicolor time-lapse processing. Both the plugin and macro are available from <https://github.com/sebsacuna/MusiJ>. The required input parameters are *pixel size, subpixels* (image magnification factor), (microscope system) *magnification, numerical aperture, alpha*, and *batch size* (number of images used for the MUSICAL image computation). For each color channel one must also specify *emission wavelength* and *threshold*. The threshold is a parameter particular to MUSICAL and determines the cutoff for what fluctuation eigenvectors goes into signal or noise space. This parameter was selected experimentally by trying values in the range of the second singular values (middle, lower and high end of the spectrum).

Unless stated otherwise in the results, the following parameters were used: emission wavelength 510 nm, pixel size 80 nm, subpixels 10, magnification 1 (already calculated for in the pixel size), alpha 4, numerical aperture, 1.420. The batch size was in the range 50 to 400 (stated for individual results).

Different threshold values were used (stated in the Results section) but were in general chosen from the range of the second singular values (as described in [22]), where the middle of this range was usually found the best.

HAWK, *Haar wavelet kernel* [23] is not a super-resolution method in itself, but a data pre-processing technique that can be used to increase data sparsity by distributing the data over more frames. The motivation behind this technique is that high-density data is difficult to analyse and leads to mislocalizations and image artefacts using e.g., traditional super-resolution techniques like single molecule localization microscopy. In the manuscript, they show improved image reconstruction also for SOFI and SRRF, relevant to the current work.

Different options available for this ImageJ plugin (retrieved from link in [23]) are: Settings: *number of levels* (3,4 or 5), *negative values: separate or absolute value*, *Output order: group by level or group by time*. Unless stated otherwise in the results, the following parameters were used: Settings: number of levels: 5, negative values: separate, Output order: group by level. These parameters were chosen from initial experimentation and based on results in the HAWK publication.

HAWK pre-processing is presented for ESI, SRRF, bSOFI and for MUSICAL, but not for SACD because of MPAC large memory requirements for the extended datasets and poor performance under initial testing (degradation of results compared to SACD alone).

Data Acquisition and Sample Preparation

SMLM data: The experimental 2D data for SMLM was retrieved from http://bigwww.epfl.ch/smlm/datasets/index.html?p=../challenge2013/datasets/Real_Long_Sequence; data courtesy of Nicolas Olivier and Debora Keller. Emission wavelength: 690 nm, NA: 1.3, number of frames: 15000. The STORM reconstruction was performed using the ThunderSTORM ImageJ plugin [24] with default parameters. The ESI images were generated as described above, but the summed ESI image was generated from 15000 image by applying ESI sequentially with 1500 and 100 output images. The MUSICAL image was generated using 1500 frames and 0.1 as threshold. The SRRF image was reconstructed from 15000 frames using the TRAC4 advanced option, with the other parameters remaining at default. The SACD image was generated as described above but using 1500 frames and order 4.

Imaging system: The data was acquired using a commercial OMX V4 optical microscope with 3 cameras and up to four-channel imaging. The objective lens was a 60X 1.42NA oil immersion lens, except for the TIRFM data, where the objective was 60X 1.49NA TIRF lens. Widefield, epifluorescence single-plane time-lapse data was acquired in sequential imaging mode of the different color channels to avoid bleed-through between the channels.

Liposomes: Liposomes were prepared according to the film hydration method [25]. Soy phosphatidylcholine (SPC; generously provided by Lipoid GmbH, Ludwigshafen, Germany) was used as main lipid ingredient in concentration of 10 mg/mL. 1-myristoyl-2-{6-[(7-nitro-2-1,3-benzoxadiazol-4-yl)amino]hexanoyl}-sn-glycero-3-phosphocholine (N; Avanti Polar Lipids, AL, USA) was chosen as fluorescent marker in 0.03 mg/mL. Excitation and emission wavelength of the incorporated fluorophore are 476 nm and 537 nm respectively.

Both lipid ingredients were dissolved in methanol and dried to a thin film through low-pressure rotary evaporation (Büchi Rotavapor R-124, Büchi Labortechnik, Flawil, Switzerland). Distilled water was used to hydrate the lipid film and form large multi-lamellar vesicles. After overnight stabilization, the vesicle size was reduced combining sonication and sequential hand extrusion through polycarbonate membranes of 400, 200 (and 100) nm sieving sizes (Whatman Nucleopore™) to the target size of A) 250 nm and B) 100 nm. The size distribution was derived from a Gaussian-like fitting of dynamic light scattering signal (Malvern Zetasizer Nano – ZS, Malvern, Oxford, UK) and resulted in A) 240±77 nm and B) 117±30 nm. The respective polydispersity indexes (Pdl) of 0.410 and 0.217 described A as a polydispersed system (Pdl>0.25) and B as a monodispersed one (Pdl<0.25). ζ-potential measurements obtained through laser doppler electrophoresis (Malvern Zetasizer Nano – ZS, Malvern, Oxford, UK) are included for completion, Table 1.

Table 1. Standard processing and characterization of liposomal formulation.

N-Lip FORMULATIONS							
N-Lip	Composition		Processing		Characterization		
	SPC conc [mg/mL]	N conc [mg/mL]	Sonication sec	Extrusion [passes]x[nm]	Size [nm]	Pdl	ζ-pot. [mV]
A	10	0.03	120	4x400 + 4x200	240±80	0.410	-8.0±3.7
B	10	0.03	120	4x400 + 4x200 + 4x100	117±30	0.217	-6.4±2.7

Both liposomal suspensions were diluted 1:1000 in distilled water to the final lipid concentration of 10 µg/mL (and fluorophore concentration to 0.03 µg/mL). 3 µL droplets were then placed on ethanol-cleaned coverslips and covered with thin (2 mm) patches of solid agarose (2 % in water) for immobilization.

Fixed-cells: Murine macrophages RAW 264.7 (ATCC® TIB-71TM, ATCC, Manassas, USA) were cultured in RPMI-1640 medium, supplemented with 1% penicillin-streptomycin and 10% fetal bovine serum. The cell culture in a 25-cm² flask was incubated at 37 °C and 5% CO₂ until 100% confluence. Cells were then scraped, counted in a Neubauer chamber and diluted to 50,000 cells/mL, prior to the final plating into 35-mm petri dishes – No. 1.5 coverglass (MatTek Corporation, Ashland, USA). The cells were fixed at a confluence of about 50% at room temperature (RT) using 4% PFA in Cytoskeletal buffer [26]. The samples were subsequently washed in PBS and labelled with Phalloidin-ATTO647N (Merck) using 3µL/100µL PBS for 1h at RT, and CellMask™ Orange Plasma Membrane Stain (ThermoFisher Scientific) using a concentration of 1 to 2000 in PBS for 5min. The samples were washed repeatedly in PBS and finally immersed in PBS for imaging.

Tissues: The samples were collected and preserved following the Tokuyasu method for cryo-sections [27]. Human chorionic tissue from full-term placenta was dissected immediately after delivery into 1 mm³ blocks, rinsed in 9 mg/mL NaCl and transferred to 1X PHEM-buffer. The blocks were incubated in 8% formaldehyde in PHEM-buffer at 4 °C overnight and immersed for 1 h in 0.12% glycine at 37 °C. Thereafter, the samples were infiltrated with 2.3M sucrose at 4 °C overnight and mounted on specimen pins before storage in liquid nitrogen. Analogously, myocardial samples were collected from anesthetized pigs using a biopsy needle. The cardiac samples were dissected, washed and further prepared in identical manner as with the placental sample.

The samples were prepared for microscopy as previously described [28]. In summary, the tissues were cryo-sectioned with an EMUC6 ultramicrotome (Leica Microsystems, Vienna, Austria), collected with a wire loop filled with a 1:1 pick-up solution of 2.3 M sucrose and 2% methylcellulose, and placed onto poly-L-lysine coated #1.5 high-precision coverslips. Subsequently, the cryo-sections were washed 3 × 7 min with PBS at 4°C and fluorescently labelled according to the experimental plan at RT. The placental tissue was incubated for 15 min in a 1:100 solution of phalloidin-ATTO647N in PBS, washed 2 × 5 min with PBS, incubated

in a 1:2000 mixture of CellMask Orange in PBS for 10 min, and washed 2×5 min with PBS before mounting. Analogously, the cardiac tissue was labelled with CellMask Orange for 10 min, followed by 2 washing steps of 5 min in PBS. Thereafter, the labelled sections were mounted onto standard microscope glass slides (placenta) or a reflective silicon chip (heart) using Prolong Gold and sealed with nail varnish. The samples were stored at 4°C and protected from the light before imaging.

Live-cell data: Rat cardiomyoblast cells (H9c2) were cultivated in glass bottom petri dishes (MatTek Corporation, Ashland, USA) and transiently transfected with organelle (mitochondria and endoplasmic reticulum KDEL) targeted fluorescent fusion proteins (OMP25-mCherry and KDEL-EGFP). Imaging was done in cell-culture medium (DMEM with 10% fetal bovine serum), using heating and an environmental chamber set at 37°C and 5% CO₂.

Simulated data: The first step of the synthetic sample generation was creating the 3D emitter distribution. The actin sample was formed by single tubes of diameter 6 nm, with emitters randomly placed on the surface with a linear density of 500 emitters per μm . A linear density was used since the size of the strands is an order of magnitude smaller than the pixel size (80 nm). In the case of mitochondria, the samples were modelled as tori distributed over a grid of 2 rows and 3 columns. Each row contains tori of the same size while each column represented a single axial position referred to as z , which is the distance between the center of mass of the tori and the coverslip. The upper row contains tori with minor radius 100 nm and major radius 300 nm, while the minor and major radii of the bottom row are 200 nm and 500 nm. With 700 nm axial position (distance from the coverslip) being the plane in focus, the tori are distributed over three planes: 500 nm, 700 nm, and 900 nm (going from left to right in the sample). The emitters are located on the surface of the tori with a density of 400 emitters per μm^2 .

To make sure that our simulated emitter densities were sufficient to support the generation of super-resolved images and to avoid potential artifacts resulting from too low emitter densities, we measured the mean Euclidean distance of the emitters to their nearest emitter neighbors and compared to the Nyquist criterion [29]. This was done using both the actual three-dimensional emitter distance and the distance of the two-dimensional image projections (the measured fluorescence signal). For the actin, the distances were 3.44 nm in 3D and 2.32 nm in 2D. For the mitochondria sample, the distances were 24.59 nm in 3D and 13.89 nm in 2D. Since none of the methods' maximum obtainable resolution is expected to

exceed 50 nm, we evaluated the sample emitter densities as sufficient for our testing purposes.

The simulations of the actin and mitochondria (tori) samples were generated using the same optical parameters: 510 nm emission wavelength, 1.42 NA, and 80 nm pixel size of the projected optical images. The photokinetic model of fluorescence was modeled using two states: emitting (on) and non-emitting (off). The time spent in each state was modeled using an exponential distribution with mean on and off times τ_{on} and τ_{off} , with blinking rates $1/(\tau_{on} + \tau_{off})$ [30]. In the implementation considered here, the blinking rates are in units of frames of the simulated image sequences, with τ_{on} fixed at 1, and τ_{off} either 3, 9 or 19, depending on the ‘fluctuation level’. The larger the off time, the higher the image sequence standard deviation image and the perceived fluctuation level. Hence, our naming convention with low, medium, and high fluctuation, correspond to $\tau_{on} = 1$, and $\tau_{off} = 3, 9$ and 19, respectively. In terms of duty cycle blinking rates, these correspond to 25%, 10% and 5%. Photobleaching was not considered for these samples.

While emitting, the emission rate was kept constant for each emitter, with the intensity at every frame computed by scaling the PSF by the emission *on* time. The Gibson-Lanni model [31] was used to model the PSF for the noise-free microscopy image sequences. To these images, the noise was added by normalizing the noise-free images to the range $i = [0,1]$, and then for the final image i_f applying the linear transformation $i_f = Poisson((a - b)i + b)$, with $a = 200$ and $b = 50$. The value of $(a - b)$ corresponds to the maximum signal, while b is an offset representing the camera dark current [32].

Evaluation of image data absent of ground truth: Evaluation of super-resolution images in lack of ground truth is a challenging task prone to both error and subjectivity. Resolution is not merely the width of slim line profiles or visible separation between two closely spaced bright spots in the image. These structures must also represent the actual underlying sample, and not noise or reconstruction artifacts. For the simulated data, evaluation can be done relatively easily as the ground truth is known. For the live-cell data on the other hand, the ground truth is not available. The evaluation was done via visual inspection following these criteria (-/+ indicate bad or good):

(-) In image areas where clearly nothing but noise or background was present, reconstructed structures are artifacts.

(-) Occurrence of suspect pattern of unlikely biological origin. Especially if these shapes change for different reconstruction parameters.

(+) Images reveals null or close to none signal in 'no object areas', but significant signal in 'object of interest' area.

(+) Image structures are consistent for different parameters (if available).

(+) Images reveal sub-resolution limit structures on object of interest areas and nowhere else. It is good if these structures are in accordance with what is already known about these structures/organelles, although this cannot be strictly required as most nanoscale cellular structures in living cells cannot be strictly assumed to have the same nanostructure as seen by electron microscopy (EM) of fixed, starkly treated cells.

(+) Excludes out-of-focus structures, rather than producing artefacts.

Other relevant aspects are ease of use and reconstruction time.

The signal to background ratio (SBR) was measured from the mean of small regions where samples were present or not. This is a difficult measure to make, as it varies throughout the image, and it is not always obvious from the images where the object of interest is or not (especially in the case of the dense mesh of the ER). Measuring the background where no objects are visible is neither fair, as for example objects in a different imaging z-plane will contribute substantially to the background and heavily challenge the reconstruction of the in-focus objects.

The intensity line profiles were measured in Fiji/ImageJ using a line width of 1. All other image processing tasks (like gamma intensity adjustment, image summation or standard deviation, insertion of scale bar etc.) were also performed in Fiji/ImageJ (version 1.52p).

Acknowledgements

General: The authors kindly thank Åsa B. Birgisdottir for providing cultures of fluorescently labelled H9c2 cells and pig heart tissue samples. Also, our gratitude to Mona Nystad for providing the placental sections and Randi Olsen for cutting all the ultrathin cryo-sections used in this study.

Funding: IO and SA acknowledge strategic funding from UiT The Arctic University of Norway. KA acknowledges funding from a Horizon 2020 Marie Skłodowska-Curie Action (749666) and a Horizon 2020 ERC Starting Grant (804233). SA acknowledges funding from the Horizon 2020 Marie Skłodowska-Curie Action (749666). BSA acknowledges funding from RCN BioTek2021 (285571) and Marie Skłodowska-Curie grant agreement No. 766181. JC and NSB received funding from the European Union's Horizon 2020 research and innovation program under the Marie Skłodowska-Curie grant agreement No. 766181.

Author contributions: KA conceived the idea. SA generated the simulation microscopy datasets and reconstructions for liposomes. JC produced and prepared the liposomes, together with their size analysis. LV did the tissue sample preparation, acquisition, and analysis. JC provided cultured macrophages for the fixed-cell experiments. ISO prepared, imaged, and analyzed the live and fixed cell-culture samples. ISO wrote the draft manuscript and prepared the figures. KA, BSA and NSB supervised the project. Writing – review & editing, all authors. All authors have read and agreed to the submitted version of the manuscript.

Competing interests: The authors declare no competing interests.

Ethical approval of tissue sections: Human placenta sections were collected at the University Hospital of North Norway according to the ethical protocol approved by the Regional Committee for Medical and Health Research Ethics of North Norway (REK Nord reference no. 2010/2058-4). Written informed consent was obtained from the participant and the sample was treated anonymously. All methods were carried out in accordance with relevant guidelines and regulations.

Pig heart sections were obtained following the ethical protocols approved by the Animal Welfare Board at UiT The Arctic University of Norway, NO-9037 Tromsø, Norway, and the Norwegian Food Safety Authority Mattilsynet, NO-9008 Tromsø. All methods were carried out in accordance with relevant guidelines and regulations.

Data and materials availability: The microscopy image data and reconstructions are available at <https://www.3dnanoscopy.com/ff-srm-review/> or upon reasonable request. The password protection will be removed when the manuscript is accepted, and the data can be made public.

References

1. L. Schermelleh, A. Ferrand, T. Huser, C. Eggeling, M. Sauer, O. Biehlmaier, G. P. C. Drummen, Super-Resolution Microscopy Demystified. *Nature Cell Biology* **21**, 72-84 (2019).
2. X. Huang, J. Fan, L. Li, H. Liu, R. Wu, Y. Wu, L. Wei, H. Mao, A. Lal, P. Xi, Fast, Long-Term, Super-Resolution Imaging with Hessian Structured Illumination Microscopy. *Nature Biotechnology* **36**, 451 (2018).
3. W. Yu, Y. Li, S. Jookan, O. Deschaume, F. Liu, S. Wang, C. Bartic, Second-Order Optimized Regularized Structured Illumination Microscopy (Sorsim) For High-Quality And Rapid Super Resolution Image Reconstruction With Low Signal Level. *Optics Express* **28**, 16708-16724 (2020).
4. A. Sandmeyer, M. Lachetta, H. Sandmeyer, W. Hübner, T. Huser, M. Müller, DMD-Based Super-Resolution Structured Illumination Microscopy Visualizes Live Cell Dynamics At High Speed And Low Cost. *bioRxiv*, 797670 (2019).
5. S. Hu, L. Liu, Y. Huang, W. Liu, Q. Wei, M. Tan, Y. Yu, Compact And Low-Cost Structured Illumination Microscopy Using An Optical Fiber Coupler. *Optics Communications* **436**, 227-231 (2019).
6. T. Dertinger, R. Colyer, G. Iyer, S. Weiss, J. Enderlein, Fast, Background-Free, 3D Super-Resolution Optical Fluctuation Imaging (SOFI). *Proceedings of the National Academy of Sciences* **106**, 22287-22292 (2009).
7. S. Geissbuehler, N. L. Bocchio, C. Dellagiacoma, C. Berclaz, M. Leutenegger, T. Lasser, Mapping Molecular Statistics with Balanced Super-Resolution Optical Fluctuation Imaging (bSOFI). *Optical Nanoscopy* **1**, 4 (2012).
8. I. Yahiatene, S. Hennig, M. Müller, T. Huser, Entropy-Based Super-Resolution Imaging (ESI): From Disorder to Fine Detail. *Acs Photonics* **2**, 1049-1056 (2015).
9. N. Gustafsson, S. Culley, G. Ashdown, D. M. Owen, P. M. Pereira, R. Henriques, Fast Live-Cell Conventional Fluorophore Nanoscopy with Imagej Through Super-Resolution Radial Fluctuations. *Nature Communications* **7**, 1-9 (2016).
10. K. Agarwal, R. Macháň, Multiple Signal Classification Algorithm for Super-Resolution Fluorescence Microscopy. *Nature Communications* **7**, 1-9 (2016).
11. W. Zhao, J. Liu, C. Kong, Y. Zhao, C. Guo, C. Liu, X. Ding, X. Ding, J. Tan, H. Li, Faster Super-Resolution Imaging with Auto-Correlation Two-Step Deconvolution. *arXiv preprint arXiv:1809.07410*, (2018).
12. F. Xu, M. Zhang, W. He, R. Han, F. Xue, Z. Liu, F. Zhang, J. Lippincott-Schwartz, P. Xu, Live Cell Single Molecule-Guided Bayesian Localization Super Resolution Microscopy. *Cell Research* **27**, 713-716 (2017).
13. Y. Eldar, M. Segev, O. Solomon, M. Mutzafi. (Google Patents, 2020).
14. R. J. Marsh, K. Pfisterer, P. Bennett, L. M. Hirvonen, M. Gautel, G. E. Jones, S. Cox, Artifact-Free High-Density Localization Microscopy Analysis. *Nature Methods* **15**, 689 (2018).

15. L.-H. Yeh, L. Waller, 3D Super-Resolution Optical Fluctuation Imaging (3D-SOFI) with Speckle Illumination, in *Computational Optical Sensing and Imaging*. Optical Society of America, Heidelberg, Germany (25-28 July 2016), pp. CW5D. 2.
16. A. Purohit, W. Vandenberg, T. Dertinger, D. Wöll, P. Dedecker, J. Enderlein, Spatio-Temporal Correlation Super-Resolution Optical Fluctuation Imaging. *EPL (Europhysics Letters)* **125**, 20005 (2019).
17. X. Yi, S. Son, R. Ando, A. Miyawaki, S. Weiss, Moments Reconstruction and Local Dynamic Range Compression of High Order Super-Resolution Optical Fluctuation Imaging. *Biomedical Optics Express* **10**, 2430-2445 (2019).
18. X. Yi, S. Weiss, Cusp-Artifacts in High Order Super-Resolution Optical Fluctuation Imaging. *Biomedical Optics Express* **11**, 554-570 (2020).
19. M. J. Mitchell, M. M. Billingsley, R. M. Haley, M. E. Wechsler, N. A. Peppas, R. Langer, Engineering Precision Nanoparticles for Drug Delivery. *Nature Reviews Drug Discovery*, 1-24 (2020).
20. J. Cauzzo, M. Nystad, A. M. Holsæter, P. Basnet, N. Škalko-Basnet, Following the Fate of Dye-Containing Liposomes In Vitro. *International Journal of Molecular Sciences* **21**(14), 4847 (2020).
21. A. A. Sekh, I. S. Opstad, A. B. Birgisdottir, T. Myrmel, B. S. Ahluwalia, K. Agarwal, D. K. Prasad, Learning Nanoscale Motion Patterns of Vesicles In Living Cells, in *Proceedings of the IEEE/CVF Conference on Computer Vision and Pattern Recognition (CVPR)*, Washington, USA (14-19 June, 2020), pp. 14014-14023.
22. S. Acuña, F. Ströhl, I. S. Opstad, B. S. Ahluwalia, K. Agarwal, Musij: An ImageJ Plugin for Video Nanoscopy. *Biomedical Optics Express* **11**, 2548-2559 (2020).
23. R. J. Marsh, K. Pfisterer, P. Bennett, L. M. Hirvonen, M. Gautel, G. E. Jones, S. Cox, Artifact-Free High-Density Localization Microscopy Analysis. *Nature Methods* **15**, 689-692 (2018).
24. M. Ovesný, P. Křížek, J. Borkovec, Z. Švindrych, G. M. Hagen, ThunderSTORM: a Comprehensive ImageJ plug-in for PALM and STORM Data Analysis and Super-Resolution Imaging. *Bioinformatics* **30**, 2389-2390 (2014).
25. A. D. Bangham, R. Horne, Negative Staining of Phospholipids and Their Structural Modification by Surface-Active Agents as Observed in the Electron Microscope. *Journal of Molecular Biology* **8**, 660-IN610 (1964).
26. PEM fixation buffer. Cold Spring Harb Protoc, (2009).
27. P. Webster, A. Webster, "Cryosectioning Fixed and Cryoprotected Biological Material for Immunocytochemistry" in *Electron Microscopy* (Springer, 2007), pp. 257-289.
28. L. E. Villegas-Hernández, M. Nystad, F. Ströhl, P. Basnet, G. Acharya, B. S. Ahluwalia, Visualizing Ultrastructural Details of Placental Tissue with Super-Resolution Structured Illumination Microscopy. *Placenta* **97**, 42-45 (2020).
29. B. Huang, M. Bates, X. Zhuang, Super-Resolution Fluorescence Microscopy. *Annual Review of Biochemistry* **78**, 993-1016 (2009).

30. A. Girsault, T. Lukes, A. Sharipov, S. Geissbuehler, M. Leutenegger, W. Vandenberg, P. Dedecker, J. Hofkens, T. Lasser, SOFI Simulation Tool: A Software Package for Simulating and Testing Super-Resolution Optical Fluctuation imaging. *PLoS One* **11**, e0161602 (2016).
31. S. F. Gibson, F. Lanni, Diffraction by a Circular Aperture as a Model for Three-Dimensional Optical Microscopy, *Journal of the Optical Society of America A* (1989).
32. M. Hirsch, R. J. Wareham, M. L. Martin-Fernandez, M. P. Hobson, D. J. Rolfe, A Stochastic Model for Electron Multiplication Charge-Coupled Devices—from Theory to Practice. *PloS one* **8**, e53671 (2013).

Supplementary Material

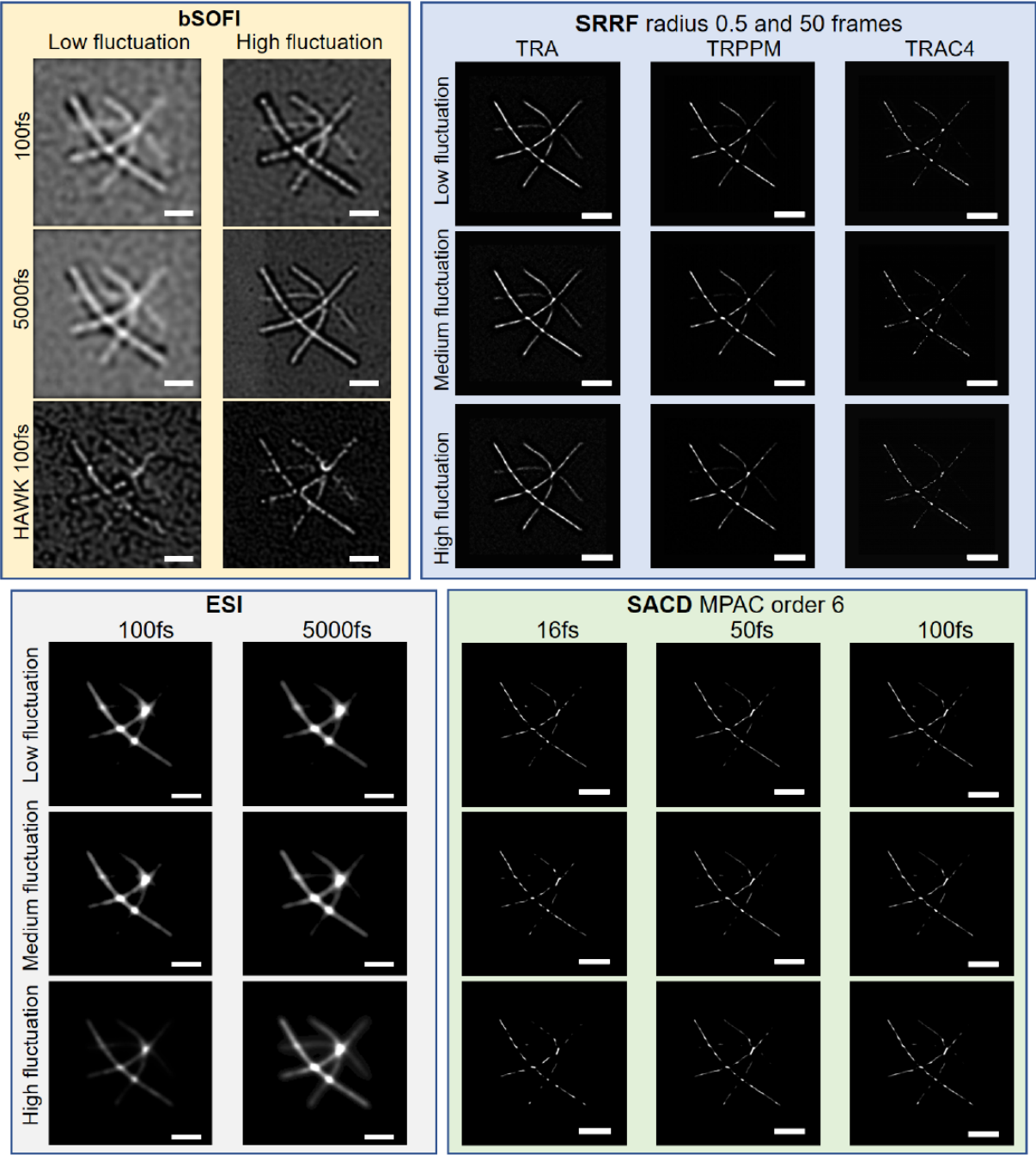


Figure S1. Simulated 3D actin strand. bSOFI for two different fluctuation levels, HAWK and different number of frames (fs). The bSOFI images improve drastically by using both HAWK and a higher number of frames, but only for the higher fluctuation level. The scale bars are 1 μm ; SRRF for different reconstruction options and fluctuation levels. The temporal radially average (TRA) includes most of the out of focus strands and also gives higher background signal for higher fluctuation level. The temporal radially pairwise product mean (TRPPM) and temporal radially auto-cumulant order 4 (TRAC 4) option, appears for this data similar and largely unaffected by the fluctuation level for this data. The actin

strand reconstructions from TRAC 4 are slimmer than for the other options, which can be explained by TRAC 4 being the SRRF options with the highest theoretical resolution improvement, namely a factor of 2 ($\nu_{order} = 2$ in the same manner as for the SOFI orders); ESI: the results for different number of frames and different fluctuation levels are very similar for ESI, except more out-of-focus structures being visible for higher fluctuation levels. To better visualize the finer image details alongside the bright spots, the ESI images are $\gamma=0.5$ intensity adjusted; SACD: The images for different number of frames and fluctuation level are for SACD nearly indistinguishable, but for the highest number of frames and highest fluctuation level, the inclusion of out-of-focus strands is slightly higher than for the remaining images. The scale bars are 1 μm .



Figure S2. Simulated 3D tori (doughnuts/mitochondria). Data overview of the three different fluctuation data sets, each containing a single frame, a sum image

of 100 frames, and the standard deviation image of 100 frames (STD); ESI: effect of fluctuation level, HAWK and number of frames. While HAWK significantly degrades the ESI image, changing the fluctuation level or the number of frames does not significantly alter the ESI results; SRRF: effect of using different options for SRRF reconstruction. The effect on the SRRF images from of changing reconstruction parameters (or options) is much larger than the effect of fluctuation level. Although the double ring from the larger torus is visible for any fluctuation level, the width of the doughnuts is more accurately represented with higher fluctuation level. The inability to resolve the inner and outer rings of the smaller doughnuts might be at least partly due to the poorer z-sectioning than MUSICAL or ESI (See Figure 2 in the main manuscript). The scale bars are 1 μm .

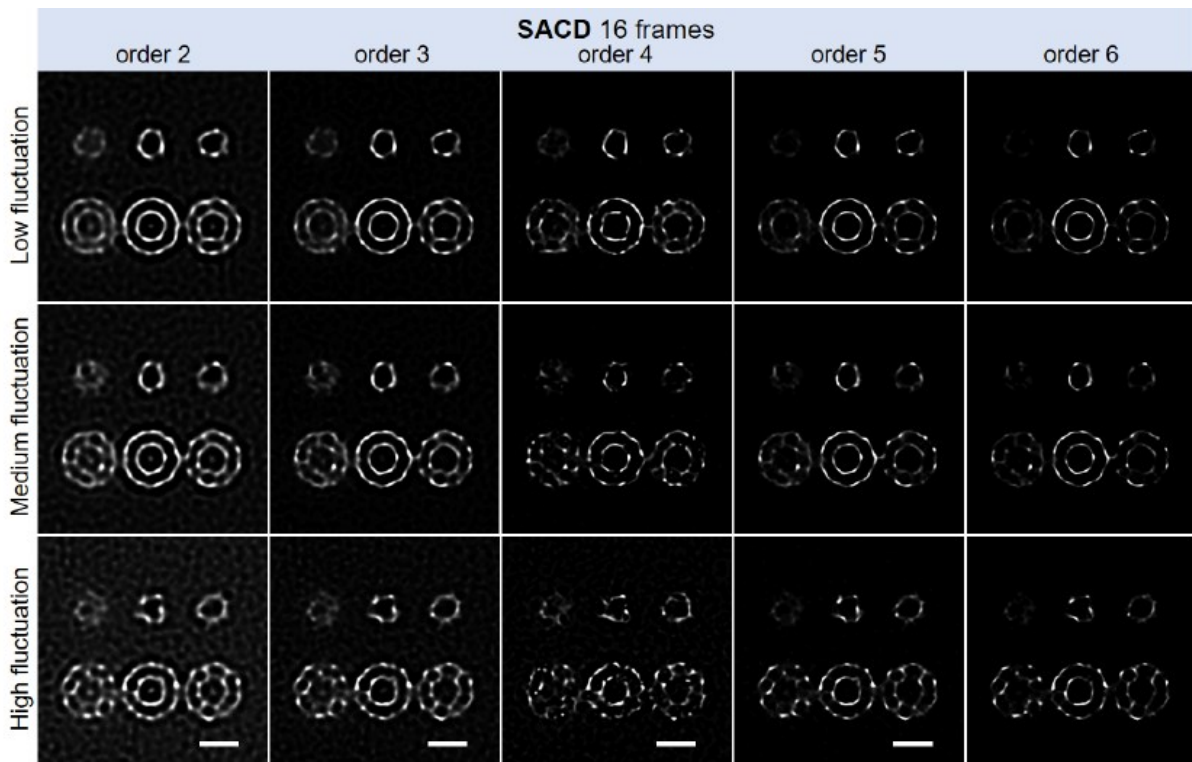


Figure S3. *Cont.*

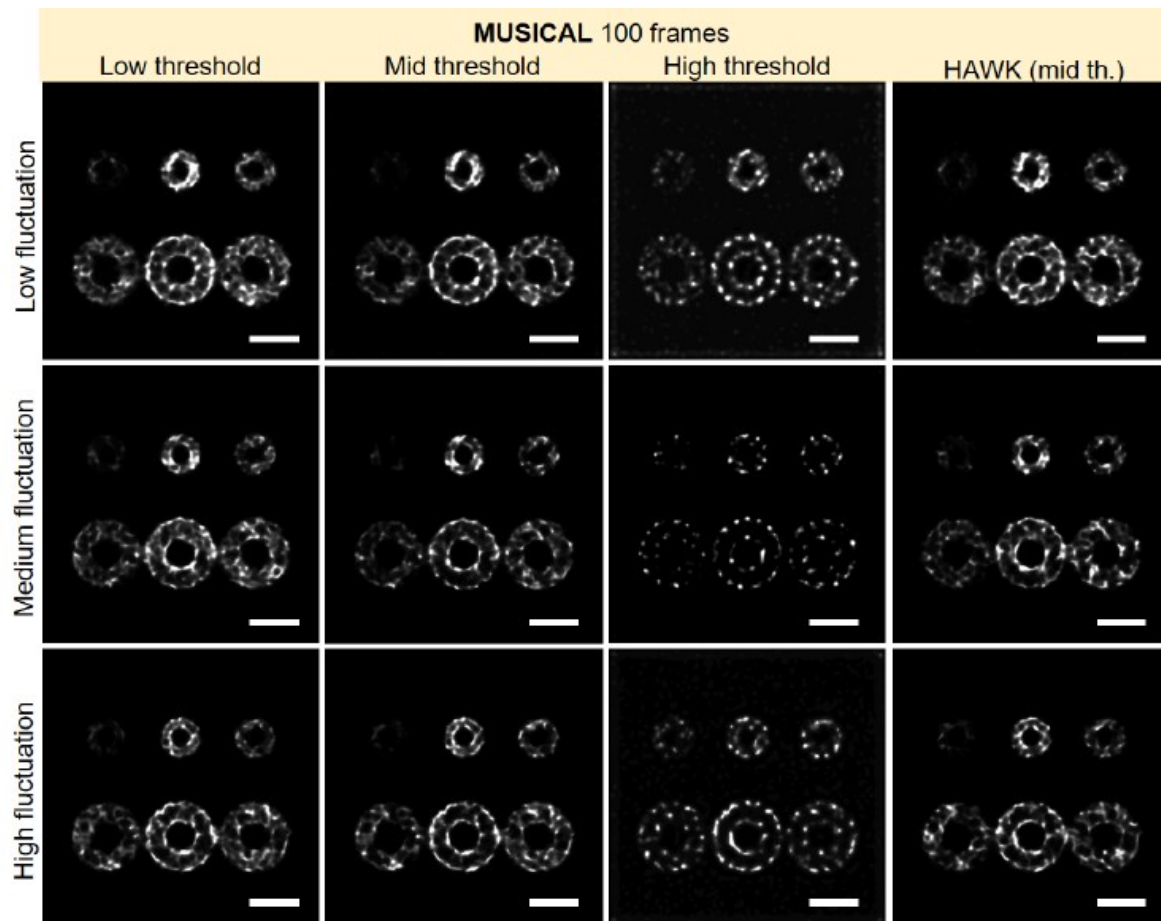


Figure S3. Simulated 3D tori. SACD: effect of fluctuation level and the MPAC (multiplane autocorrelation) order. The SACD images become worse and appear more affected by noise for higher fluctuation levels. The higher the MPAC order, the better the noise rejection and the higher rejection of out of focus structures (possibly also in-focus structures, see Suppl. Figure S 13 EPI SACD); MUSICAL: effect of different fluctuation levels and threshold parameters. The resolving power of MUSICAL becomes clearly better with higher fluctuation levels. Low, mid and high threshold are referring to the range of 2nd singular values according to the MusiJ plugin [S1]. The lower the threshold, the higher portion of the signal fluctuations are included as ‘signal’ and less as ‘noise’. This increases the information available for calculating a nanoscopy image, but also increases the contribution of potential noise and out-of-focus signal which can lead to image artifacts. HAWK preprocessing lead to similar results for MUSICAL as without HAWK.

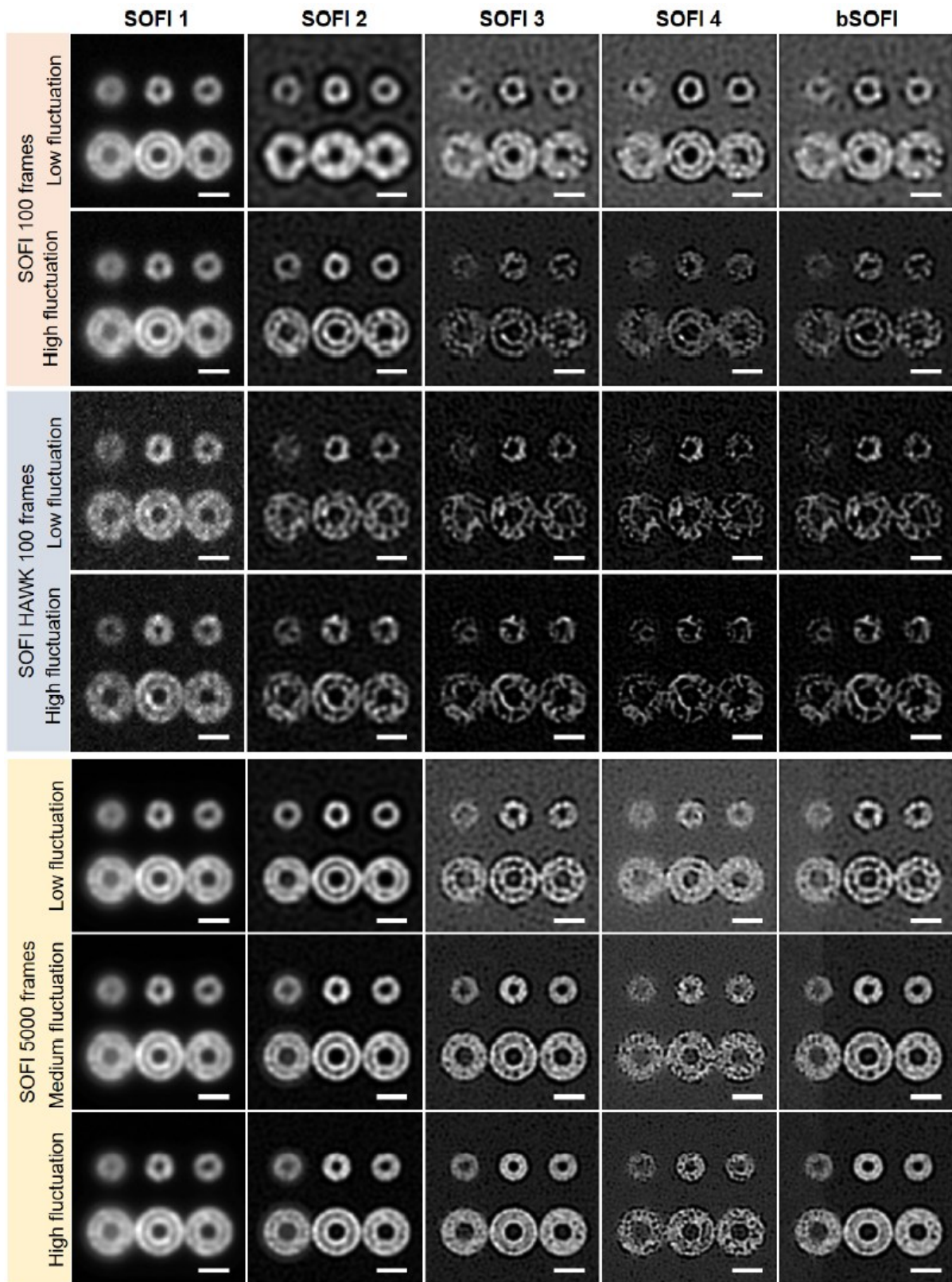


Figure S4. Simulated 3D tori: effect of fluctuation level, HAWK, and number of frames for different SOFI orders and bSOFI. The first two SOFI order, SOFI 1 and SOFI 2, are equivalent to the mean and variance images, respectively, and do not offer theoretical resolution improvement beyond the diffraction limit. SOFI 3 (third order), on the other hand, does possess theoretical super-resolving

capabilities (up to a factor of $\sqrt{3} \approx 1.73$), something which is experimentally confirmed from the in-focus tori (middle column) from the highest fluctuation level and frame number (bottom row), where the double ring characteristics of also the smallest torus can be clearly visualized. SOFI 4 appears here to capture primarily sample noise rather than further resolution increase. The bSOFI images are for these data nearly identical to SOFI 3.

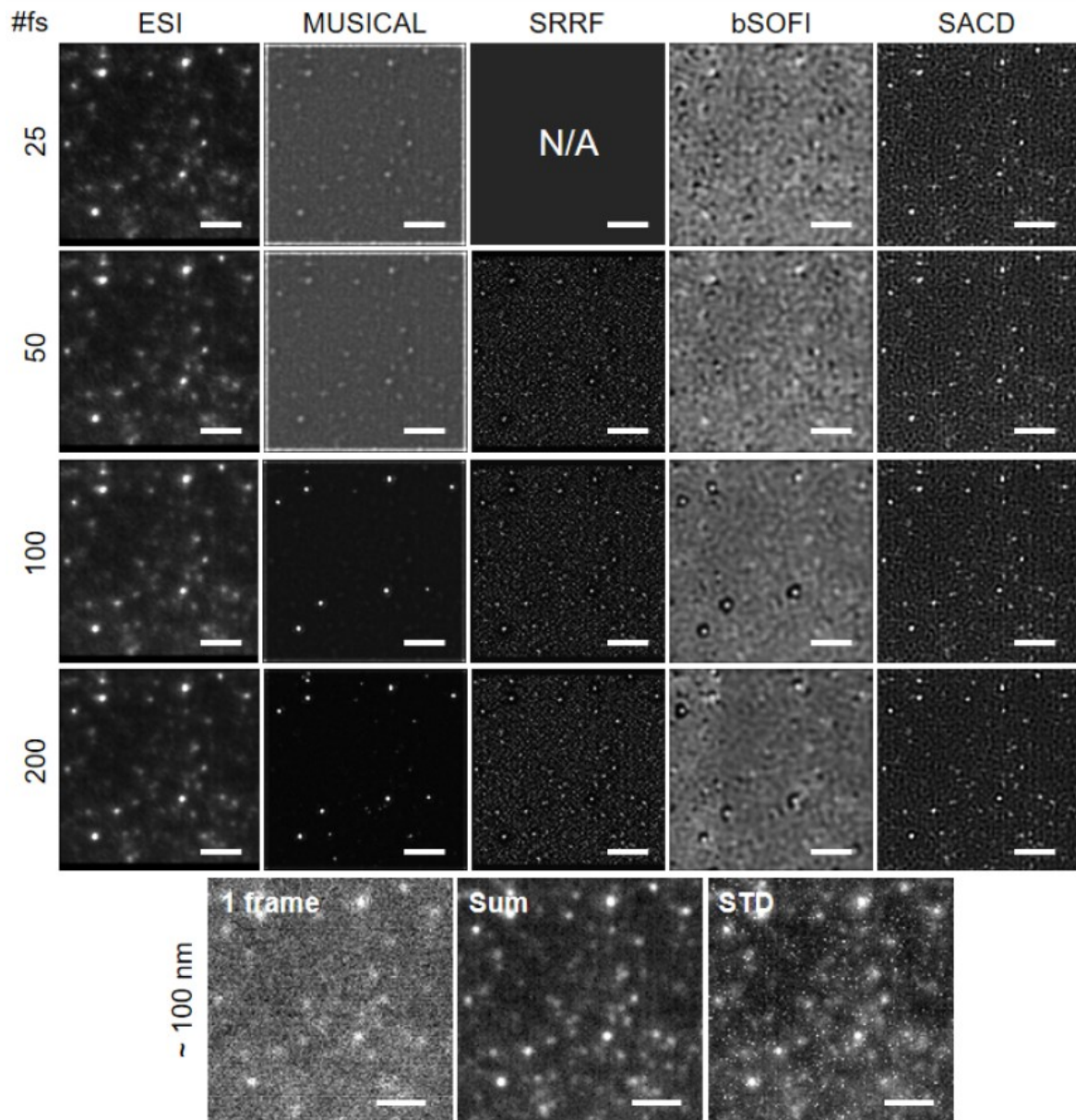


Figure S5. Liposomes 100 nm: assessment of the number of frames (#fs) parameter and an overview of the data, containing a single frame, a sum, and the standard deviation image (STD). The scale bars are 2 μm . 100 frames were chosen for further analysis, exhibiting reduced background and high visibility of image features appearing to be in-focus liposomes in the MUSCAL and bSOFI images, although the remaining techniques appear similar for all frame numbers. The ESI reconstructions are shown with gamma 0.5 for optimal visualization purpose.

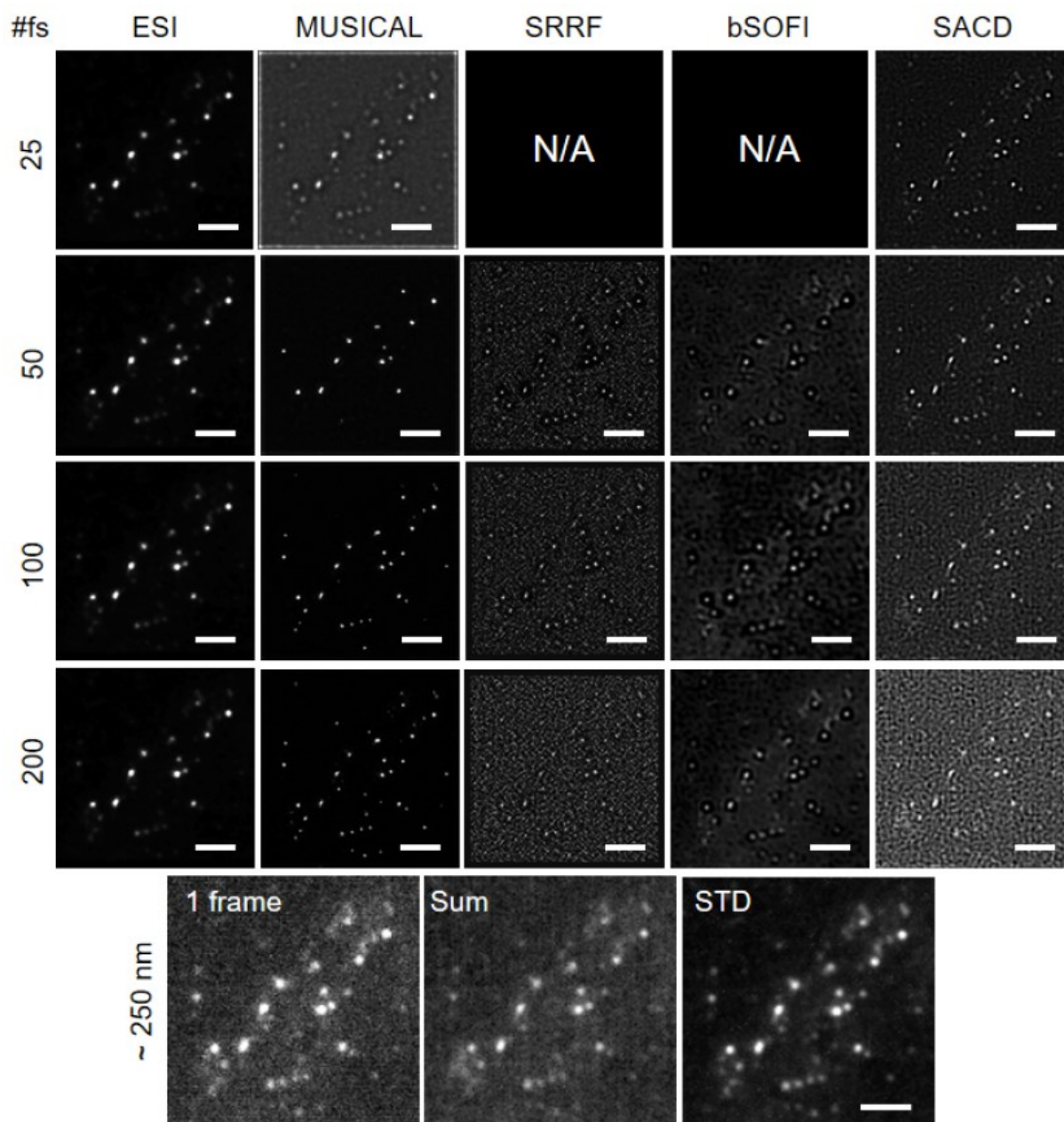


Figure S6. Liposomes 250 nm: assessment of the number of frames (#fs) parameter and an overview of the data, containing a single frame, a sum, and the standard deviation image (STD). The scale bars are 2 μm . The number of frames selected in most cases (and 'default' in case of doubt) was 100. A different frame number was chosen only in the of SACD (25 fs) and bSOFI (200 fs) for the 250 nm sample, as these results were evaluated significantly better, yielding less background artefacts. Gamma 0.5 is used for better visualization of the ESI reconstructions.

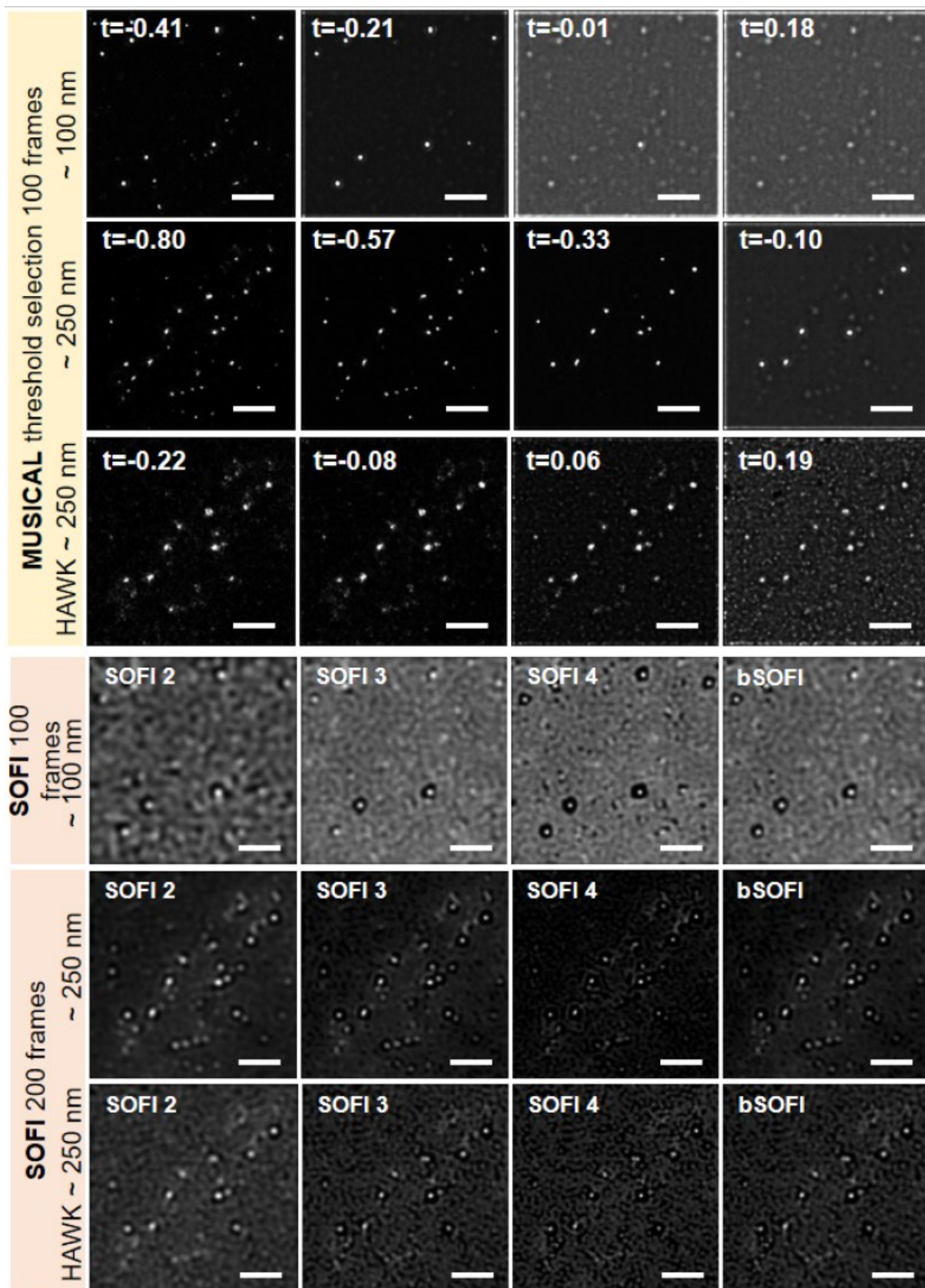
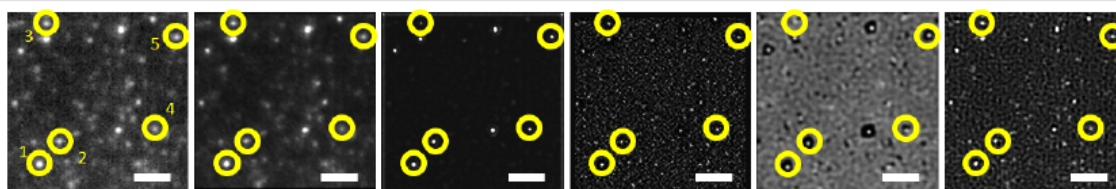


Figure S7. Liposomes 100 nm and 250 nm: assessment of the threshold parameter for MUSICAL and best SOFI method for the assessed 100 nm and 250 nm liposome data. For MUSICAL, the thresholds $t=-0.21$ (100 nm) and -0.57 (250 nm) were

found best and chosen for further analysis. For SOFI, bSOFI was found best. HAWK increased the effect of the background caused by the agarose autofluorescence signal. The scale bars are 2 μm .

100 nm	SUM [nm]	ESI [nm]	MUSICAL [nm]	SRRF [nm]	SOFI [nm]	SACD [nm]
1	366	207	33	54	183	139
2	324	188	49	45	175	136
3	328	178	43	88	231	153
4	314	218	42	49	230	165
5	285	188	36	53	188	131
MEAN	323	196	41	58	201	145
STD	29	16	7	17	27	14



250 nm	SUM [nm]	ESI [nm]	MUSICAL [nm]	SRRF [nm]	bSOFI [nm]	SACD [nm]
1	290	166	44	50	156	98
2	309	195	47	44	202	135
3	454	206	58	49	198	132
4	269	198	68	44	189	107
5	304	150	51	47	174	85
MEAN	325	183	54	47	184	111
STD	74	24	10	3	19	22

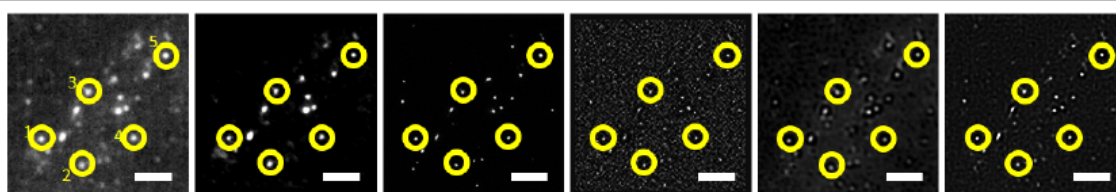


Figure S8. Table of size measurements for the 100 nm and 250 nm liposomes. The measured particles are indicated in the panels below the respective tables. The scale bars are 2 μm . The number of frames were 100, except for the cases of SACD (25 fs) and bSOFI (200 fs) for 250 nm liposome. A different number of frames were used in these cases based on the number of frames study (Suppl. Figure S6). Raw images were used for the size determinations. For optimal visualization the corrections applied were Auto brightness and contrast and gamma 0.5 for ESI.

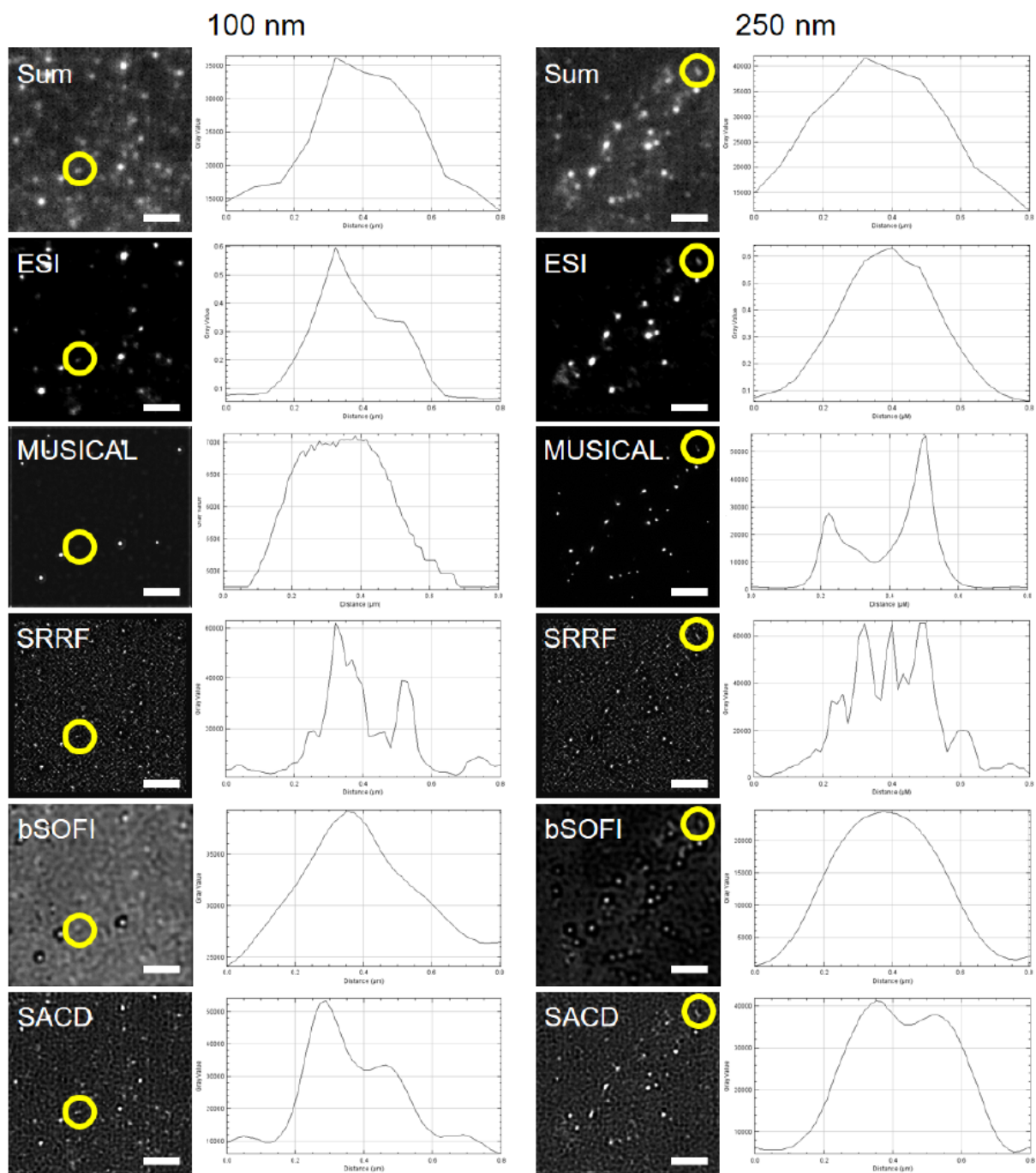


Figure S9. Resolution measurements for the 100 nm and 250 nm liposomes via line profiles. The regions containing elongated spots (indicating presence of multiple liposomes) are indicated by the yellow circles. The double dip seen by some plots can be a sign resolution enhancement. However, high prevalence of reconstruction artifacts (partly due to agarose autofluorescence), renders the measurements unreliable. Raw images were used for the profiling but shown with the optimal corrections for visual purposes (Auto brightness and contrast and gamma 0.5 for ESI).

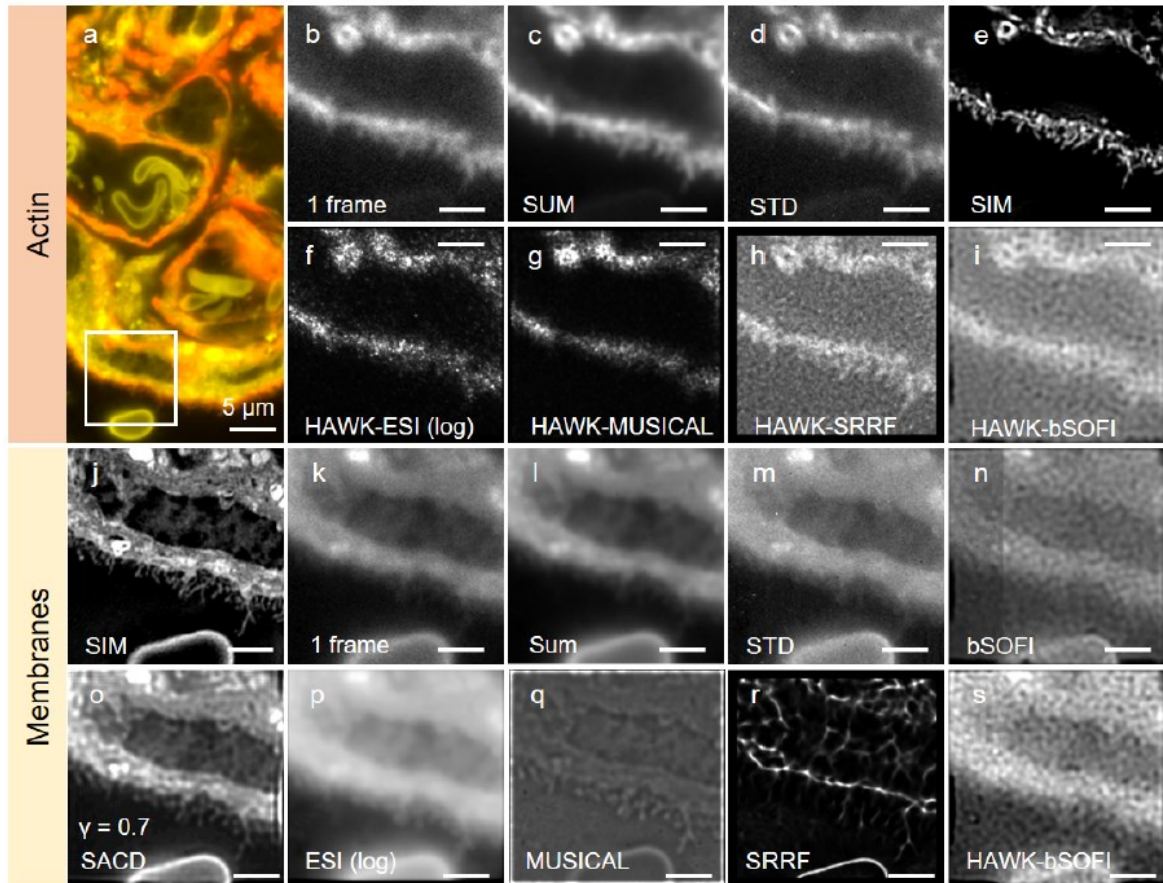


Figure S10. Placenta tissue: epi-fluorescent images of 1 μm -thick human placenta cryo-section labelled with phalloidin-ATTO647N and CellMask Orange for identification of F-actin and lipid membranes, respectively. (a) Overlaid sum image provides a large FOV of the two analyzed channels. F-actin displayed in red and membranes displayed in yellow; (b-s) Magnified view of the outlined area in a; (b-d) Overview of the sample data for the F-actin channel; (b) first frame of the image stack; (c) sum image of the image stack (400 frames); (d) standard deviation image of the image stack; (e) SIM reference image of the F-actin channel; (f-i) Results of combining HAWK (using 5 levels) along with different fluctuation methods. For this dataset, HAWK did not improve the reconstructions compared to the previous results (see Figure 6 in the main manuscript). The two bottom rows display an overview of the sample data and results for the membrane channel; (j) SIM reference image of the membrane channel; (k) first frame of the image stack; (l) sum image of the image stack; (m) standard deviation image of the image stack; (n-s) For the membrane dataset, the reconstruction algorithms exhibit similar performance as with the F-actin dataset, where SADC and MUSICAL performed the best among the techniques, revealing structural details of the tissue samples beyond what is visible in the sum image and in accordance with the SIM reference image; (i, s) Despite its potential of improving bSOFI reconstruction, the combination HAWK-bSOFI yielded degraded results for these datasets. 400 frames were used for the reconstructions. The scale bars are 2 μm .

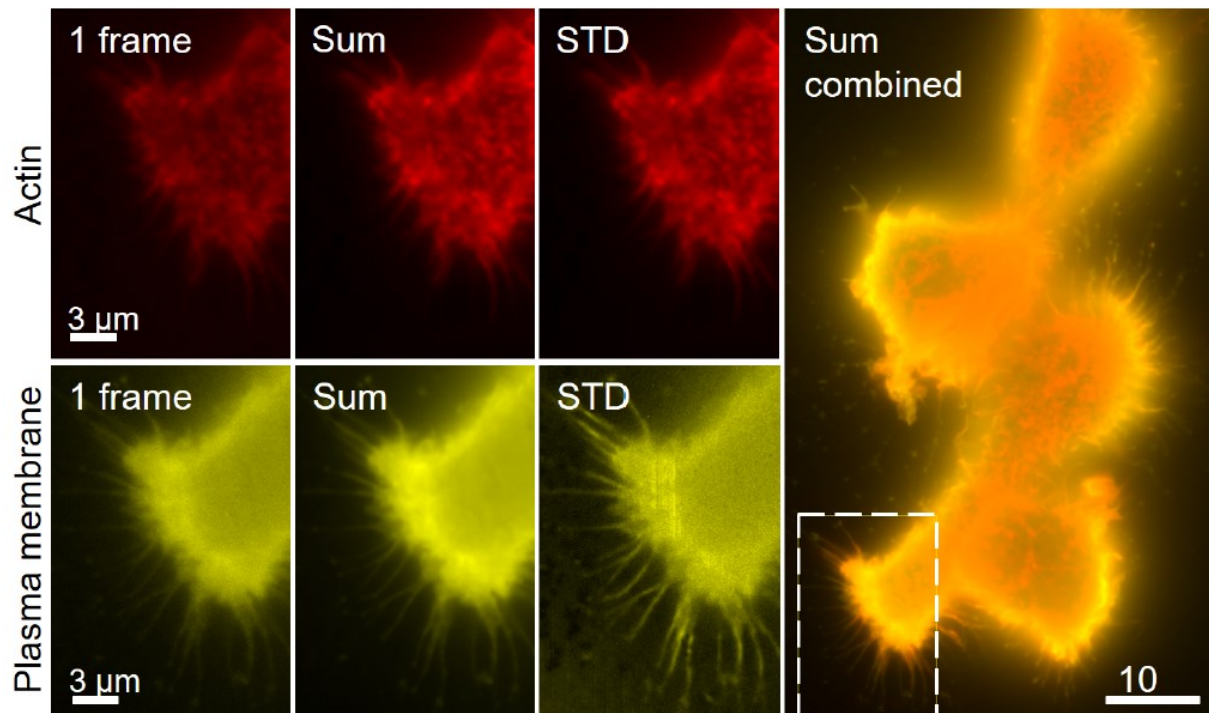


Figure S11. Overview of the (epi) dataset used for the study of fixed cell. The panels show two-channel epi-fluorescence microscopy images of cultured macrophages labelled for F-actin (phalloidin-ATTO-647N) and the plasma membrane (CellMask Orange). The panels show a single image, the sum and the standard deviation image (STD) of 500 frames, together with a larger sample area with the smaller region subjected to analysis indicated. The reconstruction results are found in Figures S12 to S15.

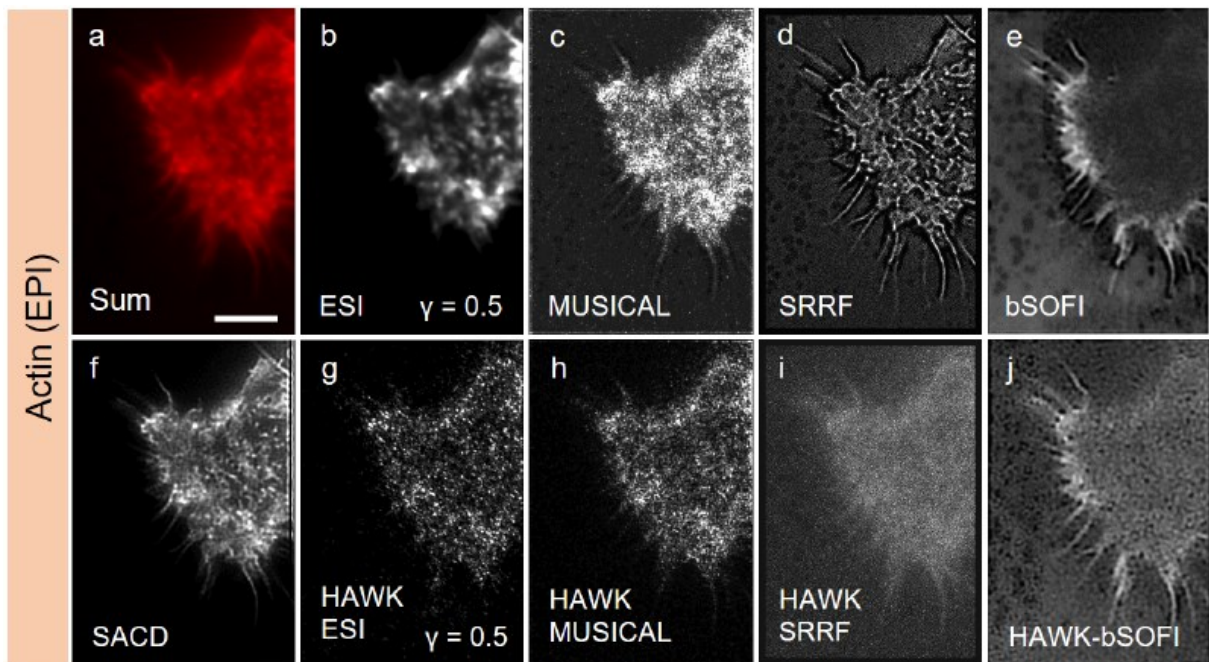


Figure S12. *Cont.*

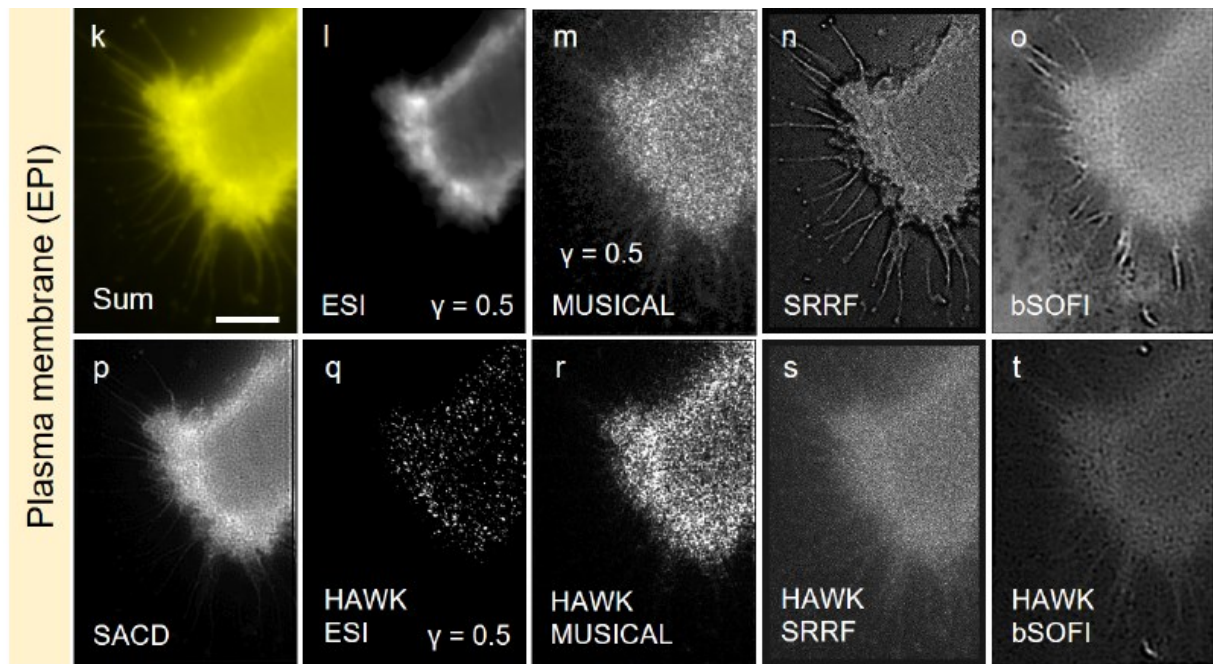


Figure S12. Results summary of fixed-cell (epi): Comparison of (the best) results for the different methods on fixed macrophages using epifluorescence microscopy. (a) Sum of 500 frames of the raw data stack (F-actin with phalloidin-ATTO-647N). The scale bar is 5 μm and apply to all panels; (b) ESI (order 4) on 500 frames. The image is $\gamma = 0.5$ intensity adjusted; (c) MUSICAL on 50 frames using threshold -1.0; (d) SRRF result on 50 frames using option TRM and radius 0.5; (e) bSOFI using 500 frames; (f) SACD with MPAC order 2 and 16 frames; (g) HAWK ESI on 4886 frames (resulting from 5 level HAWK on 500 raw frames). The image is $\gamma = 0.5$ intensity adjusted; (h) HAWK MUSICAL on 386 frames (resulting from 5 level HAWK on 50 raw frames) using threshold -0.3; (i) HAWK SRRF using 50 frames with the TRM option and radius 0.5; (j) HAWK bSOFI on 4886 frames (resulting from 5 level HAWK on 500 raw frames); (k) Sum of 500 frames of the raw data stack (plasma membrane using CellMask Orange). The scale bar is 5 μm ; (l) ESI (order 4) on 500 frames. The image is $\gamma = 0.5$ intensity adjusted; (m) MUSICAL on 50 frames using threshold -1.4; (n) SRRF result on 50 frames using option TRM and radius 0.5; (o) bSOFI using 500 frames; (p) SACD with MPAC order 2 and 16 frames; (q) HAWK ESI on 4886 frames (resulting from 5 level HAWK on 500 raw frames). The image is $\gamma = 0.5$ intensity adjusted; (r) HAWK MUSICAL using 386 frames (resulting from 5 level HAWK on 50 raw frames) and threshold -0.5; (s) HAWK SRRF using 50 frames with the TRM option and radius 0.5; (t) HAWK bSOFI on 4886 frames (resulting from 5 level HAWK).

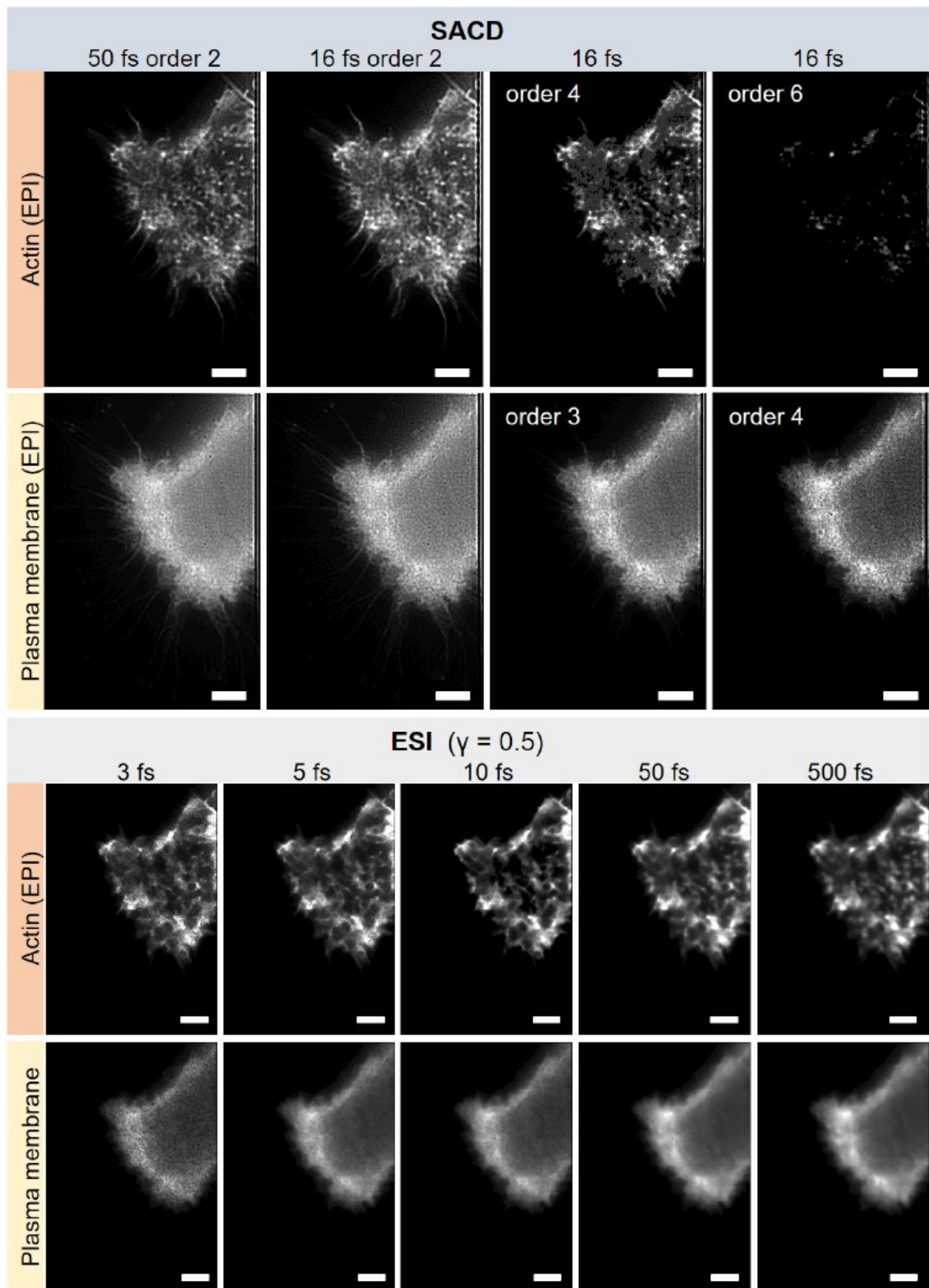


Figure S13. Fixed cell results of SACD and ESI using additional options/parameter as indicated in the figure. SACD: As also seen for the simulated data, increasing the number of frames beyond 16 does not significantly improve or change the SACD results. Increasing the MPAC order causes gradual disappearance of cellular

structures. ESI: The ESI results do not appear to improve by increasing the number of frames beyond 5 frames. The results look similar whether 5 or 500 frames are used. To enhance the visibility of finer details, the ESI images are $\gamma = 0.5$ intensity adjusted. The scale bars are 2 μm .

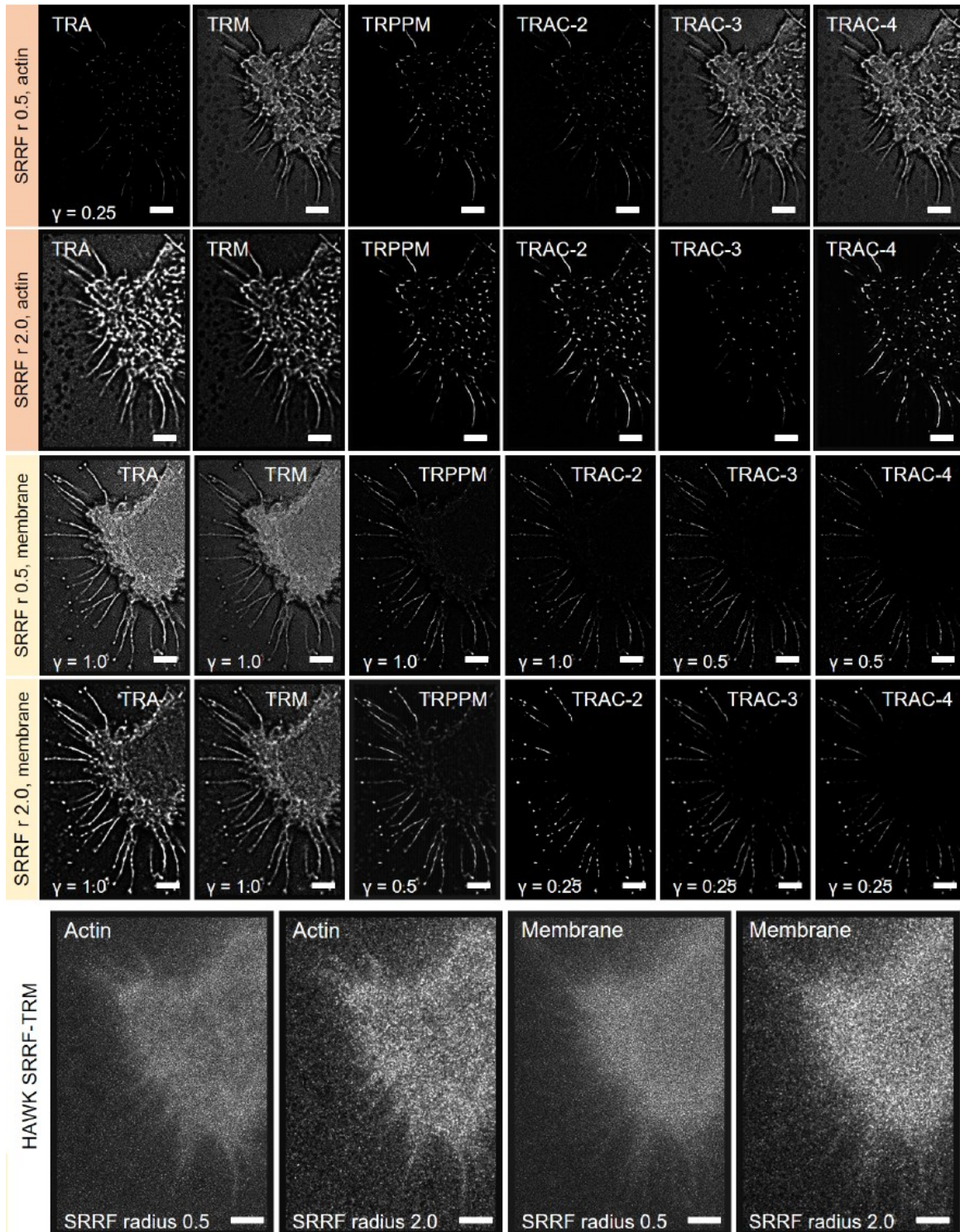


Figure S14. Fixed cell (epi): SRRF results using additional options/parameter as indicated in the figure, all with 50 frames used for the image reconstruction. The scale bars are 2 μm . The many different options offered by SRRF are problematic

as they can generate very different pictures and cellular structures, which leaves the users with difficult and subjective choices about which option, if any, accurately describes the (unknown) nanostructural details of the sample. In the case of SRRF, HAWK only produced image degradation for our samples.

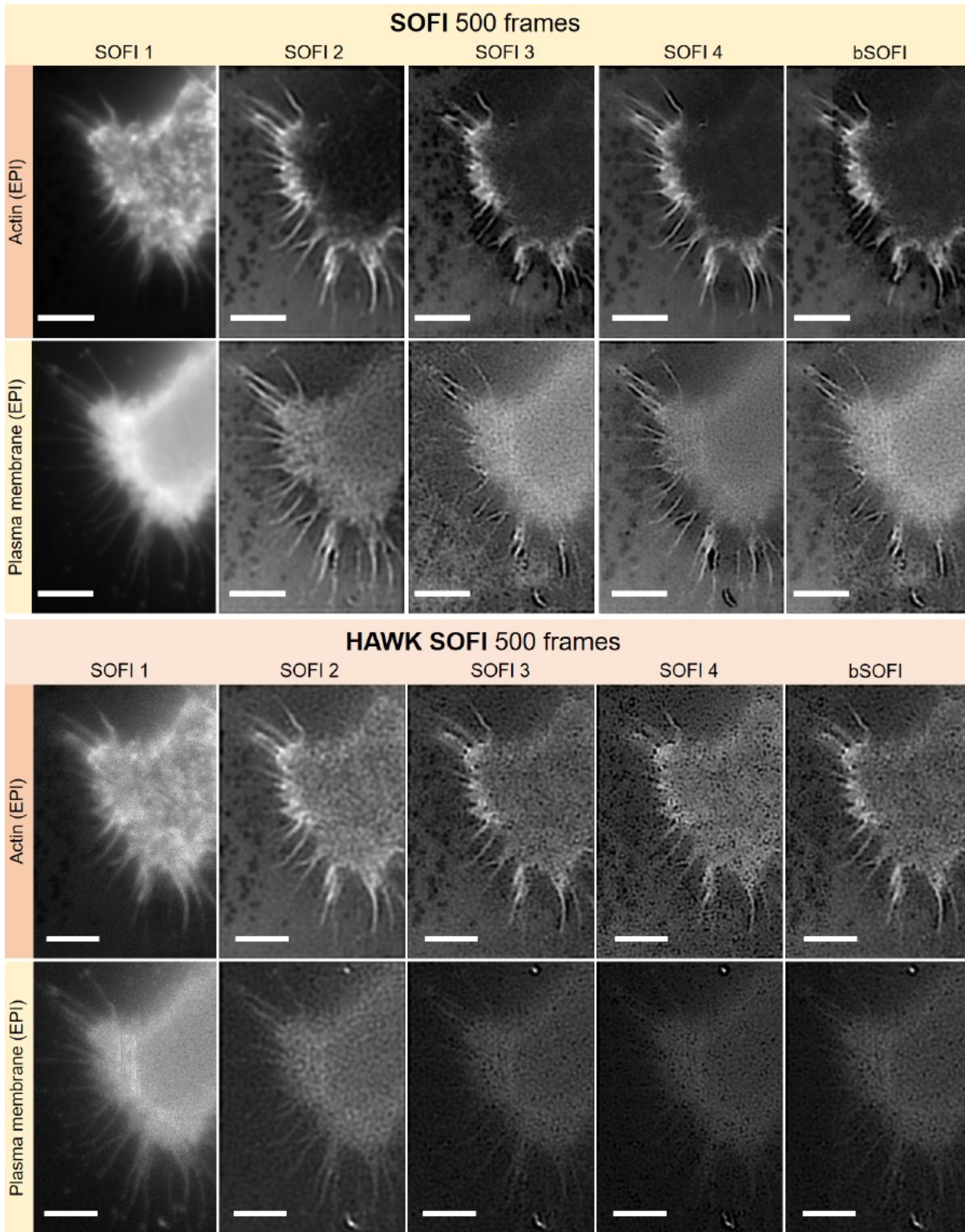


Figure S15. Fixed cell (epi): SOFI and HAWK SOFI results using additional options/parameter as indicated in the figure. The results appear not to accurately

describe the nanoscopic details of actin of membrane in macrophages. As indicated by simulations, this can be explained by low signal fluctuation of these fluorescence labels and also possible 500 frames not being sufficient for reliable SOFI reconstruction. The scale bars are 5 μm .

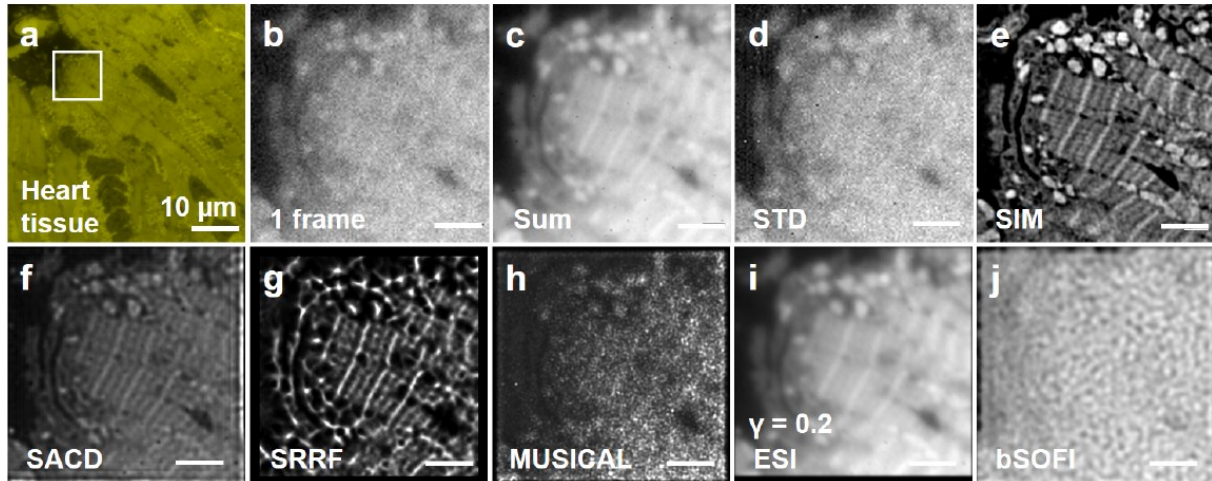


Figure S16. Heart tissue: epi-fluorescent images of 100 nm-thick pig heart cryo-section labelled with CellMask Orange for identification of lipid membranes. (a) Large FOV image of the cardiac tissue; (b-j) Magnified view of the outlined area in a. The scale bars are 2 μm ; (b) first frame of the epi-fluorescent stack. The image indicates a poor signal-to-noise ratio; (c) Sum image of the stack used for the reconstructions; (d) Standard deviation image of the same stack; (e) The reference structured illumination microscopy image, which indicates not just better contrast than the sum image but also preserving the low contrast striations throughout the selected region; (f) The SACD reconstruction shows the best correspondence with the SIM reference image; (g) The SRRF reconstruction displays subtle artifacts compared to the SIM reference image (compare e.g. larger bright spots (mitochondria) in the SIM image, and the black circles present only in the SRRF image); (h) The MUSICAL result here exhibits noticeable artifacts. (i) The ESI reconstruction (gamma transformed 0.2) is similar to the sum image in panel c. (j) The bSOFI result displays noticeable artifacts. This sample gives no out-of-focus signal, but with a high noise level and high labeling density (therefore a low level of fluctuations).

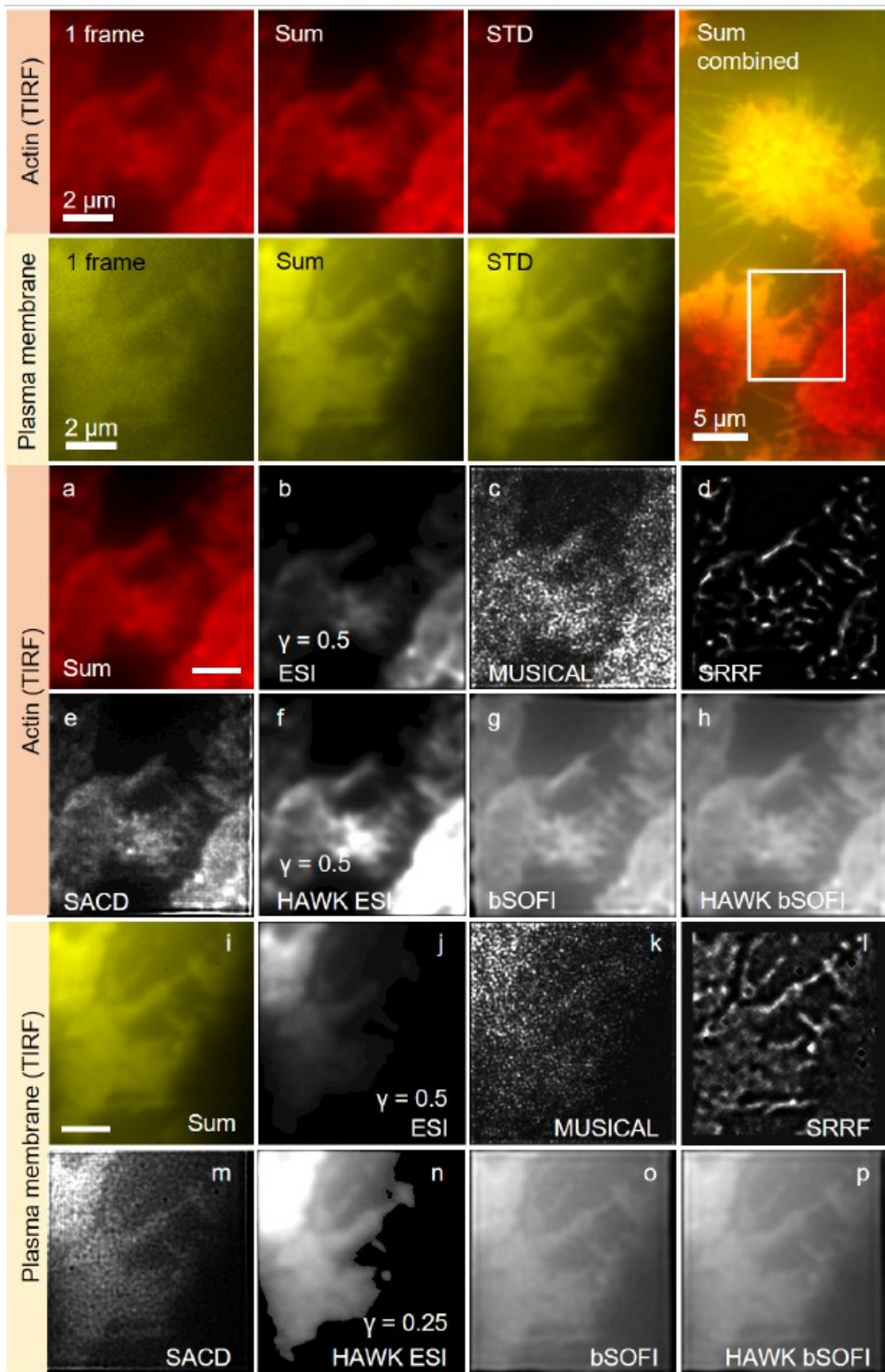


Figure S17. Overview of the TIRFM datasets (top two rows) and results summary for fixed cells. The panels show F-actin (phalloidin-ATTO-647N) and the plasma

membrane (CellMask Orange) of fixed macrophages. The panels show a single image, the sum and the standard deviation image (STD) of 500 frames, together with a larger sample area with the smaller region subjected to analysis indicated. The signal from CellMask dye caught by the coverslip surface became dominating while using TIRF illumination. *Panels a-p*: Comparison of (the best) results for the different methods on fixed macrophages using TIRFM. (a) Sum of 500 frames of the raw data stack (F-actin with phalloidin-ATTO-647N). The scale bar is 2 μm and apply to all panels; (b) ESI (order 4) on 500 frames. The image is $\gamma = 0.5$ intensity adjusted; (c) MUSICAL on 50 frames using threshold -1.3; (d) SRRF result on 50 frames using option TRM and radius 2.0; (e) SACD using MPAC order 3 and 16 frames; (f) HAWK ESI (5 level HAWK resulting in 4886 frames). The image is $\gamma = 0.5$ intensity adjusted; (g) bSOFI using 500 frames; (h) HAWK bSOFI on 4886 frames (resulting from 5 level HAWK). (i) Sum of 500 frames of the raw data stack (plasma membrane using CellMask Orange). (j) ESI (order 4) on 500 frames. The image is $\gamma = 0.5$ intensity adjusted; (k) MUSICAL on 50 frames using threshold -1.3; (l) SRRF result on 50 frames using option TRM and radius 2.0; (m) SACD using MPAC order 3 and 16 frames; (n) HAWK ESI (5 level HAWK resulting in 4886 frames). The image is $\gamma = 0.5$ intensity adjusted; (o) bSOFI using 500 frames; (p) HAWK bSOFI on 4886 frames (resulting from 5 level HAWK).

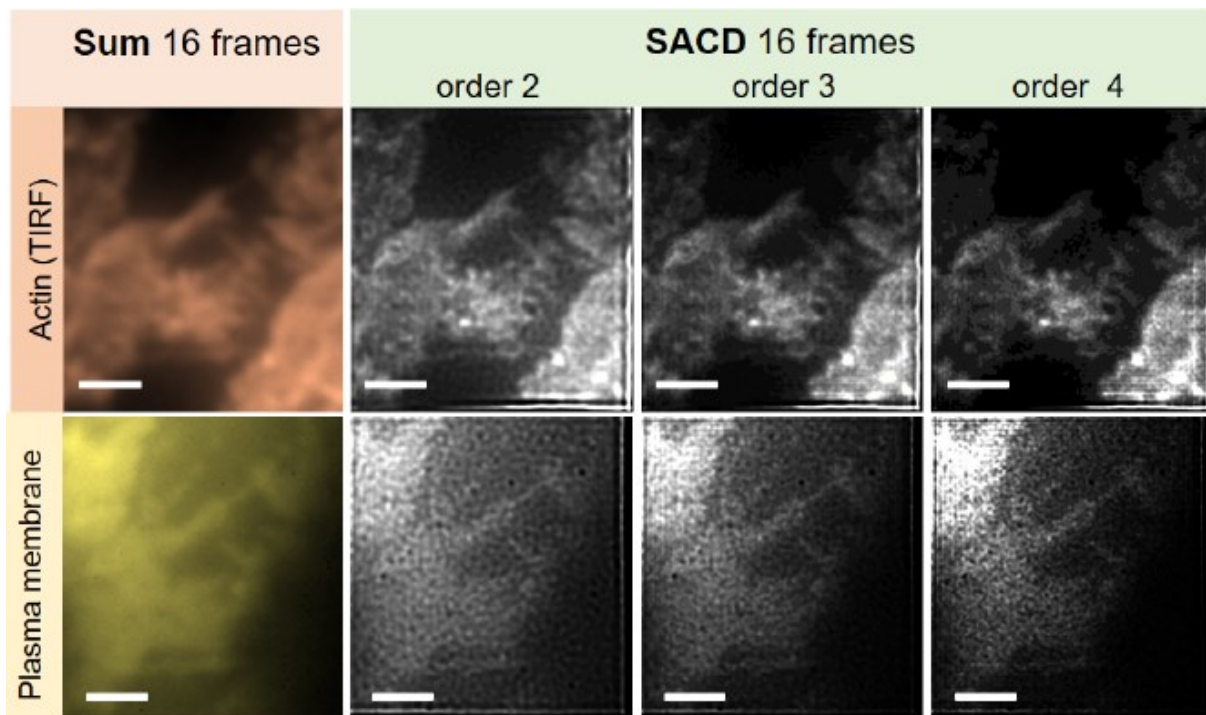


Figure S18. *Cont.*

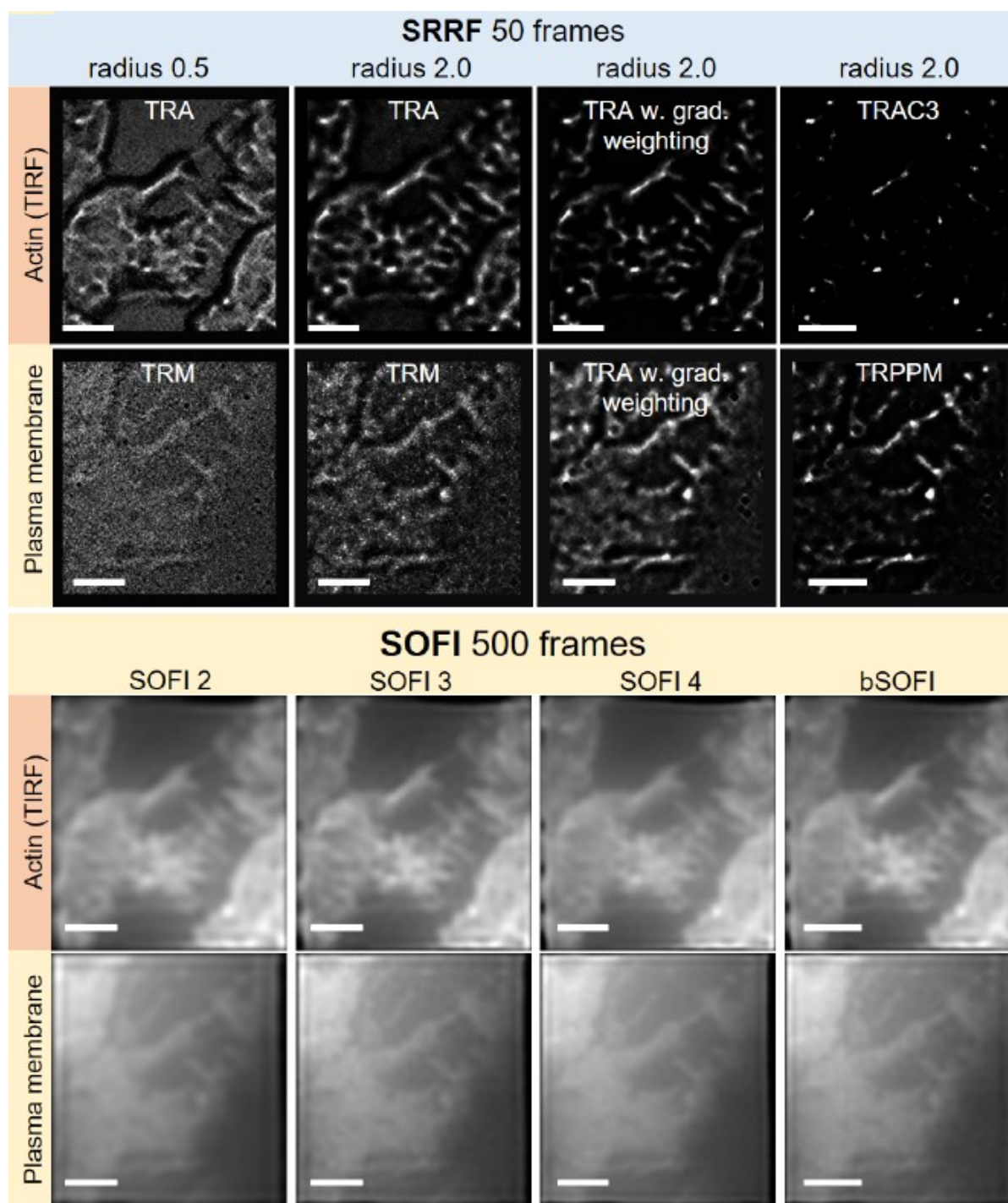


Figure S18. TIRFM of fixed macrophages: results using additional options/parameter (indicated in the figure) for SACD, SRRF and SOFI.

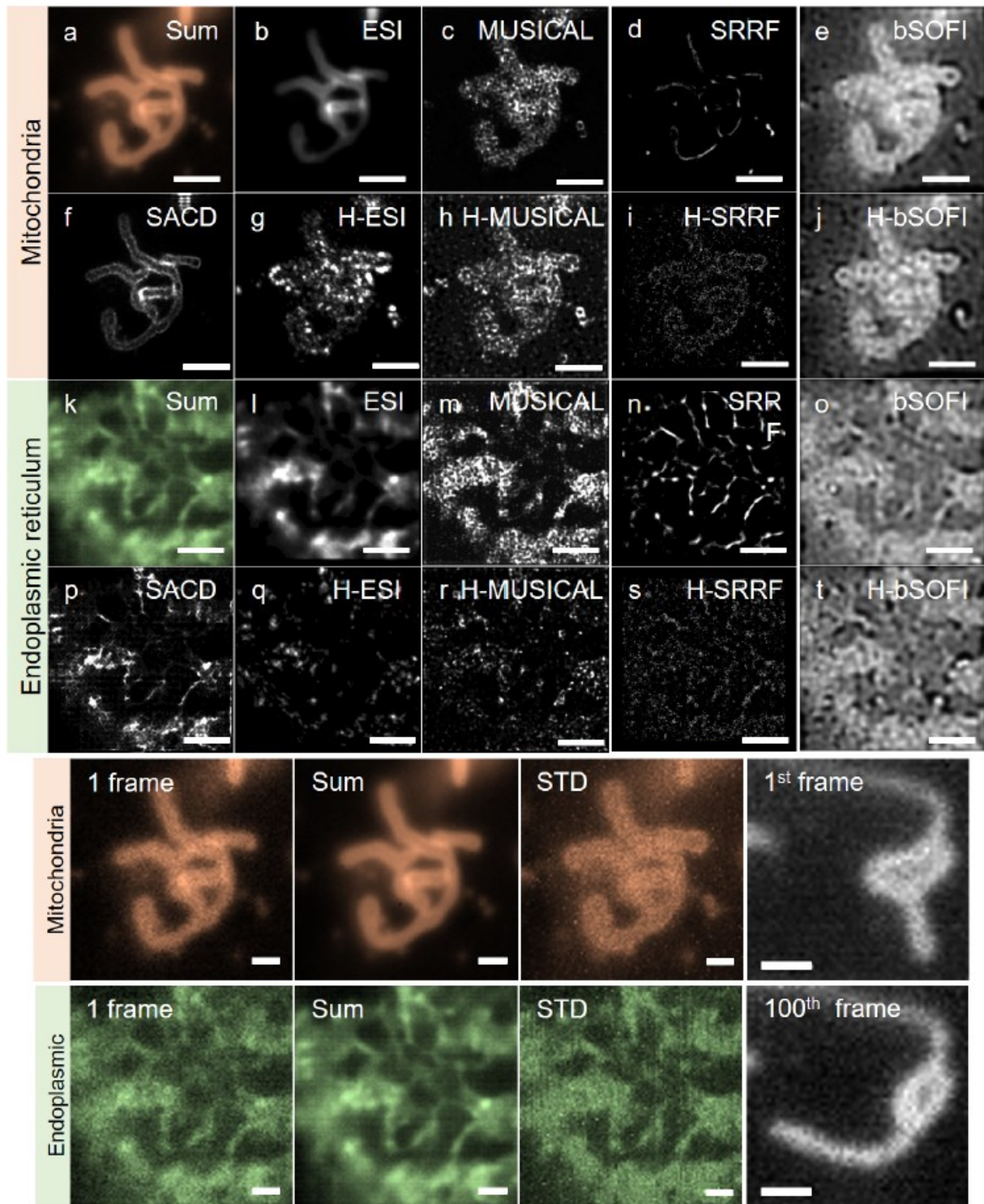


Figure S19. Results summary and data overview for live-cell data: Comparison of (the best) results for the different methods on live-cell image data (cardiomyoblasts cell-line H9c2) acquired using epifluorescence microscopy. Panels (a)-(j) are of mitochondria (outer membrane protein 25, OMP25-mCherry), and panels (k)-(t) are of the endoplasmic reticulum (KDEL-EGFP). The two datasets are two different color channels from the same cell, region and time-lapse sequence.

(a) Sum of the 64 frames (of mitochondria) used for the image reconstructions of panels (a)-(j); (b) ESI order 4; (c) MUSICAL using threshold -0.8; (d) SRRF using option TRAC order 2 and radius 0.5; (f) SACD using MPAC order 4; (g) HAWK ESI (5 level HAWK resulting in 526 frames). The image is $\gamma = 0.5$ intensity adjusted; (h) HAWK MUSICAL on 526 frames (resulting from 5 level HAWK) using threshold 0.0; (i) HAWK SRRF using option TRAC order 2 and radius 0.5; (j) HAWK bSOFI on 526 frames (resulting from 5 level HAWK);

(k) Sum of the 64 frames (of the endoplasmic reticulum) used for the image reconstructions of panels (l)-(t); (l) ESI order 4; (m) MUSICAL using threshold -0.5; (n) SRRF using option TRAC order 2 and radius 0.5; (p) SACD using MPAC order 4; (q) HAWK ESI (5 level HAWK resulting in 526 frames). The image is $\gamma = 0.5$ intensity adjusted; (r) HAWK MUSICAL on 526 frames (resulting from 5 level HAWK) using threshold 0.2; (s) HAWK SRRF using option TRAC order 2 and radius 0.5; (t) HAWK bSOFI on 526 frames (resulting from 5 level HAWK). The scale bars are 2 μm .

Bottom rows, data overview: 1st frame, sum and standard deviation (STD) image of the datasets used for panels a-t. 1st and 100th (last) frame of the 100-frame image stack used for the reconstructions of panels (g)-(l) of Figure 6 of the main manuscript. The scale bars are 1 μm .

Paper 3

Article

Characterization of Liposomes Using Quantitative Phase Microscopy (QPM)

Jennifer Cauzzo ^{1,†} , Nikhil Jayakumar ^{2,†} , Balpreet Singh Ahluwalia ², Azeem Ahmad ^{2,‡} 
and Nataša Škalko-Basnet ^{1,*} 

¹ Drug Transport and Delivery Research Group, Department of Pharmacy, Faculty of Health Sciences, University of Tromsø The Arctic University of Norway, N-9037 Tromsø, Norway; jennifer.cauzzo@uit.no

² Optical Nanoscopy Research Group, Department of Physics and Technology, Faculty of Science and Technology, University of Tromsø The Arctic University of Norway, N-9037 Tromsø, Norway; nikhil.jayakumar@uit.no (N.J.); ahluwalia@uit.no (B.S.A.); azeem.ahmad@uit.no (A.A.)

* Correspondence: natasa.skalko-basnet@uit.no; Tel.: +47-776-46-640

† These authors contribute equally to this paper.

‡ These authors contribute equally to this paper.

Abstract: The rapid development of nanomedicine and drug delivery systems calls for new and effective characterization techniques that can accurately characterize both the properties and the behavior of nanosystems. Standard methods such as dynamic light scattering (DLS) and fluorescent-based assays present challenges in terms of system's instability, machine sensitivity, and loss of tracking ability, among others. In this study, we explore some of the downsides of batch-mode analyses and fluorescent labeling, while introducing quantitative phase microscopy (QPM) as a label-free complimentary characterization technique. Liposomes were used as a model nanocarrier for their therapeutic relevance and structural versatility. A successful immobilization of liposomes in a non-dried setup allowed for static imaging conditions in an off-axis phase microscope. Image reconstruction was then performed with a phase-shifting algorithm providing high spatial resolution. Our results show the potential of QPM to localize subdiffraction-limited liposomes, estimate their size, and track their integrity over time. Moreover, QPM full-field-of-view images enable the estimation of a single-particle-based size distribution, providing an alternative to the batch mode approach. QPM thus overcomes some of the drawbacks of the conventional methods, serving as a relevant complimentary technique in the characterization of nanosystems.

Keywords: liposomes; nanomedicine; characterization; label-free; quantitative phase microscopy



Citation: Cauzzo, J.; Jayakumar, N.; Ahluwalia, B.S.; Ahmad, A.; Škalko-Basnet, N. Characterization of Liposomes Using Quantitative Phase Microscopy (QPM). *Pharmaceutics* **2021**, *13*, 590. <https://doi.org/10.3390/pharmaceutics13050590>

Academic Editors: Giuseppe De Rosa, Sandra Ristori, Virginia Campani and Ilaria Clemente

Received: 27 March 2021

Accepted: 20 April 2021

Published: 21 April 2021

Publisher's Note: MDPI stays neutral with regard to jurisdictional claims in published maps and institutional affiliations.



Copyright: © 2021 by the authors. Licensee MDPI, Basel, Switzerland. This article is an open access article distributed under the terms and conditions of the Creative Commons Attribution (CC BY) license (<https://creativecommons.org/licenses/by/4.0/>).

1. Introduction

Nanomedicine emerged as an advanced field expected to change the landscape of pharmaceutical development, promising improved drug efficacy and safety. Various types of nanoformulations (nanocarriers) have been proposed to impart biological superiority [1]. However, many promises remain to be fulfilled, and recent years oversaw the trend of “back-to-basic”, trying to ensure a better understanding of the interplay between drugs, nanocarriers, and biological environment, especially biological barriers [2].

The characterization of a nanosystem is a crucial initial step in the development of novel nanomedicine. Changes in physicochemical properties of a nanocarrier can lead to a change in their behavior, as well as biological fate. Therefore, by tailoring a nanocarrier's features, we could augment its desired pharmacological effect. However, failure to ensure reliable and robust characterization, within *in vitro* settings, would directly impair the prediction of biological fate and limit success in *in vivo* settings [3].

The carrier size, surface charge, and polydispersity (PDI) are the three major well-established properties known to affect the internalization and potentially the targeting of drug delivery systems within biological environments [4–6]. The standard widely utilized

characterization techniques are typically batch-mode analyses, such as dynamic light scattering (DLS). Being fast and easy to use, DLS allows the estimation of size distribution and polydispersity index (PDI), which reflects the uniformity of a nanosystem. The combination of DLS and electrophoretic mobility (electrophoretic light scattering) further allows the estimation of the surface charge based on the zeta-potential distribution. Nonetheless, a relevant downside to these techniques is their bias when characterizing polydispersed systems, due to their resolution being limited to a factor of 3, potentially failing to separate multimodal particle distributions [7,8]. Alternative characterization techniques are mostly microscopy-based, namely, transmission electron microscopy (TEM), scanning electron microscopy (SEM), and atomic force microscopy (AFM). These single-particle-size measurement techniques circumvent DLS disadvantage by resorting to a particle-by-particle analysis of the images. However, the widespread use of these techniques is limited by the highly complex sample preparation and their limited accessibility and cost [9].

In addition to physicochemical characterization, it is necessary to assess the behavior of nanosystem in relevant environments. The most common strategy applied to follow the fate of nanosystems is the introduction of a fluorescent label [10]. Fluorescence-based techniques can track nanosystems, potentially both *in vitro* [11] and *in vivo* [12]. Additionally, new methods have been developed to utilize fluorescence in the physicochemical characterization of the nanosystems. Size has been estimated through fluorescent microscopy [13] as well as flow cytometry [14]. Thereof, fluorescent-based techniques are powerful tools to directly establish physicochemical–behavioral relationships. However, the addition of an external component to nanosystems may affect the individual properties of both the nanosystem and the fluorophore [15]. For instance, fluorophores are known to alter nanosystems' surface properties [16] and to detach from them [11,17]. Furthermore, the fluorescent signal decays with time and is not suitable for long-term tracking. Moreover, all fluorescent techniques reliant on strong illumination can induce high phototoxicity in live biological samples.

New label-free techniques are emerging as a mean to overcome the need for a marker, while attempting to combine physicochemical and behavioral characterizations. Such techniques include surface plasmon resonance (SPR) [18], nanoparticle tracking analysis (NTA) [19], coherent anti-Stokes Raman scattering (CARS) [20], and the technique we utilized in the current work, i.e., quantitative phase microscopy (QPM) [21].

Quantitative phase microscopy (QPM) is a label-free technique that is able to detect nanometer pathlength changes by inducing minimal photo-toxicity to the study sample. QPM setups can be operated in two modes, namely, on-axis and off-axis, depending on the intended application. Off-axis quantitative phase microscopes allow imaging of highly dynamic events. The Fourier transform algorithm is used to reconstruct an image from the interferogram, providing high temporal resolution at the cost of spatial resolution, due to the filtering of object information in the Fourier domain. On the contrary, interferograms from on-axis microscopes can be reconstructed through the phase-shifting algorithm, preserving high-frequency information and high spatial resolution at the cost of temporal resolution, due to their requiring of 4–5 frames per phase per image [22]. The latter setup provides lossless and highly sensitive measurements of the specimens and is thus most suited for the characterization of sub-diffraction limit-sized nanoparticles [23].

Most of the QPM systems are implemented with either highly temporally and spatially coherent light source (laser) or low temporally and spatially coherent light source (white light). These light sources carry certain disadvantages such as speckle noise and coherent noise—when using lasers or chromatic aberration and dispersion—in the case of white light [24–28]. To overcome the challenges associated with conventional light sources, we implemented QPM with spatially low and temporally high coherent light source, also called pseudothermal light source (PTLS). Details for such type of light source can be found elsewhere [29,30].

In this study, we assessed the potential of quantitative phase microscopy as a suitable label-free technique for the characterization of nanocarriers. Liposomes were chosen as model carriers for their high therapeutic relevance [31] as well as their structural versatility.

In conventional liposomes, such as those used in our study, phospholipids represent the structural repeated unit. Figure 1a (top) shows the chemical structure of a typical phospholipid, comprising a polar head (often a zwitterion) and hydrophobic tails (generally two carbon chains of various length). When hydrating phospholipids, their dual nature drives their self-assembly into vesicular structures with a hydrophobic bilayer enclosing a hydrophilic inner core (Figure 1b). Consequently, liposomes are often used both as solubilizers and as carriers, able to entrap and protect hydrophobic or/and hydrophilic active ingredients in their respective compartments. Their size, surface characteristics, and functionality can be tailored to address the challenges of the route of drug administration they are to be applied to [32].

From a technological point of view, liposomes are nanosized and almost transparent dynamic vesicles, very complex to image if not in a dried-out condition [33]. Furthermore, in quantitative phase imaging, their very nature causes only a slight delay in the light wavefront. This low signal becomes challenging to detect and interpret in laser-based QPM systems, thus a PTLs-equipped QPM setup was selected. To ensure that QPM images are trustworthy, we introduced a fluorescent marker within liposomal bilayers (Figure 1). The fluorescent signal emitted from the labeled liposomes was used to confirm the localization of liposomes on the interferogram. A fluorescent phospholipid (N) was selected as a marker due to its chemical structure similar to the natural lipid components within the liposomal bilayer (Figure 1a). Given its insolubility in water, the fluorescent lipid can only accommodate itself within the liposomal bilayer (Figure 1b).

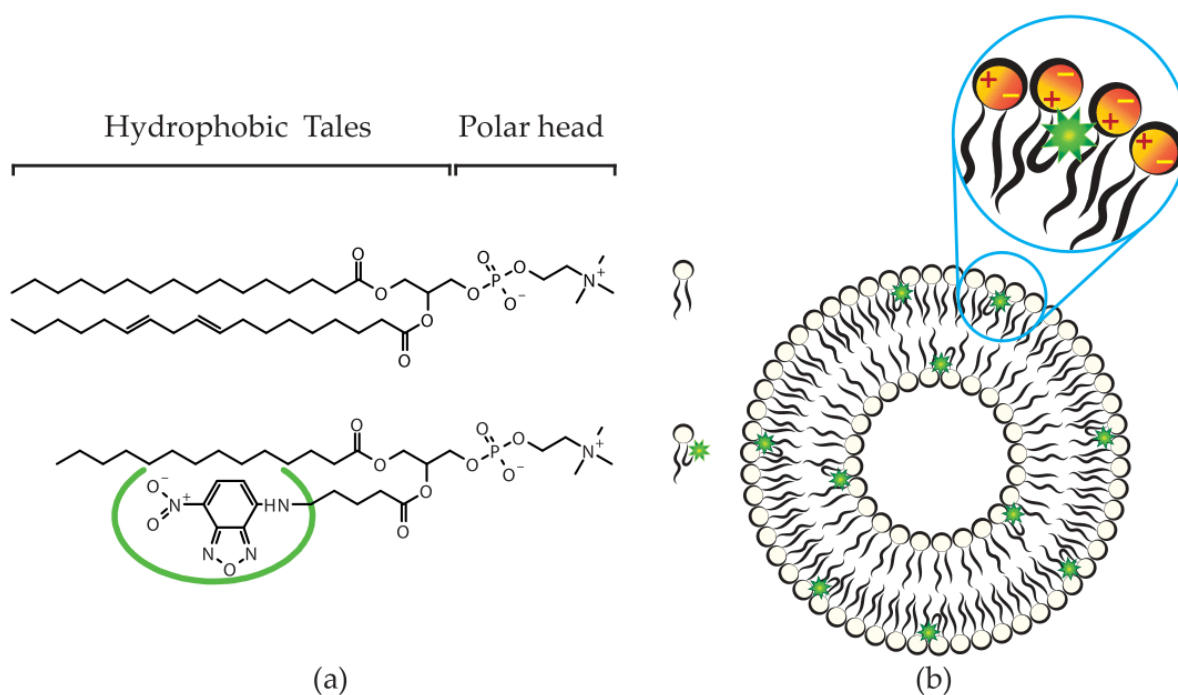


Figure 1. Liposomal formulation. Panel (a) (below) shows the fluorescently labeled phospholipid, for the visual comparison with the chemical structure of the main lipid ingredient in soy phosphatidylcholine (above). Panel (b) shows the expected random incorporation of the labeled lipid in the bilayer, according to minimal energy interaction and previous studies [34]. The molecules were drawn with ACD/ChemSketch (Freeware) 2019 2.1, according to the structures declared by the manufacturer.

2. Materials and Methods

2.1. Materials

1-myristoyl-2-[6-[(7-nitro-2-1,3-benzoxadiazol-4-yl)amino]hexanoyl]-sn-glycero-3-phosphocholine (14:0–06:0 NBD-PC, N) was purchased from Avanti Polar Lipids, Alabaster, AL, USA. Methanol, glucose, sucrose, and poly-L-lysine (PLL) were purchased from

Sigma-Aldrich, Steinheim, Germany. Soy phosphatidylcholine (Lipoid S100, SPC) was obtained from Lipoid GmbH, Ludwigshafen, Germany.

2.2. Liposome Preparation

Liposomes were prepared following the film hydration method [15]. Low-pressure rotary evaporation of a methanol solution of SPC and fluorophore N (100:1) was performed using a Büchi rotary evaporator R-124 with vacuum pump V-700 (Büchi Labortechnik, Flawil, Switzerland). The thin film in the round-bottomed flask was then re-suspended by hand shaking in 2 M sucrose solution to the final concentration of SPC 10 mg/mL and N 0.1 mg/mL. Liposomal suspensions were then stored in the fridge at 4 °C. Prior to further processing, the size distribution was determined by combining the available techniques and settings.

2.3. Liposome Size Reduction

After overnight stabilization, the liposomes were processed by hand extrusion to tailor their size distribution [15]. Polycarbonate membranes (Nucleopore®) with sieving sizes of 800, 400, and 200 nm were used stepwise, as indicated in Table 1. Further overnight stabilization was ensured before the additional characterization steps.

Table 1. Liposome processing to size reduction.

Formulation	Extrusion
N1	1 × 800 nm ¹
N2	4 × 800 nm
N3	4 × 800 nm, 4 × 400 nm
N4	4 × 800 nm, 4 × 400 nm, 4 × 200 nm

¹ Single filtration to exclude potential particle contaminants on the manufacturing.

2.4. Liposome Characterization: Size and ζ-Potential

Dynamic light scattering (DLS) was used to estimate size and zeta-potential distribution of the liposomal suspensions [35]. All dispersion were diluted 1:100 in 2 M glucose solution and analyzed with a Malvern Zetasizer Nano—ZS (Malvern, Oxford, UK).

An additional size characterization was performed on the unprocessed/filtered liposomes (N1), as the size distribution of the sample could not be reliably represented within the sensitivity range of the Malvern Zetasizer Nano—ZS (0.01–1 µm). A Particle Sizing System, Inc. Model 770 Accusizer (Santa Barbara, CA, USA), was used to estimate the size distribution in single-particle optical sensing. To optimize the sensitivity range of the instrument for the unknown particle size of the sample, both voltage thresholds were used, corresponding to size thresholds of 0.69 and 1.50 µm [36].

2.5. Liposome Immobilization for Imaging Purpose

Several immobilization strategies were attempted to obtain the liposomal suspension in monolayer without drying out the sample (Figure A1, in Appendix A). A silicon wafer with a PDMS frame was used as a support. Liposomes were diluted in a 2 M glucose solution to induce sedimentation, based on the difference in medium density inside and outside the bilayer [37]. Few microliters of liposomal suspension were applied inside the PDMS frame directly on the hydrophobic surface of the wafer, on top of a pre-jellified PLL coating, in a PLL suspension (co-jellification) and after plasma treatment of the wafer surface to increase its hydrophilicity. All setups were observed under the microscope, with and without coverslip sealing on top, and a long equilibration time was allowed for the system to stabilize the drifts on the microscope stage.

The best solution that was chosen for imaging and phase analysis was a combination of the previously used strategies. PLL was pipetted inside the PDMS frame and allowed to dry for 30 min. Few microliters of distilled water were used to rehydrate the PLL coating and then removed. The liposomal suspension pre-diluted in 2 M glucose to the final lipid

concentration of 2 $\mu\text{g}/\text{mL}$ was added on top of the coating. A coverslip was placed on top of the sample and sealed with nail polish. The wafer was then taped to the microscope stage and allowed to equilibrate for 30 min.

2.6. Imaging

A schematic diagram of the imaging system used for QPM is shown in Figure 2. A nearly on-axis geometry of the microscope and a phase-shifting algorithm were chosen for high-resolution phase reconstruction of the nanosized liposomes. For fluorescence imaging, the liposomes were illuminated at 488 nm vacuum wavelength. The emitted fluorescent light alone was recorded by the CMOS camera with a combination of 488 nm long pass and (520/35) nm band pass filters. The 488 nm filter blocks the excitation light, and the bandpass filter allows only the emitted fluorescent light to reach the camera. QPM imaging was performed at 660 nm wavelength to exclude the possibility for the fluorescence label to affect the recovered phase maps, as previously shown [38].

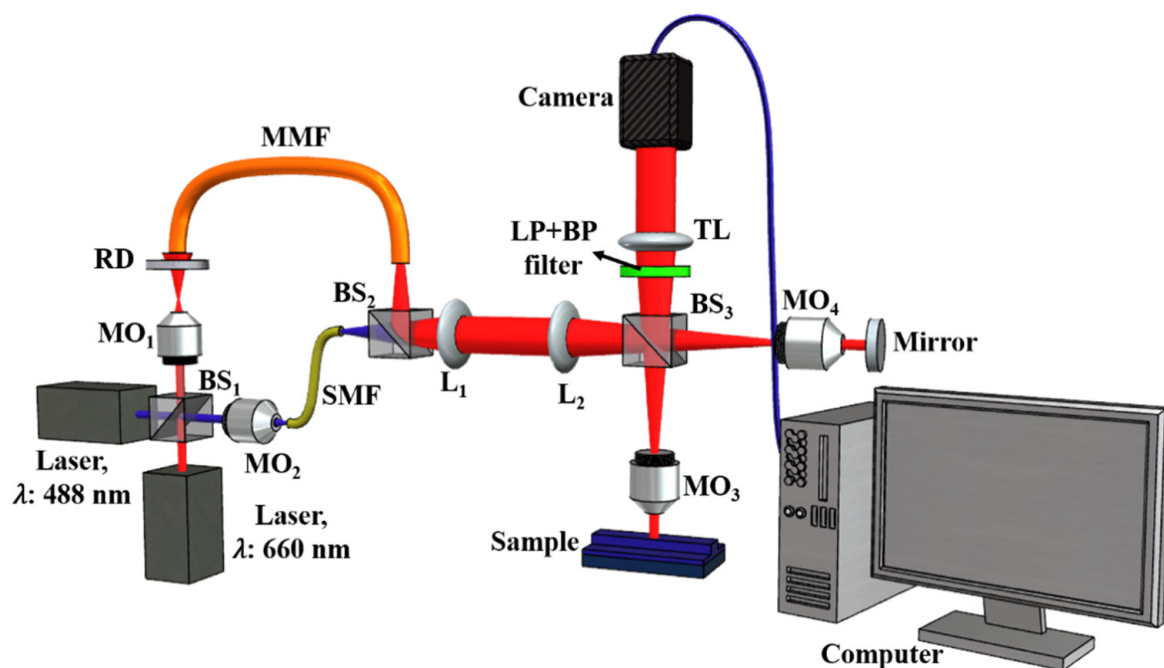


Figure 2. Schematic diagram of Linnik interferometer.

With this technique, light from a laser source is passed through a rotating diffuser before coupling into a multi-mode fiber (MMF). To obtain a wide field of illumination at the sample plane S, the diverging beam from the MMF is collected using a combination of the lenses L_1 and L_2 . The output from L_2 is split into two halves using a beam splitter (BS). One half is focused at the back aperture of a microscope objective (MO_2) to illuminate S. The reflected light off the sample plane is imaged onto a CMOS camera using BS and lens L_3 . This beam contains information about the sample under study and is referred to as the object beam. The second half known as reference beam is focused at the back aperture of the moving objective MO_3 and is reflected off a reference mirror M. The reference beam is also imaged similarly onto the CMOS camera using BS and L_3 . The reference and object beams interfere in the CMOS camera to generate an interferogram.

The phase information about the sample under consideration is encoded in this interferogram and is retrieved using the phase-shifting algorithm method.

In this work, QPM was implemented in reflection mode, using a simple upright microscope. Therefore, samples were prepared on a reflecting substrate (wafer) and covered from the top with a cover glass. This configuration can be adapted in either

inverted reflection mode or inverted transmission mode to accommodate different plates and dishes or even microfluidics devices (e.g., for cell imaging).

For the photobleaching and QPM experiment, utilizing the 1 μm -sized liposomes (N1), we acquired 26 fluorescence and phase datasets sequentially. The sample was exposed for approximately 10 s for each dataset, and photobleaching of liposomes took an average time of 4–5 min with a laser power of 20 mW on the sample plane. The acquisition time for one phase-shifted dataset using QPM was 1 s, and the switching time between fluorescence and phase imaging was around 30 s. Thus, the total time to acquire 26 fluorescence and phase datasets was approximately 18 min.

2.7. Image Processing and Analysis

2.7.1. Phase Retrieval Algorithm

The interferograms are 2D-modulated intensity (I) patterns. Mathematically, they can be defined as follows:

$$I_r(x, y) = A_r(x, y) + B_r(x, y)\cos[\phi(x, y) + \delta_r] \quad (1)$$

where the subscript r illustrates the r th phase-shifted interferogram ($r = 1, 2, 3, \dots, N$), $A_r(x, y)$ is the background, $B_r(x, y)$ is the modulation amplitude, $\phi(x, y)$ is the spatial phase information of the targeted specimen, and δ_r is the phase shift between the phase-shifted interferograms.

Assuming that $A_r(x, y)$ and $B_r(x, y)$ do not vary from one frame to the other, a new set of variables can be defined as:

$$a(x, y) = A_r(x, y),$$

$$b(x, y) = B_r(x, y)\cos\phi(x, y),$$

$$c(x, y) = -B_r(x, y)\sin\phi(x, y).$$

Equation (1) can thus be expressed as:

$$I_r(x, y) = a(x, y) + b(x, y)\cos\delta_r + c(x, y)\sin\delta_r. \quad (2)$$

With δ_r known, the advanced iterative algorithm (AIA) [39] was used to solve the unknowns, and the spatial phase map of the specimen was recovered using the relation [39]:

$$\phi(x, y) = \tan^{-1} \left[\frac{-c(x, y)}{b(x, y)} \right]. \quad (3)$$

The recovered phase map was then further utilized to calculate the thickness/height map of the sample, using the following expression:

$$\phi(x, y) = \frac{2\pi}{\lambda} [n_2(x, y) - n_1(x, y)]h(x, y), \quad (4)$$

where λ is the wavelength of light used, $n_2(x, y)$ is the refractive index of the sample, $n_1(x, y)$ is the refractive index of the surrounding medium, and $h(x, y)$ is the height/thickness of the sample. This equation implies that the phase retrieved from the interferogram is a product of the thickness of the sample and the refractive index difference between the sample and the surrounding medium.

2.7.2. Size Distribution of Liposomes

A conventional bright field/dark field microscope cannot be used for the estimation of the size of nanosized objects due to their diffraction-limited image formation. The sizes of nanoobjects (<diffraction barrier) in the recorded images appear large and equal to the diffraction limit of the microscope. The limitation of a conventional microscope can be

overcome indirectly by employing the highly sensitive QPM system, which has nanometric optical path length measurement sensitivity, for the estimation of the size of nanoobjects below the diffraction limit. Therefore, instead of directly measuring the XY size of the nanoobjects, one can measure their maximum phase/height values to estimate the size distribution by assuming their shape to be spherical. In order to estimate the size distribution of liposomes, the following steps are followed:

1. Recording of the phase-shifted interferograms of liposome samples.
2. High-resolution phase recovery by employing the AIA algorithm.
3. Removal of any background information from the recovered phase images either physically (through a reference/sample free interferogram) or numerically.
4. Convert the phase map into a height map by using Equation (4). The value of $\Delta n = (n_2 - n_1)$ is assumed to be equal to 0.04.
5. Count the number of liposomes present in the recovered height map.
6. Find the maximum height values of all liposomes using the image-processing toolbox in MATLAB and utilize these values to draw a histogram plot.

3. Results

We present liposome characterization results using both conventional batch-mode techniques and QPM. We started with DLS characterization to obtain size distribution, zeta-potential, and PdI. We then assessed the QPM label-free characterization, consisting of imaging liposome localization, integrity, and shape, gaging the potential for single-particle-based size analysis.

3.1. Conventional Characterization of Labeled Liposomes

From the original filtered batch (N1), three sequential size reduction steps were performed to obtain liposomes across the size spectra relevant for therapy (N2, N3, and N4). The corresponding size distributions are displayed in Figure 3. The upper panel shows the fitted intensity-weighted distributions to the different samples measured with DLS. As expected, the quality of the samples increased after longer processing, with sample N4 showing the best distribution (PdI = 0.11 ± 0.01), followed by N3 (PdI = 0.24 ± 0.02), while N2 showed a bimodal distribution, with PdI = 0.47 ± 0.04 . No statistically acceptable distributions were obtained for N1 in the range 0.01–1 μm because of the high polydispersity of the sample (PdI = 0.85 ± 0.08), the interference of the bigger particles, and their tendency to sediment during the measurements [40]. For this reason, N1 was measured with single-particle optical sensing, a complimentary conventional characterization with a size sensitivity range shifted towards micrometer-sized particles. This is represented in the lower panel of Figure 3 as a number-weighted distribution, with the two available voltage thresholds showcasing truncated curves, with mode of 1 μm . Interestingly, after nanosizing the vesicles, the size results did not match the expected values. Table 2 shows the expected ranges of size, PdI, and zeta-potential based on the literature [15,35,41] for corresponding extrusions of non-labeled liposomes. In particular, the intermediate processing (N2: 4×800 extrusion) did not result in a stable formulation. Furthermore, the zeta-potential exhibited strongly negative values compared to the neutral values reported in the literature for the liposomes extruded in a similar manner. The increased zeta potential values in our liposomes (N1–N4) might be contributed by the surface-available fluorescent moiety [34]. Table 2 contains an overview of the characterization (size interval, PdI, and ζ -potential), together with previously published values for non-labeled liposomes, for comparison.

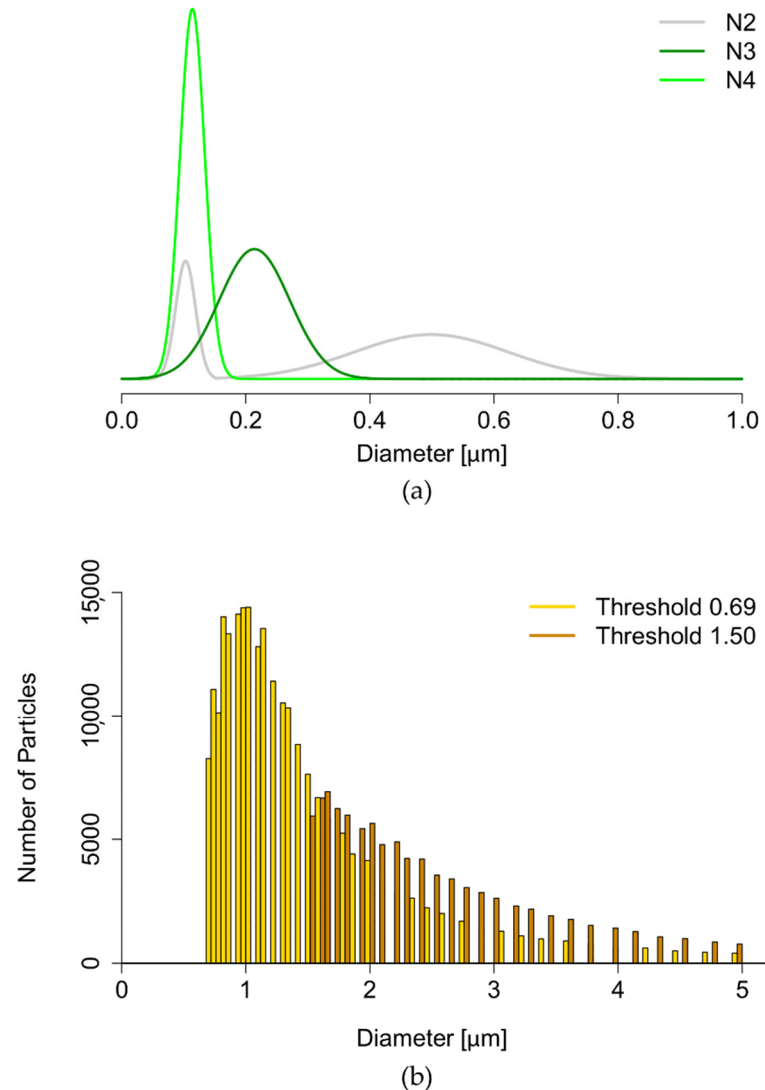


Figure 3. Conventional characterization of liposomes. (a) Intensity-weighted size distributions obtained with DLS (N2—gray, N3—dark green, N4—light green). (b) Number-weighted size distribution from single-particle optical sensing for N1, overlaying the result with size thresholds of 0.69 μm (gold) and 1.50 μm (brown).

Table 2. Conventional characterization of liposomes (Lip). Measured values (left) refer to the N-labeled formulations analyzed in this work. Expected values (right) show ranges commonly reported in the literature [15,35,41] for the correspondent processing of non-labeled liposomes. Values are expressed as mean ± standard deviation, unless otherwise indicated.

Lip	Measured Values			Expected Values		
	Size [nm]	PdI	ζ-Potential [mV]	Size [nm]	PdI	ζ-Potential [mV]
N1	1040 ¹	0.85 ± 0.08	−55.7 ± 6.3	>>1000	1	[−5, +5]
N2	499 ± 124 (74.5%) ² 103 ± 16 (25.5%)	0.47 ± 0.04	−59.8 ± 5.1	600–800	<0.250	[−5, +5]
N3	214 ± 57	0.24 ± 0.02	−57.1 ± 6.7	300–500	<0.250	[−5, +5]
N4	114 ± 20	0.11 ± 0.01	−55.4 ± 6.6	150–350	<0.250	[−5, +5]

¹ Mode (peak) of the truncated distribution (number-weighted), Figure 3b. ² Bimodal distribution described with intensity percentage for each peak in brackets.

3.2. QPM Label-Free Characterization of Liposomes

To complement the conventional characterization, liposomes were successfully immobilized on PLL-coated silicon wafers and imaged in fluorescence and phase modes for a direct comparison of the viability of the label-free technique.

The localization of liposomes using QPM is displayed in Figure 4, where phase imaging is opposed to fluorescence imaging for two different liposome sizes—100 and 200 nm. The interferograms (Figure 4a,d) and retrieved phase maps (Figure 4b,e) show it is possible to distinguish the different sizes of liposomes below the diffraction limit of light. The calibration bars for the phase images show a phase max of 60 and 200 mrad for the samples N4 and N3, respectively. This translates to diameter values of 74 and 212 nm, once fixed to 0.04 the refractive index difference between the liposomes and the medium (Δn).

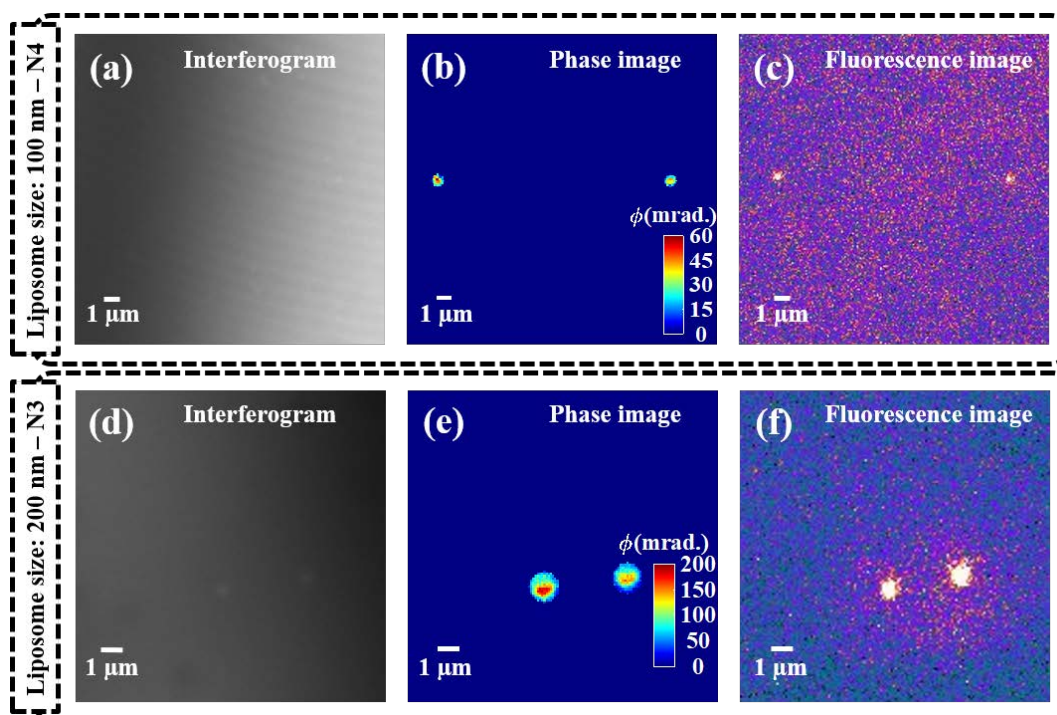


Figure 4. Single-liposome imaging. Two representative liposomes are shown in both phase and fluorescence imaging. The upper panels show the 100 nm liposomes (N4), while the lower panels display the 200 nm liposomes (N3). From left to right: (a,d) show the interferograms recorded in QPM; (b,e) the phase images retrieved from the interferograms (with calibration bar in milliradians); (c,f) the fluorescence images.

To assess the performance of QPM vs. fluorescence for prolonged imaging, the same liposome (from N1) was followed with both modes, as shown in Figure 5. The upper panels show photobleaching over time with complete signal loss and consequent loss of tracking of the liposome localization by frame 26. The lower panels display the phase maps, which continue to show the presence of a liposome even after photobleaching. No relevant structural deformations were detected throughout the process, suggesting that the loss of fluorescence did not affect the integrity of the liposome. The slight variation in the maximum phase values of the liposome as a function of time could be due to minute defocusing while acquiring the sequence of fluorescence and phase data.

When looking at the full field of view in Figure 6, we can better see how phase imaging allows for a more accurate localization of liposomes, independently of the fluorescent signal. In fact, the phase signal was present also for those liposomes that carried too little or no fluorescent label, allowing for a more accurate estimation of size distribution. The details of image processing for the estimation of size distribution are given in Section 2.7.2.

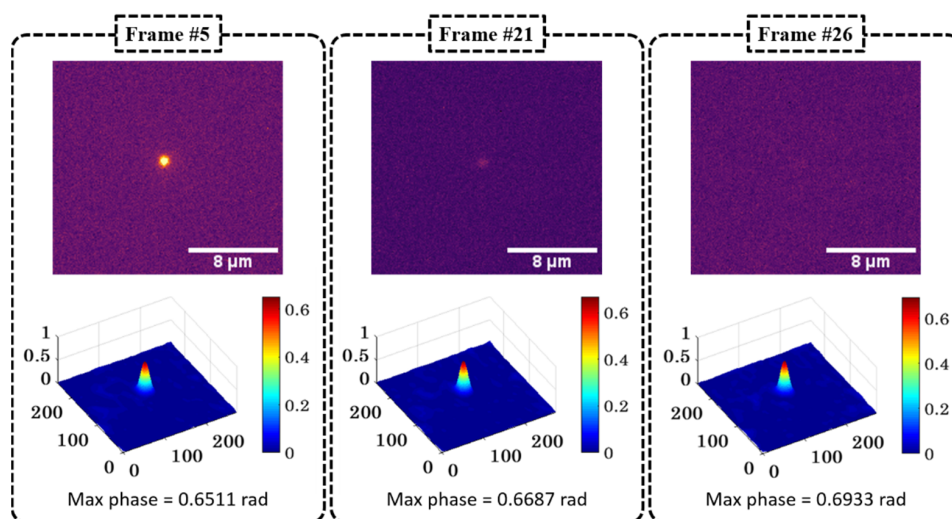


Figure 5. Single-liposome characterization over time. The sample was illuminated beyond photobleaching of the fluorescent signal without recording changes in the phase interferogram. The fluorescence images (**top**) and the phase reconstructions (**bottom**) of three sample frames (#5, #21 and #26) are presented.

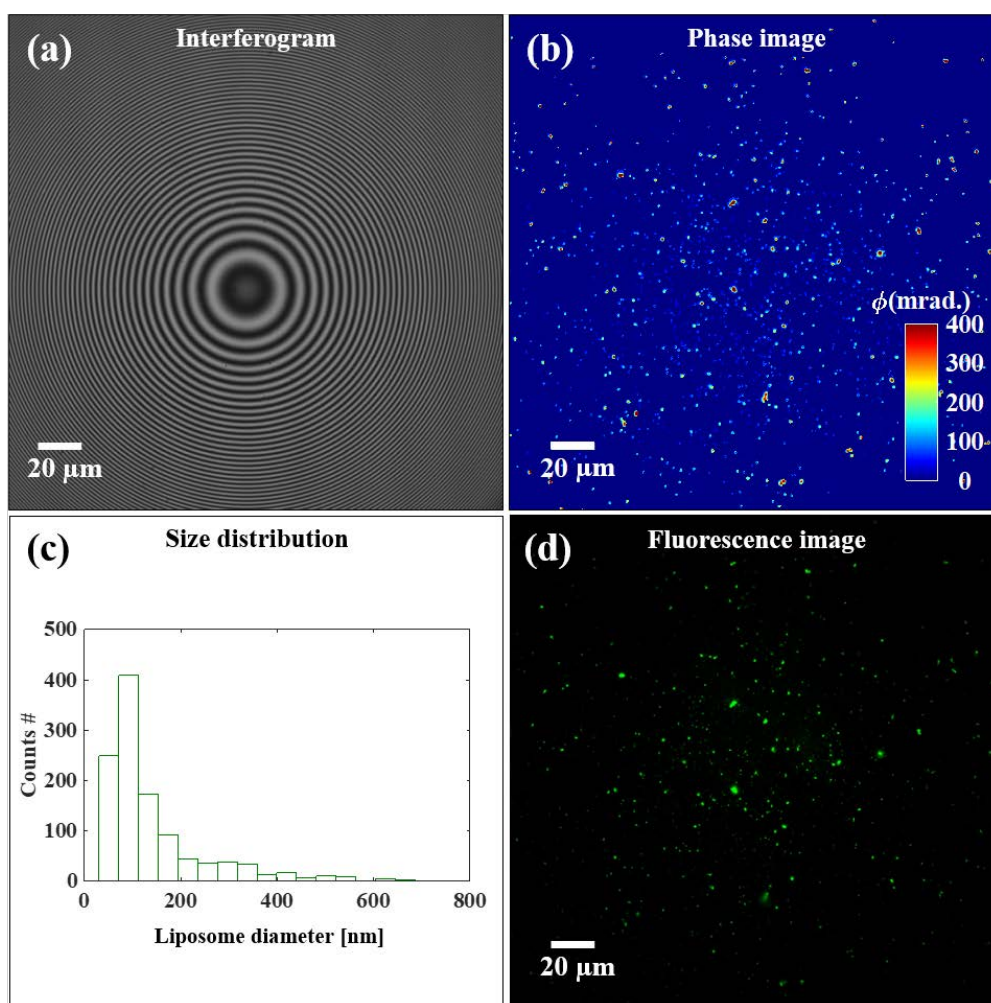


Figure 6. Full field of view of the liposome sample (N3). Panel (a) recorded interferogram; (b) phase image; (c) size distribution obtained from the sample phase image shown, and (d) fluorescence image.

4. Discussion

Lipid-based nanoparticles such as liposomes are widely used as nanomedicines because of their high biosafety. The use of lipids naturally present in cells and the adjustable size of the final particles make them relevant for both topical and systemic drug delivery. Furthermore, the presence of both a lipid bilayer and a water-based core solution allows for the loading of both hydrophobic and/or hydrophilic drugs, with great potential in many therapeutic challenges [32,42]. However, the very same versatility that contributes to their therapeutic relevance can hamper the technological characterization necessary for development processes, prior to biological testing [7]. In this work, we investigated some of the challenges related to conventional characterization methods (DLS and fluorescence-based assays) such as polydispersed samples, out-of-range particles, and labeling-dependent behavior. Furthermore, we propose QPM as a complementary technique for a deeper characterization of a nanosystem, based on a label-free single-particle analysis. Since no literature data are available on the use of QPM for liposomes characterization, at this stage, we included a fluorescent lipid (Figure 1b) within the liposomal bilayers to assist in liposomal localization during QPM characterization.

The characterization of unprocessed liposomes (N1) highlights the major challenges of conventional batch-mode analyses. Size, surface charge, and polydispersity of liposomal formulations are conventionally determined by harnessing their fast Brownian movement through intensity detection of backscattered light (DLS) [40]. Common lab-bench instruments for this purpose (e.g., Malvern Zetasizer Nano—ZS, used in this work) have a sensitivity range in the nanoscale, up to 1 μm , and their built-in Cumulants algorithm uses Gaussian fitting for the estimation of the size distribution, with resolution limited by a factor of 3 [7]. Because we used the thin-film hydration method to prepare the liposomal formulations, the re-suspension of the lipid film in the water phase was expected to form multilamellar/multivesicular macroparticles with great variability in size [43]. Hence, in the N1 sample, (I) the presence of big vesicular bodies ($>1 \mu\text{m}$) was interpreted by the software as dust contamination and excluded from the reading. (II) The tendency of these big particles to sediment during the measurement itself was translated into z-average trending by 10–30% over technical replicates of the same measurement. (III) The high polydispersity (estimated as $\text{PdI} = 0.85 \pm 0.08$) prevented a statistically acceptable fitting, resulting in a poor quality of the measurement.

For a better characterization of N1, we resorted to single-particle optical sensing, using both the available voltage thresholds to increase the accuracy of the size determination over the whole range of 0.69 to 5 μm (according to previously optimized protocols [36]). The resulting size distribution (Figure 3b) showed a truncated number-weighted distribution that still brings challenges for its interpretation. In fact, (I) the truncated distribution showed clear missing information below the lower sensitivity threshold, and (II) this number-weighted distribution was hard to compare to the DLS intensity-weighted distributions obtained for the other samples of the experiment (N2, N3, and N4, Figure 3a) [40].

Combining all available information from conventional characterization (Table 2), we noticed an unexpected size outcome for each processing (Table 1). The overall measured values of size were found to be smaller than expected from the unprocessed batch N1, down to N3 and N4—sizes that are normally very difficult to achieve with hand extrusion or, at least, require longer processing [44]. Both the smaller sizes and the instability of the batches with intermediate processing (N2) can be explained by the presence of the fluorophore in the bilayer, as this adds a layer of complexity to nanoparticle characterization. Although the use of fluorescent probes has great potential to track nanoparticle behavior in a biological environment, it comes with technological challenges in handling the formulation, such as (I) interference in DLS measurements [40], (II) surface modifications [16], (III) thermal instability [15], (IV) possible fluorophore detachment [11,17], and ultimately, (V) loss of fluorescence specificity [45].

For validation purposes, a fluorescent phospholipid (N) was chosen to ensure the least invasive labeling strategy for the phospholipid bilayer of liposomes. However, although chem-

ically linked to the hydrophobic chain of the phospholipid (Figure 1a), the NBD fluorescent moiety was shown to backflip towards the polar heads of the bilayer (Figure 1b) [34]. The increased efficiency of size reduction processing, such as hand extrusion, is therefore due to the behavior of the fluorescent moiety, which affects fluidity and viscosity of the bilayer [46]. At the same time, the position of the fluorescent moiety has a high chance of interfering with the position of the zwitterionic charges on the surface of the bilayer (Figure 1b—zoom in), consequently affecting the electrostatic interactions between the bilayer and the isotonic complex medium, thus explaining the relevant negativity of the surface [47].

To overcome the fluorophore-related downsides in nanomedicine, such as the above-mentioned technological challenges, the risk of photobleaching, and the potential phototoxicity, we focused on assessing the potential of QPM as a label-free characterization technique. As we aimed to image small liposomes (close to and below the resolution limit of light, for N3 and N4 respectively), we chose high spatial resolution over temporal resolution with on-axis microscope and phase-shifting algorithm for high-resolution and highly sensitive phase reconstruction from the recorded interferogram [22,48,49]. We achieved a successful immobilization of liposomes by pre-coating the silicon wafer support with Poly-L-Lysine. This trick allowed for non-dried-out imaging conditions, which are known to significantly affect the properties and shapes of liposomes [33]. Based on the effective immobilization of liposomes and the high spatial resolution of the setup, both diffraction-limited samples could be localized in the phase map, and their sizes differentiated (between N3 and N4) (Figure 4). As the fluorescence images in Figure 4 show, smaller liposomes presented a smaller load of dye, increasing the risk of losing track of them when relying on the sole fluorescence-based tracing in biological environment. Figure 5 shows that the rapid photobleaching of the fluorescence dye over time did not cause changes in the shape and structural integrity of the liposomes. Hence, not only is QPM independent of a fluorescent label for the detection of liposomes, but also it shows superior tracking abilities over time, as the loss of fluorescence signal does not translate in the absence/degradation of the original liposome. Furthermore, Figure 6 shows a full field of view of immobilized liposomes, both in fluorescence and in phase imaging. The higher number of liposomes visible in the phase map confirms the higher accuracy of detection that cannot be expected in label-dependent detection. Indeed, when adding both labeled and non-labeled lipids in the initial mixture, prior to evaporation and rehydration, a random distribution of the fluorescent moiety is to be expected within the sample (Figure 1b). However, the processing by hand extrusion involves “peeling” and rearrangements of the membranes that will “dilute” the dye over a larger number of smaller liposomes, potentially preventing the detection of some of them [50].

From the phase image, it is possible to obtain a size estimation of liposomes based on single-particle analysis. Choosing a $0.4 \Delta n$ between medium and liposomes, we obtained a distribution centered around 100 nm for the N3 sample. The lower size estimation when comparing to DLS can be explained by different factors. Firstly, we compared a number-weighted (QPM) with an intensity-weighted (DLS) distribution. In the latter case, as the intensity is proportional to the power of 6 of the liposome diameter (d^6), bigger particles will contribute much more to the intensity, resulting in an upwards bias, as previously shown when comparing DLS with TEM results [51]. Secondly, choosing an improper value for the refractive index of both medium and liposomes can lead to biased size estimates. This is a challenging aspect for the characterization of liposomes, as they are non-solid particles made of lipid mixtures. Figure A2 in Appendix A shows the variation of the diameter with the liposome refractive index, with downward bias as the refractive index increases. Finally, it has been shown that sub-diffraction structures can be associated with size underestimation due to the possible loss of high-frequency information during image detection [52].

Even though some optimization steps may still be required to fully utilize QPM, we have shown the potential of the method in complementing the conventional characterization of nanocarriers. The non-dried setup here used for the immobilization of

liposomes can potentially be applied for the characterization of different types of liposomes, as well as other types of lipid-based vesicles. We would expect this methodology to provide a deeper insight into the characteristics of the vesicles in their hydrated stated with rather intact morphology—as opposed to the conventional dried TEM samples. Furthermore, knowing the size of the nanosystem (thickness $h(x,y)$ in Equation (4)), QPM interferograms could be used to retrieve variations in the refractive index, thus expanding the possible applications of this technique for the morphological analysis of nanoparticles. Most interesting examples in lipid-based nanomedicine could be (I) vesicles bearing edge activators, such as deformable liposomes [35], (II) vesicles comprising glycerol within the bilayers, i.e., glycerosomes [53], (III) polymer-immobilized vesicles, such as hyalurosomes [54], (IV) surface-modified vesicles, such as liposomes for targeted immunotherapy [32], and more. However, at this stage, we can only speculate whether QPM would be easily applicable in the characterization of lipid-based vesicles where the lipid bilayers are more complex than in our case.

Future perspectives include addressing the size underestimation for sub-diffraction particles and optimizing the trade-off between spatial and temporal resolution to follow the behavior of moving nanoparticles in biological environments. This would not only allow improvement in the pre-biological characterization of nanomedicine but also provide the missing link between the technological characterization we reported here and the analysis of cellular morphology after nanoparticles treatment, recently reported to be feasible utilizing QPM [21,55,56]. Thus, QPM shows a great potential for all-in-one label-free characterization of properties and behavior of drug delivery systems.

5. Conclusions

The versatility of liposomal formulations makes their characterization challenging at times. Robust and easy-to-perform conventional techniques can fail to provide accurate results in case of high polydispersity or out-of-range nanoparticles. The characterization of nanomedicines' behavior in a biological environment—often based on the fluorescent marker incorporated within the nanocarrier—bears the risks of losing tracing specificity, causing photobleaching, and imparting photo-toxicity to the sample. QPM is hereby introduced as a complementary characterization technique with the potential of localizing, tracking over time, and allowing further image processing to obtain size distributions based on single-particle analyses.

Author Contributions: Conceptualization, all authors; methodology, J.C., N.J. and A.A.; software, N.J. and A.A.; validation, J.C., N.J. and A.A.; formal analysis, J.C., N.J. and A.A.; investigation, J.C., N.J., and A.A.; resources, B.S.A. and N.Š.-B.; data curation, J.C., N.J. and A.A.; writing—original draft preparation, J.C. and N.Š.-B.; writing—review and editing, all authors; visualization, J.C., N.J. and A.A.; supervision, B.S.A. and N.Š.-B.; funding acquisition, B.S.A. and N.Š.-B. All authors have read and agreed to the published version of the manuscript.

Funding: This project has received funding from the European Union's Horizon 2020 research and innovation program under the Marie Skłodowska-Curie grant agreement No. 766181. BSA and AA acknowledge the funding from Research Council of Norway, (project # NANO 2021–288565). Publication charges were covered by UiT The Arctic University of Norway.

Institutional Review Board Statement: Not applicable.

Informed Consent Statement: Not applicable.

Data Availability Statement: Not applicable.

Acknowledgments: The authors thank Lipoid GmbH (Ludwigshafen, Germany) for providing the Lipoid S100 used to prepare the liposomes.

Conflicts of Interest: The authors declare no conflict of interest.

Appendix A

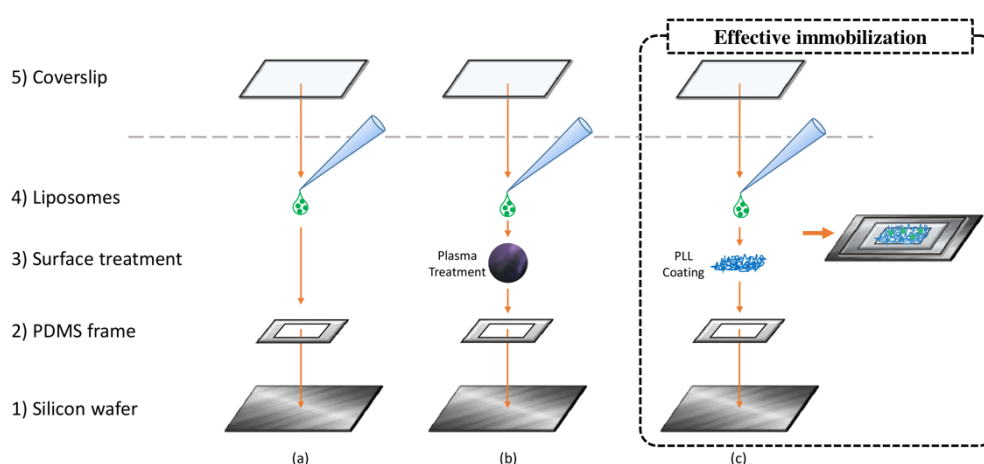


Figure A1. Non-dried immobilization setup for liposomes. In all cases, a silicon wafer was sterilized by heat and ethanol (1), and a PDMS frame was adjusted on top (2). The support was then used as such (a), after plasma treatment (b) or after coating with Poly-L-Lysine (c) (3). Few microliters of liposomal suspension were applied on top (4), and the system was allowed to equilibrate on the microscope stage. All setups were observed with and without coverslip sealing (5), but the presence of a coverslip in all cases allowed the suspension not to dry out.

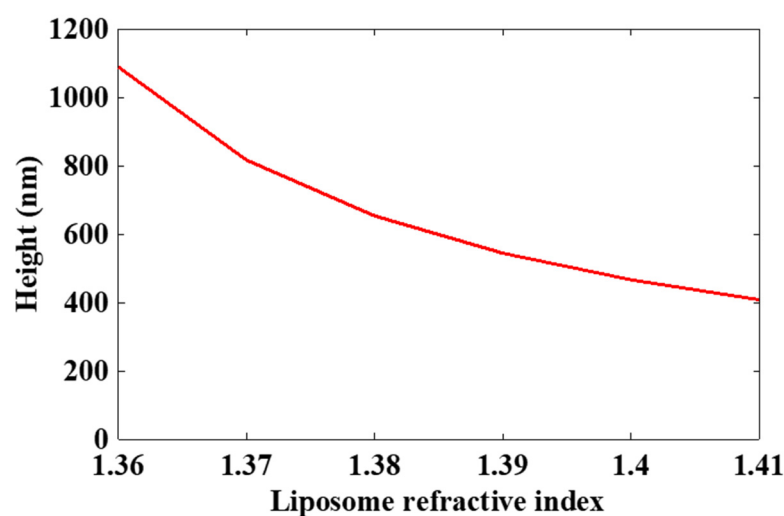


Figure A2. Variation of liposome diameter (height) as a function of the refractive index.

References

- Gadekar, V.; Borade, Y.; Kannaujia, S.; Rajpoot, K.; Anup, N.; Tambe, V.; Kalia, K.; Tekade, R.K. Nanomedicines accessible in the market for clinical interventions. *J. Control Release* **2021**, *330*, 372–397. [[CrossRef](#)]
- Cao, J.; Huang, D.; Peppas, N.A. Advanced engineered nanoparticulate platforms to address key biological barriers for delivering chemotherapeutic agents to target sites. *Adv. Drug Deliv. Rev.* **2020**, *167*, 170–188. [[CrossRef](#)]
- Fontana, F.; Figueiredo, P.; Martins, J.P.; Santos, H.A. Requirements for Animal Experiments: Problems and Challenges. *Small* **2020**, *17*, e2004182. [[CrossRef](#)]
- Danaei, M.; Dehghankhold, M.; Ataei, S.; Hasanzadeh Davarani, F.; Javanmard, R.; Dokhani, A.; Khorasani, S.; Mozafari, M. Impact of particle size and polydispersity index on the clinical applications of lipidic nanocarrier systems. *Pharmaceutics* **2018**, *10*, 57. [[CrossRef](#)] [[PubMed](#)]
- Johnston, S.T.; Faria, M.; Crampin, E.J. An analytical approach for quantifying the influence of nanoparticle polydispersity on cellular delivered dose. *J. R. Soc. Interface* **2018**, *15*, 20180364. [[CrossRef](#)] [[PubMed](#)]
- Kang, J.H.; Jang, W.Y.; Ko, Y.T. The Effect of Surface Charges on the Cellular Uptake of Liposomes Investigated by Live Cell Imaging. *Pharm. Res.* **2017**, *34*, 704–717. [[CrossRef](#)]

7. Varenne, F.; Makky, A.; Gaucher-Delmas, M.; Violleau, F.; Vauthier, C. Multimodal Dispersion of Nanoparticles: A Comprehensive Evaluation of Size Distribution with 9 Size Measurement Methods. *Pharm. Res.* **2016**, *33*, 1220–1234. [[CrossRef](#)]
8. Eleamen Oliveira, E.; Barendji, M.; Vauthier, C. Understanding Nanomedicine Size and Biological Response Dependency: What Is the Relevance of Previous Relationships Established on Only Batch-Mode DLS-Measured Sizes? *Pharm. Res.* **2020**, *37*, 161. [[CrossRef](#)]
9. Robson, A.L.; Dastoor, P.C.; Flynn, J.; Palmer, W.; Martin, A.; Smith, D.W.; Woldu, A.; Hua, S. Advantages and Limitations of Current Imaging Techniques for Characterizing Liposome Morphology. *Front. Pharmacol.* **2018**, *9*, 80. [[CrossRef](#)] [[PubMed](#)]
10. Ducat, E.; Evrard, B.; Peulen, O.; Piel, G. Cellular uptake of liposomes monitored by confocal microscopy and flow cytometry. *J. Drug Deliv. Sci. Technol.* **2011**, *21*, 469–477. [[CrossRef](#)]
11. Snipstad, S.; Hak, S.; Baghirov, H.; Sulheim, E.; Morch, Y.; Lelu, S.; von Haartman, E.; Back, M.; Nilsson, K.P.R.; Klymchenko, A.S.; et al. Labeling nanoparticles: Dye leakage and altered cellular uptake. *Cytom. A* **2017**, *91*, 760–766. [[CrossRef](#)] [[PubMed](#)]
12. Qhattal, H.S.; Hye, T.; Alali, A.; Liu, X. Hyaluronan polymer length, grafting density, and surface poly(ethylene glycol) coating influence in vivo circulation and tumor targeting of hyaluronan-grafted liposomes. *ACS Nano* **2014**, *8*, 5423–5440. [[CrossRef](#)] [[PubMed](#)]
13. Mortensen, K.I.; Tassone, C.; Ehrlich, N.; Andresen, T.L.; Flyvbjerg, H. How to Characterize Individual Nanosize Liposomes with Simple Self-Calibrating Fluorescence Microscopy. *Nano Lett.* **2018**, *18*, 2844–2851. [[CrossRef](#)] [[PubMed](#)]
14. Simonsen, J.B.; Larsen, J.B.; Hempel, C.; Eng, N.; Fossum, A.; Andresen, T.L. Unique Calibrators Derived from Fluorescence-Activated Nanoparticle Sorting for Flow Cytometric Size Estimation of Artificial Vesicles: Possibilities and Limitations. *Cytom. A* **2019**, *95*, 917–924. [[CrossRef](#)]
15. Cauzzo, J.; Nystad, M.; Holsaeter, A.M.; Basnet, P.; Skalko-Basnet, N. Following the Fate of Dye-Containing Liposomes In Vitro. *Int. J. Mol. Sci.* **2020**, *21*, 4847. [[CrossRef](#)]
16. Rodriguez-Lorenzo, L.; Fytianos, K.; Blank, F.; Von Garnier, C.; Rothen-Rutishauser, B.; Petri-Fink, A. Fluorescence-Encoded Gold Nanoparticles: Library Design and Modulation of Cellular Uptake into Dendritic Cells. *Small* **2014**, *10*, 1341–1350. [[CrossRef](#)]
17. Munter, R.; Kristensen, K.; Pedersbaek, D.; Larsen, J.B.; Simonsen, J.B.; Andresen, T.L. Dissociation of fluorescently labeled lipids from liposomes in biological environments challenges the interpretation of uptake studies. *Nanoscale* **2018**, *10*, 22720–22724. [[CrossRef](#)]
18. Suutari, T.; Silen, T.; Saari, H.O.; Desai, D.; Kerkelä, E.; Laitinen, S.; Yliperttula, M.; Karaman, D.S.; Rosenholm, J.M.; Viitala, T.; et al. Real-Time Label-Free Monitoring of Nanoparticle Cell Uptake. *Small* **2016**, *12*, 6289–6300. [[CrossRef](#)] [[PubMed](#)]
19. Kim, A.; Ng, W.B.; Bernt, W.; Cho, N.-J. Validation of size estimation of nanoparticle tracking analysis on polydisperse macromolecule assembly. *Sci. Rep.* **2019**, *9*, 1–14. [[CrossRef](#)]
20. Kong, C.; Pilger, C.; Hachmeister, H.; Wei, X.; Cheung, T.H.; Lai, C.S.W.; Lee, N.P.; Tsia, K.K.; Wong, K.K.Y.; Huser, T. High-contrast, fast chemical imaging by coherent Raman scattering using a self-synchronized two-colour fibre laser. *Light. Sci. Appl.* **2020**, *9*, 25. [[CrossRef](#)]
21. Patel, M.; Feith, M.; Janicke, B.; Alm, K.; El-Schich, Z. Evaluation of the Impact of Imprinted Polymer Particles on Morphology and Motility of Breast Cancer Cells by Using Digital Holographic Cytometry. *Appl. Sci.* **2020**, *10*, 750. [[CrossRef](#)]
22. Ahmad, A.; Dubey, V.; Butola, A.; Tinguely, J.-C.; Ahluwalia, B.S.; Mehta, D.S. Sub-nanometer height sensitivity by phase shifting interference microscopy under environmental fluctuations. *Opt. Express* **2020**, *28*, 9340–9358. [[CrossRef](#)] [[PubMed](#)]
23. Park, Y.; Depeursinge, C.; Popescu, G. Quantitative phase imaging in biomedicine. *Nat. Photonics* **2018**, *12*, 578–589. [[CrossRef](#)]
24. Popescu, G. *Quantitative Phase Imaging of Cells and Tissues*; McGraw-Hill Education: New York, NY, USA, 2011.
25. Bhaduri, B.; Edwards, C.; Pham, H.; Zhou, R.; Nguyen, T.H.; Goddard, L.L.; Popescu, G. Diffraction phase microscopy: Principles and applications in materials and life sciences. *Adv. Opt. Photonics* **2014**, *6*, 57–119. [[CrossRef](#)]
26. Ahmad, A.; Dubey, V.; Singh, G.; Singh, V.; Mehta, D.S. Quantitative phase imaging of biological cells using spatially low and temporally high coherent light source. *Opt. Lett.* **2016**, *41*, 1554–1557. [[CrossRef](#)]
27. Dubois, A.; Grieve, K.; Moneron, G.; Lecaque, R.; Vabre, L.; Boccara, C. Ultrahigh-resolution full-field optical coherence tomography. *Appl. Opt.* **2004**, *43*, 2874–2883. [[CrossRef](#)]
28. Ahmad, A.; Dubey, V.; Singh, V.R.; Tinguely, J.-C.; Øie, C.I.; Wolfson, D.L.; Mehta, D.S.; So, P.T.; Ahluwalia, B.S. Quantitative phase microscopy of red blood cells during planar trapping and propulsion. *Lab. Chip.* **2018**, *18*, 3025–3036. [[CrossRef](#)]
29. Ahmad, A.; Mahanty, T.; Dubey, V.; Butola, A.; Ahluwalia, B.S.; Mehta, D.S. Effect on the longitudinal coherence properties of a pseudothermal light source as a function of source size and temporal coherence. *Opt. Lett.* **2019**, *44*, 1817–1820. [[CrossRef](#)] [[PubMed](#)]
30. Dubey, V.; Popova, D.; Ahmad, A.; Acharya, G.; Basnet, P.; Mehta, D.S.; Ahluwalia, B.S. Partially spatially coherent digital holographic microscopy and machine learning for quantitative analysis of human spermatozoa under oxidative stress condition. *Sci. Rep.* **2019**, *9*, 3564. [[CrossRef](#)]
31. Greish, K.; Mathur, A.; Bakhiet, M.; Taurin, S. Nanomedicine: Is it lost in translation? *Ther. Deliv.* **2018**, *9*, 269–285. [[CrossRef](#)] [[PubMed](#)]
32. Filipczak, N.; Pan, J.; Yalamarty, S.S.K.; Torchillin, V.P. Recent Advancements in liposome technology. *Adv. Drug Deliv. Rev.* **2020**, *156*, 4–22. [[CrossRef](#)]
33. Chen, C.; Zhu, S.; Huang, T.; Wang, S.; Yan, X. Analytical techniques for single-liposome characterization. *Anal. Methods* **2013**, *5*, 2150–2157. [[CrossRef](#)]

34. Kay, J.G.; Koivusalo, M.; Ma, X.; Wohland, T.; Grinstein, S. Phosphatidylserine dynamics in cellular membranes. *Mol. Biol. Cell* **2012**, *23*, 2198–2212. [[CrossRef](#)]
35. Ternullo, S.; Basnet, P.; Holsaeter, A.M.; Flaten, G.E.; de Weerd, L.; Skalko-Basnet, N. Deformable liposomes for skin therapy with human epidermal growth factor: The effect of liposomal surface charge. *Eur. J. Pharm. Sci.* **2018**, *125*, 163–171. [[CrossRef](#)]
36. Martins, S.; Tho, I.; Ferreira, D.C.; Souto, E.B.; Brandl, M. Physicochemical properties of lipid nanoparticles: Effect of lipid and surfactant composition. *Drug Dev. Ind. Pharm.* **2011**, *37*, 815–824. [[CrossRef](#)] [[PubMed](#)]
37. Di Maio, I.L.; Carl, D.; Langehanenberg, P.; Valenzuela, S.M.; Battle, A.R.; Al Khazaaly, S.; Killingsworth, M.; Kemper, B.; von Bally, G.; Martin, D.K. Structural properties of liposomes from digital holographic microscopy. *BioMEMS Nanotechnol. II* **2016**, *6030*, 60361R-1. [[CrossRef](#)]
38. Ban, S.; Min, E.; Ahn, Y.; Popescu, G.; Jung, W. Effect of tissue staining in quantitative phase imaging. *J. Biophotonics* **2018**, *11*, e201700402. [[CrossRef](#)] [[PubMed](#)]
39. Wang, Z.; Han, B. Advanced iterative algorithm for phase extraction of randomly phase-shifted interferograms. *Opt. Lett.* **2004**, *29*, 1671–1673. [[CrossRef](#)]
40. Bhattacharjee, S. DLS and zeta potential—What they are and what they are not? *J. Control Release* **2016**, *235*, 337–351. [[CrossRef](#)]
41. Joraholmen, M.W.; Basnet, P.; Acharya, G.; Skalko-Basnet, N. PEGylated liposomes for topical vaginal therapy improve delivery of interferon alpha. *Eur. J. Pharm. Biopharm.* **2017**, *113*, 132–139. [[CrossRef](#)]
42. Sercombe, L.; Veerati, T.; Moheimani, F.; Wu, S.Y.; Sood, A.K.; Hua, S. Advances and challenges of liposome assisted drug delivery. *Front. Pharmacol.* **2015**, *6*, 286. [[CrossRef](#)] [[PubMed](#)]
43. Bangham, A.D.; Horne, R. Negative staining of phospholipids and their structural modification by surface-active agents as observed in the electron microscope. *J. Mol. Biol.* **1964**, *8*, 660–668. [[CrossRef](#)]
44. Zhang, H. Thin-Film Hydration Followed by Extrusion Method for Liposome Preparation. In *Liposomes: Methods and Protocols*; D'Souza, G.G.M., Ed.; Springer: New York, NY, USA, 2017; pp. 17–22. [[CrossRef](#)]
45. Lacroix, A.L.; Vengut-Climent, E.; de Rochambeau, D.; Sleiman, H.F. Uptake and Fate of Fluorescently Labeled DNA Nanostructures in Cellular Environments: A Cautionary Tale. *ACS Cent. Sci.* **2019**, *5*, 882–891. [[CrossRef](#)] [[PubMed](#)]
46. Venable, R.M.; Zhang, Y.; Hardy, B.J.; Pastor, R.W. Molecular dynamics simulations of a lipid bilayer and of hexadecane: An investigation of membrane fluidity. *Science* **1993**, *262*, 223–226. [[CrossRef](#)] [[PubMed](#)]
47. Khandelia, H.; Mouritsen, O.G. Lipid gymnastics: Evidence of complete acyl chain reversal in oxidized phospholipids from molecular simulations. *Biophys. J.* **2009**, *96*, 2734–2743. [[CrossRef](#)]
48. Wang, Z.; Millet, L.; Mir, M.; Ding, H.; Unarunotai, S.; Rogers, J.; Gillette, M.U.; Popescu, G. Spatial light interference microscopy (SLIM). *Opt. Express* **2011**, *19*, 1016–1026. [[CrossRef](#)]
49. Lee, K.; Kim, K.; Jung, J.; Heo, J.; Cho, S.; Lee, S.; Chang, G.; Jo, Y.; Park, H.; Park, Y. Quantitative phase imaging techniques for the study of cell pathophysiology: From principles to applications. *Sensors* **2013**, *13*, 4170–4191. [[CrossRef](#)]
50. Bhardwaj, U.; Burgess, D.J. Physicochemical properties of extruded and non-extruded liposomes containing the hydrophobic drug dexamethasone. *Int. J. Pharm.* **2010**, *388*, 181–189. [[CrossRef](#)] [[PubMed](#)]
51. Khlebtsov, B.; Khlebtsov, N. On the measurement of gold nanoparticle sizes by the dynamic light scattering method. *Colloid J.* **2011**, *73*, 118–127. [[CrossRef](#)]
52. Butola, A.; Popova, D.; Prasad, D.K.; Ahmad, A.; Habib, A.; Tinguely, J.C.; Basnet, P.; Acharya, G.; Senthilkumaran, P.; Mehta, D.S. High spatially sensitive quantitative phase imaging assisted with deep neural network for classification of human spermatozoa under stressed condition. *Sci. Rep.* **2020**, *10*, 1–12. [[CrossRef](#)]
53. Manca, M.L.; Zaru, M.; Manconi, M.; Lai, F.; Valenti, D.; Sinico, C.; Fadda, A.M. Glycosomes: A new tool for effective dermal and transdermal drug delivery. *Int. J. Pharm.* **2013**, *455*, 66–74. [[CrossRef](#)] [[PubMed](#)]
54. Manca, M.L.; Castangia, I.; Zaru, M.; Nácher, A.; Valenti, D.; Fernández-Busquets, X.; Fadda, A.M.; Manconi, M. Development of curcumin loaded sodium hyaluronate immobilized vesicles (hyalurosomes) and their potential on skin inflammation and wound restoring. *Biomaterials* **2015**, *71*, 100–109. [[CrossRef](#)] [[PubMed](#)]
55. Luther, E.; Mendes, L.P.; Pan, J.; Costa, D.F.; Torchilin, V.P. Applications of label-free, quantitative phase holographic imaging cytometry to the development of multi-specific nanoscale pharmaceutical formulations. *Cytom. A* **2017**, *91*, 412–423. [[CrossRef](#)]
56. Sternbæk, L.; Kimani Wamaita, M.; Gawlitza, K.; Janicke, B.; Alm, K.; Wingren Gjørloff, A. Digital holographic microscopy: Macrophage uptake of nanoprobe. *Imaging Microsc.* **2019**, *1*, 21–23.

Paper 4

Oh well.

E xe robe...

Che cossa vutto.

(proverbio veneto)

